

**Hydrothermal dolomitization
of Paleozoic successions in Northern Spain:
petrophysical properties and structural control**

INAUGURAL – DISSERTATION
zur Erlangung der Doktorwürde
der Naturwissenschaftlich-Mathematischen Gesamtfakultät
der Ruprecht-Karls-Universität
Heidelberg

vorgelegt von
MSc. Ingrid Natalia Muñoz Quijano
aus Pasto, Kolumbien

Heidelberg, im November 2014

Gutachter:
Prof. Dr. Thilo Bechstädt
Prof. Dr. Gabriel Gutiérrez Alonso

Tag der mündlichen Prüfung: 13.02.2015

A mi familia, quienes en la distancia fueron mi constante apoyo, mi fuente de inspiración y mi aliciente

ACKNOWLEDGMENTS

I would like to express my sincere gratitude to my supervisor Thilo Bechstädt for offering me the opportunity to work in Heidelberg, to increase my knowledge during this research, as well as for his revisions, suggestions, and his patience with my thesis.

I am extremely thankful to:

Gabriel Gutiérrez Alonso, University of Salamanca, who always was a big support. Being it a push in the right direction or providing a deeper insight, his advice was very helpful.

ENI S.p.A. Exploration and Production Division, San Donato Milanese, and especially to Paola Ronchi for not only sponsoring this research financially, but also for manifold help and all guidance throughout the whole project.

Maria Boni, Univ. of Naples, for help, comments and explanations in the field of geochemistry.

Fabio Lapponi and Marta Gasparini, who started with this research field in northern Spain and were a great source of knowledge.

Sarah Gleeson, Michael Joachimski and Bernd Kober, who provided geochemical analyses and supplied data as well.

Ronald Bakker and Rosario Terraciano, who offered invaluable help, advice, support, and feedback with the fluid inclusions analysis.

Thanks also to the staff of the laboratories of Heidelberg and Salamanca universities, your help was essential. Also to everyone in the Institut für Geowissenschaften, University of Heidelberg, for assistance in all administrative tasks. Thanks go to all that helped me to improve and complete this research project.

I thank all my colleagues and friends especially Judith, Christian, Enric, Esteban, Sonja, Dominik, and Francisco, who made the institute almost a warm home.

I am also indebted to all the members of the Mensa-team, Bladimiro, Raquel, Ana, Gustavo, Matias, Sabrina, Jordi, Jorham, Sergio, Felipe, Ton, Carolina and many others for entertaining discussions.

Thanks a lot to my distant friends Margarita, Alejandra, Patricia, Mencha, Ruben, Montse, Mauricio, Maria Elena, Paty, Shila and Ivan, because you always supported me on some part of the life with your friendship.

Thanks to the persons of HGC consortium in Colombia, for discussing my dissertation and giving me good working conditions.

Special Thanks to my brother Jhon Jorge, for being my hero and for helping me with the final edition.

CONTENTS**ACKNOWLEDGMENTS****ABSTRACT** xv**KURZFASSUNG** xvi**CHAPTER 1** 1
INTRODUCTION

1.1 Aims and scope	1
1.2 Area of research	2
1.3 Previous studies	3
1.4 Methods	5
1.4.1 Geological maps and transects	6
1.4.2 Sample classification and preparation	6
1.4.3 Sample scans	6
1.4.4 Stereomicroscopic analysis	6
1.4.5 Image analysis	6
1.4.6 Thin section microscopy	6
1.4.7 Cathodoluminescence (CL) microscopy	7
1.4.8 Fluid inclusions analyses	7
1.4.9 Crush leach analyses	8
1.4.10 O and C stable isotope analyses	8
1.4.11 Trace elements measurements	9
1.4.12 Petrophysical analyses	9

CHAPTER 2
GEOLOGICAL SETTING AND STRUCTURAL EVOLUTION 11

CHAPTER 3	
DOLOMITE CHARACTERIZATION AND DISTRIBUTION IN THE FIELD	21
CHAPTER 4	
DOLOMITE CLASSIFICATION	27
4.1 Textures of dolomite rocks	27
4.2 Fabrics of dolomite rocks	29
CHAPTER 5	
PETROGRAPHY	33
5.1 Replacive Dolomite (Dol A)	33
5.2 Void Filling Dolomite (Dol B)	34
5.3 Calcite (Cal1 - Cal2)	35
CHAPTER 6	
PETROPHYSICS AND SPATIAL ANALYSIS	37
6.1 Poroperm values in relation to textures and fabrics	38
6.1.1 Texture of dolomite bodies and poroperm values	38
6.1.2 Dolomite fabrics and poroperm values	38
6.1.3 Zebra characterization and poroperm values	39
6.2 Spatial analysis	41
6.2.1 Orientation of structural data in relation to macroporosity	41
6.2.2 Spatial distribution of the poroperm data	43
6.2.3 Textures of dolomites and poroperm distribution: details	44
6.2.4 Textures of dolomites and poroperm distribution: details	45
CHAPTER 7	
IMAGE ANALYSIS	51
CHAPTER 8	
GEOCHEMICAL ANALYSES AND SPATIAL DISTRIBUTION	57

8.1. Elemental geochemistry	57
8.1.1 XRD analyses	57
8.1.2 ICP-ES, SEM-EDX-WDX analyses	58
8.2. Isotope geochemistry	64
8.2.1 Oxygen and carbon isotopic composition	64
8.2.2 Strontium isotopic composition	67
 CHAPTER 9	 71
FLUID INCLUSION (FI) STUDY	
9.1 Fluid inclusion petrography	71
9.2 Fluid inclusion microthermometry	73
9.2.1 Microthermometry in Dol A	76
9.2.2 Microthermometry of Dol B	76
9.3 Raman spectroscopy	77
9.4 Preliminary discussion of microthermometric data	79
9.5 Salinity and temperature	80
9.6 Crush-leach analyses	82
 CHAPTER 10	 87
DISCUSSION	
10.1 Dolomite occurrence, petrography, and regional poroperm properties	87
10.2 Geochemistry	90
10.2.1 Stoichiometry and degree of order	90
10.2.2 Elemental geochemistry	90
10.2.3 Isotope geochemistry	92
10.3 Fluid characterization	95
10.4 Age of dolomitization	96

CHAPTER 11	99
MODEL OF DOLOMITIZATION AND POROSITY FORMATION	
CHAPTER 12	107
CONCLUSIONS	
REFERENCES	111
ANNEXES	131
ANNEX 1	
DIGITAL FILE ATTACHMENT	
GEOLOGICAL AND DOLOMITE DISTRIBUTION MAP	
ANNEX 2	
MACROSCOPIC DESCRIPTION	
ANNEX 3	
PETROGRAPHIC DESCRIPTION	
ANNEX 4	
CATHODOLUMINESCENCE DESCRIPTION	
ANNEX 5	
STRUCTURAL DATA	
ANNEX 6	
POROPERM RCA & IMAGE ANALYSES	
ANNEX 7	
ELEMENTAL GEOCHEMISTRY	
ANNEX 8	
ISOTOPE GEOCHEMISTRY	
ANNEX 9	
MICROTHERMOMETRY (FI)	
ANNEX 10	
CRUSH LEACH DATA	

TABLES

Table 1: Comparison between geochemical data from the Cambrian-hosted dolomites and the Carboniferous-hosted dolomites (Lapponi, 2007).	4
Table 2: Porosity data from RCA and image analyses, the former analyses giving also permeabilities.	54
Table 3: Elemental geochemistry from ICP-ES, and SEM-EDX-WDX analyses. The concentrations of Ca and Mg are reported in %, the ones of Na, Fe, Mn, and Sr in ppm. Min.= minimum value, Mean = mean value, Max. = maximum value, Std. Dev. = standard deviation.	59
Table 4: O and C isotope geochemistry: $\delta^{18}\text{O}$ and $\delta^{13}\text{C}$ (‰ PDB) are reported for the different mineral phases analysed.	64
Table 5: $^{87}\text{Sr}/^{86}\text{Sr}$ ratios of different mineral phases. In parenthesis is the number of measured samples. Min. = minimum value, Mean = mean value, Max = maximum value, Std. Dev. = standard deviation.	67
Table 6: Main microthermometric data of different mineral phases in fluid inclusions.	73
Table 7: Main microthermometric values of different mineral phases.	81

FIGURES

Fig. 1.1: Geological map of the Cantabrian Zone, NW Spain (modified from Alonso et al., 2009), showing the study area within the blue frame.	2
Fig. 1.2: Tectonic units of the Cantabrian Zone, NW Spain (modified from Alonso et al., 2009) with the study area within the red frame.	3
Fig. 2.1: Geological sketch map of the Variscan Belt of central and Western Europe (modified from Martínez Catalán, 1990).	11
Fig. 2.2: Association of post-tectonic igneous activity in the NW of Iberia (from Fernández-Suárez et al., 2000).	14
Fig. 2.3: Geological sketch of the West-European Variscan belt, showing the differences between the inner and outer arc (from Gutiérrez-Alonso et al., 2004a).	15
Fig. 2.4: Different processes recorded in the Cantabrian Orocline and their relationship to the two main phases of oroclinal formation, the acquisition of twin strains (and associated stresses) during deformation, the age of various magmatic pulses, and the age of sedimentary basins (from Weil et al., 2012).	16
Fig. 2.5: Effect of lithospheric bending around a vertical axis, and the proposed deformation mechanism of tangential longitudinal strain (from Gutiérrez-Alonso et al., 2004a).	16
Fig. 2.6: Sketch illustrating the delamination process caused by post-orogenic oroclinal bending (from Gutiérrez-Alonso et al., 2012).	17
Fig. 2.7: Structural sketch of the central sector of the León Thrust showing its relation with the surrounding structure (from Alonso et al., 2009).	18
Fig. 3.1: Dolomite distribution and sampling profiles, SW Cantabrian Zone.	22
Fig. 3.2: Colour contrast of dolomite bodies: (a) Orthophoto of Viadango area (SIG PAC image); (b) irregular dolomite body, Viadango.	23
Fig. 3.3: Geometry of dolomite bodies. (a) Irregular and sub-vertical contacts in Nocedo de Curueño area; (b) spotty dolomite in Salamón area.	23
Fig. 3.4: Propagation structures of dolomitization, (a) fractures in Llamazares area, (b) net system in Salamón area, (c) spot of dolomite in Nocedo de Curueño area.	24

Fig. 3.5: (a) Dolomitized crinoidal limestones of the Valdeteja Fm. In Millaró area; (b) stylolites preserved in dolomite, in Isoba area.	24
Fig. 3.6: Porosity scale in dolomite bodies: (a) large scale macroporosity, Isoba; (b) medium scale porosity, Millaró; (c) microscopic scale porosity (cathodoluminescence picture), Isoba.	25
Fig. 3.7: (a) Talc Mine <i>La Respina</i> , Puebla de Lillo. (b) Former Fe Mine <i>Saliciencia Lakes</i> , Somiedo.	26
Fig. 4.1: Basic textures in dolomite rocks.	27
Fig. 4.2: Textures of dolomite rocks in outcrops: (a) massive (locality Cofiñal); (b) banded (locality Millaró); (c) breccia (locality San Emiliano 2); (d) proportions of the different textures.	28
Fig. 4.3: Basic types of dolomite fabrics.	29
Fig. 4.4: Subdivision of the observed zebra fabrics (modified from Davies, 2004; Davies & Smith, 2006).	30
Fig. 4.5: Different dolomite fabrics: (a) meso zebra; (b) micro zebra; (c) vuggy; (d) fine non macroporous; (e) coarse non macroporous (sucrosic); (f) breccia; (g) proportion of the different fabrics observed.	31
Fig. 5.1: Microphotographs in thin section of Sample 167, Sierra del Turrón: (a) normal under polarized light, and (b) cathodoluminescence characteristics of Dolomite A1. Sty: Stylolite observed.	33
Fig. 5.2: Microphotographs in thin section of Sample 28, Lugueros. Dolomite A2, B1, B2 and Cal 1 filling secondary porosity. Views under: (a) normal polarized light, and (b) cathodoluminescence. Porosity is well defined.	34
Fig. 5.3: Microphotographs in thin section of Sample 202, Llamazares, showing Dolomite B2 and Calcite 2 under (a) normal polarized light, and (b) cathodoluminescence., Slight displacements along microfractures are observed (one is marked).	35
Fig. 6.1: Φ/k values: plots with (a) normal scale, (b) log-log scale, and (c) log-log scale (mean values).	37
Fig. 6.2: Φ/k data grouped according to the different textures of the dolomite bodies: plots with (a) normal scale, (b) log/normal scale, (c) log/normal scale (mean values). (d) Column diagram of the mean values.	38

Fig. 6.3: $\Phi_{II/k}$ data grouped according to the different fabrics of the dolomites: Graphs show (a) normal scale, (b) log/normal scale, (c) log/normal scale (mean values). (d) Column diagram of the mean values.	39
Fig. 6.4: $\Phi_{II/k}$ data grouped according to the sizes of the rhythmic bands. Graphs have (a) normal scale, (b) log/normal scale, (c) log/normal scale (mean values). (d) Column diagram (mean values).	40
Fig. 6.5: $\Phi_{II/k}$ plots grouped according to the orientation of the rhythmic bands. Plots have (a) normal scale, (b) log/normal scale, (c) log/normal scale (mean values). (d) Column diagram (mean values).	40
Fig. 6.6: $\Phi_{II/k}$ plots grouped according to the shape of the rhythmic bands. Graphs have (a) normal scale, (b) log/normal scale, (c) log/normal scale (mean values), and are plotted (d) as column diagram (mean values).	41
Fig. 6.7: Orientation of bedding direction to alignment of macroporosity ($S_o \wedge S_p$) along the E-W transect. Shaded zone: interval with $S_o \wedge S_p < 30$.	42
Fig. 6.8: Spatial distribution of porosity and permeability along the E-W transect	43
Fig. 6.9: Mean values of porosity in rocks of different textures (breccia, massive, banded) and lithology (dolomite-limestone, limestone) along the E-W transect.	44
Fig. 6.10: Mean values of permeability in rocks of different textures (breccia, massive, banded) and lithology (dolomite-limestone, limestone) along the E-W transect.	45
Fig. 6.11: Different fabrics and corresponding mean poroperm values along the E-W transect.	46
Fig. 6.12: E-W poroperm distribution according to the mean size of the rhythmic zebra bands. (a): Mean porosity values; (b): mean permeability values.	47
Fig. 6.13: Poroperm values according to the orientation of the rhythmic zebra bands. (a): Mean values of porosity; (b): mean values of permeability.	48
Fig. 6.14: Poroperm values related to the shape of the rhythmic zebra bands. (a): Mean values of porosity; (b): mean values of permeability.	49
Fig. 7.1: Scale of image analysis. (a) Macro scale: outcrop of dolomite with massive texture and vuggy fabric. Isoba (b) Medium scale: hand sample, plugs and slab. Millaró(c) Micro scale: thin section. Isoba.	51

Fig. 7.2: Example of image analysis applied to a dolomite sample (Pie-dräsecha). (a) Original scanned picture; (b) image of porosity; (c) image of dolomite cement.	52
Fig. 7.3: Example of image analysis applied to a dolomite sample (Pie-dräsecha). (a) P1: original porosity, P2: final porosity; (b) and (c) frequency diagrams of porosity area and percentage of pores, according to the maximum pore diameter.	53
Fig. 7.4: Plot of IA porosity versus Δ factor (IA-plug porosity). Some of the fabric types are restricted to certain areas of the diagram.	53
Fig. 7.5: Distribution of pore diameters in relation to the different dolomite fabrics.	54
Fig. 7.6: Mean porosity values according to image analyses of the dolomite fabrics along the E-W transect.	55
Fig. 8.1: Stoichiometry versus ordering. Dol A and Dol B show very similar values.	57
Fig. 8.2: Mean mol % CaCO ₃ (a) and OR values (b) along the E-W transect.	58
Fig. 8.3: Relation between Ca and Mg for the two dolomite phases.	60
Fig. 8.4: Mean Ca values of Dol A and Dol B along the E-W transect.	60
Fig. 8.5: Mean Mg values of the two dolomite phases along the E-W transect.	61
Fig. 8.6: Mean Na values of Dol A and Dol B along the E-W transect.	61
Fig. 8.7: Mean Fe (a) and Mn (b) contents (in ppm) along the E-W transect.	62
Fig. 8.8: Correlation between the Fe and Mn contents of Dol A and Dol B.	63
Fig. 8.9: Mean Sr values of Dol A and Dol B along the E-W transect.	63
Fig. 8.10: O and C isotope composition of the different carbonate phases.	65
Fig. 8.11: $\delta^{18}\text{O}$ values along the E-W transect.	66
Fig. 8.12: $\delta^{13}\text{C}$ values along the E-W transect.	66
Fig. 8.13: Relation between Sr contents and $^{87}\text{Sr}/^{86}\text{Sr}$ ratios for host limestones and dolomite phases.	68

Fig. 8.14: Variation between $\delta^{18}\text{O}$ and $^{87}\text{Sr}/^{86}\text{Sr}$ ratios.	68
Fig. 8.15: Variation between $\delta^{13}\text{C}$ and $^{87}\text{Sr}/^{86}\text{Sr}$ ratios.	69
Fig. 8.16: $^{87}\text{Sr}/^{86}\text{Sr}$ values in an E-W transect.	69
Fig. 9.1: Microphotographs of: (a) Dol A1 with cloudy appearance due to FIIs; (b) irregular shaped, 2-phase, liquid-rich FIIs in Dol A2; (c) FI inclusions elongated along the direction of growth of a saddle dolomite (Dol B); (d) Dol B with two phase, liquid-rich fluid inclusions; (e) fluid inclusions in Quartz. All microphotographs were taken at <i>Troom</i> 25°C.	72
Fig. 9.2: Frequency histograms for homogenization temperatures (T_h) in different mineral phases. (a) Dol A; (b) Dol B; (c) Calcite 1; (d) Quartz.	74
Fig. 9.3: Frequency histograms for melting temperatures (T_m) in different mineral phases. (a) Dol A; (b) Dol B; (c) Calcite 1; (d) Quartz.	75
Fig. 9.4: Covariance plot T_m - T_h , showing differences between the four mineral phases analyzed.	75
Fig. 9.5: Dol A microthermometry-values from different localities: (a) frequency distribution of T_h ; (b) frequency distribution of T_m ice; (c) covariance plot T_h - T_m ice.	76
Fig. 9.6: Dol B microthermometry-values from different localities: (a) Frequency distribution of Th ; (b) frequency distribution of T_m ice; (c) Th - T_m ice covariance plot.	77
Fig. 9.7: Raman spectra (a) at room temperature; (b) after normal heating-cooling procedure at -150 °C; (c) after normal heating- cooling procedure at -80 °C; (d) after normal heating-cooling procedure at -50 °C (modified from Lapponi et al., 2007).	78
Fig. 9.8: Raman spectra in fluid inclusions at -190°C after a composite heating-cooling procedure. Three different solid phases are recognizable: (a) ice and hydrohalite; (b) a third unknown salt-hydrate phase (hydro-X) (modified from Lapponi et al., 2007).	79
Fig. 9.9: Covariance plots T_h -salinity, showing differences between four mineral phases: (a) salinity NaCl eq. wt %; (b) salinity MgCl_2 eq. wt%.	81
Fig. 9.10: Covariance plots T_h -salinity, showing differences between localities: (a) Dol A FIIs, salinity in NaCl eq. wt %; (b) Dol A FIIs, salinity in MgCl_2 eq. wt %; (c) Dol B FIIs, salinity in NaCl eq. wt %; (d) Dol B FIIs, salinity in MgCl_2 eq. wt %.	82

Fig. 9.11: Fluid Inclusions crush-leach plots. (a) Log-log plot of Br versus Cl diagram; (b) plot of molar Na/Br versus Cl/Br ratios; (c) plot of molar K/Cl versus Cl/Br ratios; (d) water-rock interaction plot presenting molar K/Na versus Li/Na ratios.	84
Fig. 9.12: Crush-leach fluid composition of Dol B Carboniferous rocks in Cantabria zone: Log (Cl) vs. Log (Br) diagram (modified after Lapponi, 2007).	85
Fig. 9.13: Fluid Inclusions crush-leach plot of molar K/Cl versus Cl/Br ratios; K-feldspar dissolution indicated by localities.	85
Fig. 10.1: Eastern zone (a), Central zone (b), Western zone (c), each showing similar poroperm values in the dolomites according to texture, fabric, and structural relationships.	89
Fig. 10.2: O and C isotope composition of the different carbonate phases. The mean values of $\delta^{18}\text{O}$ and $\delta_{13}\text{C}$ are plotted together with the standard deviation range. The isotope composition of Late Carboniferous marine calcites (MC) from Spain (Grossman, 1994) is reported together with the hypothetical isotope composition of coeval marine dolomites (MD), assuming a 3‰ difference in $\delta^{18}\text{O}$ between calcite and dolomite (Land, 1980, 1985).	93
Fig. 10.3: $^{87}\text{Sr}/^{86}\text{Sr}$ ratios of the analyzed phases compared to potential Sr reservoirs (corrected to 270–275 Ma).	94
Fig. 10.4: Precipitation temperature versus O isotopic composition of the dolomite phases analyzed. $\delta^{18}\text{O}$ of the fluid in equilibrium was calculated using the fractionation equation of Land (1983). Modified from Gasparrini et al. (2006).	96
Fig. 11.1: Regional model of tectonic evolution and dolomitization scenario in the Cantabrian zone.	101
Fig. 11.2: Model of dolomitization: Shallow water basins in Early Permian time contain strongly evaporated seawater. This concentrated seawater is percolating downward and set into motion as convective fluid, dolomitizing areas further to the south (orange areas) especially near larger faults, but also parts of the overthrust Picos de Europa unit to the north. For further explanation see the text.	102
Fig. 11.3: Patterns of outcrop analogues with reservoir characteristics in the Cantabrian zone	105

ABSTRACT

The Cantabrian Zone in NW Spain represents the foreland fold and thrust belt of the Variscan orogen, formed by Precambrian basement covered by an almost complete succession of Palaeozoic sediments, mostly deposited on a passive margin. Most of the succession underwent deformation with almost no internal strain (Pastor-Gálán et al., 2009), and in most areas with only a diagenetic overprint. This includes, however, several thermal events (only locally up to the epizone) and different episodes of fluid flow. One of these epigenetic fluid flow events produced pervasive dolomitization on a large scale covering over 1000 km² in todays outcrops. The present research focused on this post-orogenic hydrothermal dolomitization, which strongly increased porosity and permeability in large volumes of rocks. It affected mainly Carboniferous but to a smaller degree also older carbonate successions. Earlier research (Gasparini et al., 2006; Lapponi et al., 2007) concentrated on the type of dolomite and its geochemical and isotopic characteristics, as well as the fluids generating this dolomite (very saline, originally evaporitic brines with elevated temperature). Of special interest was the timing of dolomitization (latest Carboniferous/earliest Permian) and the relation with the geodynamic setting: dolomitization was associated, at least time wise, with the bending of the Cantabrian Arch (see Gutiérrez-Alonso et al., 2004; Weil et al., 2013) related with a lithospheric delamination-induced thermal event. These main results were confirmed by this research.

The investigated area was distinctly extended compared with the mentioned earlier research. A study of petrophysical properties, geochemistry and fluid inclusions was carried out, in relation to the characterization of the dolomite bodies and the structural setting. Of special interest was the amount, types and regional distribution of porosity and permeability. Various parameters such as crystal size, orientation of the porosity in relation to dolomite textures and fabrics, and eventual rhythmicity of pore space are used to identify regional dolomitization patterns. The data from the investigated outcrops within the large area of research serve to outline areas of increased porosity and permeability. The latter favourable factors might allow to predict locations of dolomite reservoirs with enhanced porosity elsewhere.

Large bodies of hydrothermal dolomite were favoured by: (i) a restricted and large reservoir of highly evaporated sea water; (ii) intense fracturing acting as fluid flow pathways; and (iii) a high thermal gradient enhancing convectional fluid flow. Positive petrophysical properties are affected by specific dolomite fabrics (Zebra, Vuggy, and Non Macro Porous), over-dolomitization reduced dramatically porosity.

The outermost western region of the Cantabrian Orocline provides a combination of the most positive factors for potential dolomite hydrocarbon reservoirs. Here the dolomite bodies are large, petrophysical properties are favourable, fracturation intensity is high and over-dolomitization is low.

KURZFASSUNG

Die Kantabrische Zone Nordwest-Spaniens repräsentiert den Falten- und Überschiebungsgürtel des Variszischen Vorlandes. Die Abfolge besteht aus präkambrischem Basement überlagert von einer fast kompletten Abfolge paläozoischer Sedimente, die zum großen Teil auf einem passiven Ozeanrand abgelagert wurden. Der Großteil der Kantabrischen Zone erfuhr Deformation mit fast keinem internen Strain (Pastor-Galán et al., 2009) und verblieb fast überall im diagenetischen Bereich. Allerdings kam es zu mehreren geothermalen Ereignissen, die nur örtlich bis zu einer epizonalen Überprägung führten. Wichtig sind verschiedene Fluid-Flow Ereignisse. Eines dieser epigenetischen Ereignisse von Flüssigkeitsströmungen erzeugte eine sehr umfassende, großräumige Dolomitisierung mit einer horizontalen, heute aufgeschlossenen Ausdehnung von mehr als 1000 km².

Das Forschungsvorhaben war auf diese post-orogene, hydrothermale Dolomitisierung fokussiert, welche die Porosität und Permeabilität großer Gesteinsvolumina wesentlich verbesserte. Ein Großteil dieser Dolomitisierung erfolgte in karbonen Abfolgen, untergeordnet auch in prä-karbonen karbonatischen Gesteinspaketen. Frühere Forschungsarbeiten (Gasparrini et al., 2006; Lapponi et al., 2007) waren auf die Dolomittypen und deren geochemische und isotopische Charakterisierung konzentriert, ferner auf die Art der Fluide (hoch saline, ursprünglich evaporitische „Brines“ mit erhöhter Temperatur), welche die Dolomitisierung bewirkten. Von besonderem Interesse war auch der Zeitpunkt der Dolomitisierung (spätestes Karbon / frühestes Perm) und die Beziehung zu den geodynamischen Abläufen: die Dolomitisierung war zumindest zeitlich verbunden mit der Biegung des Kantabrischen Bogens (vergleiche Gutiérrez-Alonso et al., 2004; Weil et al., 2013), die wiederum im Zusammenhang stand mit einem durch lithosphärische Delamination bewirkten thermalen Ereignis. Diese Ergebnisse wurden durch die vorliegende Arbeit bestätigt.

Das Arbeitsgebiet wurde gegenüber jenem der früheren Arbeiten wesentlich erweitert. Schwerpunkt lag nunmehr auf den petrophysikalischen Eigenschaften, der Geochemie und der Untersuchung von Flüssigkeitseinschlüssen in Verbindung zu der Charakteristik der Dolomitkörper und deren struktureller Prägung. Von besonderem Interesse für diese Arbeit waren das Ausmaß der Porosität, die Porositätstypen und deren regionale Verbreitung, ferner die Permeabilität. Regionale Dolomitisierungstypen wurden unterschieden aufgrund von Parametern wie Kristallgröße, Orientierung der Porosität in Beziehung zu Texturen und Gefüge des Dolomits, sowie eventuelle Rhythmität der Anordnung des Porenraumes. Die Daten der großräumig verteilten Aufschlüsse ermöglichen es, positive Faktoren für die Bildung erhöhter Porosität und Permeabilität zu erkennen. Diese können dann auf wirtschaftlich bedeutendere Dolomit-Reservoirs in anderen Teilen der Welt übertragen werden.

Die Bildung großer Körper hydrothermalen Dolomits wurden begünstigt durch: (i) ein abgeschnürtes, großes Reservoir hoch evapierten Meerwassers; (ii) intensive Klüftung sowie Störungen, die als Migrationsbahnen der Fluide dienen; und (iii) ein hoher geothermischer Gradient der einen konvektiven Fluidstrom erlaubt. Positive petrophysikalische Eigenschaften werden durch spezifische Dolomitgefüge hervorgerufen („Zebra“, „Vuggy“, und „Non Macro Porous“), wohingegen Überdolomitisierung die Porosität dramatisch verringerte.

Die westlichen Randbereiche der Kantabrischen Orokline weisen eine Kombination von Faktoren auf, die positiv für potentielle Kohlenwasserstoff-Reservoirs sind. Die Dolomitkörper haben große Erstreckung, die petrophysikalischen Parameter sind günstig, die Frakturierung ist hoch und Überdolomitisierung wenig ausgeprägt.

INTRODUCTION

1.1 Aims and scope

The Cantabrian Zone (CZ) is the core of the Iberian Massif in the NW of Spain, and represents a foreland basin of the Variscan orogen, formed by Precambrian basement covered by an almost complete succession of Palaeozoic sediments. This stratigraphic pile was thrusted and folded in the Late Carboniferous during the Variscan orogeny. The tectonic units in the Cantabrian Zone possess a thin-skinned style (Pérez-Estaún et al., 1988, 1991), underwent deformation with almost no internal strain (Pastor-Galán et al., 2009), and show a mostly only diagenetic overprint. This includes, however, several thermal events (only locally up to the epizone) and different episodes of fluid flow. One of these fluid flow events produced pervasive dolomitization on a large scale, affecting predominantly, but not exclusively, the carbonate successions of Late Carboniferous age (Paniagua et al., 1993; Gómez-Fernández et al., 2000; Gasparrini, 2003; Gasparrini et al., 2006; Carriere, 2006; Lapponi, 2007, Lapponi et al., 2007, 2014).

Large dolomite bodies occur in most of the thrust tectonic units in the CZ. This together with the variety of lithologies affected by dolomitization indicates an orogen-wide, large-scale fluid flow. It is interpreted to be due to a lithospheric delamination process during the late Variscan (Gutiérrez-Alonso et al., 2004), which is related with orocline development, causing the necessary thermal gradient to facilitate the fluid flow and precipitation of “hydrothermal” dolomites (Gasparrini, 2003; Gasparrini et al., 2006; Lapponi et al., 2014).

The main aim of the research presented here is to broaden further the knowledge on the regional dolomitization process and its effects. This includes characterization of the dolomite bodies and of their distribution in the working area, the amount, types and regional distribution of porosity and permeability, as well as the lithological and structural controls favouring higher porosity-permeability (PoroPerm) values. Various parameters such as crystal size, eventual rhythmicity of pores, orientation of porosity and permeability in relation to dolomite textures, fabrics and tectonic grain are used to identify ubiquitous general patterns. Special emphasis was laid on the relationship between structural changes (at local and regional scale) and dolomitization. In addition, this study evaluates in more detail and in a broader area than previously done the petrological characteristics, the geochemistry including isotopes, and the fluid inclusions of the dolomites to characterize the type of dolomitizing fluids.

The data from the investigated outcrop analogues might serve to outline factors favouring increased porosity and permeability and to predict areas of better quality in hydrocarbon-producing dolomite reservoirs elsewhere.

This research was financed by the industrial sponsor Eni S.p.A. Exploration and Production Division, San Donato Milanese, Italy, and co-supervised by Paola Ronchi from the above-mentioned company. The study was carried out at the Geosciences Institute of the University of Heidelberg, Germany, as well as the laboratories of Eni, San Donato Milanese.

1.2 Area of research

The working area covers approximately 2000 km² and comprises the domain with the best outcrops of large dolomite bodies, the southern part of the Cantabrian Zone in the northwest of the Iberian Peninsula. The Cantabrian Zone (CZ) is the core of the curved Iberian Massif, and represents a foreland basin of the Variscan orogen, formed by Precambrian basement covered by Palaeozoic sediments (Fig. 1.1).

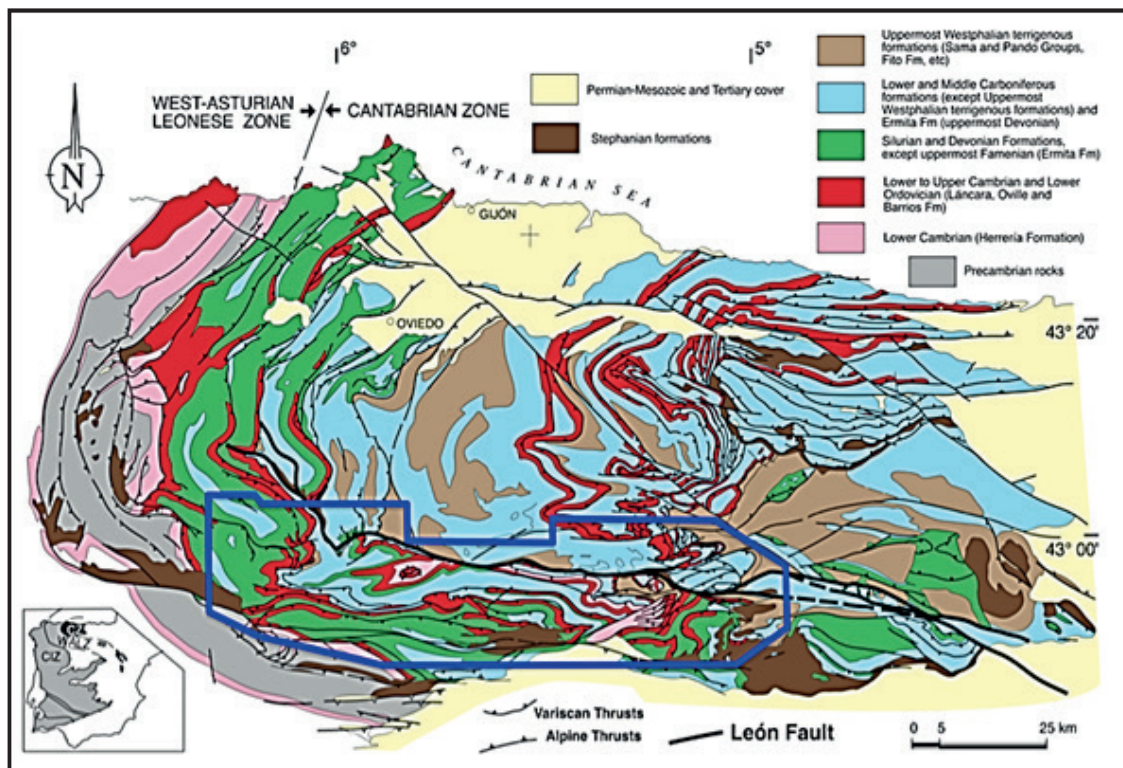


Fig. 1.1: Geological map of the Cantabrian Zone, NW Spain (modified from Alonso et al., 2009), showing the study area within the blue frame.

New interpretations of the León fault outline also a new geological division of the Cantabrian Zone (Alonso et al., 2009), which is subdivided according to stratigraphic features and tectonic units into the Somiedo Unit, Bodón-Ponga Unit, Esla Unit, Valsurcio Unit, and Pisuerga-Carrión Unit. The working area partly covers four of these units (Fig. 1.2).

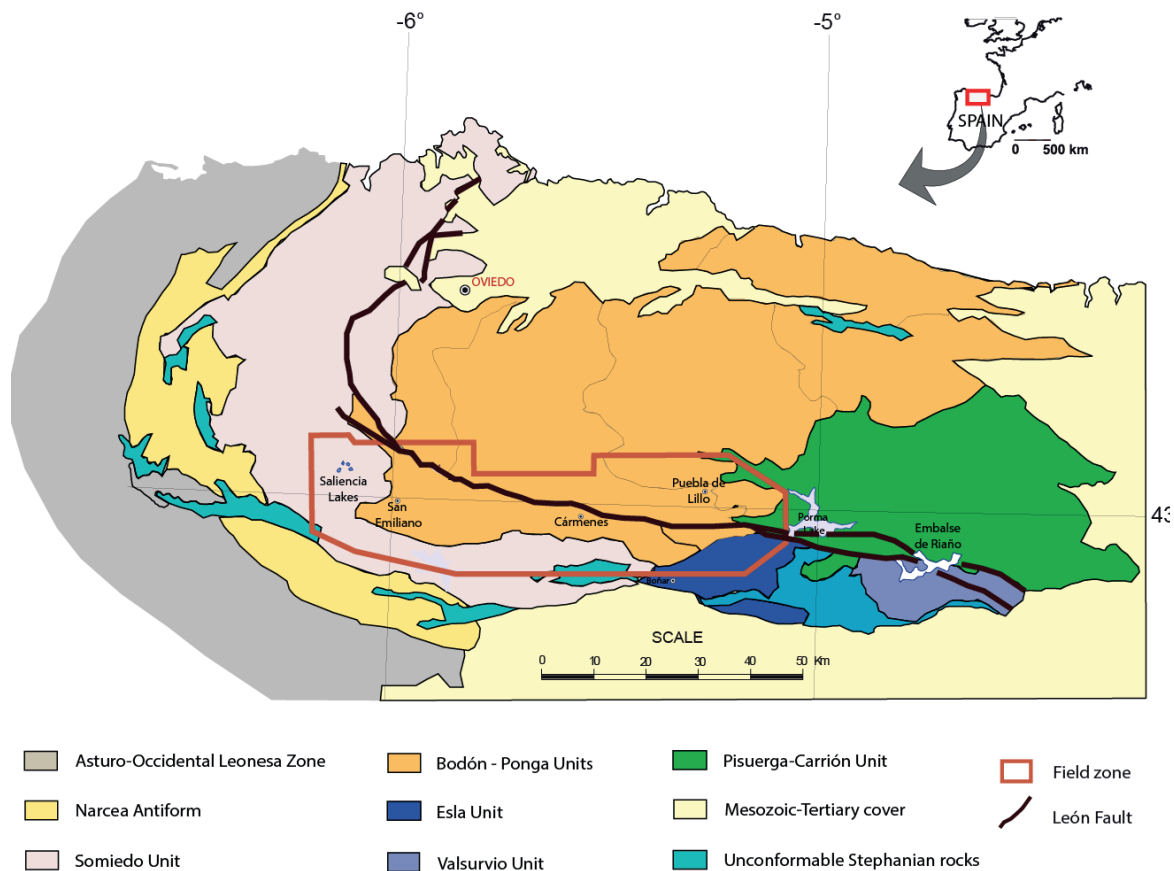


Fig. 1.2: Tectonic units of the Cantabrian Zone, NW Spain (modified from Alonso et al., 2009) with the study area within the red frame.

1.3 Previous studies

Two important previous studies dealt already with the dolomitization process in the centre of the present study area in the southern Cantabrian Zone. These are the doctoral theses of Gasparrini (2003) and Lapponi (2007), which were partly published (Gasparrini et al., 2006a, b; Lapponi et al., 2007, 2014). The studies concentrated on the description of the different types of dolomite and its geochemical and isotopic characteristics, the fluids generating this dolomite (marine, very saline, originally evaporitic brines of higher temperature), the timing of dolomitization (probably Latest Carboniferous/Early Permian), and the general relation with the geodynamic setting: dolomitization is associated, at least time-wise, with the bending of the Cantabrian Arc (see Gutiérrez-Alonso et al., 2004, 2012; Weil et al., 2010, 2013) together with its related lithospheric delamination and a linked thermal event.

Gasparrini et al. (2006a) outlined the main episodes of late diagenesis in the Carboniferous carbonates of mainly the Bodón thrust unit and defined the causes of dolomitization as well as the origin of the dolomitizing fluids. For this study, transmitted light and cathodoluminescence microscopy, X-ray diffraction and ICP-ES analyses, O, C and Sr isotope geochemistry and fluid inclusion investigation, comprising microthermometry and Raman spectroscopy was employed. Gasparrini et al. (2006a)

postulated that dolomitization occurred during the Early Permian, when predominantly strike-slip tectonics followed the main Variscan compression. During this period, the Cantabrian Zone had reached its curved shape (Gutiérrez-Alonso et al., 2004) and was undergoing an increased heat and fluid flow. This is also indicated by the intrusion of many granitoid bodies apparently related with the lithospheric delamination (Gutiérrez-Alonso et al., 2011).

Subsequently, the Cambrian carbonate succession of the Láncara Fm. was investigated (Lapponi, 2007; Lapponi et al., 2007, 2014). The same bundle of petrographic and geochemical methods was used, and in addition crush-leach analyses, to distinguish and characterize the late epigenetic dolomitizing fluid. The data revealed that a coeval fluid flow with similar composition and geological processes affected both the Cambrian and the Carboniferous carbonate successions. Geochemical and petrographic evidences indicate that the dolomitization of the Cambrian Láncara carbonates was directly related to the same event that produced the massive dolomitization affecting the Namurian and Westfalian carbonate succession, as summarized in Table 1. Schneider et al. (2008) were able to show, that in the central part of the area investigated in the present study, the dolomitizing fluids only sparsely entered the Devonian carbonates; despite their rare occurrence, fluid characteristics are the same as for the dolomites in the Cambrian and the Carboniferous, studied by Gasparri et al. (2006a, b) and Lapponi et al. (2007, 2014).

Table 1: Comparison between geochemical data from the Cambrian-hosted dolomites and the Carboniferous-hosted dolomites (Lapponi, 2007).

	Cambrian-hosted dolomite		Carboniferous-hosted dolomite	
	Dol A	Dol B	Dol A	Dol B
TH (°C) (mode)		80 to 110		100 to 150
$\delta^{18}\text{O}$ (PDB)	-13.29 to -4.20	-12.67 to -4.15	-10.58 to -2.96	-11.97 to -4.19
$\delta^{13}\text{C}$ (PDB)	-1.26 to 1.38	-1.12 to 1.19	1.86 to 5.42	1.74 to 5.30
$^{87}\text{Sr}/^{86}\text{Sr}$	0.7958 to 0.71168	0.70919 to 0.71114	0.70810 to 0.70921	0.70846 to 0.70908
Sr (ppm)	16 to 99	14 to 100	16 to 41	12 to 102
Fe (%)	0.22 to 4.58	0.27 to 1.82	0.08 to 0.61	0.06 to 0.55
Mn (ppm)	218 to 2496	483 to 1371	167 to 814	216 to 901
Na (%)	0.01 to 0.04	0.01 to 0.04	0.02 to 0.05	0.01 to 0.06

Large dolomites bodies have been recognized in other areas of the Cantabrian zone, mainly in the East. (e.g. Paniagua et al., 1993; Gómez-Fernández et al., 2000; Grimmer, 2000), but the dolomite description in these papers is less detailed. In some regional studies the dolomitization process is attributed to a product of the last stages of the Variscan deformation and closing of the Ibero Armoricam Arc (e.g. Gutierrez-Alonso et al., 2004; Fernandez-Suarez et al., 2000; Muñoz-Quijano et al., 2007).

Focused on economic geology issues, Tornos & Spiro (2000) described the talc deposits of Puebla de Lillo (Cantabrian Zone) in the east of the present working area, hosted by hydrothermal dolomites replacing Carboniferous limestones.

According to these authors, the talc mineralization resulted from a regional-scale episodic hydrothermal activity related to early Alpine wrench faulting. Geochemically, two previous hydrothermal events recognized correspond well with the regional hydrothermal dolomitization of the Carboniferous successions further westwards (Gasparri et al., 2006a, b). Thermodynamic considerations, fluid inclusion data, and comparison with other regional studies (Tornos & Spiro, 2000) suggest that dolomite (events I and II) formed at temperatures between 100 ° and 280 °C, the talc-forming event (III) spans temperatures between 280 ° and 405 °C, and the post-ore carbonates and quartz (IV) precipitated between 65 ° and 170 °C.

Other large-scale dolomitizations occurred in the western part of the Basque-Cantabrian Basin, but are distinctly younger in age. These are related to Albian to Turoanian transtensional faults connected with high heat flow (Dewit et al., 2012, 2014; Lopez-Cilla et al., 2013; Shah et al., 2012; Iriarte et al., 2012; Nader et al., 2012; Swennen et al., 2012; López-Horgue et al., 2010). The Rubian magnesite deposit in the neighboring West Asturian–Leonese Zone is caused by Mg-rich hydrothermal brines, formed by the metasomatic replacement of hydrothermal dolomite. Magnesite formation was therefore genetically linked to dolomitization-related hydrothermal processes of possible late-Variscan times (Killias et al., 2006). These deposits share textural and geochemical characteristics with other sparry magnesite deposits in the Palaeozoic carbonate rocks of the Spanish Pyrenees and the Mississippi Valley-type Zn–Pb and Fe deposits in the Basque-Cantabrian basin. These have been interpreted as hydrothermal metasomatic deposits as well, formed by dolomite replacement (Velasco et al., 1987, 1994, 2003; Lugli et al., 2000, 2002; Fernandez-Nieto et al., 2003; Symons et al., 2009).

1.4 Methods

The field area covers a region of about 2000 km² in the southern part of the Cantabrian Zone. In the following the different petrographical, petrophysical and geochemical methods applied are described. An intense mining of geological data (see digital file attachment) was undertaken prior to the field work, carried out in two seasons from July to October 2007 and July to August 2008. Over 280 rock samples of dolomitized and undolomitized rocks, mainly carbonates of the Late Carboniferous succession were collected. The samples were taken along 41 profiles approximately perpendicular to the strike direction of the carbonate successions. The following geological maps of Spain (IGME), scale 1:50,000, have been used: sheets 76, 77, 78, 79, 101, 102, 103, 104, 105 and 129. The SIGPAC GIS orthophotos, property of the Castilla y Leon Province, were also employed for a better delineation of the dolomites bodies (<http://www.sigpac.jcyl.es/visor/>).

1.4.1 Geological maps and transects

Systematic geological mapping of the spatial distribution of dolomite bodies and their relation with stratigraphy and tectonic structure was carried out in order to evaluate the amount of dolomitized and of undolomitized rock volumes. Structural data were processed, dolomite structures classified, and fabrics and their spatial distribution evaluated.

One map shows the general distribution of the dolomite bodies and another one the semi-quantitative distribution of the various dolomite types (Annex 1 and 2). Another map puts relatively homogeneous zones on display, based on the integration of the structural, petrophysical, and geochemical data (Annex 3). Porosity and permeability variables were calculated statistically, and an E-W transect was constructed in order to describe the spatial distribution of the PoroPerm properties.

The digitization of the maps used the above-mentioned geological maps of Spain and the SIGPAC GIS orthophotos as a base.

1.4.2 Sample classification and preparation

The samples were cut in cubes, slabs, and thin sections. All of the more than 280 samples were analyzed and classified macroscopically. A large set of these was prepared for more detailed analyses (see below).

1.4.3 Sample scans

After cutting the samples in three perpendicular orientations, they were scanned in a flatbed scanner; the pictures taken were used in image analysis for porosity characterization.

1.4.4 Stereomicroscopic analysis

Thin sections were observed under the stereomicroscope LEICA MZ16, high-tech optics carrier; the pictures taken were used in the fabrics study.

1.4.5 Image analysis

For image analysis the software Image Pro 6.3 was used on photographs or scanned polished rock slabs with the aim of quantitatively characterizing the pore structures and the amount of dolomite cement.

1.4.6 Thin section microscopy

From the most representative samples of both dolomite and precursor limestone 70 unpolished thin sections (50-60 µm) were prepared. The sections were observed under transmitted light, using a Leica MPV-SP microscope. The crystal diameter of the various carbonate phases is reported in µm. The crystal sizes were classified according to Folk (1965).

1.4.7 Cathodoluminescence (CL) microscopy

Cathodoluminescence (CL) microscopy has become a popular tool in carbonate petrography. Luminescence in carbonates is caused mainly by the presence of trace elements in solid solution. Less important causes of luminescence are distorted crystal surfaces and cracks, distorted internal structures between mosaic and intergrown crystals. Inhomogeneities of composition between different parts of a crystal, impurities in surface sites and interstitial lattice sites, and charge displacements due to abnormally ionized or sized atoms and/or separated cation-anion pairs (e.g. Gies, 1976; Nickel, 1978; Mariunin, 1979). These factors interact to a certain degree, and the above sites are the potential centres of activation, temporary storage of energy, and emission of radiation in the form of luminescence (Machel, 1985).

CL microscopy was carried out on all thin sections in order to better characterize the relations of the different mineral phases and the growth features. The minerals were classified for extinct CL, luminescence, CL colour, intensity and zoning, using a Leica DM-RP microscope, a cold cathode instrument CITL 8200mk3, employing a beam voltage between 15 to 20 kV and a current of 300 to 600 μ A.

1.4.8 Fluid inclusions analyses

Fluid inclusions (FIs) are mineral imperfections, consisting of fluid-filled micro cavities sealed within crystals. During crystal growth, small droplets of the mother solution may be trapped, named primary FIs. Inclusions trapped and developed after the crystallization of the host and along microfractures are named secondary FIs.

The study of FIs may give useful information on temperature and composition of the fluids, which precipitated the mineral phases or re-equilibrated with these. Roedder (1984), Shepherd et al. (1985), and Goldstein & Reynolds (1994) discussed exhaustively the techniques of FI studies and applications in Earth Sciences.

15 double polished thick sections (100-120 μ m) were prepared and analyzed for fluid inclusions (FI) and microthermometry. The sections were prepared by means of cold technique reaching a maximum temperature of 35 °C, in order to prevent re-equilibration and/or decrepitation of the FIs by overheating. Microthermometric measurements were carried out at the Institute of Geosciences, University of Heidelberg (Germany), using a Linkam TH 600 stage, and at the Institute of Geosciences, University of Leoben (Austria) (laboratory of Ronald Bakker), using a Linkam MDS 600 stage.

The inclusions were cooled and heated at different rates according to the nature of the sample. Temperatures of phase changes were recorded, including nucleation temperature (T_n), melting temperature (T_m) and/or eutetic temperature (T_e) (depending on the FI size), and finally homogenization temperature (T_h).

After the measurements, thermodynamic calculations were carried out to determine composition and density of the fluids trapped in the inclusions. The calculations employed the program-package FLUIDS (Bakker 2001b, 2003), including the programs AQSO1, AQSO2, AQSO3, BULK AND LONER 32.

At first salinity of the FIs was calculated with a composition close to the H₂O-MgCl₂ system (Dubois & Marignac, 1997) with the program AQSO3. This was due to the originally assumed predominance of Mg²⁺ ions in the analyzed leachate, considering a very complex H₂O-MgCl₂-(NaCl+CaCl₂) system, following Gasparrini (2003).

The AQSO1 program is used to convert the salinity of different types of FIs in eq. wt. % NaCl according to the H₂O-NaCl system (Bodnar, 1993). This is often used for thermodynamic calculations. However, as the later obtained crush-leach data have shown, the analyzed fluid inclusions are deprived in Mg, because of the dolomitization process. The salinity calculations are only rough estimates, therefore.

1.4.9 Crush leach analyses

This destructive technique allows the chemical analysis of the fluid released from FIs by bulk sample crushing, i.e. the analysis of the content of a large number of FIs. Consequently, it is preferably applied to samples containing only one type of FIs, homogeneous in composition. The presence of more than one generation of FIs in a sample would result in the characterization of an artificially mixed fluid, with no geological relevance (Banks & Yardley, 1992).

12 samples were crushed and handpicked under binocular microscope in order to take more than 1g of material for crush leach analyses, which were measured at the University of Alberta, Edmonton, Canada (Laboratory of Sarah Gleeson).

1.4.10 O and C stable isotope analyses

Dolomitization has been a subject of debate and has interested carbonate geologists for decades. Because a vast amount of Mg is needed to convert limestones to dolomites, the fluid/rock ratio during dolomitization is presumed to be very large. The source(s) of the fluid responsible for dolomitization is therefore one of the important issues to explore. (Yui & Gong, 2003).

O- and C-isotope composition of dolomite has therefore been commonly employed to infer the source(s) of the dolomitizing fluid, which is supposed to have buffered the O-, or even C-isotope system during dolomitization (e.g., Land, 1980).

¹⁸O/¹⁶O and ¹³C/¹²C isotope ratios are widely used to define the conditions of carbonate diagenesis. The O isotope composition of fluids was given as difference (in ‰) relative to the V-PDB or SMOW (Standard Mean Ocean Water) international standard. The average O isotope composition of present day seawater has 0 ‰. A fluid with positive δ¹⁸O value is enriched in ¹⁸O relative to V-PDB or SMOW, whereas negative values indicate relative depletion of the fluid in the heavy isotope.

15 samples were analysed for O and C isotope ratios at the Geozentrum Nordbayern, University Erlangen-Nürnberg (Germany)(laboratory of Michael Joachimski). Carbonate powders were extracted from rock slices drilled by means of a dental-drill. A minimum of 0.3 g per sample were analysed.

1.4.11 Trace elements measurements

SEM and WDX microanalyses were carried out in the Eni laboratories, San Donato Milanese (Italy) to determine the distribution of the most important trace elements (Sr, Fe, Mn) and the variation of the Ca/Mg ratio in cements and matrix of 3 samples. Around 50-60 analyses for each sample were carried out to compare different diagenetic phases.

A Jeol 840A SEM, coupled with an EDS Oxford Link ISIS Series 300 and an Oxford WDX 600, was used for these analyses, which give quantitative data of the trace element contents (ppm order) found in a micro-volume of sample (typically $1 \mu\text{m}^3$ and less). The measurement error is a few ppm units. Carbonate standards were prepared to ensure the accuracy of the analysis. All thin section analyses were performed on selected zones of carbonate crystals and identified by means of petrography.

1.4.12 Petrophysical analyses

The nature of reservoir rocks containing oil and gas dictates the quantities of fluids trapped within the void space of these rocks, the ability of these fluids to flow through the rocks, and other related physical properties. The measure of the void space is defined as the porosity of the rock, and the measure of the ability of the rock to transmit fluids is called the permeability (Tiab & Donaldson, 2011).

The petrophysical properties of dolomite petroleum reservoirs and aquifers vary depending on the petrographic texture of the dolomite. Understanding diagenetic history, and crystal textures that may result because of various diagenetic conditions, can be a predictor of petrophysical properties of dolomite reservoirs (Woody et al., 1996).

PoroPerm analyses were carried out in the Eni laboratories, San Donato Milanese (Italy) on most of the 280 samples collected. Properties measured were:

(i) Absolute permeability

Absolute permeability is a metric of how easily a single saturated fluid can flow through a porous medium (Holmes et al., 2011).

The plugs were loaded into a Hassler core holder and a sleeve pressure of 20 bar was applied to eliminate possible by-passing of gas around the sample. Nitrogen gas passes through the sample in axial direction under steady-state and laminar flow conditions. Gas permeability was calculated by application of Darcy's law, according to the following equation:

$$k = 2000 \frac{L \mu Q P_2}{A (P_1^2 - P_2^2)}$$

where:

k = gas permeability, mD

L = sample length, cm

A = sample cross-section area, cm²

m = nitrogen viscosity, cp

P_1, P_2 = sample inlet and outlet pressure, atm

Q = nitrogen flow rate (measured at the outlet pressure P_2), cm³/s

μ = dynamic viscosity

(ii) Porosity by resaturation method

Porosity determines reservoir storage capacity. It is defined as the ratio of void space, commonly called pore volume, to bulk volume and is reported either as a fraction or a percentage. Almost all hydrocarbon reservoirs are composed of sedimentary rocks in which porosity values generally vary from 10 to 40% in sandstones and from 5 to 25% in carbonates (Coneybeare, 1967; Keelan, 1982).

Several methods have been developed to measure the pore volume of a sample. One of this called the fluid resaturation method. A clean and dried sample is weighed, then saturated with a liquid of known density, and subsequently reweighed (Cone & Kersey, 1992; Torsæter & Abtahi, 2003).

On completion of the permeability measurements, the samples were evacuated to 10-5 mbar and then pressure saturated under a synthetic formation brine at 150 bar. Ambient porosity was obtained using the following equation:

$$(\text{Weight}_{\text{saturated}} - \text{Weight}_{\text{dry}}) / (\text{Weight}_{\text{saturated}} - \text{Weight}_{\text{immersed}})$$

where :

$\text{Weight}_{\text{saturated}}$ = weight of the brine saturated sample, g

$\text{Weight}_{\text{dry}}$ = weight of the dry sample, g

$\text{Weight}_{\text{immersed}}$ = Archimedes' weight

2. GEOLOGICAL SETTING AND STRUCTURAL EVOLUTION

The western part of the Iberian Peninsula is formed by the Iberian Massif, which is divided into six zones with differing geological features. These are the Cantabrian Zone (CZ), West Asturian-Leonese Zone (WALZ), Central Iberian Zone (CIZ), Ossa Morena Zone (OMZ), South Portuguese Zone (SPZ) and Galicia-Tras-Os-Montes Zone (GTMZ) (Lotze, 1945; modified by Julivert et al., 1972; Farias et al., 1987; Arenas et al., 1988). These units represent the westernmost outcrops of the European Variscan orogen (Fig. 2.1) and are characterized by four main types of rocks: autochthonous Neoproterozoic and Paleozoic sediments of the Gondwana margin, allochthonous complexes, Variscan granites, and syn-orogenic sediments (Martínez-Catalán, 1990; Martínez-Catalán et al., 2004).

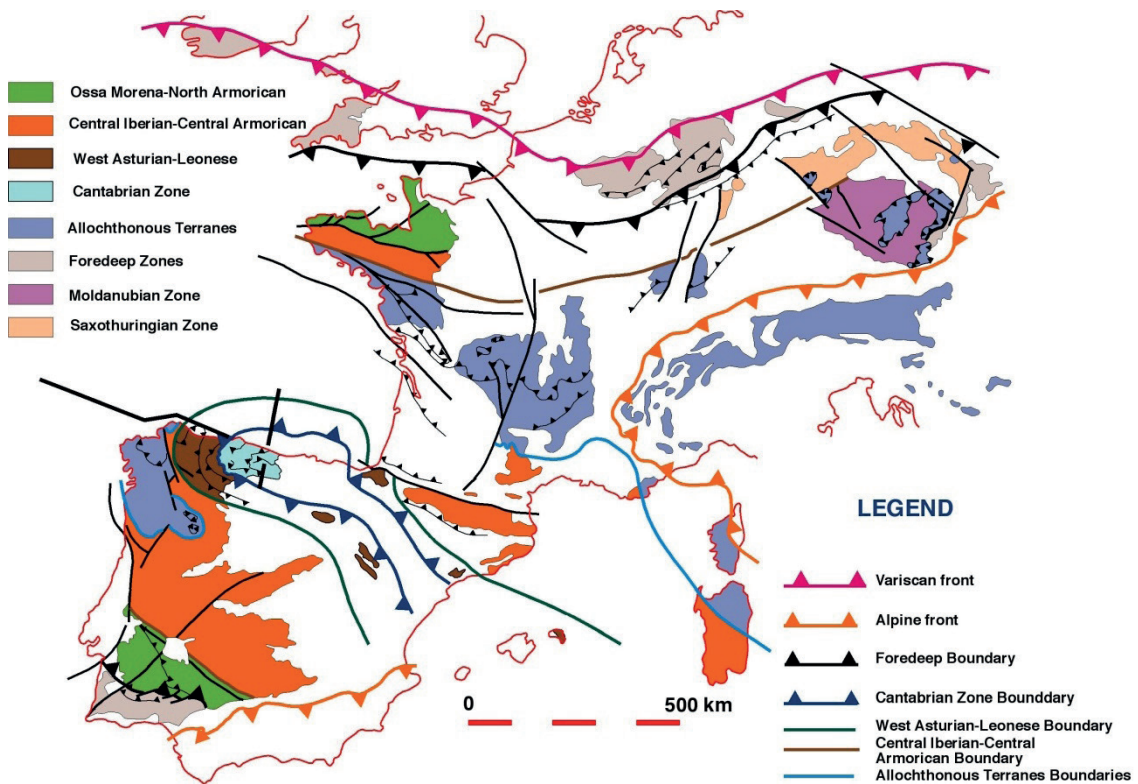


Fig. 2.1: Geological sketch map of the Variscan Belt of central and Western Europe (modified from Martínez Catalán, 1990).

The Variscan orogen was formed during a complex collision between Laurentia and Gondwana in the late Paleozoic. Following the closure of the ocean(s) located between Laurentia and Gondwana, the Variscan orogeny extended in the east to the Caucasus, and in the southwest to the Appalachian and Ouachita Mts. in North America (Matte, 1986, 1991, 2001). Four periods are generally distinguished in its evolution: (i) the eo-Variscan, from about 480 to 400 Ma, marking the initial convergence of the oceanic domains opened during the Ordovician; (ii) the mid-Variscan (400–350 Ma), which was a period of continental collision and nappe stacking; (iii) the neo-Variscan (350–320 Ma), with continued convergence controlling the intra-continental tectonic evolution; and (iv) the post-collisional period (320–290 Ma) with

continental collapse and stabilization of a continental crust (Faure et al., 1997; Rossi et al., 2006).

The Variscan orogeny began in the NW of Iberia during the Late Devonian, about 380 to 370 Ma (Martínez-Catalán et al., 1997; Dallmeyer et al., 1997; Rodriguez et al., 2003). The first Variscan tectono-metamorphic events (D1) are recorded in the allochthonous terrain GTMZ, while the deformation did not reach the CZ before the Westfalian. The development of the orogenic wedge started during the Early Devonian, during the closure of an oceanic domain, and gradually reached eastern regions (Perez-Estaún et al., 1991; Martínez Catalán et al., 1996). Essentially syn-orogenic sedimentation is mostly preserved in the CZ and started in the Early Carboniferous. Sediment sources changed dramatically from emerged areas within the foreland to the relief created in the distal area by the continually shortening orogen (Martínez-Catalán et al., 2007, 2009). In relation to the orogenic activity, the Carboniferous sedimentary deposits of the Cantabrian Zone can be divided into three intervals: (i) Tournaisian - Namurian (359 to 318 Ma), representing the transition from pre- to syn-orogenic successions; (ii) Namurian – Upper Westfalian (318 to 306 Ma), formed by syn-orogenic successions deposited in the foreland basin; (iii) Upper Westfalian - Stephanian (306 to 290 Ma), including both syn-orogenic deposits of the foreland basin and late / post-orogenic successions deposited over the already structured orogen (Fernandez et al., 2004).

The lowermost Carboniferous corresponds environmentally to an area stretching from a shallow marine platform to relatively deeper parts of a sedimentary basin (Sanchez de la Torre et al., 1983; Wendt & Aigner, 1985). Sedimentation in the Early Carboniferous comprises the Baleas, Vegamián, and Alba Fms. (Tournaisian - Viséan). These conformably overlie the Upper Devonian sandstones and display reduced thicknesses due to very low sedimentation rates, facies regularity and significant lateral extension.

The middle syn-orogenic successions show multiple stacked platforms that are progressively replaced by siliciclastics towards the foreland (Fernandez et al., 2004). Syn-orogenic sedimentation is well preserved in the SPZ and CIZ; in the internal areas, successions with turbidites and flyschoid characteristics represent probable syn-orogenic deposits corresponding to the Early Namurian (324 Ma) (Martínez Catalán et al., 2004).

In the Cantabrian Zone during the Namurian A the sedimentary basin consisted of a large carbonate platform separated from the orogen by a foredeep. These two environments correspond to the restricted Barcaliente Fm. carbonates and the turbiditic Olleros Fm. During the Namurian B - Westfalian A the carbonate platform diminished in size and the more open marine, mostly shallow neritic Valdeteja Fm. was deposited. The foredeep gradually migrated further to the E. The former platform subsided and was covered by clastics. In the Westfalian A the developing trough was filled and terrigenous deposits replaced most of the carbonates. In the W these clastic sediments form the San Emiliano Fm. and the Lena and Sama groups. The latter reached their maximum thickness in the Bodon-Ponga units. Only in the Picos de Europa (part of the Bodon-Ponga units) carbonate sedimentation (Picos de Europa Fm.) continued during all of the Westfalian and even into the Stephanian (Alonso et

al., 2009; Aramburu & Bastida, 1995).

The upper part of the stratigraphic pile contains syn-orogenic sediments of the fore-land basin and late / post orogenic deposits. These rocks show a more local character than the earlier deposited sediments. The late / post orogenic successions are clearly discordant above varied substrates (Colmenero et al., 2002; Pastor-Galán et al., 2013).

Burial dolomites are most widespread in the middle to Upper Carboniferous carbonate formations of the CZ, but can be found more locally in older carbonate successions as well (Cambrian Lancara Fm., Devonian La Vid, St. Lucia, and Portilla Fms.). A short overview on the Carboniferous carbonate formations involved in the dolomitization process is given below therefore.

The Alba Fm. (Viséan) is mostly less than 30 m thick, has a wide extension and sharply overlies older rocks. Sedimentation rates were extremely low (Veselovsky et al., 2008). This formation consists of micritic, bioclastic and fossiliferous nodular limestones with a typical dark red to pinkish colour. The middle part of the formation contains red shales and red radiolarite horizons (Alonso et al., 1990). The Adrián Member is a dark grey limestone, which formed during earliest Namurian time and represents the transition to the Barcaliente Fm. (Kullmann et al., 1977; Hemleben & Reuther, 1980; Reuther, 1980).

The Barcaliente Fm. (Namurian A) is 200-350 m thick. This formation consists of dark grey to black, micritic and bituminous limestones. Regular bedding and lamination are typical. The beds are tabular or slightly wavy. Fossil content (often bioclastic in nature) is generally very low (Wagner et al., 1971; Alonso et al., 1990). Normal gradation is the most common sedimentary structure at the base of the formation. In the middle part, lamination as well as bioturbation increase in importance. Towards the top, bioturbation predominates. In the uppermost part intervals with remnants of evaporites (evaporite crystal pseudomorphs) occur together with syn-sedimentary breccias (Reuther, 1977; González-Lastra, 1978; Hemleben & Reuther, 1980). The uppermost debris interval is named the Porma Breccia. The breccia clasts are a chaotic mixture of angular to sub-rounded and heterometric clasts, embedded in normal Barcaliente ground mass (Kullmann et al., 1977; Reuther, 1977). The transition from the Barcaliente to the overlying Valdeteja or San Emiliano Fms. can be abrupt. The Barcaliente Fm. possibly formed in a low energy, restricted environment, with partly euxinic and at the end partly evaporitic bottom conditions and relatively low rates of sedimentation (Evers, 1967; Wagner et al., 1971; Veselovsky et al., 2008). This formation was most strongly affected by the epigenetic dolomitization.

The Valdeteja Fm. has a variable thickness (0 to 500 m) and a less continuous distribution than the Barcaliente Fm. The base of the formation is relatively isochronous (Namurian A-B), whereas the top is strongly diachronous (Namurian B to Westfalian A: Lobato et al., 1984; Alonso et al., 1990). The transition to the San Emiliano Fm. is generally gradual. The Valdeteja Fm. consists of different lithologies, dominated by light grey, massive limestones, with some intercalations of more distinctly bedded limestones and marls. Various faunas exist with bioherm-forming algae being dominant (Wagner et al., 1971). Locally, oolites occur. The Valdeteja Fm. formed mostly

in a shallow neritic environment (Evers, 1967; Eichmüller, 1985).

During most of the Carboniferous, the CZ was located in front of the Variscan orogen. It formed a foreland basin, which became progressively deformed and incorporated into the orogen (Julivert, 1978; Marcos & Pulgar, 1982; Rodriguez-Fernandez, 1983; Agueda et al., 1991), forming intramontane basins (e.g. Heward, 1978a, b; Colmenero et al., 1993). Due to the close relation of sedimentation with tectonic activity, this part of the succession is more varied than the underlying one. In addition, the tectonic activity produced diverse intrusive igneous rocks, related to the orocline development in the lower Permian (Fernandez-Suarez et al., 2000; Gutiérrez-Alonso et al., 2011a) (Fig. 2.2).

The CZ is characterized by thin-skinned tectonics with a transport direction towards the core of the arc (Sitter, 1962; Julivert, 1971; Pérez-Estaún et al., 1988). In Variscan time, deformation resulted from the emplacement of regional thrusts and folds, followed by late fracturing (Julivert, 1971; Julivert & Marcos, 1973; Pérez-Estaún & Bastida, 1990).

Of special interest for the timing of increased heat flow and associated dolomitization are the latest magmatic events, which in the CIZ began at about 310 Ma, some 50 Ma after the main event of Variscan collision. Underneath the CZ the magmatic peak was between 300 and 290 Ma (Fernández-Suárez et al., 2000; Gutiérrez-Alonso et al., 2011a). These authors interpreted the magmatism as due to lithospheric delamination, associated with the formation of the post-Variscan Ibero Armorican Arc (IAA) (Fig. 2.2).

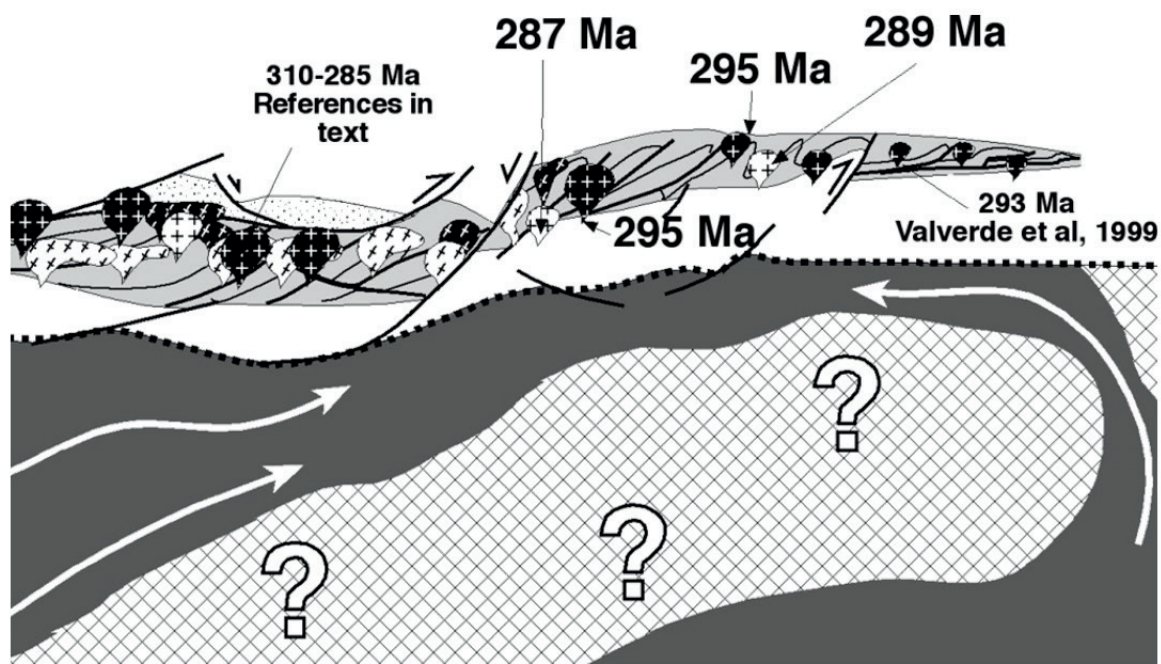


Fig. 2.2: Association of post-tectonic igneous activity in the NW of Iberia (from Fernández-Suárez et al., 2000).

The IAA is a very special feature of the Variscan orogen of western Europe. Detailed studies of deformation and structure (Ries & Shackleton, 1976; van der Voo et al., 1997; Weil et al., 2000, 2010, 2013b; Weil & van der Voo, 2002; Aerden, 2004; Gutiérrez-Alonso et al., 2004a, 2011a, b, 2012, 2013; Alonso et al., 2009; Pastor-Galán et al., 2011, 2012a, b; Shaw et al., 2012) prove a late change in the relative movement of the plate: changes in the strain pattern caused large-scale folding and bent the originally linear N-S trending orogenic belt to form the spectacular orocline of the IAA.

The earlier mentioned tectonostratigraphic zones of Iberia can be grouped into two sets (Gutiérrez-Alonso et al., 2004a) in relation to the orocline: the core or inner arc corresponds to the CZ, and the outer arc to the WALZ, CIZ, OMZ and Armorican Domain (Fig. 2.3). More recently the orocline has been subdivided into the Cantabrian Orocline in the north and the Central Iberian Orocline in the west and south (Weil et al., 2013b).

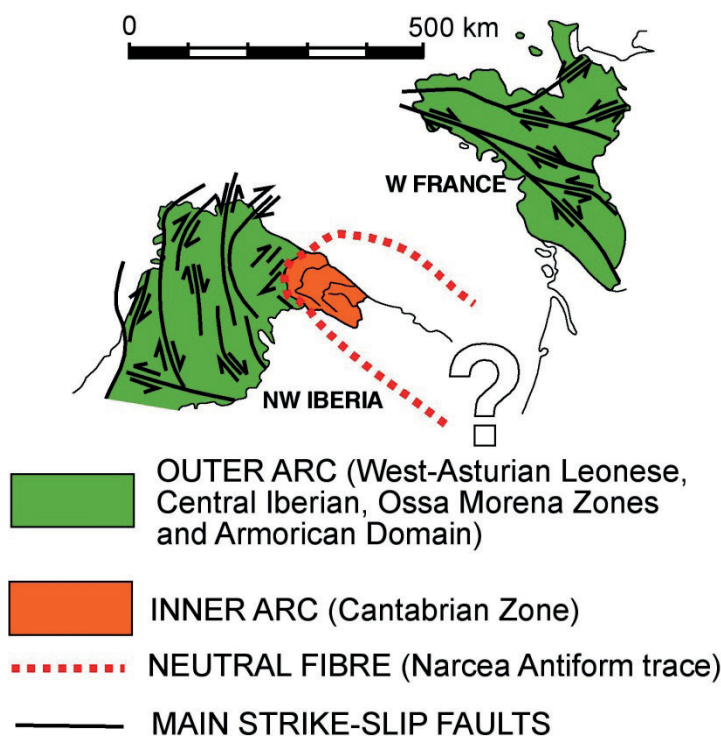


Fig. 2.3: Geological sketch of the West-European Variscan belt, showing the differences between the inner and outer arc (from Gutiérrez-Alonso et al., 2004a).

Petrologic, geologic, geochemical and geochronologic data all point to magmatic and tectonothermal activity occurring penecontemporaneously with oroclinial buckling over a short 10 m.y. time window at the end of the Carboniferous. Temporal and spatial relationships link these processes with thinning in the outer and thickening in the inner arc, and ultimately foundering and delamination of the mantle lithosphere under western Europe. Such cause and effect linkages help explain many previously enigmatic geologic events related to post-orogenic Variscan Europe (Weil et al., 2013a) (Fig. 2.4).

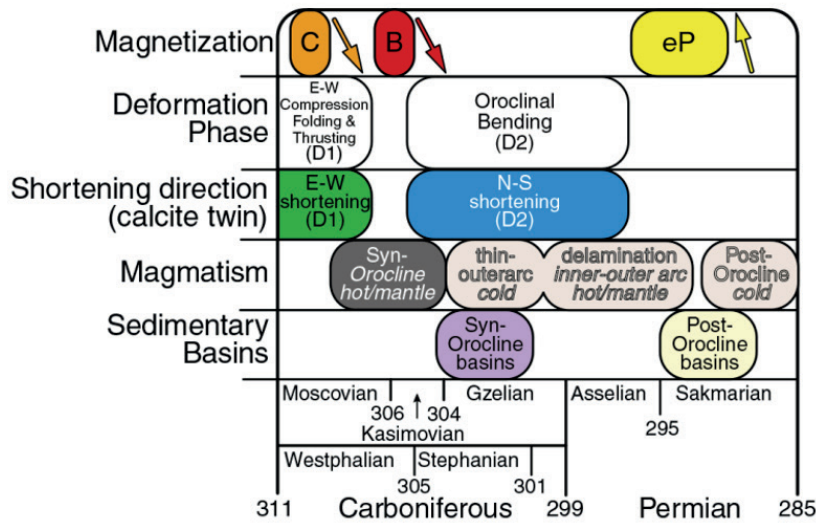


Fig. 2.4: Different processes recorded in the Cantabrian Orocline and their relationship to the two main phases of orocline formation, the acquisition of twin strains (and associated stresses) during deformation, the age of various magmatic pulses, and the age of sedimentary basins (from Weil et al., 2013a).

These sets in the IAA, show a longitudinal, arc-parallel shear deformation, characterized by the mentioned shortening in the inner and extension in the outer arc (Fig. 2.5). The neutral fibre, a sub-vertical plane without stretching or shortening marks the boundary between the two sets: it corresponds to the Narcea Antiform (Gutiérrez-Alonso et al., 2004a, 2012) and an out-of-sequence thrust system developed and reactivated on the southern limb (Pisuerga-Carrion Unit) (Pastor-Galán et al., 2014).

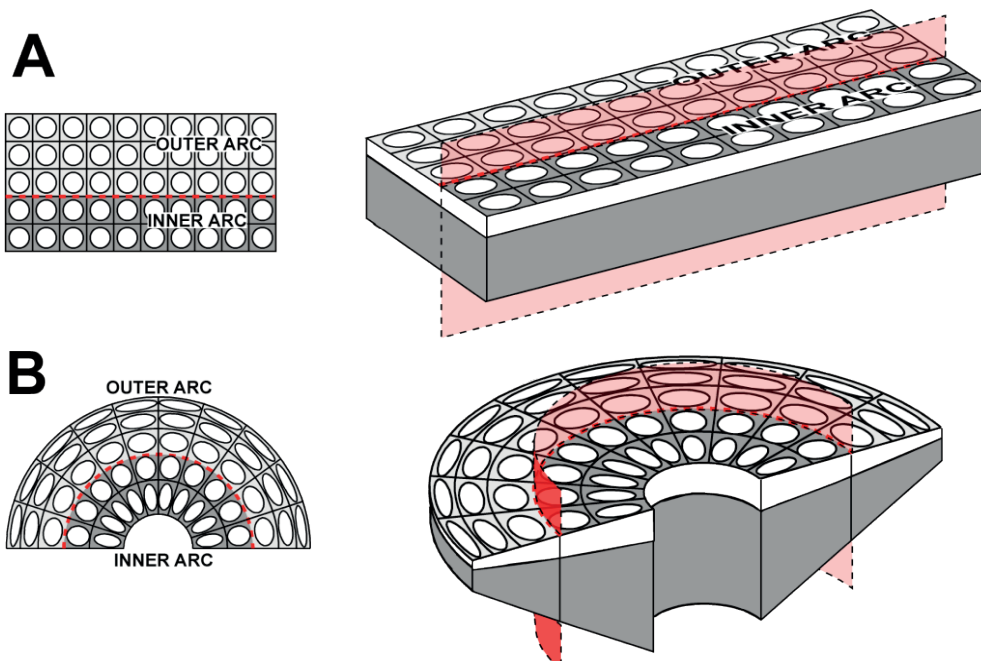


Fig. 2.5: Effect of lithospheric bending around a vertical axis, and proposed deformation mechanism of tangential longitudinal strain (from Gutiérrez-Alonso et al., 2004a).

The differences between the two sets are the result of post-orogenic oroclinal folding, which caused a lithospheric mantle thickening beneath the inner arc and lithospheric thinning under the external arc. This process initiated delamination, due to the lithospheric mass imbalance beneath the inner arc: upwelling asthenospheric mantle replaced the sinking lithosphere (Fig. 2.6) (Gutiérrez-Alonso et al., 2004a, b, 2011, 2012; Pastor-Galán et al., 2012a,b).

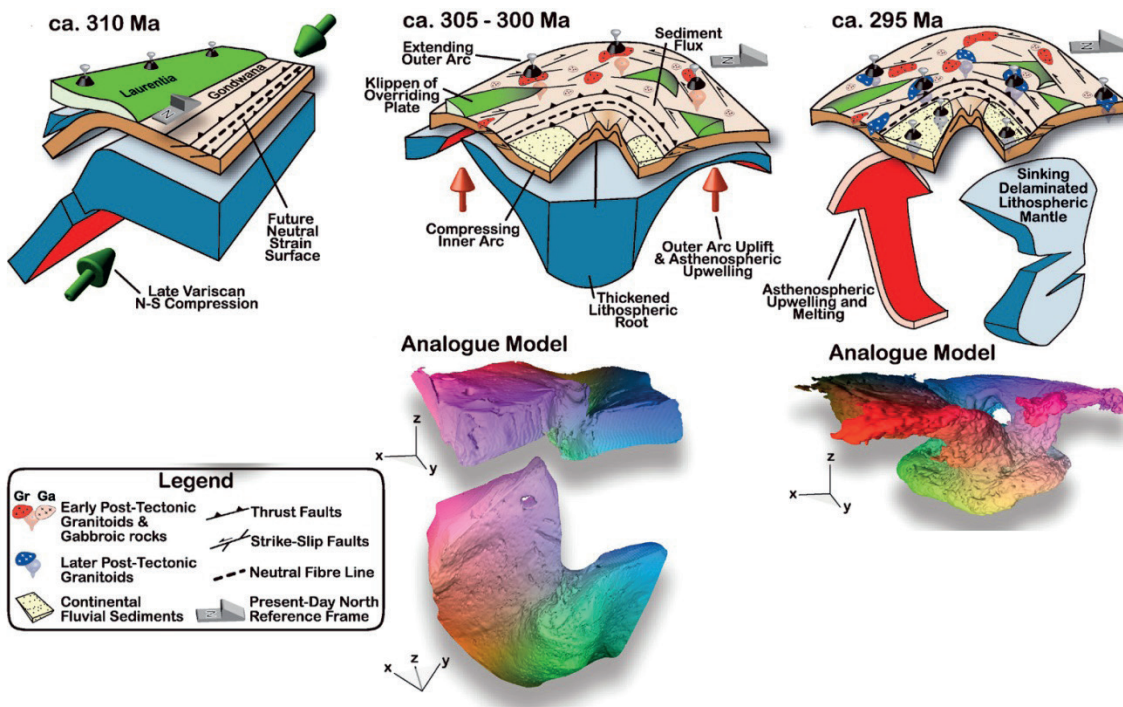


Fig. 2.6: Sketch illustrating the delamination process caused by post-orogenic oroclinal bending (from Gutiérrez-Alonso et al., 2012).

The model of Gutiérrez-Alonso et al. (2004a, 2012) explains the structural, metamorphic, igneous and hydrothermal characteristics in the late Variscan of this part of southwestern Europe. The extensive burial dolomitization of Carboniferous and older limestones in the core (CZ) of the orocline is one of the strongest evidences of extensive fluid flow at higher temperatures during late Variscan time.

In central and western Europe, post-Variscan migration of highly saline fluids was widespread as well (Behr et al., 1987, 1993; Wilkinson et al., 1995; Heijlen et al., 2001). Movement of these crustal fluids is thought to be fault controlled (Behr et al., 1993; Heijlen et al., 2001). One of the most important fluid-flow events was dated at 270 Ma in western Europe (Schneider, 2000; Boni et al., 2001), an age which coincides with post-thrusting Permian extensional tectonics and with the timing inferred for the dolomitization in the CZ (Gasparrini et al., 2006 a; Lapponi et al., 2007, 2014).

Fluid migration for the dolomitization process in the CZ was controlled firstly by the main tectonic lineaments of the area, and secondly by bedding, lamination and

stylolite planes of the precursor rocks (Gasparrini et al., 2006a). At a regional level, several authors have claimed a strict tectonic control of dolomitization in the CZ (Martínez-García, 1981; Paniagua & Rodriguez-Pevida, 1988; Gómez-Fernández et al., 1993, 2000; Crespo et al., 2000; Grimmer, 2000; Tornos & Spiro, 2000).

In the southern branch of the Cantabrian Zone, there is an outstanding tectonic feature that has long been under discussion. It consists of a complex set of E-W trending faults that crosscut all of the preceding structures, including several thrust units. The main faults of this set are the León Fault in the north, and the Sabero-Gordón fault in the south of the working area. The León Fault played a prominent role for fluid circulation as already suggested by Gasparrini et al. (2006a) due to the almost complete dolomitization of the parts of the Bodón Unit closer to the fault. The León out-of-sequence thrust is rooted in a lower crust detachment (Keller et al., 2007) and the thrust facilitated emplacement of Early Permian igneous rocks and the circulation of associated hot fluids (García-López et al., 2013).

According to some authors, the León and Sabero-Gordón faults are originally strike-slip and were later reactivated, mainly as reverse faults (Marcos, 1968a; Julivert et al., 1971; Marcos et al., 1979; Heward & Reading, 1980). According to more recent work, the León Fault displays all features of a breaching thrust (Alonso et al., 2009). On the southern arm of the Cantabrian Zone, the León Fault trace is sinuous, trending alternatively NE and NW, following the same direction as frontal and lateral structures of the thrust sheets in the area (Alonso, 1987; Alonso et al., 1989; Alonso et al., 2009) (Fig. 2.7).

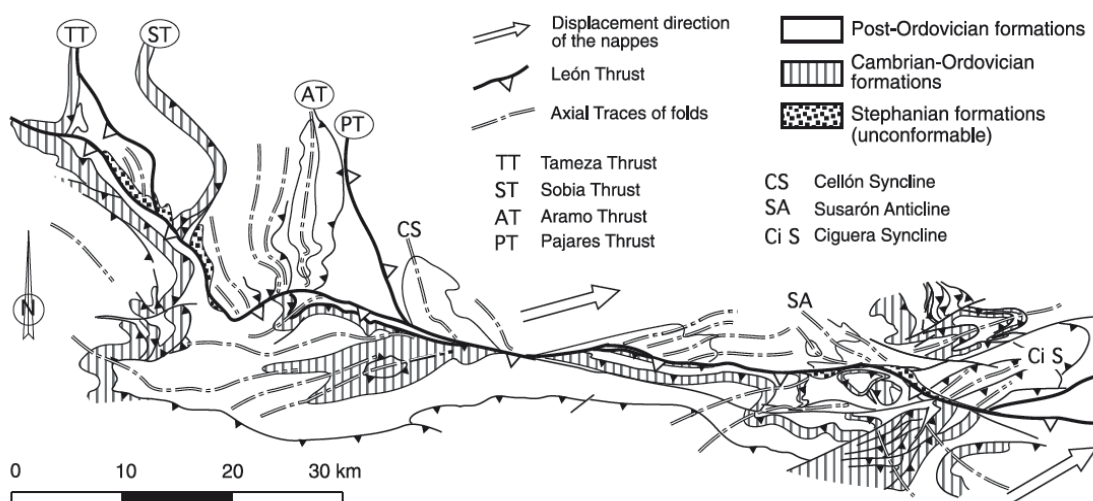


Fig. 2.7: Structural sketch of the central sector of the León Thrust showing its relation with the surrounding structure (from Alonso et al., 2009).

During Alpine orogenesis, as a result of a crustal scale thrusting the Cantabrian Zone was uplifted and exhumed (Alonso et al., 1996; Gallastegui, 2000). However, the Alpine orogeny caused little internal deformation in the uplifted block, in which some Variscan folds and thrusts were slightly reactivated (Pulgar et al., 1999) and Mesozoic sediments were locally distinctly tilted. An early Alpine regional-scale hydrothermal activity related to wrench faulting took place (Tornos & Spiro, 2000): the talc deposits of Puebla de Lillo (Cantabrian Zone) are due to this late hydrothermal activity, but its regional extensin is not well understood.

3. DOLOMITE CHARACTERIZATION AND DISTRIBUTION IN THE FIELD

Dolomite bodies are irregularly distributed but show an increase in volume from east towards west.

The measured 41 sections (Fig. 3.1) are located in four of the aforementioned structural domains (Fig. 1.2). From E to W these are:

Pisuerga-Carrión Unit:

Sections Cremenes and Salamón II: dolomite is mainly found in the Caliza de Montaña Fm. (largely equivalent to Barcaliente/Valdeteja Fms. elsewhere); less extensive dolomites occur in the underlying Alba Fm., especially in its uppermost part.

Esla Unit:

Section Salamón: the carbonate rocks of the Carboniferous Ciguera-Lois Formation contain only small bodies of dolomite.

Bodón-Ponga Unit:

Sections Cofiñal, Isoba, Valdecastillo, Lillo Talc Mine, Montuerto, Nocedo de Curueño, Braña, Lugueros, Llamazares, Canseco, Getino, Pontedo, Valporquero, Providencia Mine, Peña Carba, Millaró, Villanueva de la Tercia, Poladura, Viadango, Viadango II, Sierra del Turrón, Cubillas de Arbas, Caldas de Luna, Robledo de Caldas, Sena de Luna, Rabanal, Villafeliz, Villasecino, San Emiliano, and San Emiliano II: extended dolomite bodies occur in the Barcaliente and Valdeteja Fms. Widespread dolomitization affected especially the central part of this unit, between Villamanín and San Emiliano. In quite some localities, dolomites occur in the uppermost part of the Alba Fm. and in the Lancara Fm. as well (Lapponi, 2007). Their distribution is not uniform, however. Only small outcrops of dolomite are recognized in the regions between Cofiñal-Isoba and Valdecastillo-Cármenes.

Somiedo Unit:

Sections Piedrasecha, Saliencia, Valle del Lago, La Cueta, La Cueta II, Cacabalillo, Vega Viejos, and Malva: the dolomite volume increases from south (Piedrasecha) towards northwest (Somiedo). The Carboniferous Caliza de Montaña Fm. is again the main carbonate rock affected by dolomitization, although the Devonian Portilla and Santa Lucia Formations are also dolomitized (localities Cacabalillo and Cueta).

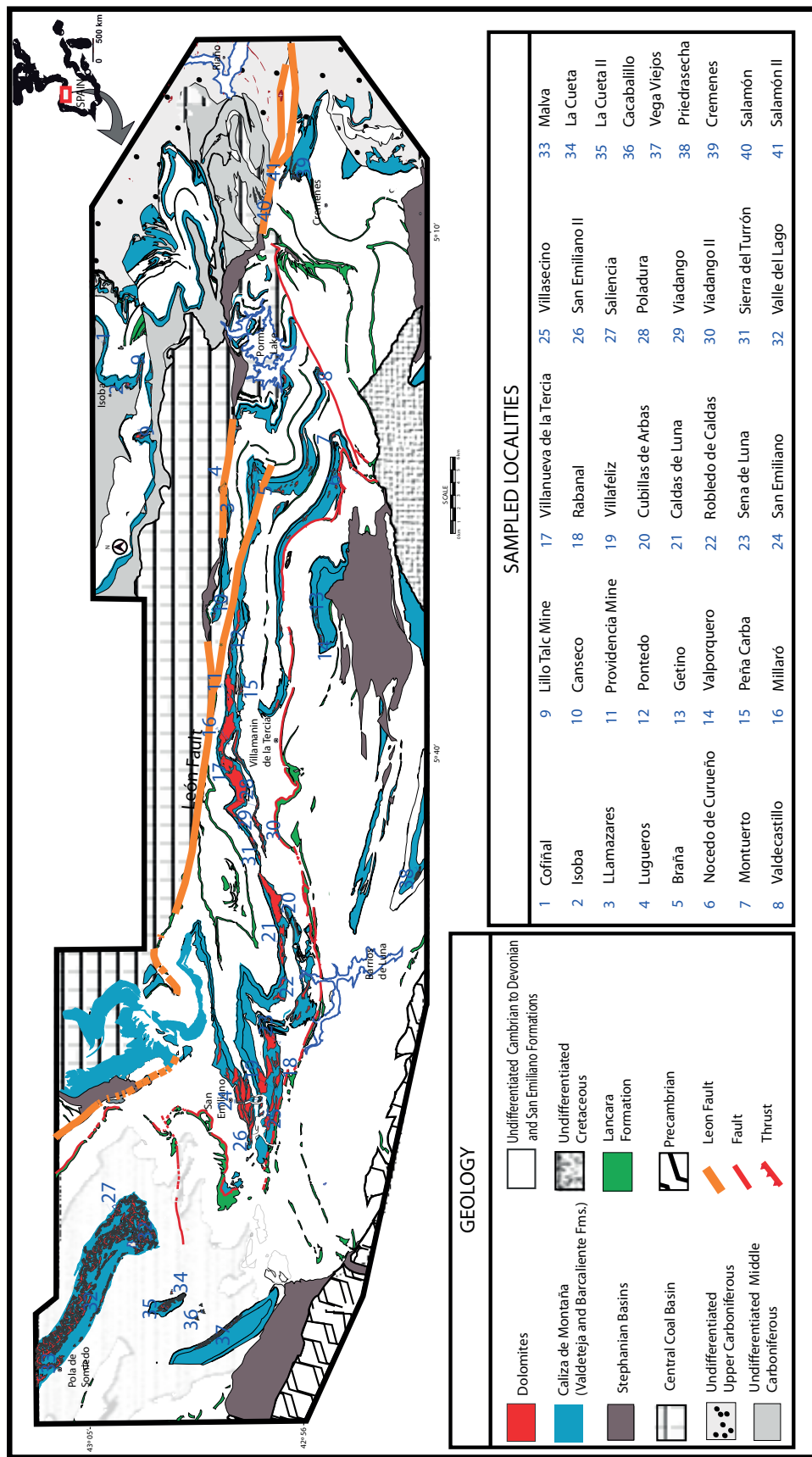


Fig. 3.1: Dolomite distribution and samples profiles, SW Cantabrian Zone.

In the field, the differentiation between dolomite and limestone was facilitated by the clear colour contrast (Fig. 3.2) between weathered limestones, which are light grey, and weathered dolomites, which appear yellowish-brown to dark grey. This contrast is mainly due to different lichen populations coating the rocks and was even observed in air-photographs (Fig. 3.2a).

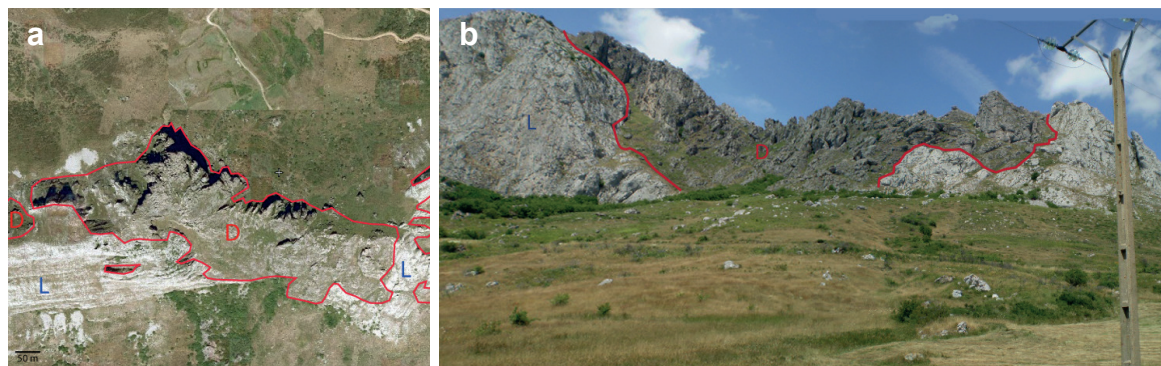


Fig. 3.2: Colour contrast of dolomite bodies: (a) Orthophoto of Viadango area (SIG-PAC image); (b) irregular dolomite body, Viadango.

The geometry of the dolomites in the field is varied, from extremely irregular masses to sub-vertical bodies and dykes and to small spots. The scale varies from centimeters to decameters to kilometers (Figures 3.2, 3.3).

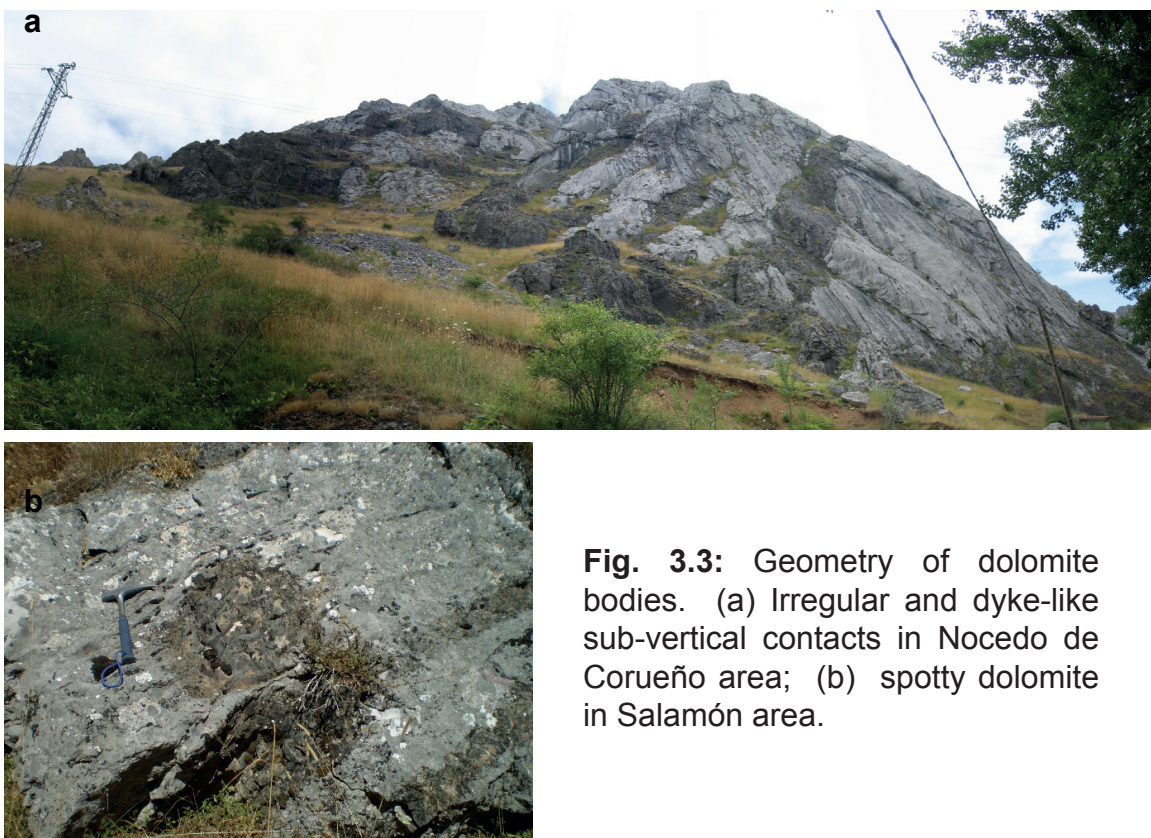


Fig. 3.3: Geometry of dolomite bodies. (a) Irregular and dyke-like sub-vertical contacts in Nocedo de Corueño area; (b) spotty dolomite in Salamón area.

Dolomite-limestone contacts are very sharp and abrupt, normally cutting both bedding planes and sedimentary structures. The propagation from dolomite to limestone in the front of dolomitization occurs in a few centimeters or even less (Fig. 3.4) by fractures, net systems and spots of unknown reason.

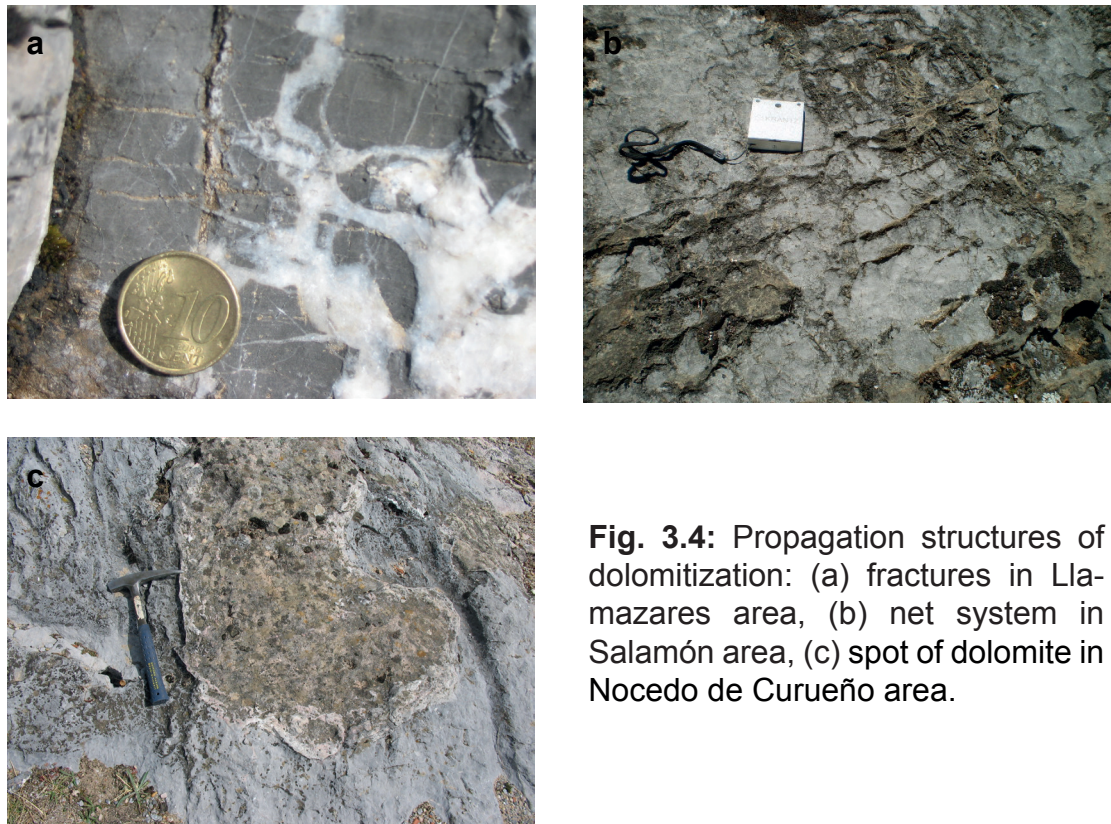


Fig. 3.4: Propagation structures of dolomitization: (a) fractures in Llamazares area, (b) net system in Salamón area, (c) spot of dolomite in Nocedo de Curueño area.

The dolomitization strongly overprints the precursor rocks. Lamination and/or stylolite planes are only locally preserved; this better preservation is more likely to occur in the Barcaliente Fm. Relics of fossils with a strong degree of recrystallization are recognizable in the Barcaliente Fm. (especially crinoids) as well as Valdeteja, Portilla, and Santa Lucia Fms. (Fig. 3.5).



Fig. 3.5: (a) Dolomitized crinoidal limestones of the Valdeteja Fm., Millaró area; (b) stylolites preserved in dolomite, Isoba area.

An economically important characteristic of the dolomite bodies is the porosity, consisting of fairly widespread cavities, elongated to roundish in shape. The scale of the pores varies from several cms to sub-millimetres (Fig. 3.6). A detailed study of the porosity will be given in chapter 4.



Fig. 3.6: Porosity features in dolomite bodies: (a) large scale macroporosity, Isoba; (b) medium scale porosity, Millaró; (c) microscopic scale porosity (cathodoluminescence picture), Isoba.

Some dolomite occurrences are associated with mineralizations, which were mainly emplaced after dolomitization. Ore deposits are mostly hosted in dolomitized Carboniferous carbonates. In the eastern part of the study area, mineralizations of As, Sb, Cu, Ni, Co, Hg and U ores occur near Salamon (Luque et al., 1990; Alonso et al., 2002). In the region between Isoba and Puebla de Lillo, talc deposits are hosted within the dolomites. Between Villamannin and Cármenes in the centre of the working area, Cu–Ni–Co–U–As–S mineralizations were mined in Mina Providencia and Mina Profunda and occur also elsewhere. A strong enrichment in Fe within dolomites in the Carboniferous was used in earlier times for mining in the area of the Saliencia lakes (Fig. 3.7). Pb–Zn–Ba mineralizations occur in the Lancara Fm. at different localities mainly in the Somiedo region.

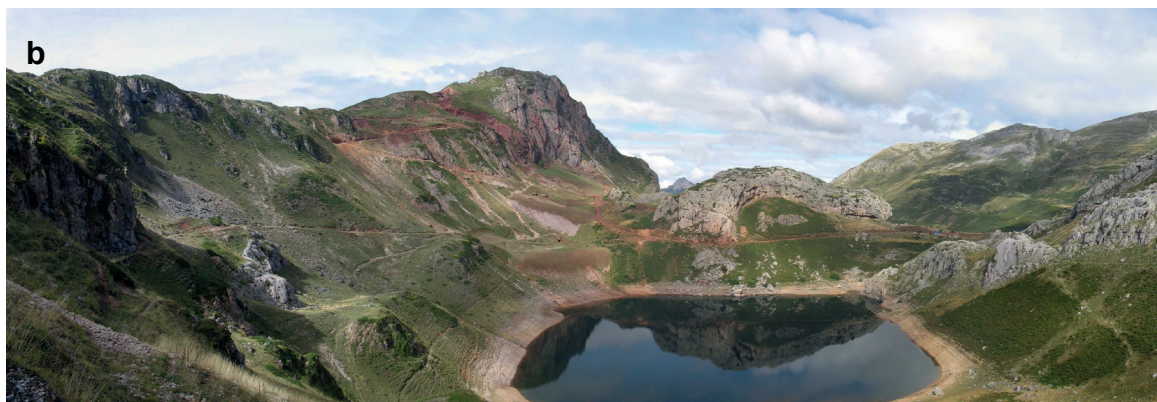


Fig. 3.7: (a) Talc Mine *La Respina*, Puebla de Lillo. (b) Former Fe Mine *Saliencia Lakes*, Somiedo.

4. DOLOMITE CLASSIFICATION

Petrographically, dolomites usually were classified according to crystal size distribution and crystal boundary shape. This classification is descriptive, but carries genetic implications because size distribution is controlled by both nucleation and growth kinetics, and crystal-boundary shape is controlled by growth kinetics (Sibley & Gregg, 1987). Also paragenetic relationships have been used (Tornos & Spiro, 2000; Randazzo & Zachos, 1984; Gasparini, 2003; Gasparini et al., 2006a).

In order to describe the formation and evolution of potential hydrothermal dolomites and hydrocarbon reservoir facies, other classifications focused on the rock fabrics, on composition, texture, and diagenetic overprint of the host-facies and on the effects of shear stress and pore-fluid-pressure (Davies, 2004, 2007; Davis & Smith, 2006).

In this work a modified and extended classification is suggested, which incorporates on one hand the texture of dolomite outcrops, and on the other hand the internal fabrics (porosity, crystal size, and eventual rhythmicity, e.g. zebra bands) (Annex 2).

4.1 Textures of dolomite rocks

Three basic types (massive, banded, and breccia) are defined according to the macroscopic features of the dolomite rocks (see Fig. 4.1).

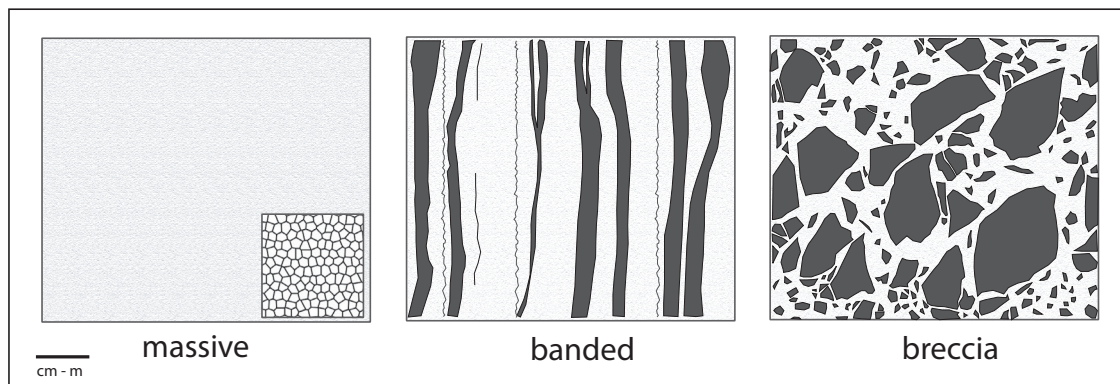


Fig. 4.1: Basic textures in dolomite rocks.

Massive

Massive dolomites are characterized by aggregates of crystals, showing uniform crystal sizes, giving a granular appearance. This is the most abundant type in the samples collected (74%) (Fig. 4.2 a, d).

Banded

The term refers to usually well-bedded, mostly banded dolomites, characterized by an alternation of light grey or yellow and dark grey dolomite bands. The single bands possess thicknesses ranging from mms to tens of cms. These bands follow broadly the stratification, lamination or stylolite planes. Dark bands are less abundant than light bands, the latter showing larger thicknesses and better porosities. This is the second most abundant type in the samples collected (20%) (Fig. 4.2 b, d).

Breccia

These dolomite types are characterized by angular to subangular fragments of the host rock, wrapped in a fine matrix, also affected by dolomitization. This type is less abundant in the samples collected (6%) (Fig. 4.2 c, d) and is restricted to certain areas.

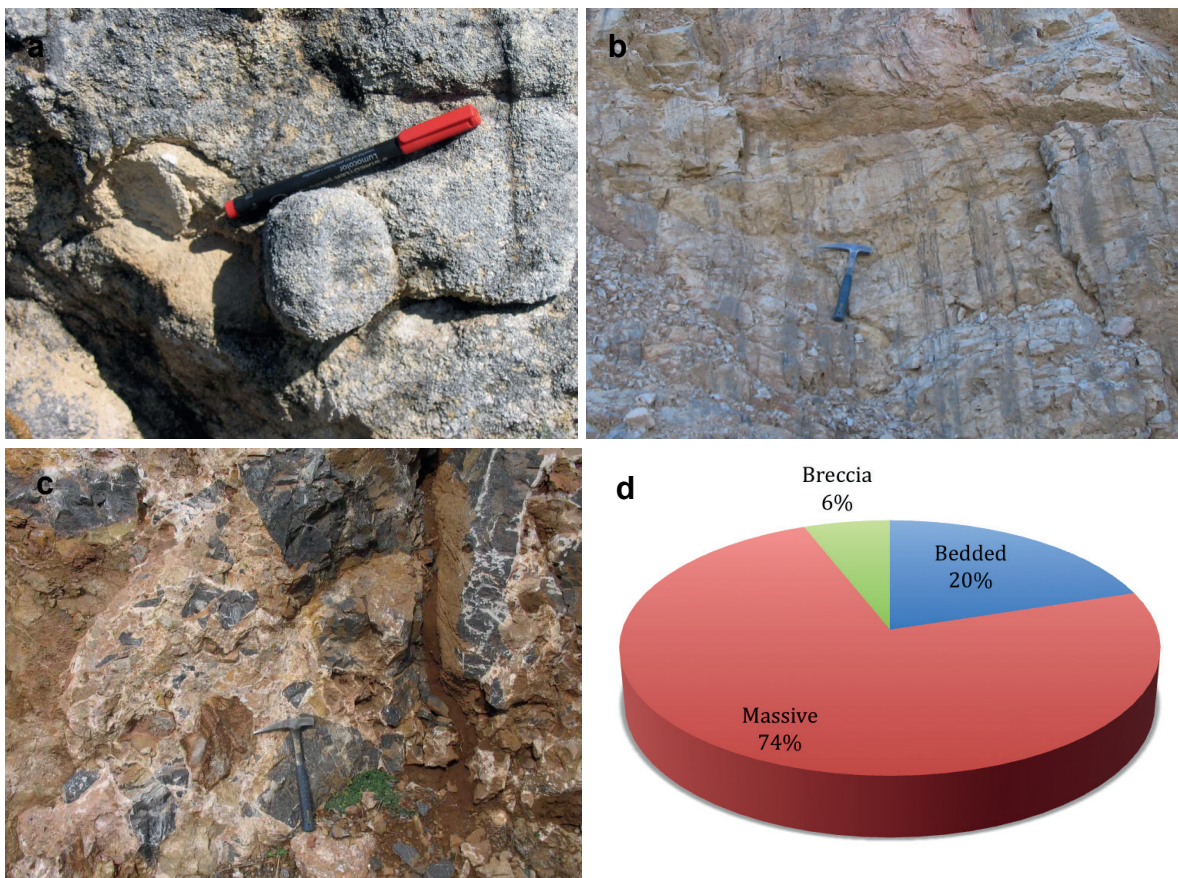


Fig. 4.2: Textures of dolomite rocks in outcrops: (a) massive (locality Cofiñal); (b) banded (locality Millaró); (c) breccia (locality San Emiliano 2); (d) proportions of the different textures.

4.2 Fabrics of dolomite rocks

In addition to the macroscopic appearance of dolomites, the internal fabrics allow a more detailed classification. The fabrics can often be distinguished by the naked eye and depend on the distribution of porosity, crystal size and eventual rhythmicity (Fig. 4.3). Four basic types are distinguished: zebra (meso and micro), vuggy, non macroporous (fine, coarse, the latter also called sucrosic) and breccia. The proportions of these are given in Fig. 4.5e.

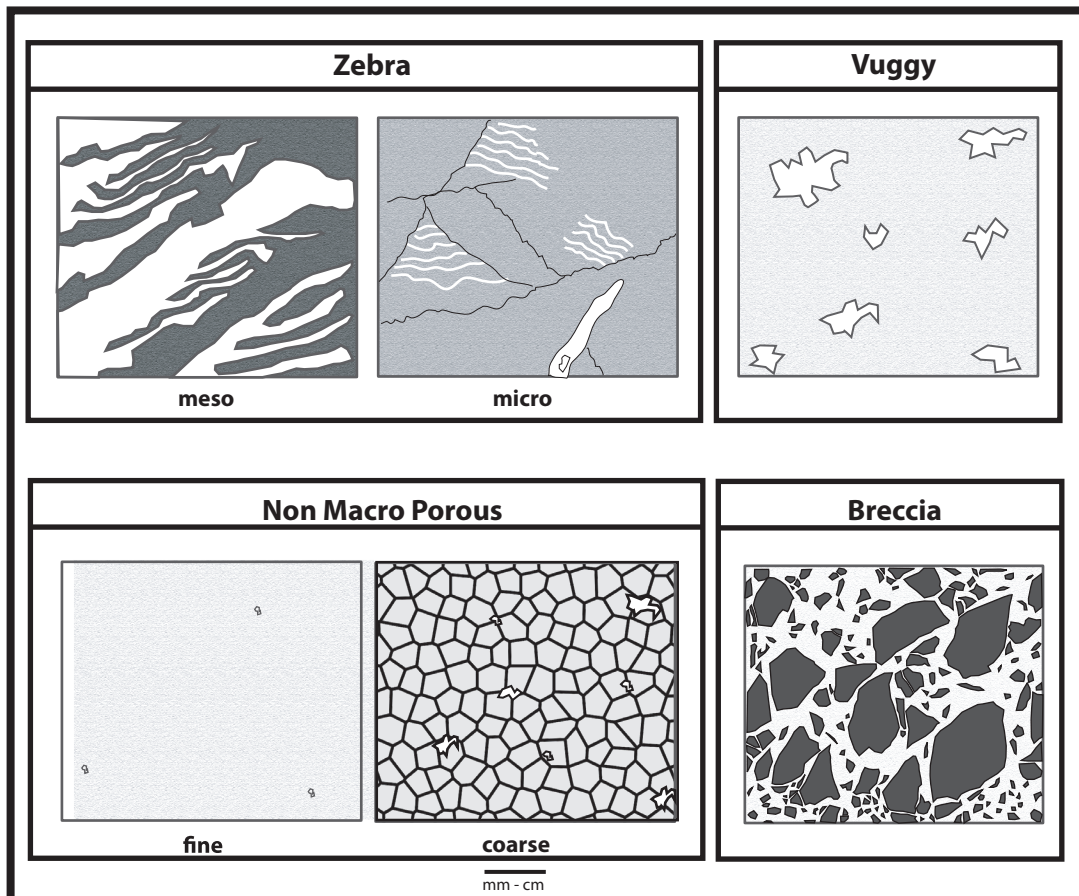


Fig. 4.3: Basic types of dolomite fabrics.

Zebra

This fabric comprises a repetition of rhythmic, mosaic dolomite and “sparry” dolomite (dolomite cement). The crystals of the latter grew in bipolar directions with partly larger open spaces in between the cement bands, which are oriented opposed to one another. Depending on the size of the rhythmic zebra bands, micro zebra ($<5\text{ mm}$) and meso zebra ($>5\text{ mm}$) are recognized. Both zebra fabrics can be further subdivided in subtypes (Fig. 4.4). In terms of the relationship to the bedding, the following subtypes can be distinguished: parallel, perpendicular, inclined. With regard to the relationship to the shape the subtypes are: chevron, planar, sigmoidal (Figs. 4.4, and 4.5 a, b).

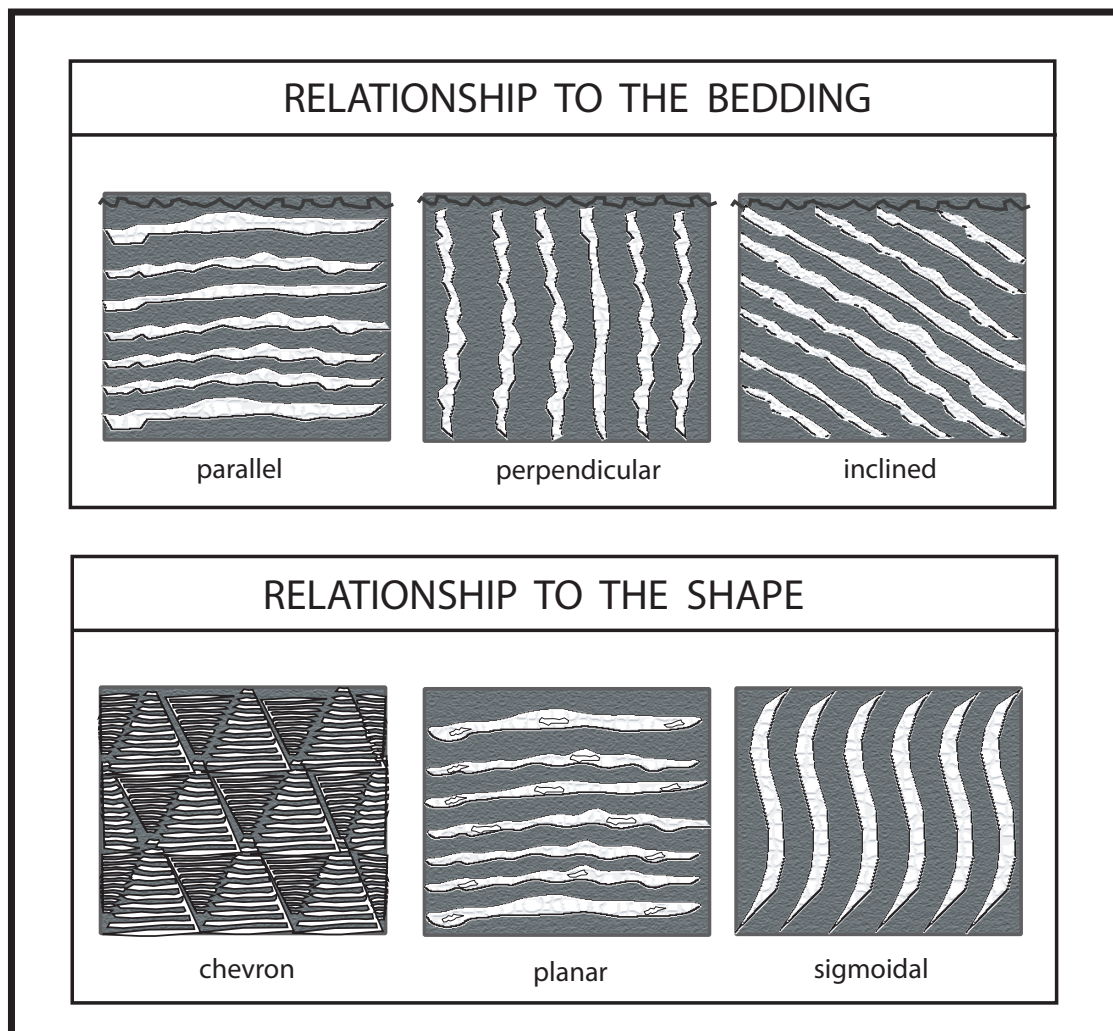


Fig. 4.4: Subdivision of the observed zebra fabrics (modified from Davies, 2004; Davies & Smith, 2006).

Vuggy

This fabric is characterized by the presence of vugs (several mms to cms in size), observable by the naked eye inside the dolomite rock, often filled with calcite or saddle dolomite. There are different shapes: rounded, elongated and angular; the cavities can be aligned or scattered (Figs. 4.3 and 4.5c).

Non Macroporous

This fabric shows uniform crystal sizes; large pores or rhythmicity cannot be observed. Two subtypes were differentiated (after the scale of crystal sizes, Folk 1965): (i) fine, being finely crystalline and tight; (ii) coarse (or sucrosic), being coarsely to extremely coarsely crystalline (Figs. 4.3 and 4.5 d, e).

Breccia

The breccia type contains samples of various genesis, containing several fragment types and shapes in a fine-grained fragmented dolomitized matrix (Figs. 4.3 and 4.5 f).

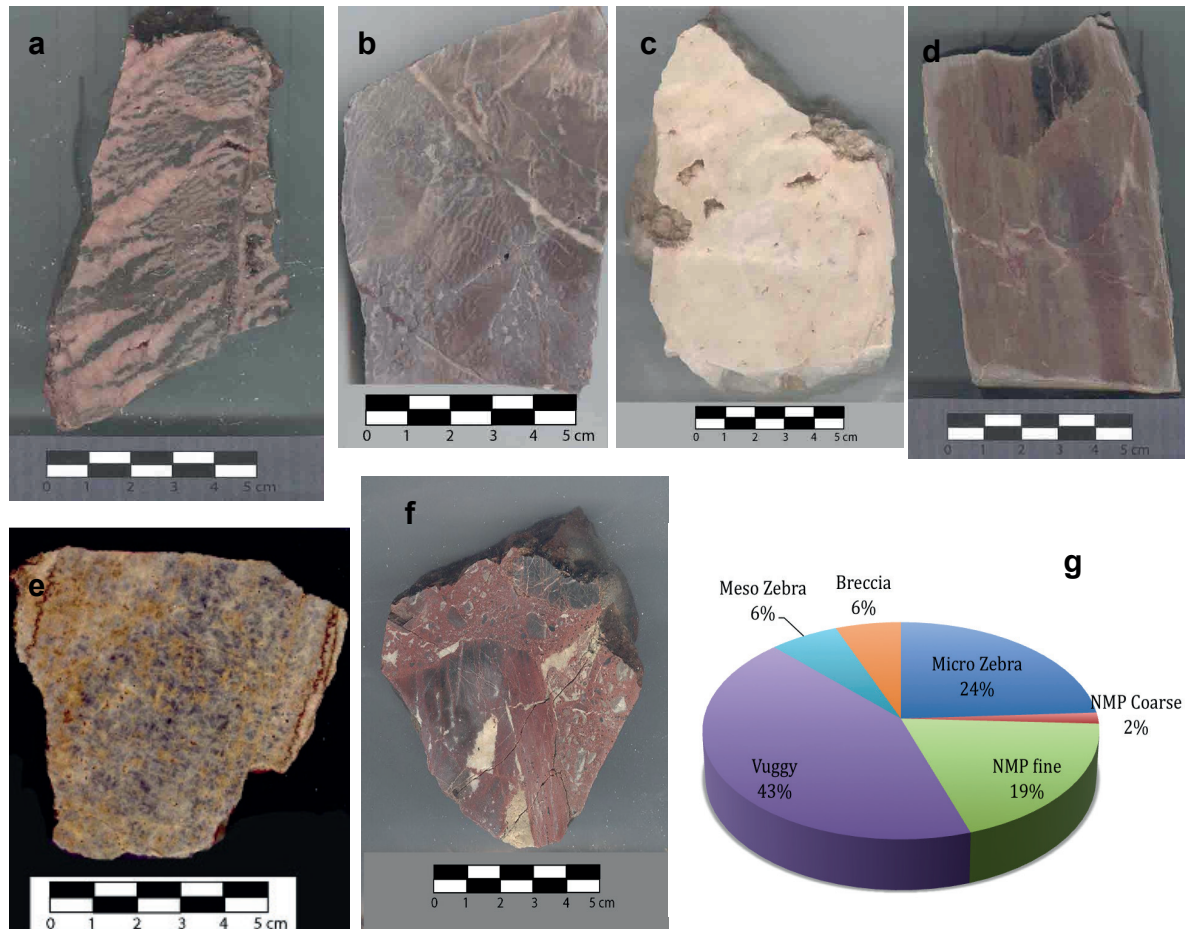


Fig. 4.5: Different dolomite fabrics: (a) meso zebra; (b) micro zebra; (c) vuggy; (d) non macroporous fine; (e) non macroporous coarse (sucrosic); (f) breccia; (g) proportions of the different fabrics observed.

5. PETROGRAPHY

70 uncovered thin sections (50–60 µm) were classified according to Sibley & Gregg (1987). This classification is based on crystal size (from “aphanocrystalline”, 0.001–0.004 mm, to “very coarsely crystalline”, 1–4 mm), crystal distribution (“unimodal” or “polymodal”), and shape of crystal boundaries (“planar”, “transitional”, and “non planar”). In addition, paragenetic relationships can be used as well. Gasparini (2003) and Gasparini et al. (2006a) recognized four dolomite types. The first two are Dolomite A (replacive event), and the other two, which fill cavities, are Dolomite B (void filling event). Remaining open cavities and microfractures are only locally filled with late calcite (C).

The same samples were analyzed with cathodoluminescence microscopy and five main types of luminescence are recognized: (i) dull red to orange, unzoned, (ii) dark red, zoned, (iii) mottled dull red to mottled dull orange, (iv) brightly orange unzoned, and (v) lightly orange with intense concentric zonation. The CL details of the main four dolomite types are reported in Annexes 3 and 4.

5.1 Replacive Dolomite (Dol A)

This type is widely distributed in the study area and is the major constituent of the samples (65%). Dolomite A1 (Dol A1): mostly non-planar texture, commonly finely crystalline (10–20 µm), becoming medium crystalline (up to 80 µm) towards discontinuity planes. The dolomite often follows such discontinuity planes, mainly stylolites. CL colours are dull red or orange, unzoned, with scattered bright-red, micron-sized spots (Fig. 5.1). Intercrystalline porosity is very limited, because the crystals are strongly interlocked. In some samples recrystallized fossils occur, mainly crinoids, but also corals (in the Devonian formations).

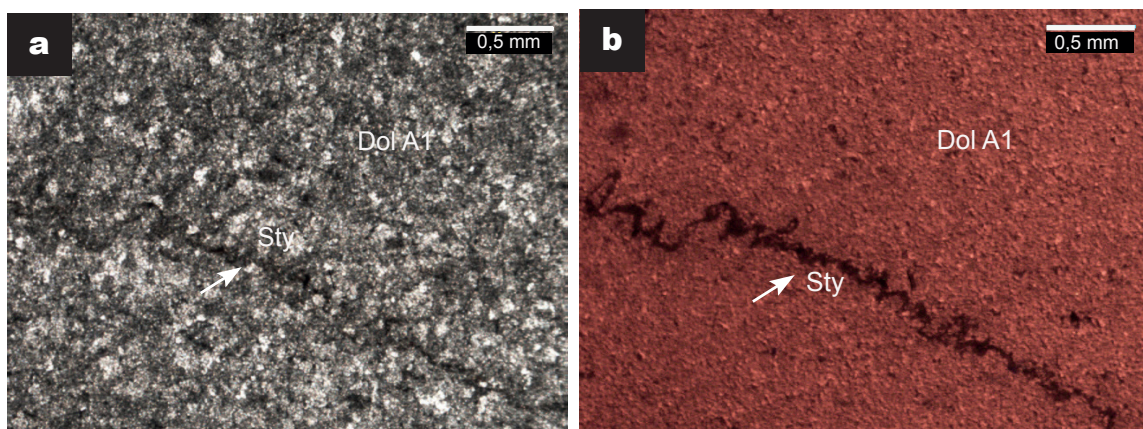


Fig. 5.1: Microphotographs of thin section of Sample 167, Sierra del Turrón: (a) normal polarized light, and (b) cathodoluminescence characteristics of Dolomite A1. Sty and arrow: Stylolite observed.

Dolomite A2 (Dol A2): also of non-planar texture; crystal size varies from finely crystalline to coarsely crystalline (50-200 µm). The crystal size distribution is mostly unimodal, but locally polymodal crystal distribution occurs due to the presence of fossils and other allochems in the host limestones. CL colour characteristics are similar to Dol A1, with only slight variations between unzoned, mottled dull red to mottled dull orange. The intercrystalline porosity is low, due to interlocked crystals, but some samples show a slightly increased porosity together with larger crystal sizes (Fig. 5.2).

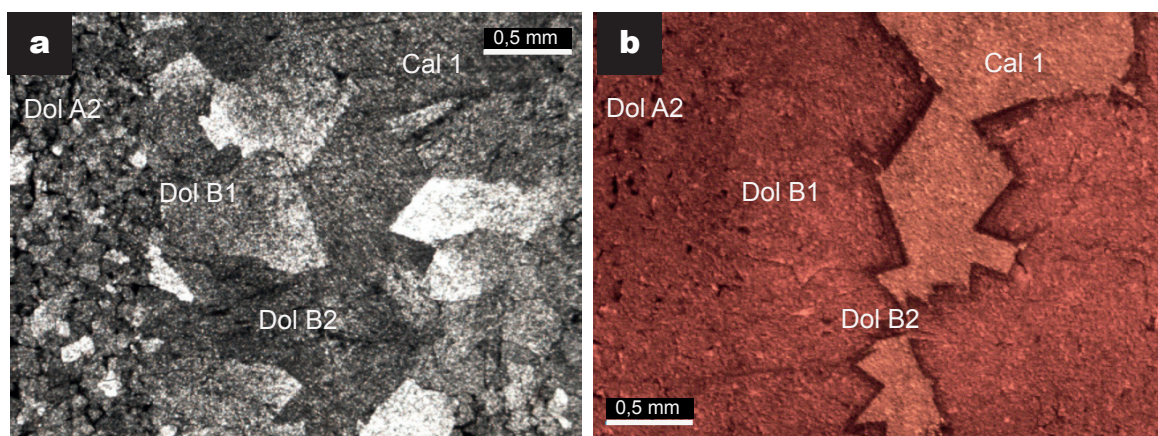


Fig. 5.2: Microphotographs of thin section of Sample 28, Lugueros. Dolomite A2, B1, B2 and Cal1 fill secondary porosity: (a) normal polarized light, and (b) cathodoluminescence. Porosity is well defined.

5.2 Void Filling Dolomite (Dol B)

Volumetrically, this type represents 27% of the samples investigated and is divided as follows:

Dolomite B1: textures vary from non-planar to planar-subhedral, medium to coarsely crystalline. Typical for these saddle dolomites, filling veins and other types of porosity, is the undulose extinction. CL colours are mostly similar to the ones of replacive dolomites. Only in a few cases, especially in veins, the colour tends to be dull orange (Fig. 5.2).

Dolomite B2: planar-subhedral crystal textures with a clear concentric zonation at the crystal terminations. The crystal sizes vary from coarse to very coarse. CL colour is dull red with slight variations in its intensity. Zonation is clearly observed in the crystals, with intercalation of dark red zones parallel to the crystal growth. In some samples, a slight displacement of crystals along microfractures has been identified (Fig. 5.3).

5.3 Calcite (Cal1 - Cal2)

Although calcite is rare (<6%), two types of late calcite (Cal1, Cal2), filling cavities and fractures, are observed. These are easily recognizable in the cathodoluminescence analysis. Cal1 presents a bright orange colour, in some samples of varying intensity. Cal2 shows a strong concentric zonation of thick non-luminescent and very thin bright orange zones (Fig. 5.3).

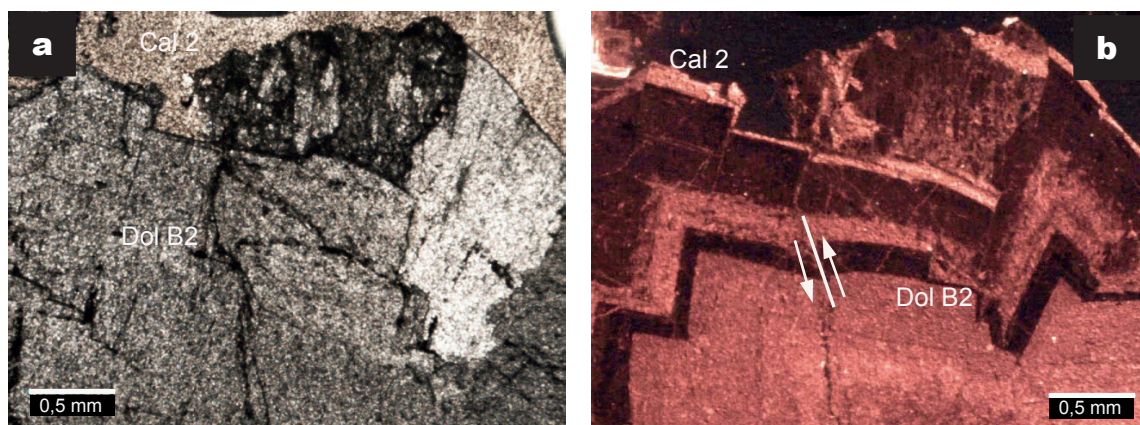


Fig. 5.3: Microphotographs of thin section of Sample 202, Llamazares, showing Dolomite B2 and Calcite 2 under (a) normal polarized light, and (b) cathodoluminescence. Slight displacements along microfractures are observed (one is marked).

6. PETROPHYSICS AND SPATIAL ANALYSIS

Dolomites are characterized by a high to medium porosity. This porosity is caused/influenced by the following factors: amount of fractures, dissolution, recrystallization, cementation, and compaction.

The petrophysical properties of dolomite vary depending on the texture. Diagenetic history and crystal textures may be the result of different conditions, and can be a predictor of petrophysical properties (Woody & Gregg, 1996).

Petrophysical analyses of porosity and permeability of about 250 samples were performed at the laboratories of Eni, San Donato Milanese, using Absolute permeability and Porosity by resaturation method. The relation of poroperm properties to the classifications described above was analyzed statistically (using mainly the arithmetic mean) and an eventual spatial distribution of porosity and permeability was investigated.

Porosity (Φ) and permeability (k) of the dolomites have a certain relation: porosity values cluster between 0.55% and 12%, and permeability values between 0.01 mD and 11.3 mD. Samples from dolomites near the contact dolomite-limestone show smaller porosities and permeabilities. Φ ranges between 1.6 – 4.2%, and permeability values between 0.02 – 1.2 mD. Limestone samples have even lower values of poroperm properties, strongly differing from the dolomitized rocks (Fig. 6.1).

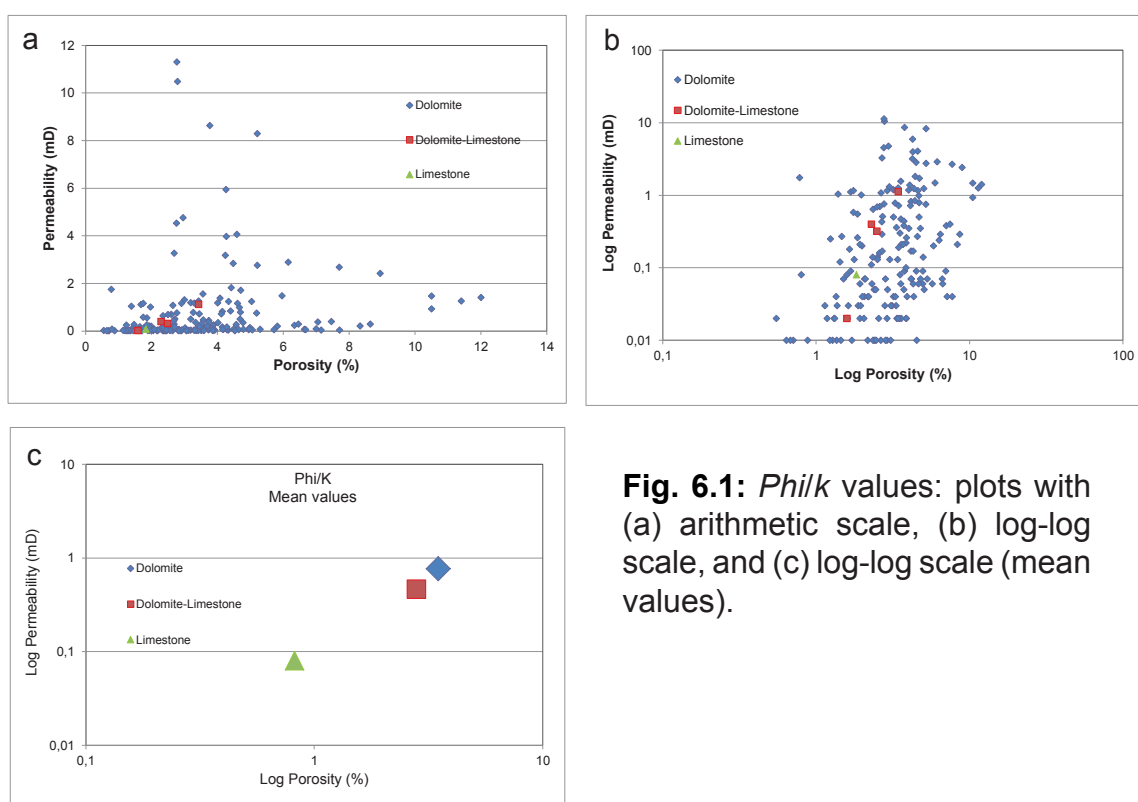


Fig. 6.1: Φ/k values: plots with (a) arithmetic scale, (b) log-log scale, and (c) log-log scale (mean values).

6.1 Poroperm values in relation to textures and fabrics

6.1.1 Texture of dolomite bodies and poroperm values

Samples with banded textures have the highest poroperm values (mean ϕ : 3.87%; mean k : 1.79 mD), whereas samples with massive textures show a wide range with the second best mean values (ϕ : 3.42%; k : 0.58 mD). The latter type mainly possesses coarse crystal sizes (see later, internal structures). The other types show partly fair ϕ , but low k values: the range of poroperm properties from samples with breccia textures is low (mean ϕ : 3.14%, mean k : 0.37 mD). Samples from neighbouring limestones and from the contact dolomite-limestone show the lowest ϕ values. The latter have, however, k values slightly higher than those from dolomite with breccia texture (Fig. 6.2).

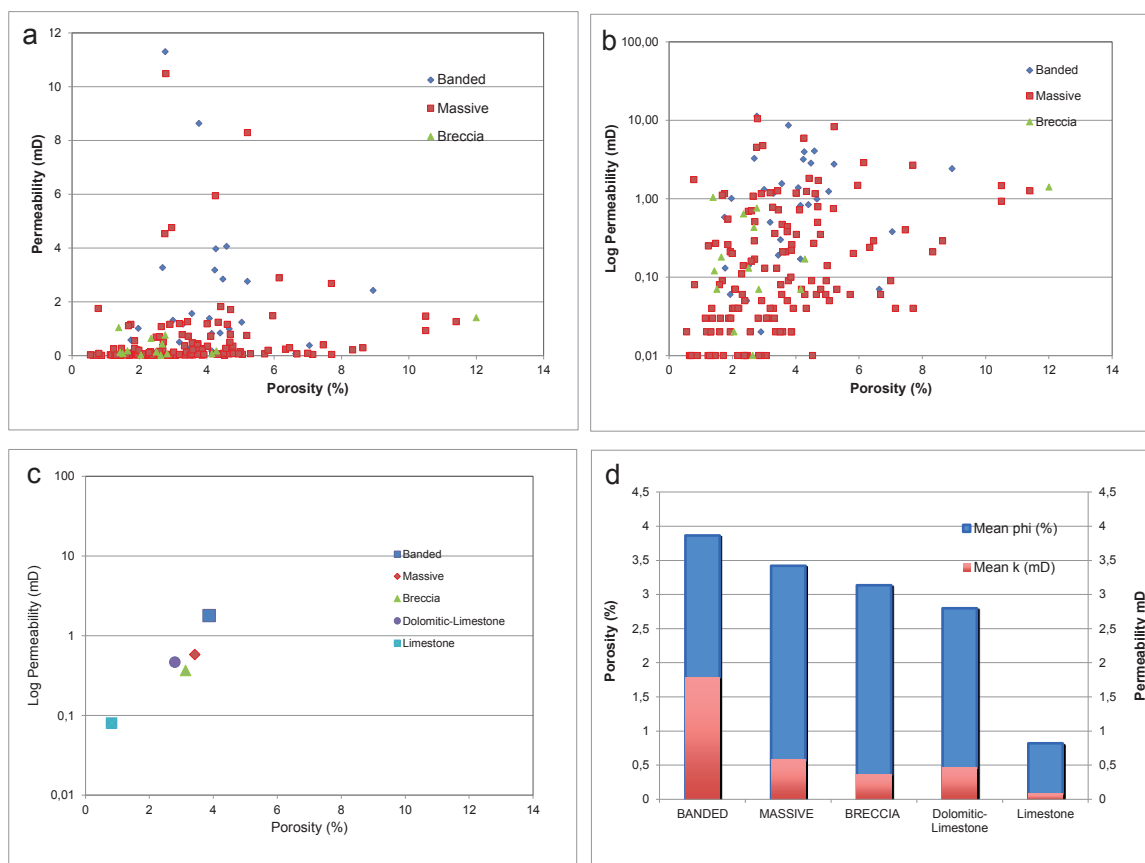


Fig. 6.2: ϕ/k data grouped according to the different textures of the dolomite bodies: plots with (a) normal scale, (b) log/normal scale, (c) log/normal scale (mean values), (d) column diagram of the mean values.

6.1.2 Dolomite fabrics and poroperm values

The fabrics present in the dolomites have a distinct effect on the amount of porosity and permeability. Samples showing the coarse non macroporous (sucrosic) fabric have the best poroperm values (mean ϕ : 5.31%; mean k : 2.69 mD), followed by

dolomites with the meso zebra fabric (mean ϕ : 3.07%; mean k : 2.09 mD) and the micro zebra fabric (mean ϕ : 4.07%; mean k : 1.21 mD). Samples with vuggy, breccia, and fine non macro porous fabrics show lower mean porosity values (between 3.64 to 2.46%) and very low mean k values (between 0.59 to 0.25 mD) (Fig. 6.3).

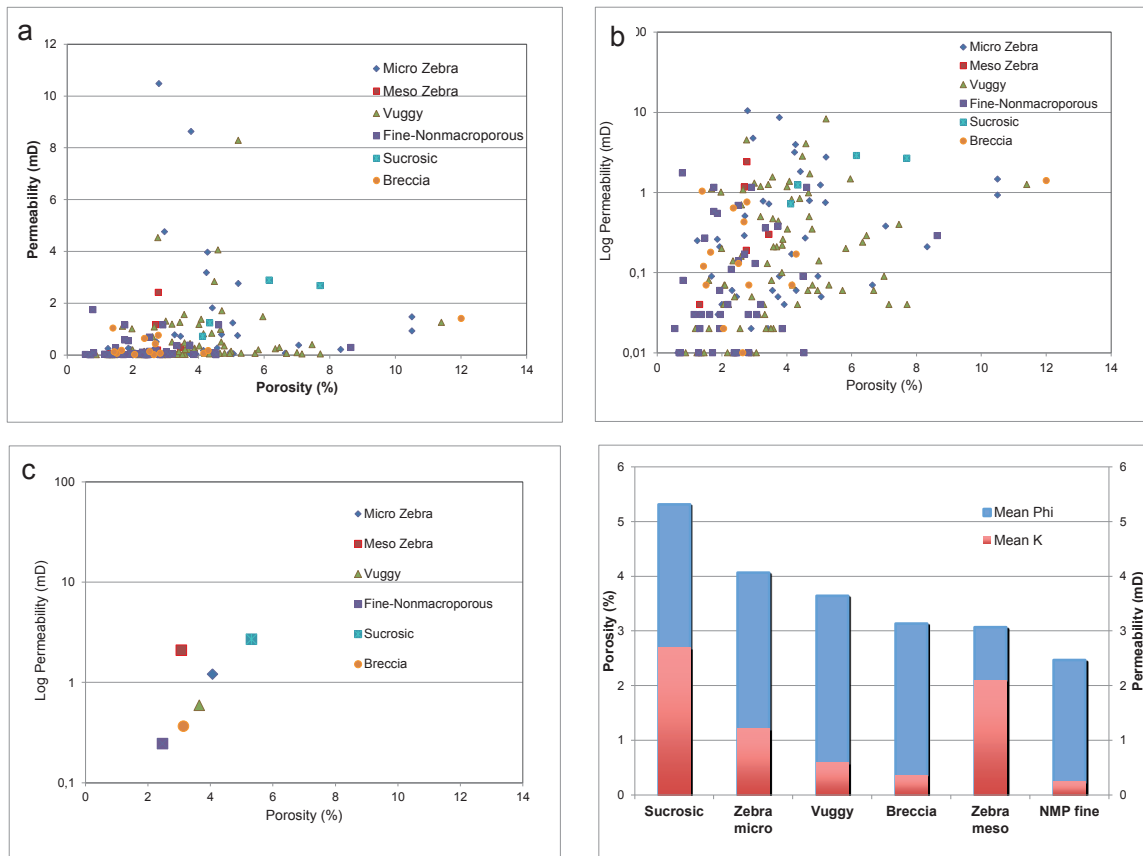


Fig. 6.3: ϕ/k data grouped according to the different fabrics of the dolomites: Graphs show (a) normal scale, (b) log/normal scale, (c) log/normal scale (mean values), (d) column diagram of the mean values.

6.1.3 Zebra characterization and poroperm values

Size of the rhythmic bands and poroperm values:

Most of the samples with better porosities belong to the micro zebra type (pores less than 5 mm), showing mean ϕ values of 4.07%; the samples with meso zebra fabrics have mean ϕ values of 3.07%. In terms of permeabilities, however, the mean k values are higher in the meso zebra fabrics (2.09 mD) than in the micro zebra fabrics (1.21 mD) (Fig. 6.4).

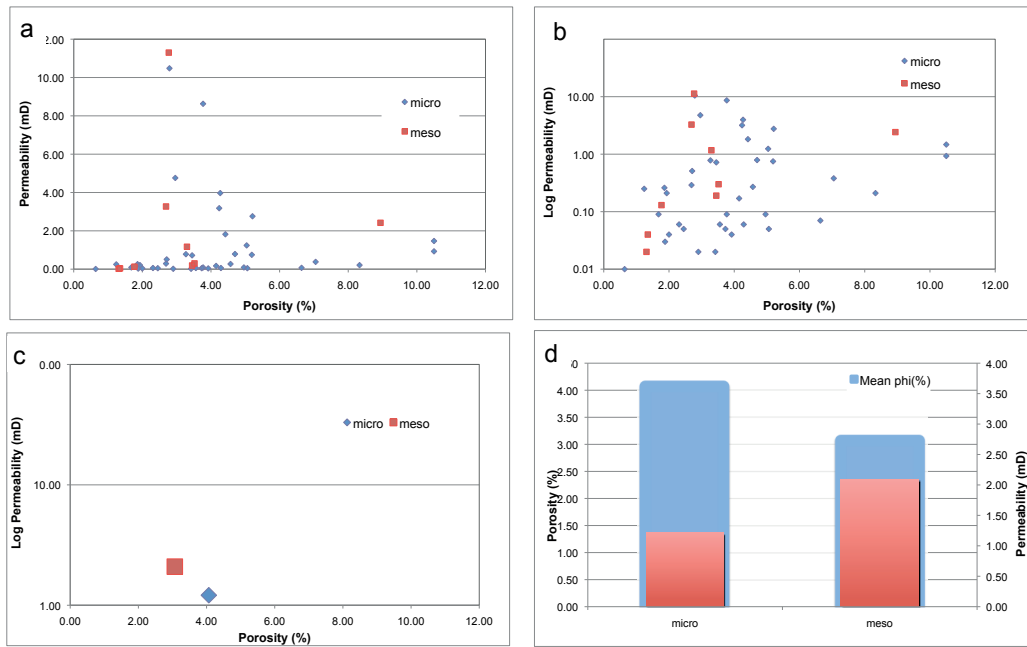


Fig. 6.4: Φ/k plots of the rhythmic bands. (a) normal scale, (b) log/normal scale, (c) log/normal scale, (mean values), (d) column diagram (mean values).

Orientation of the rhythmic zebra bands to bedding and related poroperm values:

In this group, the parallel type shows the best poroperm values (mean ϕ : 3.87%, mean k : 2.64 mD); for the other two types the porosity values are comparable with the former, but the permeabilities are distinctly lower (Fig. 6.5).

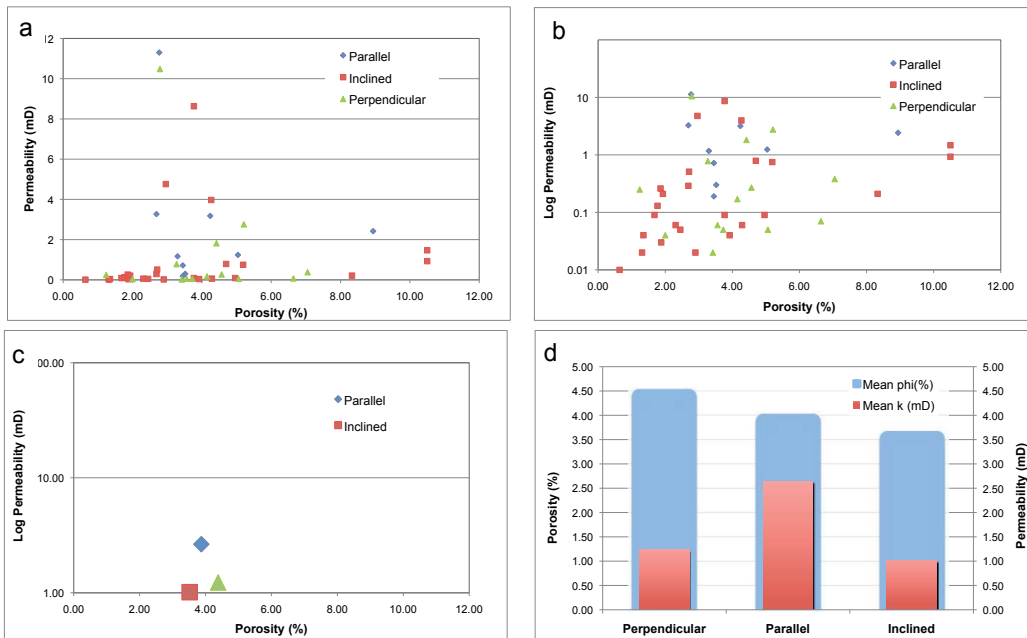


Fig. 6.5: Φ/k plots grouped according to the orientation of the rhythmic bands in relation to bedding. (a) normal scale, (b) log/normal scale, (c) log/normal scale (mean values), (d) column diagram (mean values).

Shape of the zebra bands:

Samples with zebra structures of chevron shape (mean ϕ 4.53%) and planar shape (mean ϕ : 4.20%) have the best porosity values, but only the latter show higher permeabilities (mean k : 1.56 mD) (Fig. 6.6).

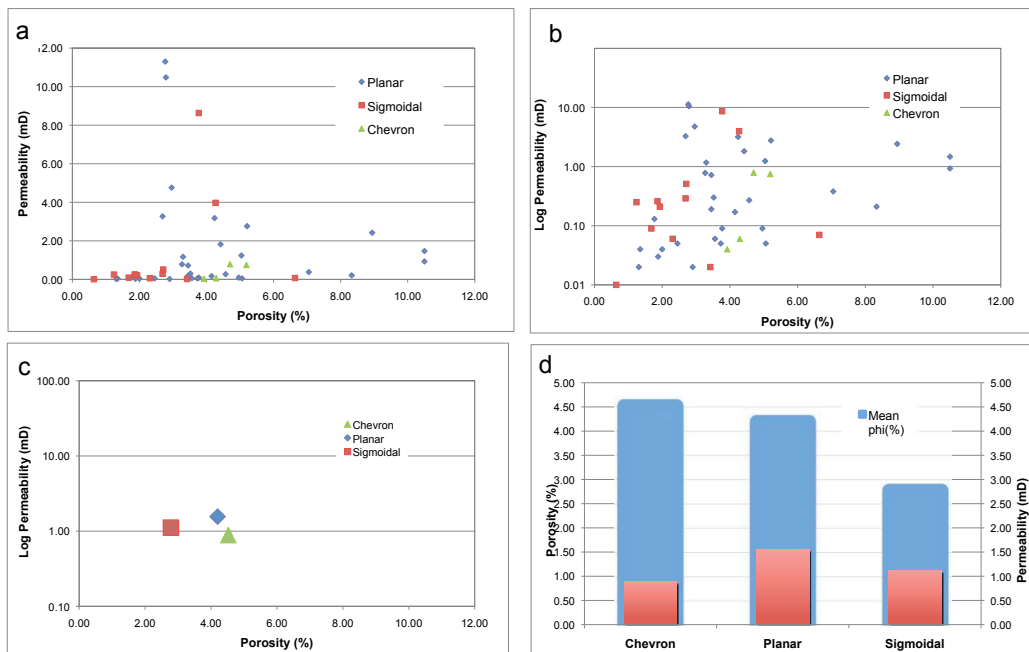


Fig. 6.6 Φ/k plots grouped according to the shape of the rhythmic bands. (a) normal scale, (b) log/normal scale, (c) log/normal scale (mean values), (d) column diagram (mean values).

6.2 Spatial analysis

All data were projected onto an E-W transect through the working area. This helps in the analysis and correlation of the spatial distribution of attributes (structural data, types of dolomite bodies and their internal fabrics). Areas with similar characteristics can be identified, linked to the spatial continuity.

6.2.1 Orientation of structural data in relation to macroporosity

The angle between bedding direction (S_o) and orientation of macroporosity (S_p) varies from parallel ($S_o \wedge S_p \approx 0^\circ$) to perpendicular ($S_o \wedge S_p \approx 90^\circ$). The measured data are shown in Annex 5. When the angles between S_o and S_p are low ($<30^\circ$), porosity is favourably affected: these higher porosity values might be due to the combination of bedding-parallel microporosities with the slightly inclined orientation of macroporosities (Annex 5). These characteristics occur mainly between Cofiñal - Talc Mine and Caldas de Luna - Villafeliz. Areas in between (mainly Sierra del Turrón and Canseco) show a large spread of the structural data, unfavourable and favourable for poroperm values ($S_o \wedge S_p < 30^\circ$) (Fig. 6.6).

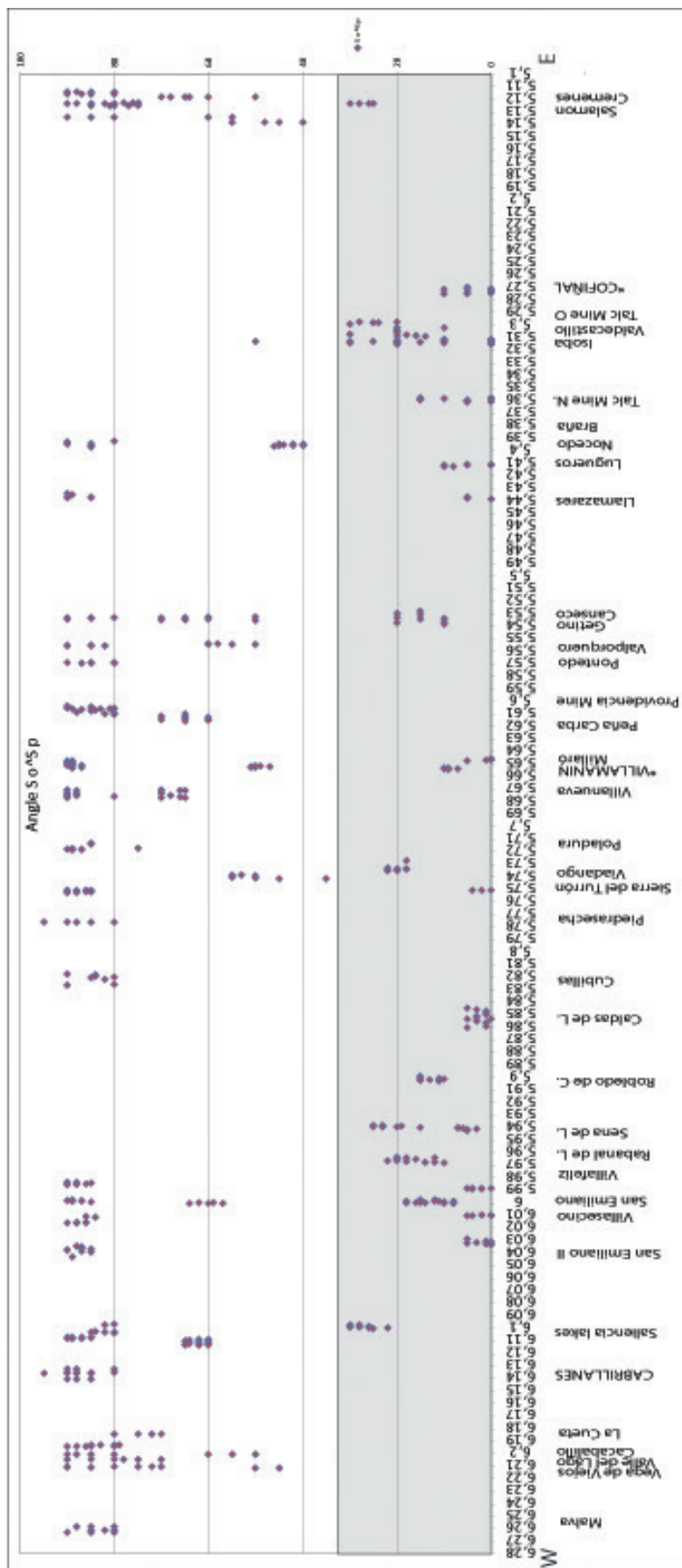


Fig. 6.7: Orientation of bedding direction to alignment of macroporosity ($S_o^S_p$) along the E-W transect.

Shaded zone: interval gives the values of $S_o^S_p < 30$.

In comparable subsurface settings a structural analysis of bedding versus orientation of macroporosity from borehole imaging might outline higher porous intervals/areas. The mentioned favourable areas relate only to porosity, regardless of permeability.

6.2.2. Spatial distribution of the poroperm data

The second dataset relates to E-W changes of porosity and permeability. A first evaluation included all poroperm data; subsequently more detailed evaluations concentrated on areas with especially favourable poroperm values in relation to the textures and fabrics of the dolomites bodies.

Mean porosities range between 2% and 8% and have fluctuating values along the E-W transect; higher values are found in the areas between Viejos – Cabalillo, San Emiliano – Villafeliz, Caldas de Luna – Poladura, and in the eastern core of the Cantabrian orocline (Talc Mine – Isoba) (Figure 6.7).

Mean permeability values range between 0.1 mD and 10.5 mD. Higher values are found in the following areas: Viejos – Cacabalillo, and Talc Mine – Isoba. Slightly increased mean values occur in San Emiliano – Villafeliz, Sierra del Turrón and Valporquero – Getino (Figure 6.8).

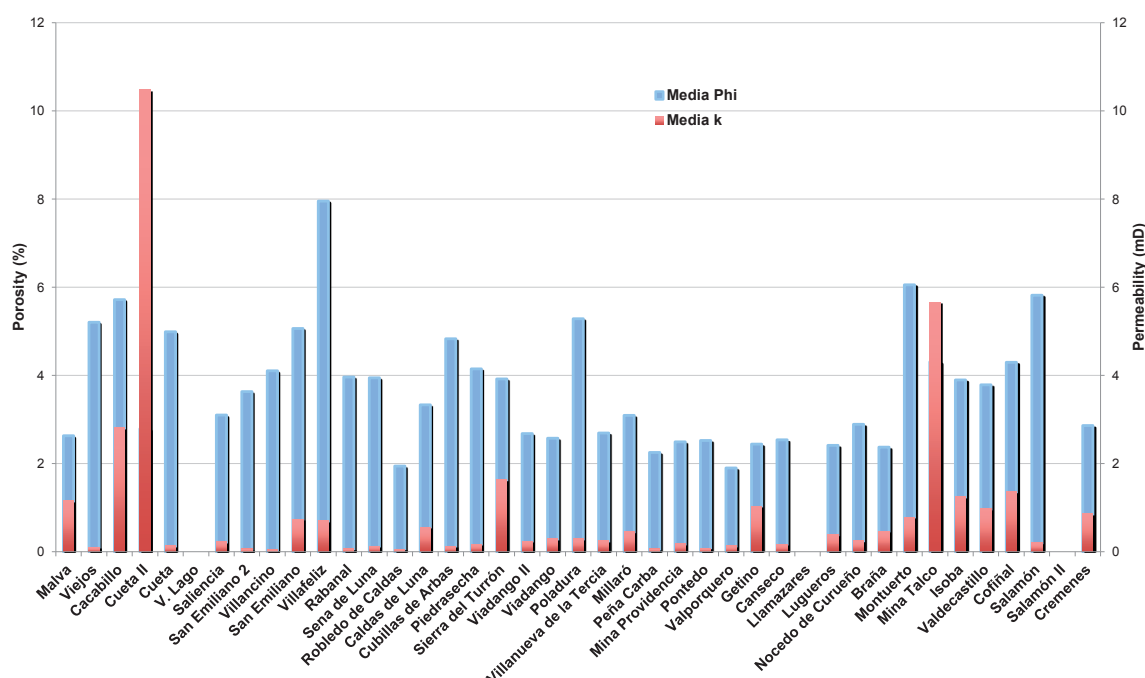


Fig. 6.8: Spatial distribution of porosity and permeability along the E-W transect.

In Fig. 6.8 the mean values of porosity and of permeability can also be compared. Poroperm is favourable in these areas: Cacabalillo – Cueta, San Emiliano – Villafeliz, Caldas de Luna - Sierra del Turrón – Poladura and Talc Mine – Cofiñal.

The data show a relation to the internal textures and fabrics of the dolomites, especially the angle between bedding direction and orientation of porosity (see Fig. 6.5 and below).

6.2.3 *Textures of dolomites and poroperm distribution: details*

A more detailed analysis was focused on the textures of the dolomite bodies. Samples with banded textures have the best poroperm values (mean ϕ : 3.87%, mean k : 1.79 mD); these occur mainly from Saliencia to San Emiliano in the west, Piedrasedra – Sierra del Turrón in the central part, and Talc Mine – Cofiñal in the east (Fig. 6.8).

Samples with massive textures contain the second best values (mean ϕ : 3.42%, mean k : 0.58 mD). High values correlate to highly fractured regions such as Cababallo – Cueta and San Emiliano – Villafeliz, or alternatively to areas with larger crystal sizes like Talc Mine – Cofiñal (Fig. 6.8).

Samples with breccia textures have somewhat lower poroperm values (mean ϕ : 3.14%, mean k : 0.37 mD), showing the relatively best values in the central part of the transect (Sierra del Turrón – Viadango) and in the east (Montuerto and Isoba) (Figs. 6.9 and 6.10).

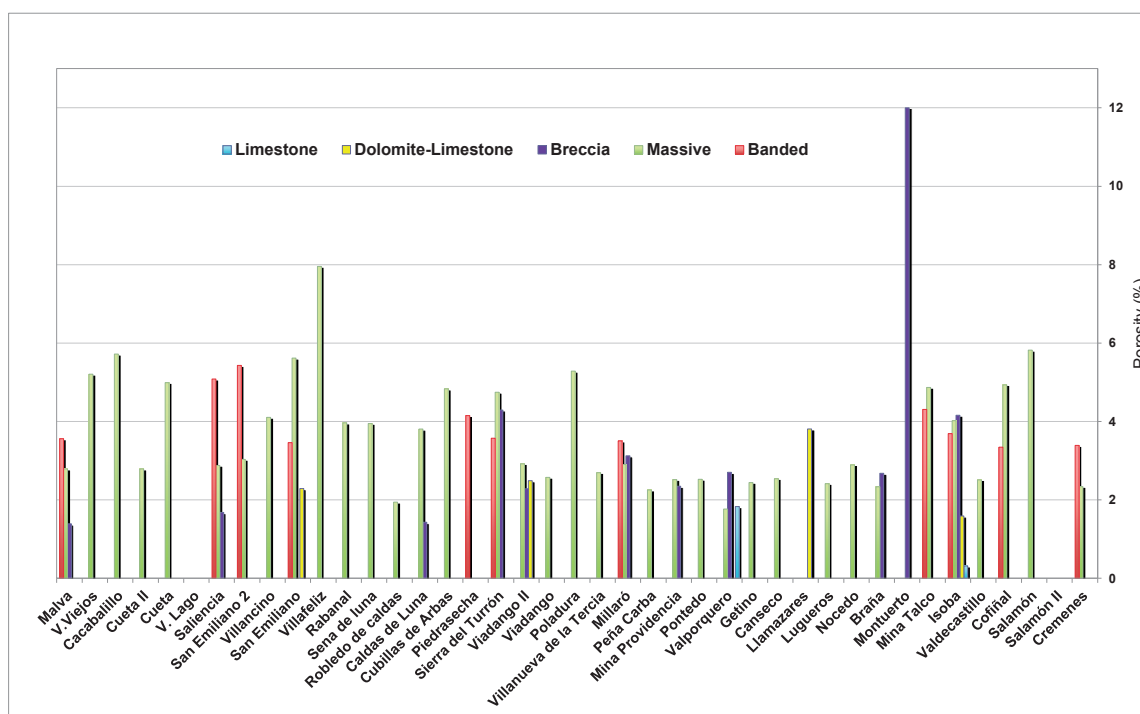


Fig. 6.9: Mean values of porosity in rocks of different textures (breccia, massive, banded) and lithology (dolomite-limestone, limestone) along the E-W transect.

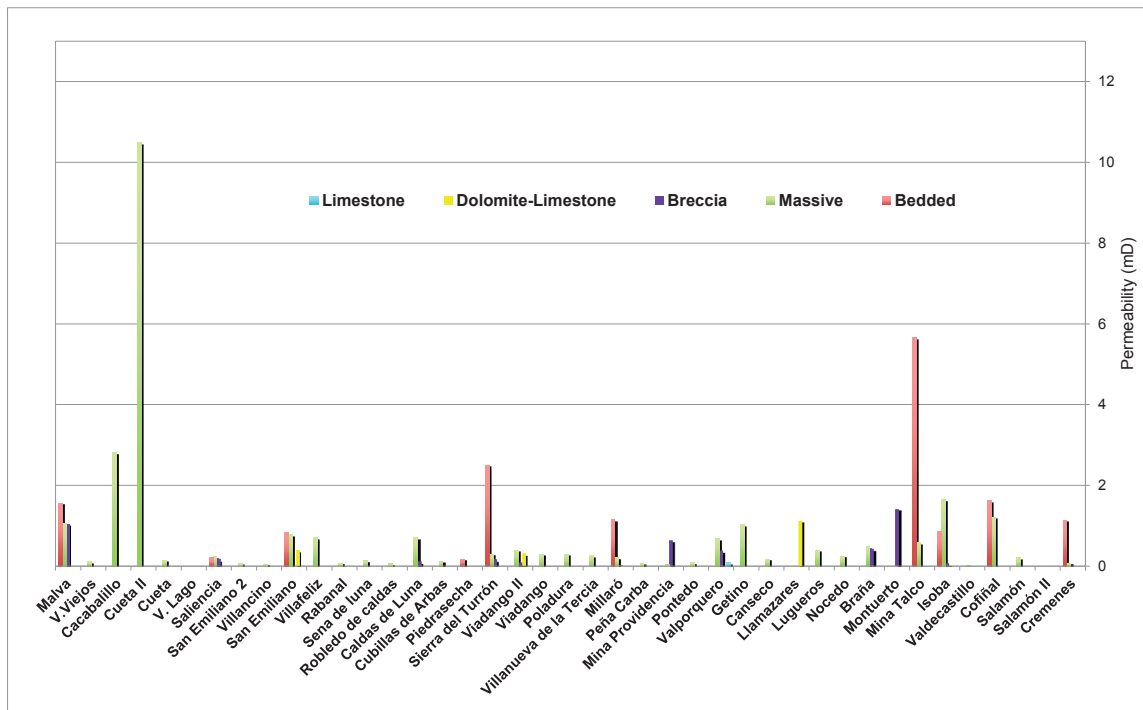


Fig. 6.10: Mean values of permeability in rocks of different textures (breccia, massive, banded) and lithology (dolomite-limestone, limestone) along the E-W transect.

6.2.4 Fabrics of dolomites and poroperm distribution: details

Samples with coarse, non macro porous (sucrosic) fabrics show the best poroperm values (mean ϕ : 5.31%, mean k : 2.69 mD). These occur mainly in the east (Isoba-Cofiñal; Fig. 6.9). In the same area the samples with meso zebra fabrics show favourable porosities as well and good permeabilities (mean k : 2.09 mD) (Fig. 6.10).

Samples with micro zebra fabrics have the second best porosities (mean ϕ : 4.07%), but much less favourable permeabilities (mean k : 1.21 mD) than the meso zebra fabrics. The micro zebras are concentrated in the western region (Vega Viejos-Cueta, San Emiliano-Villafeliz) (Fig. 6.11).

Rocks with vuggy and with breccia fabrics are widespread, have fair porosities (between 3.14% and 3.54%), but low permeabilities. Samples with non macro porous fabrics (with fine crystals) have the lowest poroperm properties; slightly better values occur only if this type occurs in highly fractured areas, as in the west of the transect (Fig. 6.11).

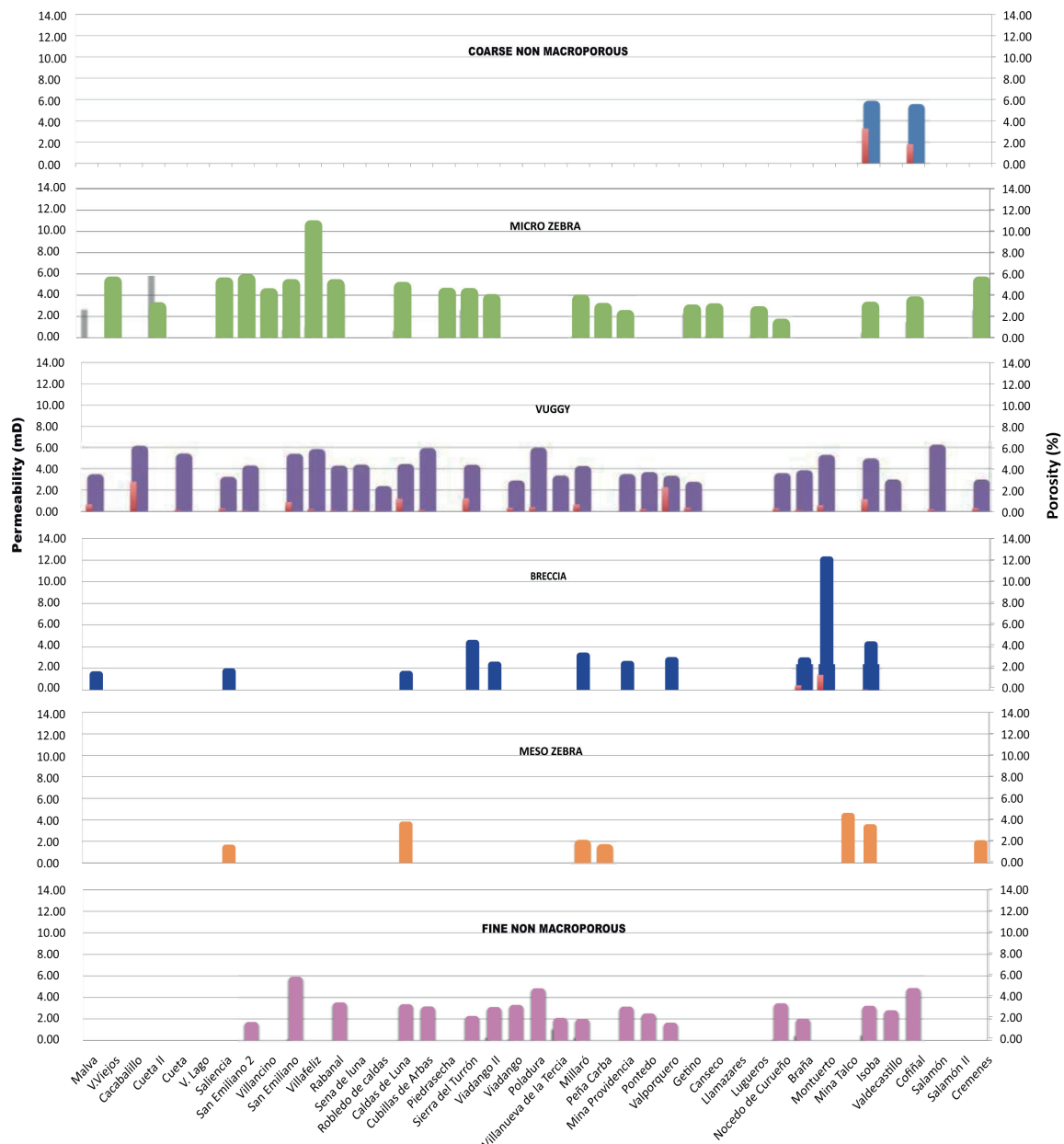


Fig. 6.11: Different fabrics and corresponding mean poroperm values along the E-W transect.

Rocks with zebra fabrics show high poroperm values and are widespread in the study area. As mentioned earlier, samples with micro zebra fabrics have better porosities (mean ϕ : 4.07%), but lower permeabilities (mean k : 1.21) than meso zebra fabrics (mean k : 2.09 mD). For micro zebra fabrics, rocks with the best porosities are concentrated in the west, mainly between San Emiliano and Villafeliz (Figure 6.12), whereas higher permeabilities are not directly related to the zebra porosities but occur in highly fractured zones like Cueta in the west, Sierra del Turrón in the

central part, and between the Talc Mine (*La Respina*) and Isoba (Fig. 6.12) in the east of the transect.

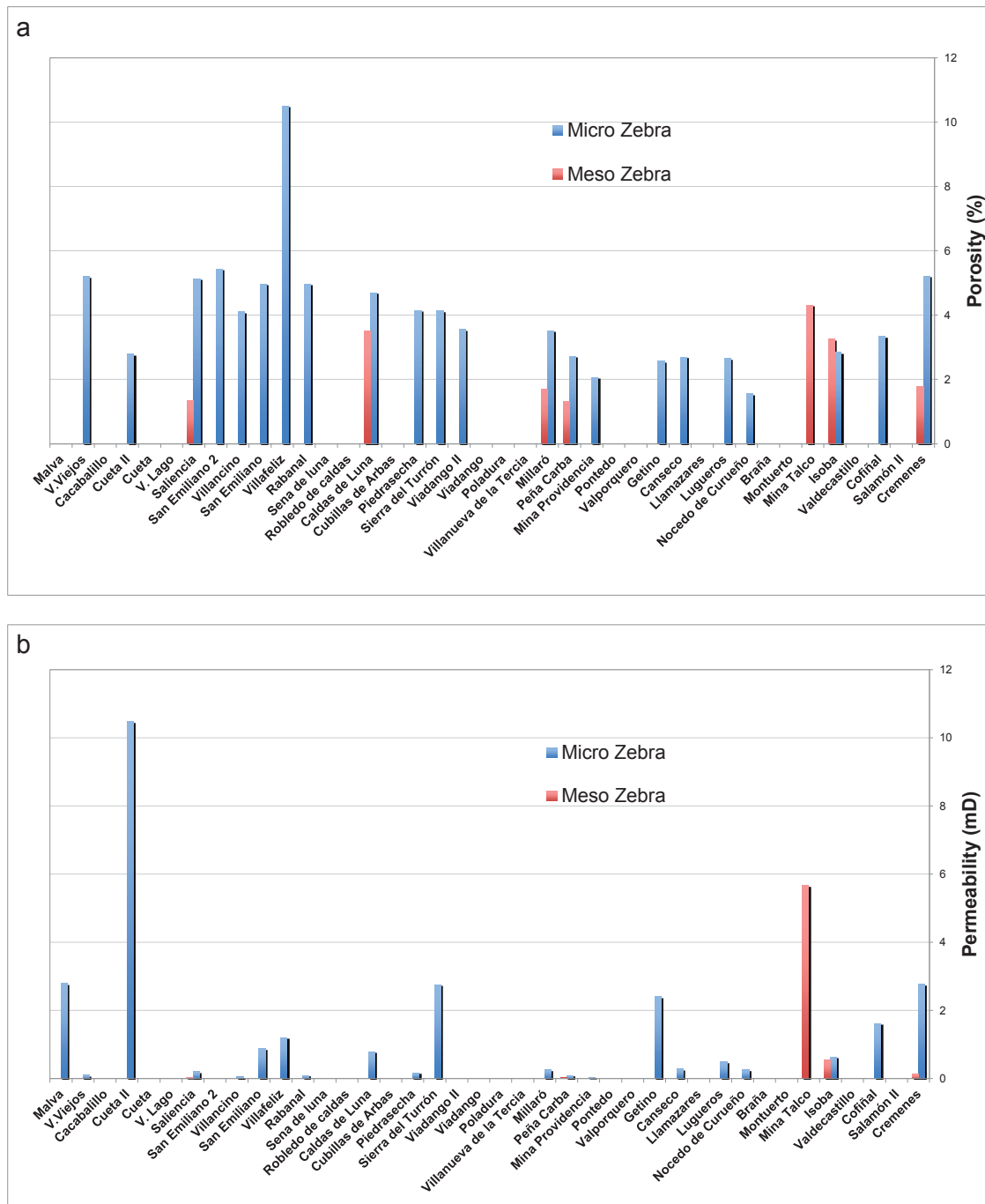


Fig. 6.12: E-W poroperm distribution according to the mean size of the rhythmic zebra bands. (a): Mean porosity values; (b): mean permeability values.

As pointed out before, the regional poroperm distribution is also influenced by the relationship between the direction of the rhythmic bands and the bedding. In the eastern sector relatively high poroperm values are represented by the parallel zebra type, frequently occurring in the region between the Talc Mine (*La Respina*) and Cofiñal (Fig. 6.13).

The perpendicular and inclined zebra types show higher porosities towards the west (Fig. 6.13a), but permeabilities are not directly related and show a spatially complex pattern. High values occur in the west (Cueta sector, perpendicular type), in the central part (Sierra del Turrón, inclined type), and in the east (parallel zebra type) (Fig. 6.13b).

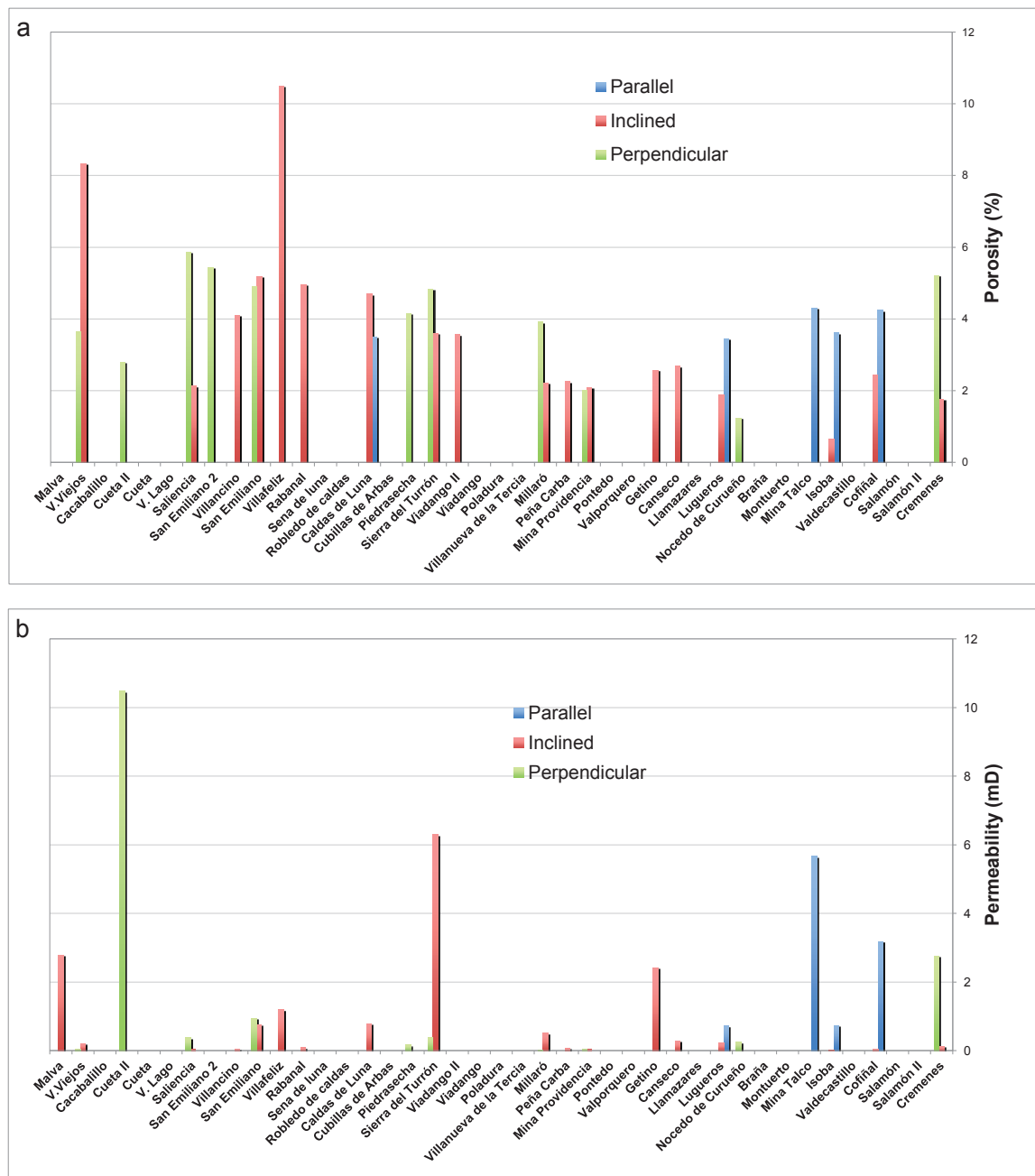


Fig. 6.13: Poroperm values according to the orientation of the rhythmic zebra bands. (a): Mean values of porosity; (b): mean values of permeability.

If we consider the shape of the rhythmic zebra bands, higher porosities are related to samples with the planar zebra type, closely followed by the chevron zebra type and by the sigmoidal zebra type. In terms of regional distribution, the best porosities

occur between San Emiliano - Villafeliz in the west (Fig. 6.14a). Permeabilities show again differences in their spatial distribution related to porosities: high values are to be found in the Cueta sector in the west and the Talc Mine area (La Respina) in the east (both with planar zebra type); in the central part some higher values have been found in the Sierra del Turrón area (chevron zebra and sigmoidal zebra type) (Fig. 6.14b).

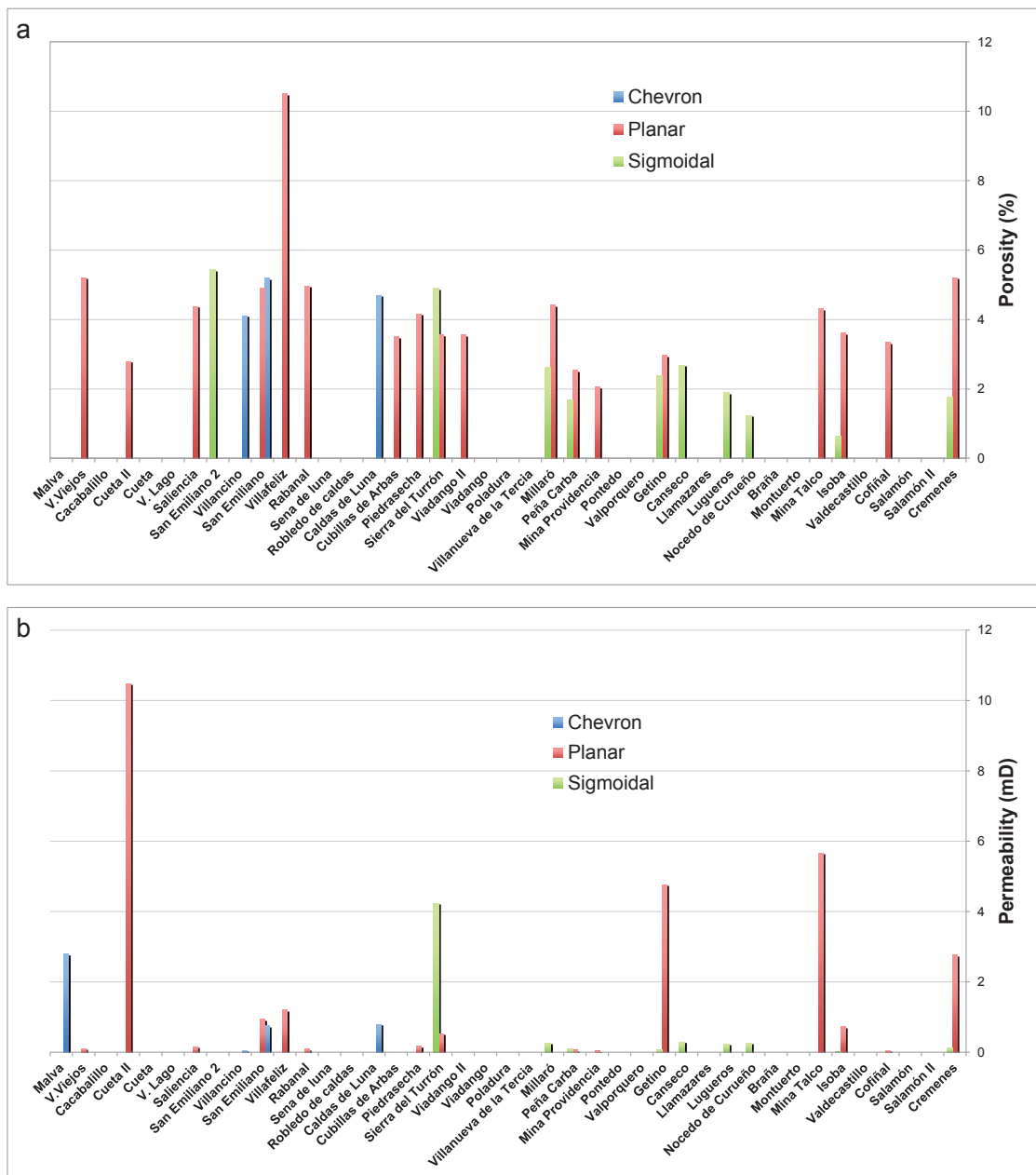


Fig. 6.14: Poroperm values related to the shape of the rhythmic zebra bands. (a): Mean values of porosity; (b): mean values of permeability.

7. IMAGE ANALYSIS

The various types of textures and fabrics of the dolomites show strong differences of poroperm values and pore shapes. Image analysis was carried out (i) to quantitatively define the different porosity types and values and compare these with the classical porosity measurements, and (ii) to outline the original porosity before cementation (and compaction) and the amount of cement in the pores. The image analysis was performed in the *Eni* laboratories, San Donato Milanese (Annex 6), applying the software *Image Pro 6.3*. Image analysis can be made at different scales, from outcrops (macro scale) to hand specimens and slabs (medium scale) to thin sections (micro scale)(Fig. 7.1). High resolution photographs or scans of 200 polished rock samples were chosen for image analysis. The various types of internal textures and fabrics of the dolomites show strong differences of poroperm values and pore shapes.



Fig. 7.1: Scale of image analysis. (a) Macro scale: outcrop of dolomite with massive texture and vuggy fabric. Isoba. (b) Medium scale: hand sample, plugs and slab. Millaró. (c) Micro scale: thin section. Isoba.

The following procedure was applied:

1. From the original scanned picture (Fig. 7.2a) the pore space was separated from the background and a binary image of the pores created (Fig. 7.2b).
2. The same procedure (1) was used also for the white dolomite cements that are isolated and measured separately. The resolution is 0.5 mm. The microporosity <0.5 mm is therefore not considered (Fig. 7.2c).

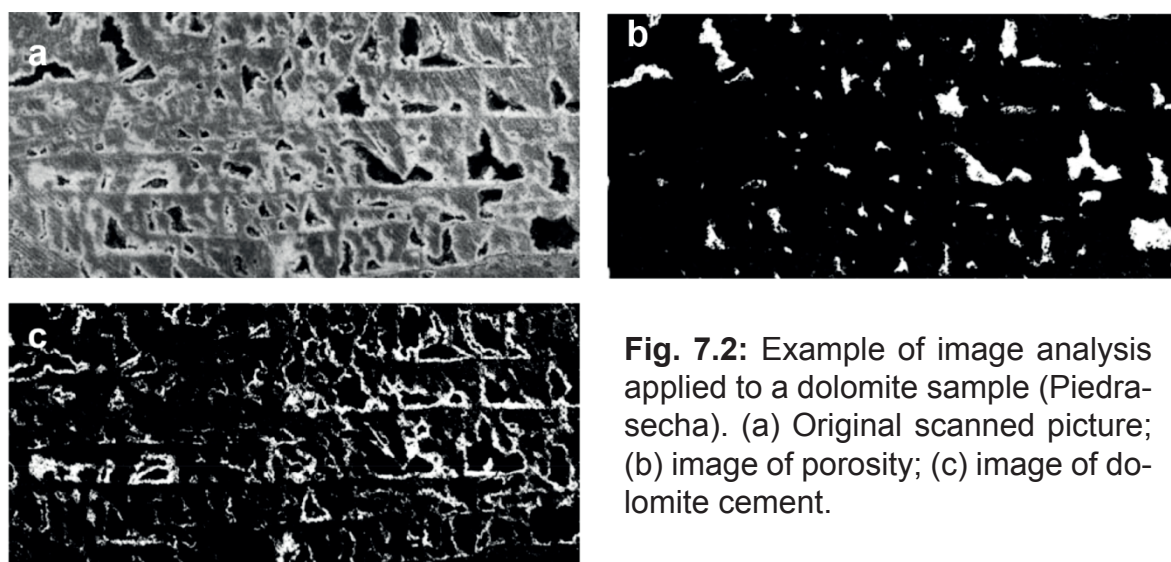
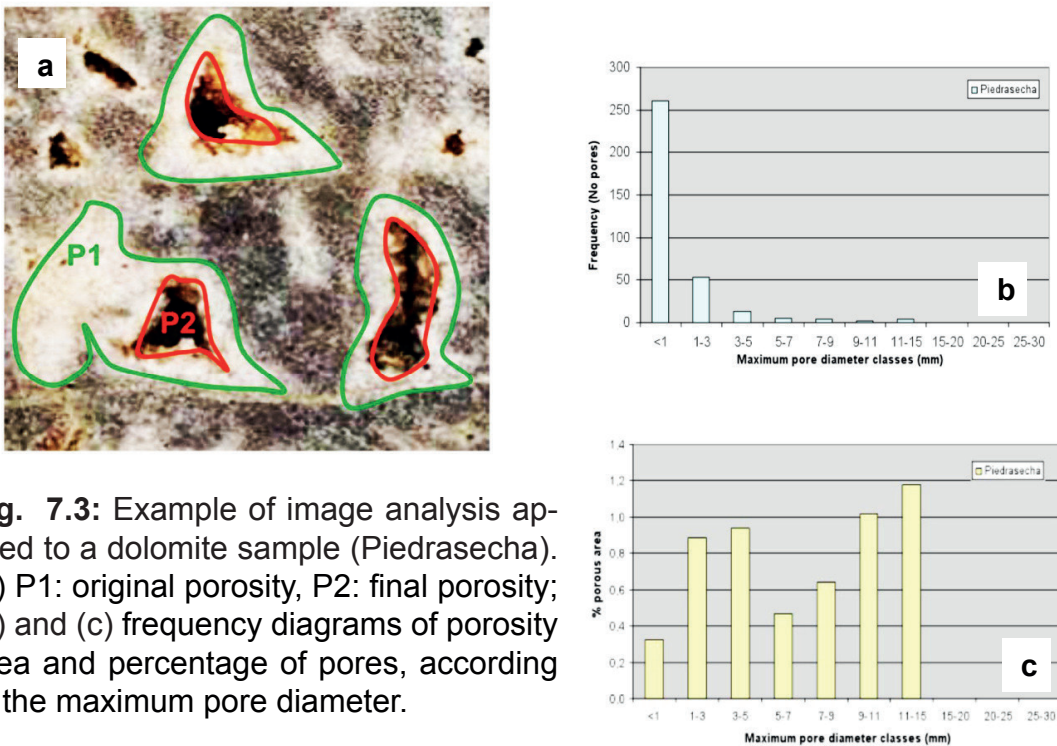


Fig. 7.2: Example of image analysis applied to a dolomite sample (Piedra-secha). (a) Original scanned picture; (b) image of porosity; (c) image of dolomite cement.

These two steps resulted in an automatic analysis of:

- Amount of present total porosity in 2D
- Average maximum pore diameter in 2D
- Frequency diagrams of the porosity area and the percentage of pores in 2D, according to the maximum pore diameter, referred to diameter classes (ranges: <1, 1-3, 3-5, 5-7, 7-9, 9-11, 11-15, 15-20, 20-25, 25-30 mm) (Fig. 7.3 b, c)
- Total amount of dolomite cements in 2D
- Amount of original porosity (present porosity + amount of dolomite cements) in 2D
- Porosity loss (dolomite cements /original porosity x 100) in 2D (Fig. 7.3a)



Using Routine Core Analysis (RCA), high RCA porosity values are represented by the coarse non macroporous (sucrosic) type, followed by micro zebra, vuggy, meso zebra, and fine non macroporous types. When porosity of IA is higher than plug porosity, the samples contain large macropores, which are not measurable from the plugs in heterogeneous samples. In microporous samples plug porosity is usually higher than porosity obtained from IA, because IA cannot detect very small pores. The meso zebra, coarse non macroporous (sucrosic), and fine micro zebra have high microporosities (Fig. 7.4).

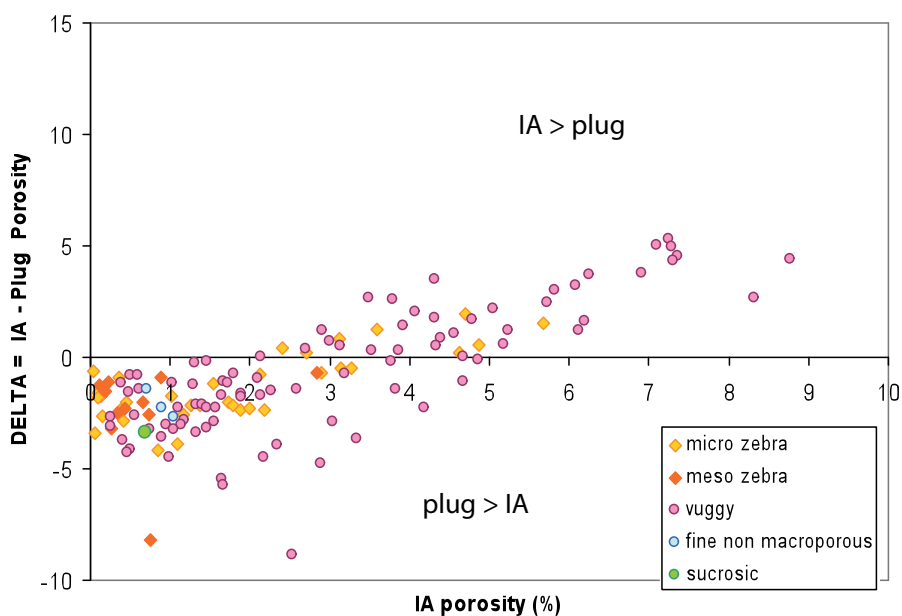


Fig. 7.4: Plot of IA porosity versus Δ factor (IA-plug porosity). Some of the fabric types are restricted to certain areas of the diagram.

All results of the image analysis are summarized in Table 2.

Table 2: Porosity data from plugs (RCA) and image analyses, the former ana-lyses giving also permeabilities.

	PLUGS		Image Analysis					
	Porosity (%)	Permeability (mD)	porosity (%)	Avg. Mean Max diameter (mm)	Aver. Maximum diameter (mm)	Maximum diameter (mm)	Porosity loss (%)	
Dolostone type	Meso Zebra	3.1	2.1	1.0	0.3	2.9	10.0	56.0
	Micro Zebra	4.1	1.2	2.0	0.4	6.3	19.0	16.0
	Vuggy	3.6	0.6	3.5	0.7	10.0	48.0	17.0
	Sucrosic	5.3	2.7	0.7	0.3	1.6	1.6	
	Fine Non Macroporous	2.5	0.2	0.5	0.3	2.5	3.3	

The best porosity and permeability values are represented by dolomites with coarse non macroporous (sucrosic) and micro zebra fabrics. Microporosity is high in sucrosic samples. Maxima of pore diameters have been observed in vuggy fabrics. Dolomite cement reduces dramatically the porosity, mainly in the samples with meso zebra fabrics (Fig. 7.5).

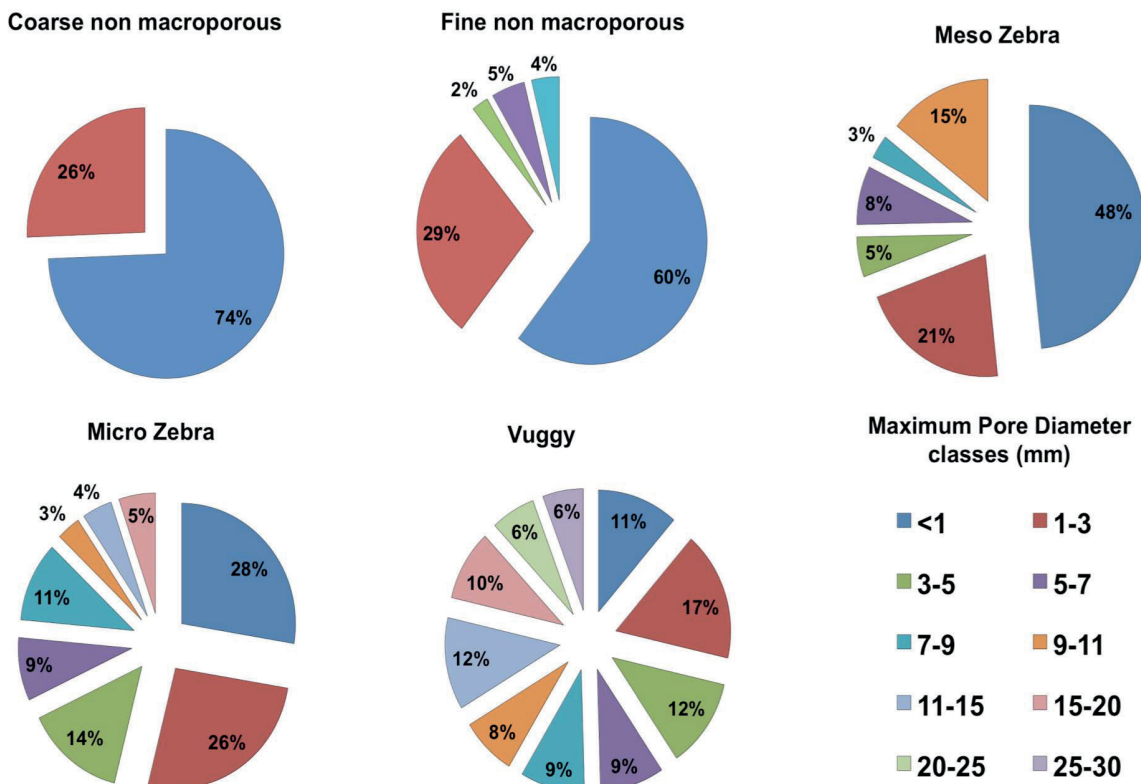


Fig. 7.5: Distribution of pore diameters in relation to the different dolomite fabrics.

The values of the porosity calculated from image analyses were projected on the earlier discussed E-W transect. Our evaluation concentrated on areas with especially favourable porosity values in relation to the fabrics and characteristics of the dolomites. The vuggy fabric has higher porosity values due to the larger pore diameters. The micro zebra fabric has higher porosities than the macro zebra fabric, due to the lower amount of dolomite cement. In the central region (Piedrasecha – Canseco) and in the eastern region (Llamazares – Cremenes) the vuggy type is frequent and contains the mentioned high *phi* values, whereas in the west (Malva – Cubillas de Arbas) the micro zebra fabric often occurs, having highest *phi* values (Fig. 7.6).

For the eastern zones (mainly Isoba-Cofiñal) the RCA porosity shows higher values for the meso zebra and the coarse non macroporous (sucrosic) fabrics; IA analyses show a drastic decrease of the original porosity due to strong cementation.

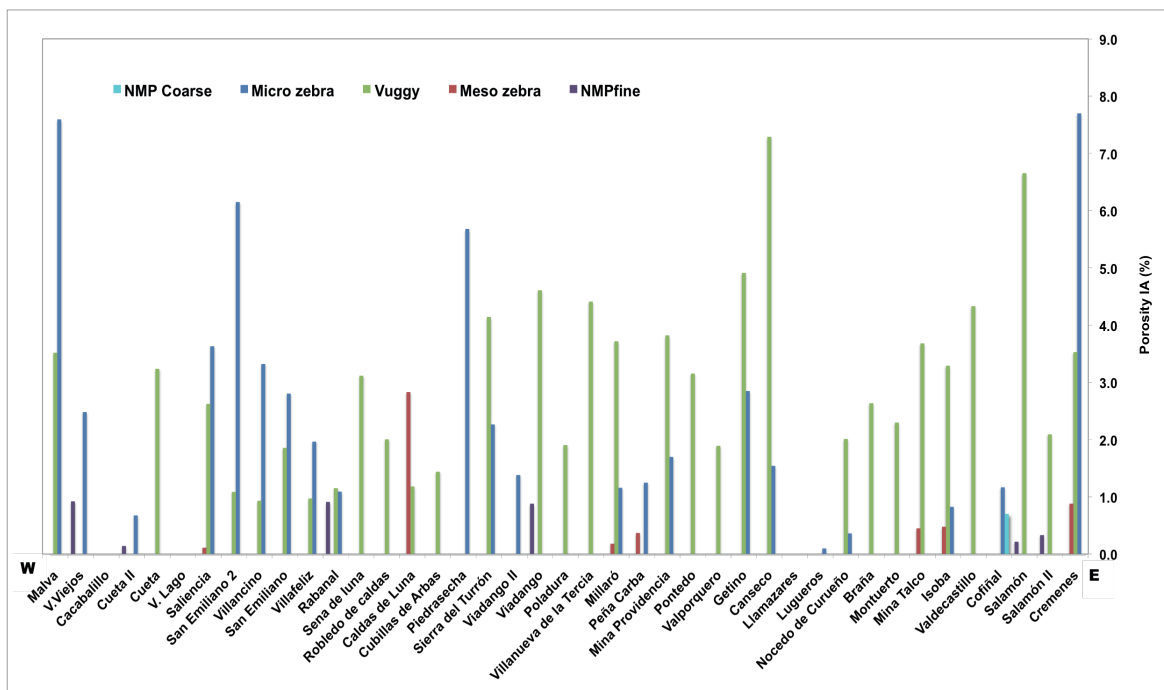


Fig. 7.6: Mean porosity values according to image analyses of the dolomite fabrics along the E-W transect.

8. GEOCHEMISTRY

Geochemical and isotope properties of the dolomites are important to understand the process of dolomitization better, for instance water/rock interactions, effects of temperature, and origin of dolomitizing fluids. In this chapter, new data are combined with published geochemical results (Gasparini, 2003; Gasparini et al., 2006 a, b; 2007, Lapponi et al., 2007a, b, 2014). The actual location of the geochemical data discussed is given as well.

8.1. ELEMENTAL GEOCHEMISTRY

8.1.1. XRD analyses

35 dolomite samples analyzed to determine bulk mineralogy, stoichiometry and degree of order (OR) come from the central region of the working zone. They belong to the Alba, Barcaliente and Valdeteja formations. The results for mol % CaCO₃ and OR are reported in Annex 7.

The X-ray patterns of the different dolomites do not show remnants of the precursor calcite. Among the non-carbonate phases, minor quartz, pyrite and hematite have been detected. Considering only the carbonate phases, the analyzed samples approximate 100% dolomite.

All of the dolomite samples (Dol A and Dol B) analyzed for stoichiometry and OR exhibit sharp diffraction peaks. The values of d_{104} are quite constant and range between 2.8827 and 2.8894 Å. These d_{104} values correspond to calcium contents between 48.9 and 51.1 mol % CaCO₃; most samples fall within the narrower range of 48.9 and 50.1 mol % CaCO₃, only two samples are outside. The OR varies between 0.54 and 1, with a clear maximum between 0.75 and 1 (Fig. 8.1).

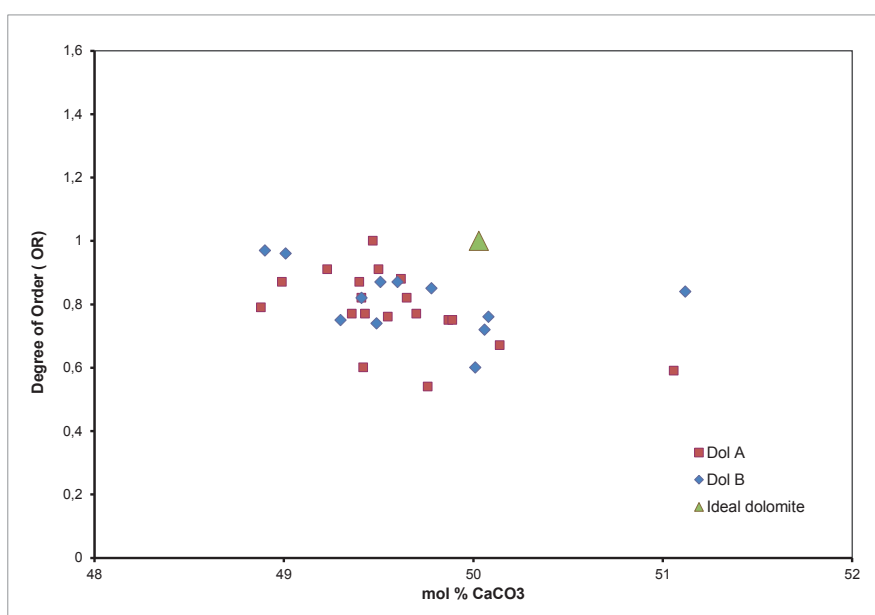


Fig. 8.1: Stoichiometry versus ordering. Dol A and Dol B show very similar values.

In both dolomite phases, high Ca values occur mainly in Dol B and this only at two localities: Mina Providencia and Canseco (Fig. 8.2a). No trend could be established for the OR (Fig. 8.2b).

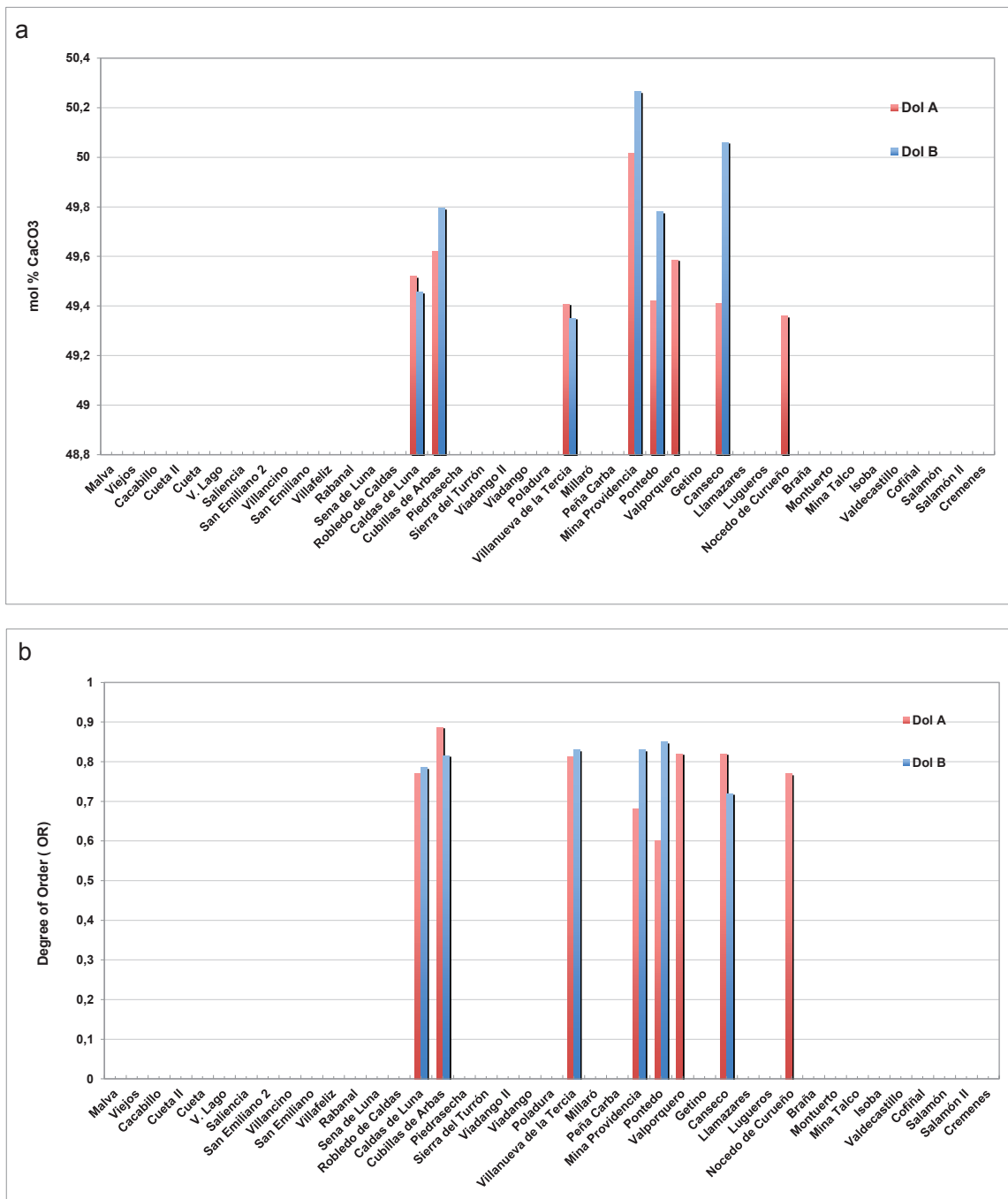


Fig. 8.2: Mean mol % CaCO_3 (a) and OR values (b) along the E-W transect.

8.1.2. ICP-ES, SEM-EDX-WDX analyses

The values obtained by XRD were compared with microprobe analyses of four other samples from different localities. Transects across the thin sections with Dol A and Dol B were measured for Ca, Mg, Sr, Na, Fe, and Mn (results are reported in An-

next 7). The detection limits of the microprobe for these elements are generally very close to the observed concentrations.

The samples analyzed by ICP-ES belong mostly to the Bodón Unit and correspond to 14 samples from host limestones (H), 19 from Dol A and 14 from Dol B. No differences could be observed between dolomite sub-phases. The concentrations of the main elements in the different mineral phases are summarized in Table 3, giving minimum, maximum, and mean values as well as the standard deviation. All of the analyzed samples belong to the Barcaliente Fm. and Valdeteja Fm.

Table 3: Elemental geochemistry from ICP-ES, and SEM-EDX-WDX analyses. The concentrations of Ca and Mg are reported in %, the ones of Na, Fe, Mn, and Sr in ppm. Min.= minimum value, Mean = mean value, Max. = maximum value, Std. Dev. = standard deviation.

Phase		Ca (%)	Mg (%)	Na (ppm)	Fe (ppm)	Mn (ppm)	Sr (ppm)
Host	min	32.57	0.04	100	100	8	179
	mean	37.08	0.24	221	831	84	573
	max	39.95	0.45	400	3100	463	950
	Std. Dev	2.45	0.11	105	873	118	247
Dol A	min	17.21	9.89	200	800	167	12
	mean	18.59	11.01	353	2316	383	23
	max	20.61	12.31	500	6100	814	71
	Std. Dev	0.82	0.61	118	1579	192	13
Dol B	min	17.48	10.16	100	600	213	10
	mean	19.25	10.87	300	2522	404	24
	max	22.73	12.31	600	6100	901	108
	Std. Dev	1.22	0.51	130	1559	181	24

Calcium (Ca) and magnesium (Mg)

The host limestones show variable concentrations of Ca and Mg. Ca varies between 32% and 39% (mean 37%), whereas Mg varies between 0.04% and 0.45 % (mean 0.24%) (see Table 3).

Dol A and Dol B show some differences of the Ca and Mg contents. The mean Ca content is 18.59 % in Dol A and 19.25% in Dol B. The mean Mg content for Dol A is 11.01%, and for Dol B 10.87%. Ca and Mg contents show a scattered distribution (Fig. 8.3).

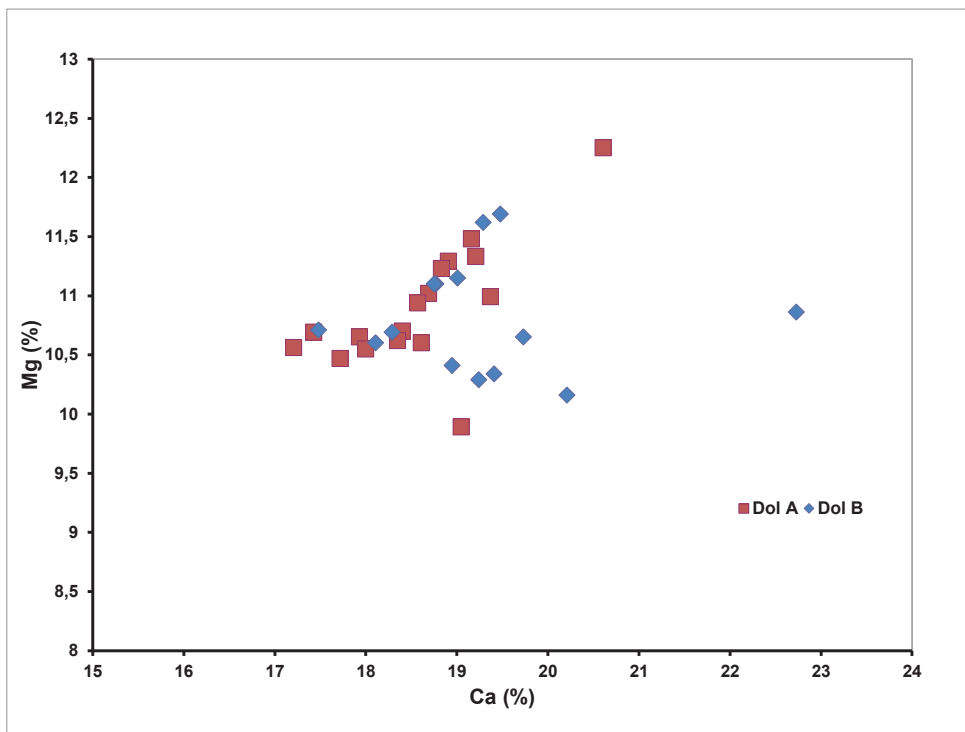


Fig. 8.3: Relation between Ca and Mg for the two dolomite phases.

In the E-W transect (Fig. 8.4) no systematic variation of the Ca content was observed for the different dolomite phases. Mean values are quite constant (Table 3).

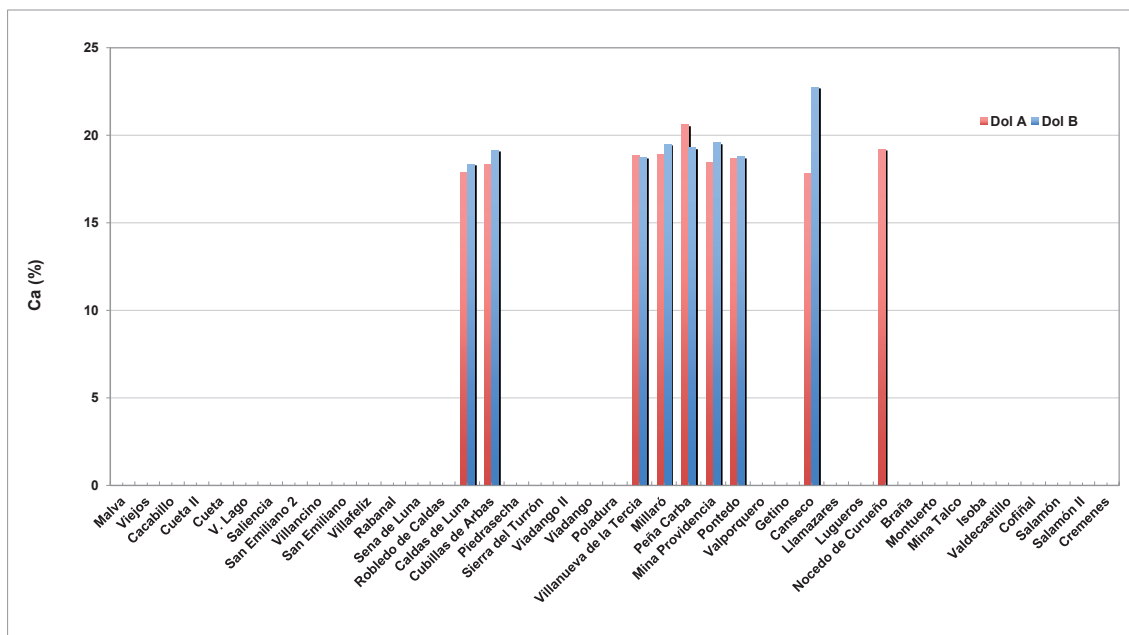


Fig. 8.4: Mean Ca values of Dol A and Dol B along the E-W transect.

The Mg content shows some variation along the transect, with higher values for Dol A in Peña Carba and Villancino (Fig. 8.5).

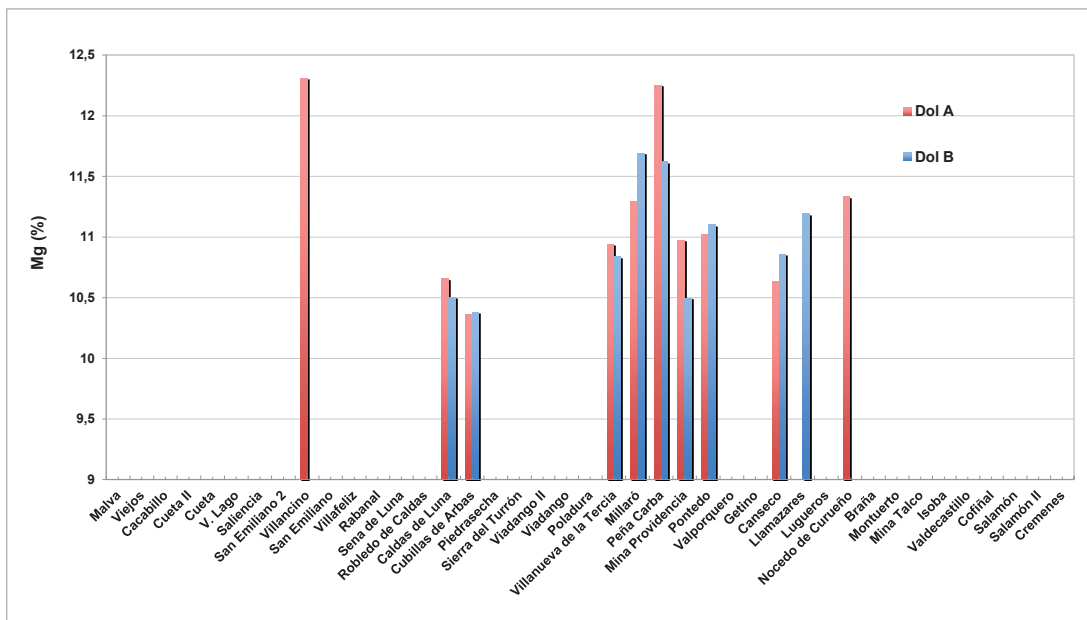


Fig. 8.5: Mean Mg values of the two dolomite phases along the E-W transect.

Sodium (Na)

The host limestones have Na contents in the range of 100-400 ppm, with the mean at 227 ppm. In Dol A Na concentrations are between 200 and 500 ppm with the mean at 353 ppm, in Dol B values range between 100 and 600 ppm, with the mean at 350 ppm (see Table 3). The Mean Na concentrations of the precursor limestones are therefore distinctly lower than those of the dolomite phases. The Na contents show a variation along the transect: Caldas de Luna, Millaró and Pontedo have high values in some of the dolomite phases (400 to 500 ppm) (Fig. 8.6); in the latter and in Canseco there are distinct differences between Dol A and Dol B.

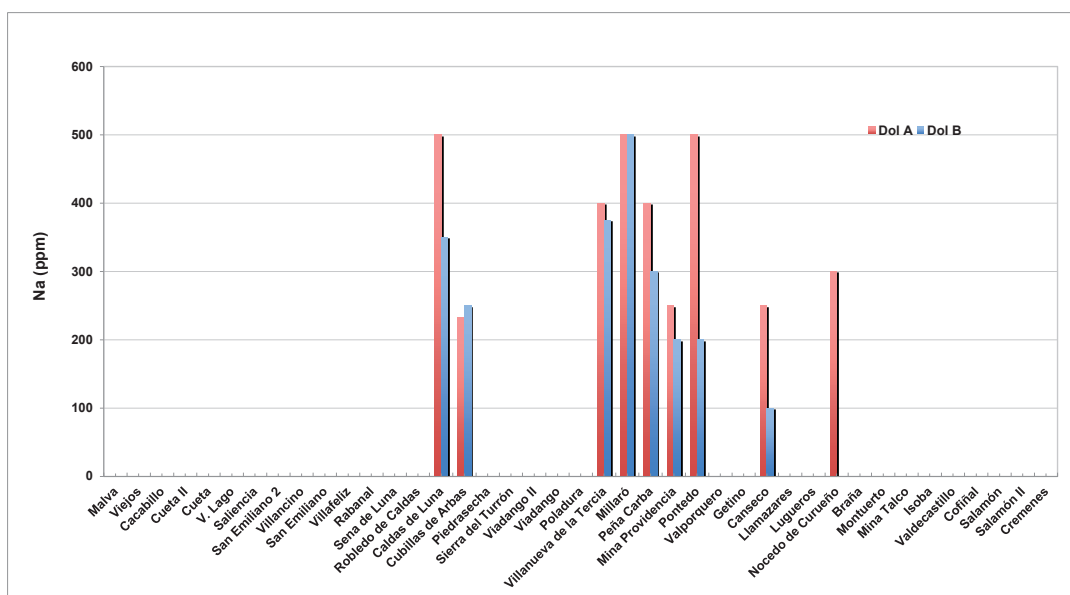


Fig. 8.6: Mean Na values of Dol A and Dol B along the E-W transect.

Iron (Fe) and manganese (Mn)

The host limestones show variable concentrations of Fe and Mn. Fe varies between 100 and 3100 ppm (mean 831 ppm), whereas Mn varies between 8 and 463 ppm (mean 84 ppm). Fe contents of Dol A range between 800 and 6100 ppm

(mean 2316 ppm), and of Dol B between 600 and 6100 ppm (mean 2522 ppm). Mean Mn content for Dol A is 383 ppm (with a range between 167 and 814 ppm), and for Dol B 404 ppm (range between 213 and 901 ppm). All dolomite phases display higher mean Fe and Mn contents than the host limestones (see Table 3).

Fe and Mn contents of the different dolomite phases show some E-W variation. Mean Fe contents are especially high (2000 ppm - 5500 ppm) in Cubilla de Arbas and Mina Providencia for Dol A and Canseco for both dolomite phases (Fig. 8.7a). Mean Mn contents are high (400 ppm – 900 ppm) in Villancino (Dol A), Caldas de Luna-Cubillas de Arbas (Dol B) and Canseco (both dolomite phases) (Fig. 8.7b).

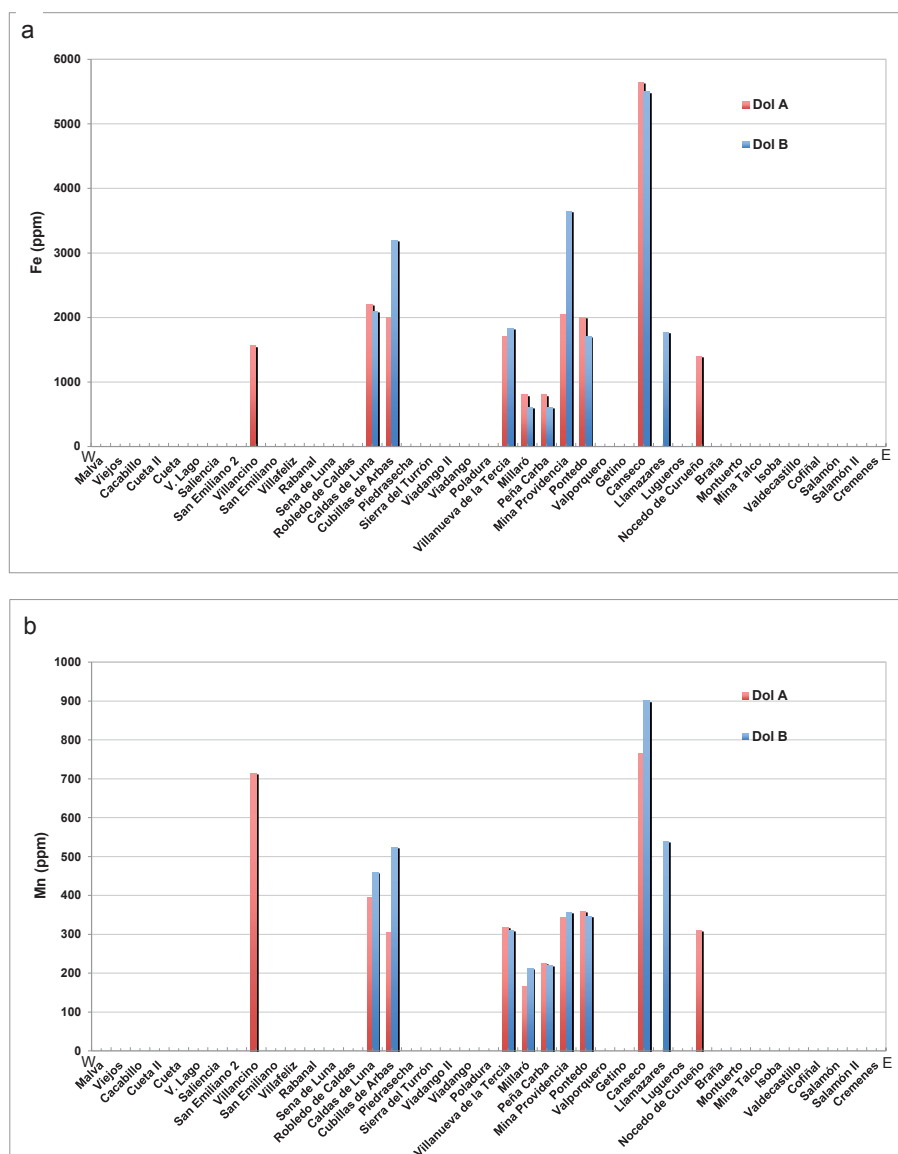


Fig. 8.7: Mean Fe (a) and Mn (b) contents (in ppm) along the E-W transect.

The Fe and Mn contents show a statistically significant positive correlation (Fig. 8.8), with a degree of confidence (R^2) of 0.97 for Dol B and 0.72 for Dol A.

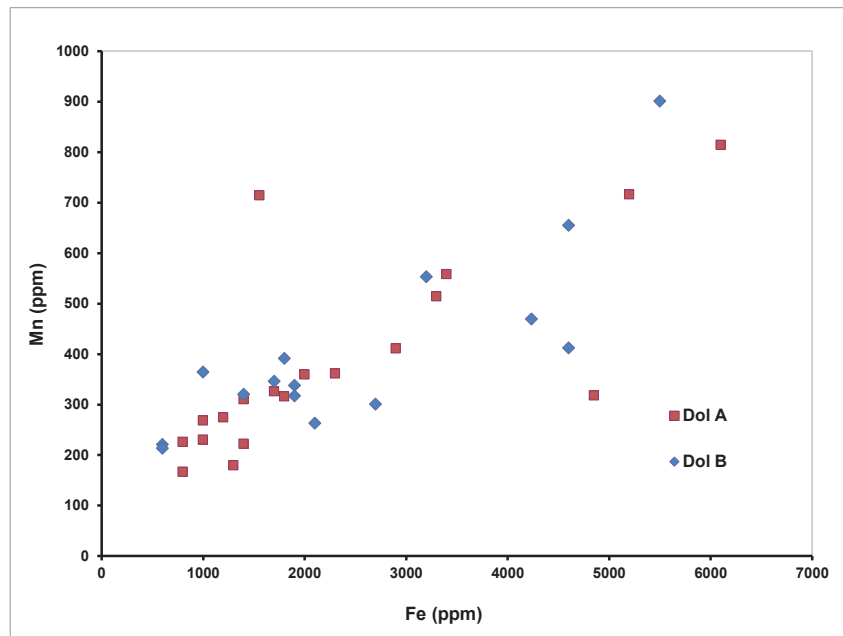


Fig. 8.8: Correlation between the Fe and Mn contents of Dol A and Dol B.

Strontium (Sr)

The Sr contents in the host limestones are quite variable and range between 179 and 950 ppm, with the mean at 573 ppm. The Sr content of the dolomite phases is distinctly lower. Dol A has a mean Sr content of 23 ppm, and Dol B of 24 ppm. Higher mean Sr values have only been found in Dol B at Canseco (Fig. 8.9).

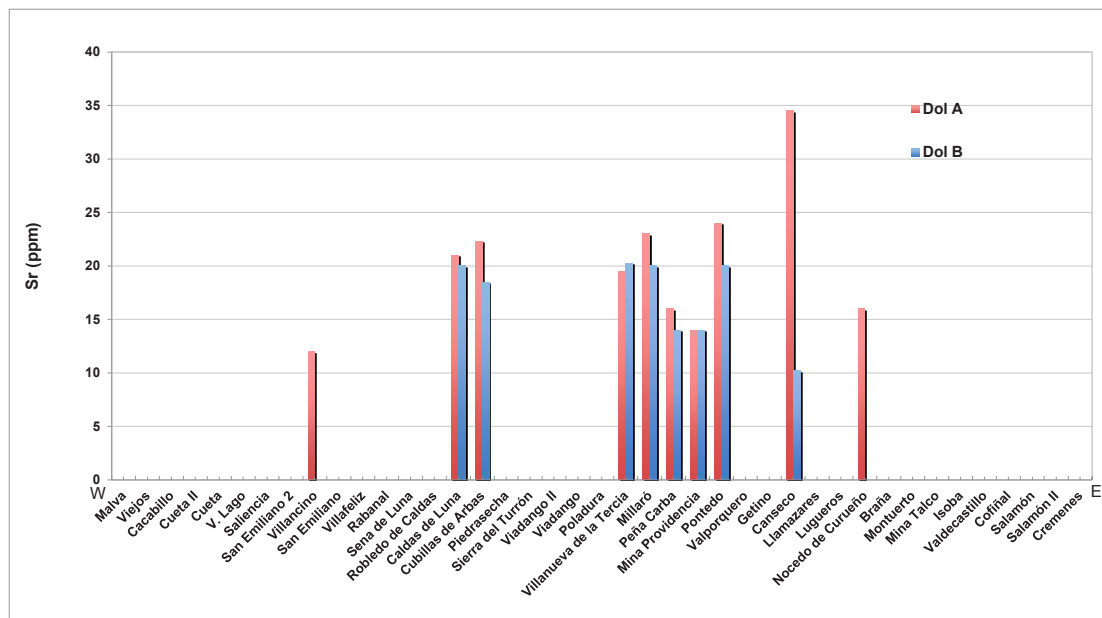


Fig. 8.9: Mean Sr values of Dol A and Dol B along the E-W transect.

8.2. ISOTOPE GEOCHEMISTRY

8.2.1. Oxygen and carbon isotopic composition

The dolomites and host limestones of much of the research area are already well investigated in terms of oxygen and carbon isotopes: 138 carbonate samples have been analysed in previous research of our group (Gasparrini, 2003; Gasparrini et al., 2006 a, b). Due to the extension of the present working area to the east and west, 15 new samples from the Barcaliente and Valdeteja Fms were analysed for $\delta^{18}\text{O}/\delta^{16}\text{O}$ and $\delta^{13}\text{C}/\delta^{12}\text{C}$ ratios at the GeoZentrum Nordbayern, University of Erlangen-Nürnberg (Germany).

Together, these sample sets cover (in brackets: number of analyses) host limestones (31), Dol A (57), Dol B (37), Cal 1 (9), and Cal 2 (10). In Annex 8 the results are reported in per mil (\textperthousand) relative to the V-PDB standard. In Fig. 8.10 the mean values of $\delta^{18}\text{O}$ and $\delta^{13}\text{C}$ for the different analyzed phases are plotted, together with the standard deviation range ($\pm 1\sigma$) (see Table 4).

Phase		$^{87}\text{Sr}/^{86}\text{Sr}$
Host	Min	0,708082
	Mean	0,708118
	Max	0,708147
	std. dev.	0,000028
Dol A	Min	0,7084
	Mean	0,70874
	Max	0,709207
	Std. Dev.	0,00031
Dol B	Min	0,708458
	Mean	0,708981
	Max	0,70957
	Std. Dev.	0,000417
Cal 1	Min	0,708502
	Mean	0,70862
	Max	0,708738
	Std. Dev.	0,000167
Cal 2		0,708416

Table 4: O and C isotope geochemistry: $\delta^{18}\text{O}$ and $\delta^{13}\text{C}$ values (in \textperthousand V-PDB) are reported for the different mineral phases analyzed. Min.= minimum value, Mean = mean value, Max. = maximum value, Std. Dev. = standard deviation.

The host limestones (H) show $\delta^{18}\text{O}$ values between -7.7 and 2.1‰. The mean value

is $-2.2\text{\textperthousand}$. The $\delta^{13}\text{C}$ values for the host limestones are always positive and range between 3.1 and $5.3\text{\textperthousand}$. The mean value is $4.3\text{\textperthousand}$.

The $\delta^{18}\text{O}$ and $\delta^{13}\text{C}$ values of the different dolomite phases cluster in the same broad area. The latter is characterized by a large spread in $\delta^{18}\text{O}$ values and quite consistent $\delta^{13}\text{C}$ values. The $\delta^{18}\text{O}$ values for the different dolomites are distinctly more negative than those of the host limestones, whereas the $\delta^{13}\text{C}$ values are very similar (Fig. 8.10).

The main feature of Cal 1 and Cal 2 is a significant depletion in ^{18}O and ^{13}C relative to the other carbonate phases. In particular, Cal 1 has the most negative $\delta^{18}\text{O}$ values, whereas Cal 2 has the most negative $\delta^{13}\text{C}$ values (Fig. 8.10).

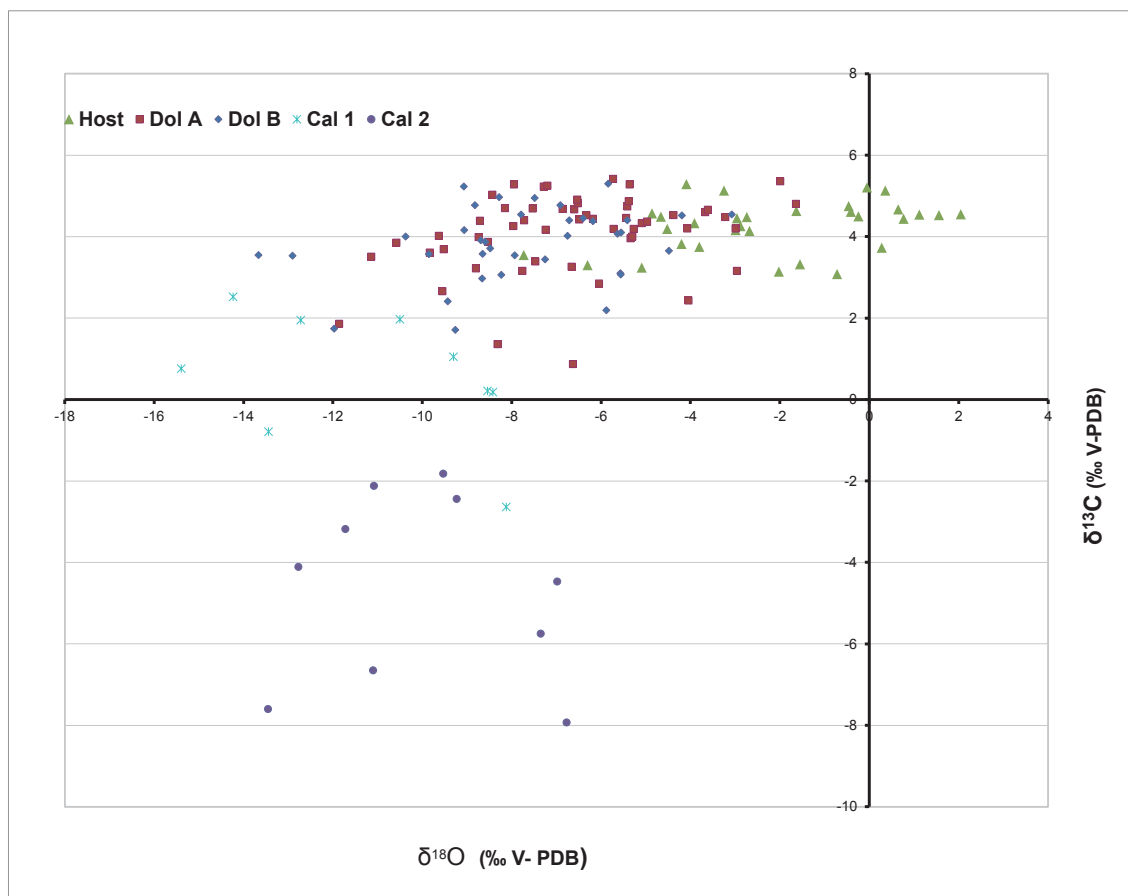


Fig. 8.10: O and C isotope composition of the different carbonate phases. For a plot of the mean values together with the standard deviation see Fig. 10.2.

Dol B shows more negative O isotope ratios in the east between Mina Talco - Isoba, (Fig. 8.11). More negative O isotope ratios of Dol A are irregularly distributed. A non-systematic fluctuation was also observed for the C isotope ratios, in this case for both dolomite phases (Fig. 8.12).

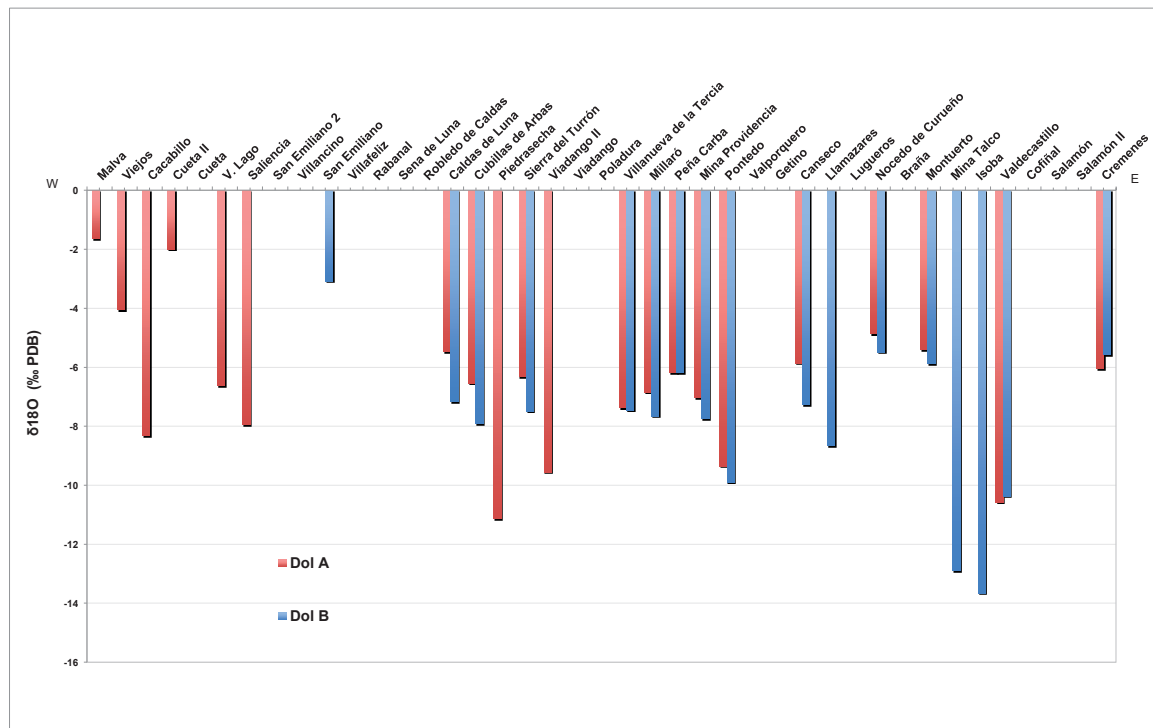


Fig. 8.11: $\delta^{18}\text{O}$ values along the E-W transect.

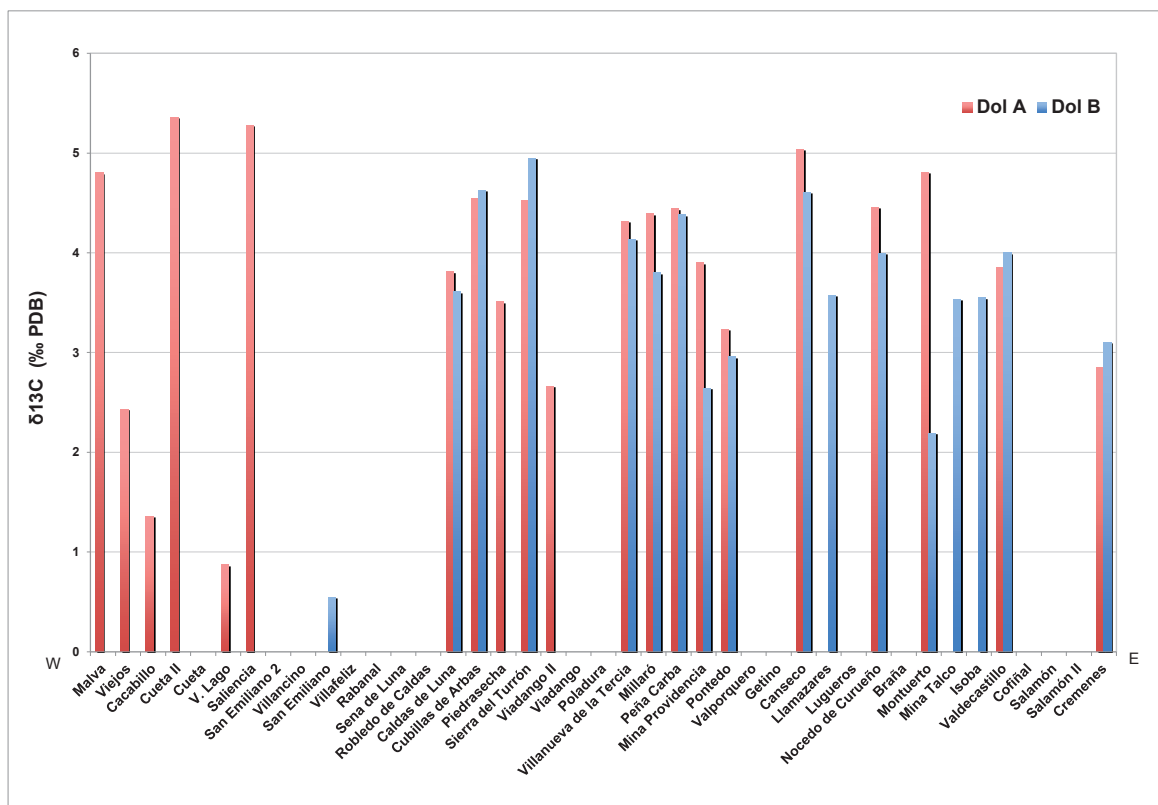


Fig. 8.12: $\delta^{13}\text{C}$ values along the E-W transect.

8.2.2. Strontium isotopic composition

Within this project, three samples from the Bodon Unit were measured for Sr isotopes; these analyses add up to earlier measurements (Gasparrini, 2003; Gasparrini et al., 2006 a, b). All of the samples belong to the Barcaliente Fm. and correspond to: four host limestones (H), five Dol A, four Dol B, two Cal 1 and one Cal 2. No separation was made between Dol A and Dol B sub-phases.

The results are reported as $^{87}\text{Sr}/^{86}\text{Sr}$ ratios in Annex 8 (see also Table 5).

Phase		$^{87}\text{Sr}/^{86}\text{Sr}$
Host	Min	0,708082
	Mean	0,708118
	Max	0,708147
	std. dev.	0,000028
Dol A	Min	0,7084
	Mean	0,70874
	Max	0,709207
	Std. Dev.	0,00031
Dol B	Min	0,708458
	Mean	0,708981
	Max	0,70957
	Std. Dev.	0,000417
Cal 1	Min	0,708502
	Mean	0,70862
	Max	0,708738
	Std. Dev.	0,000167
Cal 2		0,708416

Table 5: $^{87}\text{Sr}/^{86}\text{Sr}$ ratios of different mineral phases. In parenthesis is the number of measured samples. Min. = minimum value, Mean = mean value, Max = maximum value, Std. Dev. = standard deviation.

The host limestones have very consistent $^{87}\text{Sr}/^{86}\text{Sr}$ ratios between 0.708082 and 0.708147, with the mean at 0.708118. The Sr isotope ratios for samples of Dol A range between 0.708400 and 0.709207, with the mean at 0.708740. $^{87}\text{Sr}/^{86}\text{Sr}$ ratios for Dol B samples range between 0.708458 and 0.709270, with the mean at 0.708981. Dol B has higher Sr isotope ratios than Dol A, and both dolomite phases have higher mean $^{87}\text{Sr}/^{86}\text{Sr}$ values than the host limestones.

The samples of Cal 1 display relatively consistent $^{87}\text{Sr}/^{86}\text{Sr}$ ratios with the mean at 0.708620. The $^{87}\text{Sr}/^{86}\text{Sr}$ ratio for the only sample of Cal 2 is 0.708416. Both Cal 1 and Cal 2 have therefore Sr isotope ratios slightly higher than the mean values of the host limestones, but within the range of ratios reported for the dolomites.

If we look at the Sr contents versus $^{87}\text{Sr}/^{86}\text{Sr}$ ratios (Fig. 8.13), Dol B samples have slightly higher values than Dol A, but strongly differ from those of the host limestones.

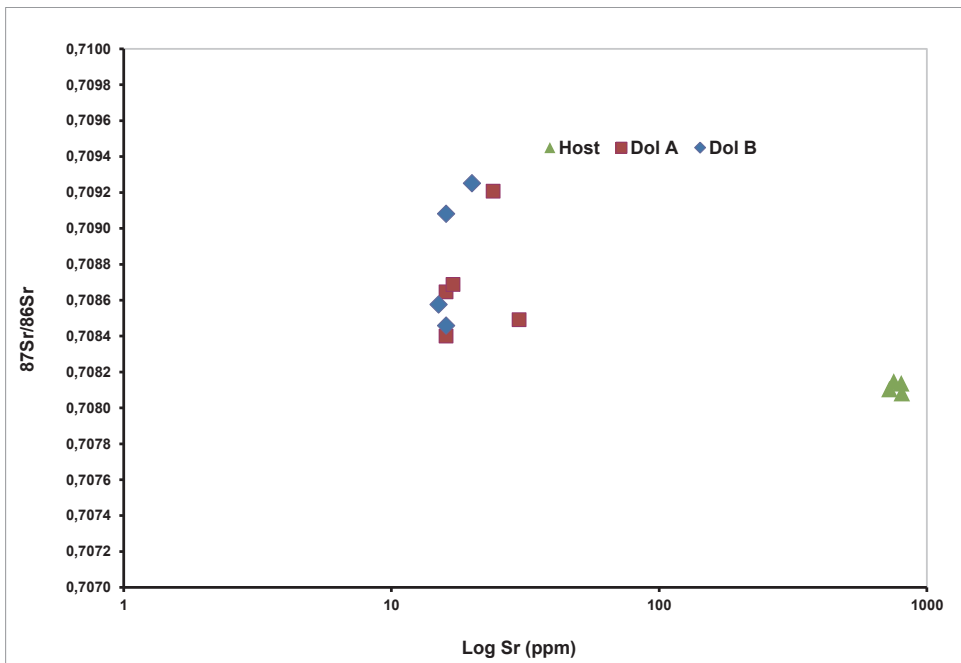


Fig. 8.13: Relation between Sr contents and $^{87}\text{Sr}/^{86}\text{Sr}$ ratios for host limestones and dolomite phases.

The plots $\delta^{18}\text{O}$ versus $^{87}\text{Sr}/^{86}\text{Sr}$ and $\delta^{13}\text{C}$ versus $^{87}\text{Sr}/^{86}\text{Sr}$ (Figs. 8.14 and 8.15) do not show any significant grouping between the different dolomite phases. Inverse covariation between $\delta^{18}\text{O}$ and $^{87}\text{Sr}/^{86}\text{Sr}$ values from the host limestones towards the diagenetic phases (both dolomites and calcites) is observed (Figure 8.14). No covariation is seen between $\delta^{13}\text{C}$ and $^{87}\text{Sr}/^{86}\text{Sr}$ values from the host limestones towards the dolomites, and inverse covariation between $\delta^{13}\text{C}$ and $^{87}\text{Sr}/^{86}\text{Sr}$ values from the host limestones towards the calcites (Fig. 8.15).

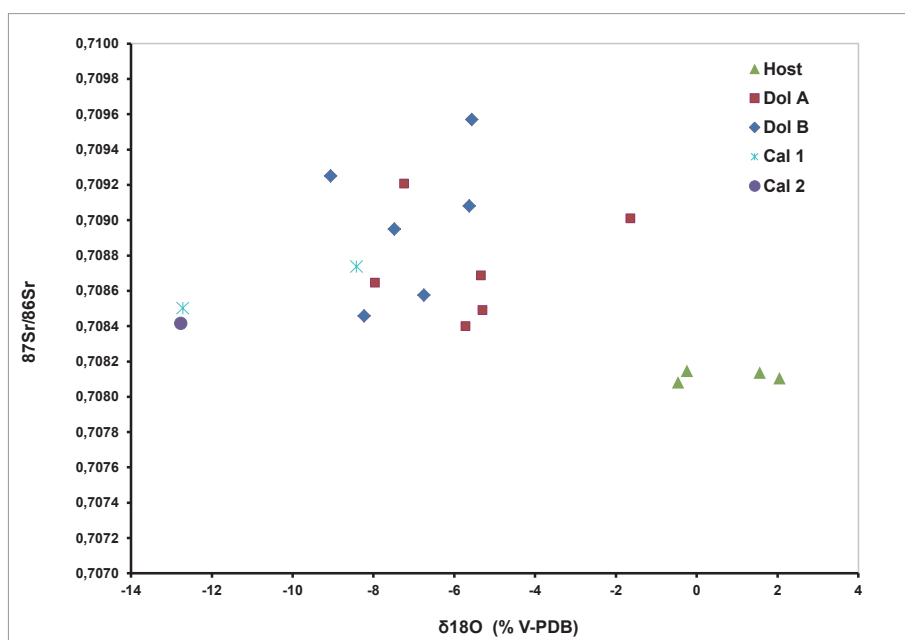


Fig. 8.14: Variation between $\delta^{18}\text{O}$ and $^{87}\text{Sr}/^{86}\text{Sr}$ ratios.

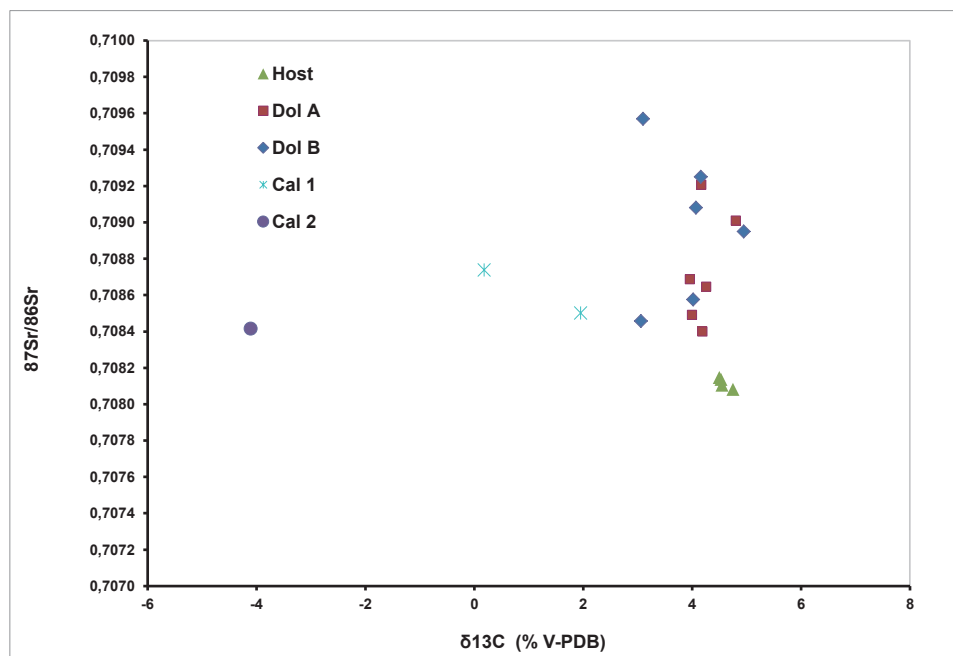


Fig. 8.15: Variation between $\delta^{13}\text{C}$ and ${}^{87}\text{Sr}/{}^{86}\text{Sr}$ ratios.

In the E-W transect (Fig. 8.16) the ${}^{87}\text{Sr}/{}^{86}\text{Sr}$ ratios of the different dolomite phases do not show any consistent trend. High values occur in Crémenes (only Dol B analyzed), Pontedo (Dol A and Dol B) and Malva (only Dol A analyzed). In Peña Carba the Sr isotope values of Dol A are the lowest of all measurements, also distinctly lower than the Dol B data from the same locality.

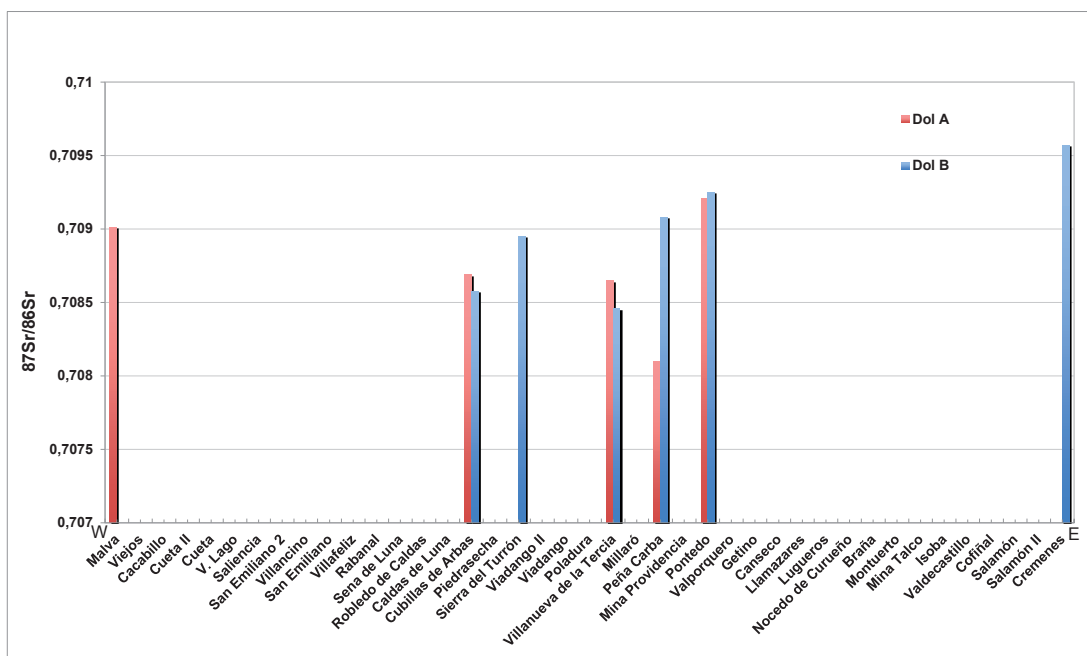


Fig. 8.16: ${}^{87}\text{Sr}/{}^{86}\text{Sr}$ values in an E-W transect.

9. FLUID INCLUSIONS (FIs)

Fluid inclusion (FI) petrography, microthermometry and other more specific methods of investigation help in unravelling temperature and composition of the dolomitizing fluid.

9.1 Fluid inclusion petrography

A detailed petrographic study of the previously described mineral phases (see chapter 5) revealed the presence of many different types of primary and secondary FIs (Fig. 9.1).

The Dol A1 crystals display a uniform cloudiness and appear dark, due to the small size ($<1 \mu\text{m}$) of the many FIs (Fig. 9.1a) present, which are too small for microthermometric measurements.

FIs in Dol A2 are densely distributed throughout individual crystals and are mainly concentrated in the crystal cores. Primary FIs are up to $4 \mu\text{m}$ in length and have an irregular shape. Most of the inclusions are two-phase and liquid-rich (Fig. 9.1b). The degree of fill (F) ranges between 0.83 and 0.94. Less commonly FIs with a one-phase, all liquid fill are observed.

Dol B commonly host FIs uniformly distributed in the crystals. Locally, these crystals have inclusion-rich cores and inclusion-free, clear rims. Most of the inclusions are two-phase, liquid-rich with F ranging from 0.80 to 0.97. Larger inclusions (up to $12 \mu\text{m}$ in length) occur preferentially in the outer part of the crystal cores or along crystal growth zones. The inclusions have mostly an irregular to lobate shape, some are elongated along the growth directions of the saddle dolomite crystals (Fig. 9.1 b, c).

Cal 1 is characterized by abundant FIs mostly confined to growth-zone boundaries, with sizes up to $20 \mu\text{m}$ in length and a spheroidal to oblate shape. The FIs are two-phase, liquid-rich with a degree of fill between 0.85 and 0.97. Secondary FIs are less frequently observed; they are located along trails and sealed fractures, with sizes less than $2 \mu\text{m}$ in length, spheroidal in shape and one-phase all liquid fill. These inclusions of later origin were not considered in the present study.

FIs in Cal 2 are isolated and do not occur along growth zones or along trails. Usually these FIs are monophase, all liquid. They generally have sizes up to $30 \mu\text{m}$ in length and irregular forms, but negative crystal shapes are also common.

Only a few samples in the eastern study area contain quartz crystals associated with dolomites (Fig. 9.1e). The FIs in Quartz are up to $30 \mu\text{m}$ in length, and their shape is sub-rounded to elongated. Two-phase inclusions are dominant, which are liquid-rich with a degree of fill (F) from 0.82 to 0.83.

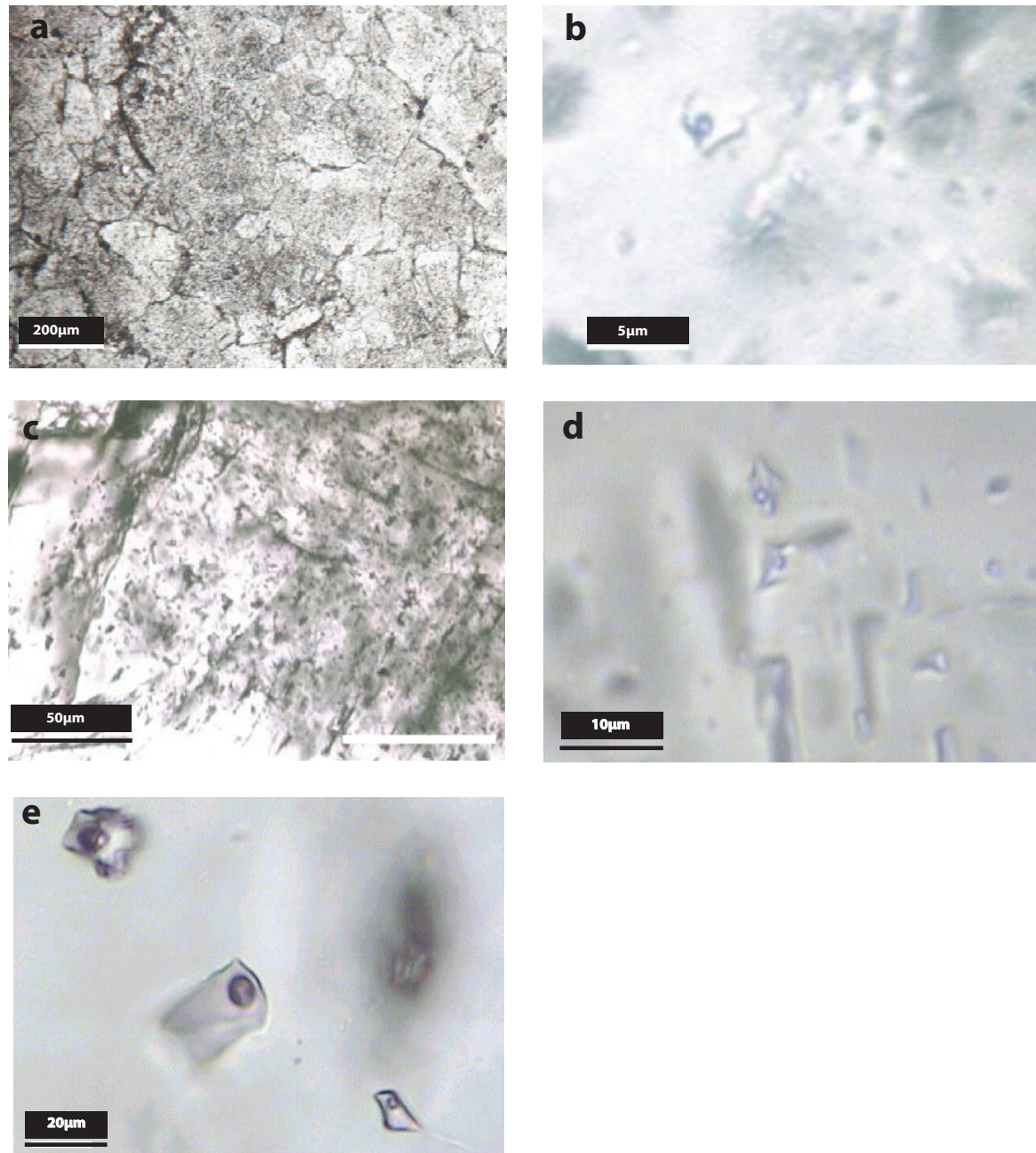


Fig. 9.1: Microphotographs of: (a) Dol A1 with cloudy appearance due to many FIs; (b) irregular shaped, 2-phase, liquid-rich FIs in Dol A2; (c) FIs elongated along the direction of growth of a saddle dolomite (Dol B); (d) Dol B with liquid-rich, two phase FIs; (e) FIs in Quartz. All microphotographs were taken at room temperature (25°C).

9.2 Fluid inclusion microthermometry

Microthermometry was carried out in samples from 18 localities (seven localities were already measured by Gasparrini et al., 2006 a). FIs were investigated in Dol A, Dol B (most of the analyses), and in few samples of Cal 1 and 2, as well as Quartz. All the phase changes measured in these inclusions are reported in Annex 9, together with the bulk density and composition of the different samples; the main results are summarized in Table 6.

Table 6: Main microthermometric data of different mineral phases in fluid inclusions.

Phase		Th °C	Tm °C
Dol A	Min	78.8	-36.5
	Mean	127.0	-33.0
	Max	196.5	-30.1
	Mode	140.0	-32.0
Dol B	Min	93.1	-39.5
	Mean	132.8	-32.9
	Max	205.5	-27.1
	Mode	140.0	-32.0
Calcite 1	Min	93.9	-26.5
	Mean	111.8	-22.8
	Max	145.6	-17.9
	Mode	120.0	-24.0
Quartz	Min	154.7	-23.5
	Mean	176.1	-21.9
	Max	191.9	-21.2
	Mode	190.0	-20.0

The FIs homogenization measurements were carried out before freezing runs, to avoid stretching of FIs by the expanding ice. All FIs homogenized in the liquid phase (despite Cal 2). After total homogenization, FIs were cooled and the temperatures of nucleation T_n gas as well as T_n ice were measured (see Annex 9).

Due to the small size of the FIs and their metastable behaviour, the low temperature measurements were problematic for all of the mineral phases investigated. The real first melting temperature (T_e) could not be determined. The temperature values reported in Table 6 represent only the upper constraints of the real T_e . Many phase changes at low temperatures (i.e. melting of salt hydrates) could not be identified and in most FIs only the melting temperatures of ice (T_m ice) were measured, the latter often corresponding to T_m final, the final melting temperatures. In the small FIs

the melting of the last ice crystal could not be seen; in such cases, upon rapid cooling of the FIs, a last sudden movement of the vapour bubble was usually observed, which was taken as indicator of $T_{m\text{ ice}}$.

Frequency histograms of the homogenization temperature (T_h) (Fig. 9.2), melting temperature (T_m) (Fig. 9.3), and T_m - T_h covariance plots (Fig. 9.4) show differences between the four mineral phases analysed. Quartz occurs in a few samples from Isoba only, and the measurements show clear differences to the calcite phases according to T_h and T_m . The calcite phases have lower T_h (mean: 112 °C), and T_m ranges between -26.5 and -17.9 °C. Quartz phases are characterized by higher T_h (mean 176.1 °C), whereas T_m is in a similar range as calcite (between -23.5 and 21.2 °C).

The main fluid inclusion characteristics of the dolomite phases are explained in the next paragraphs.

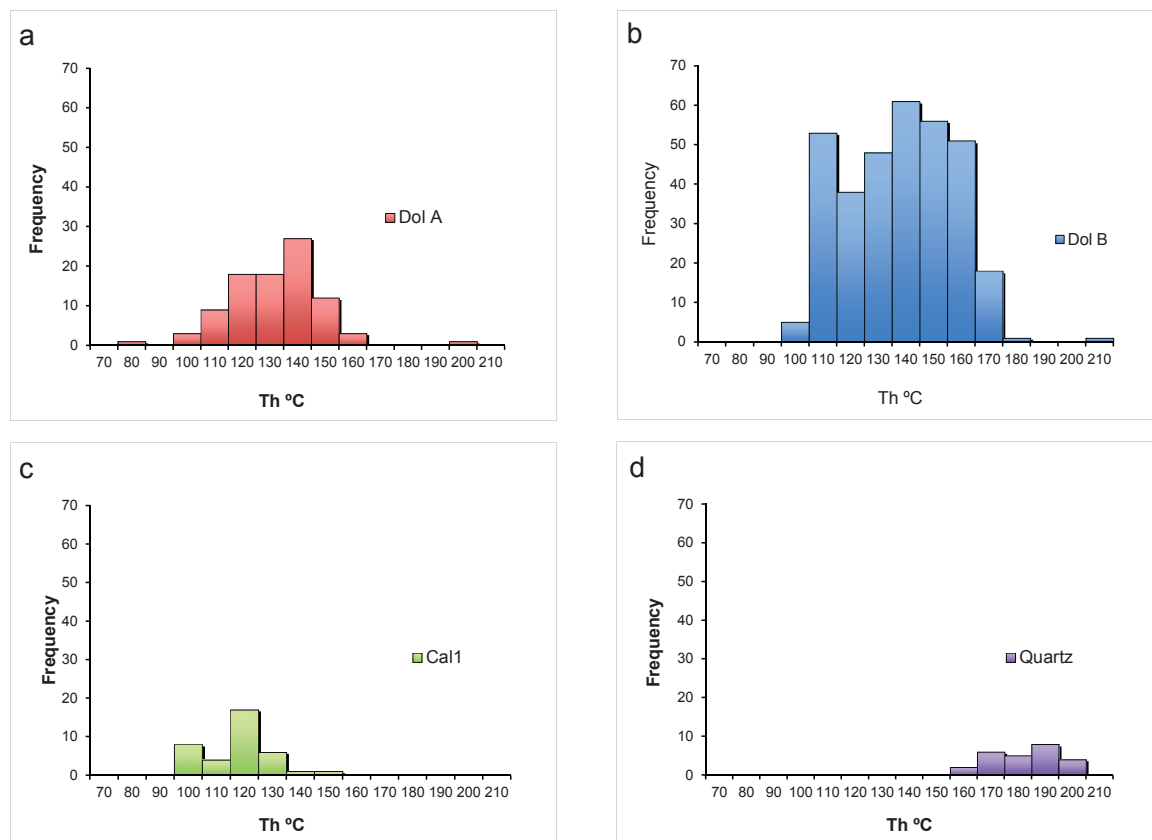


Fig. 9.2: Frequency histograms for homogenization temperatures (T_h) in different mineral phases. (a) Dol A; (b) Dol B; (c) Calcite 1; (d) Quartz.

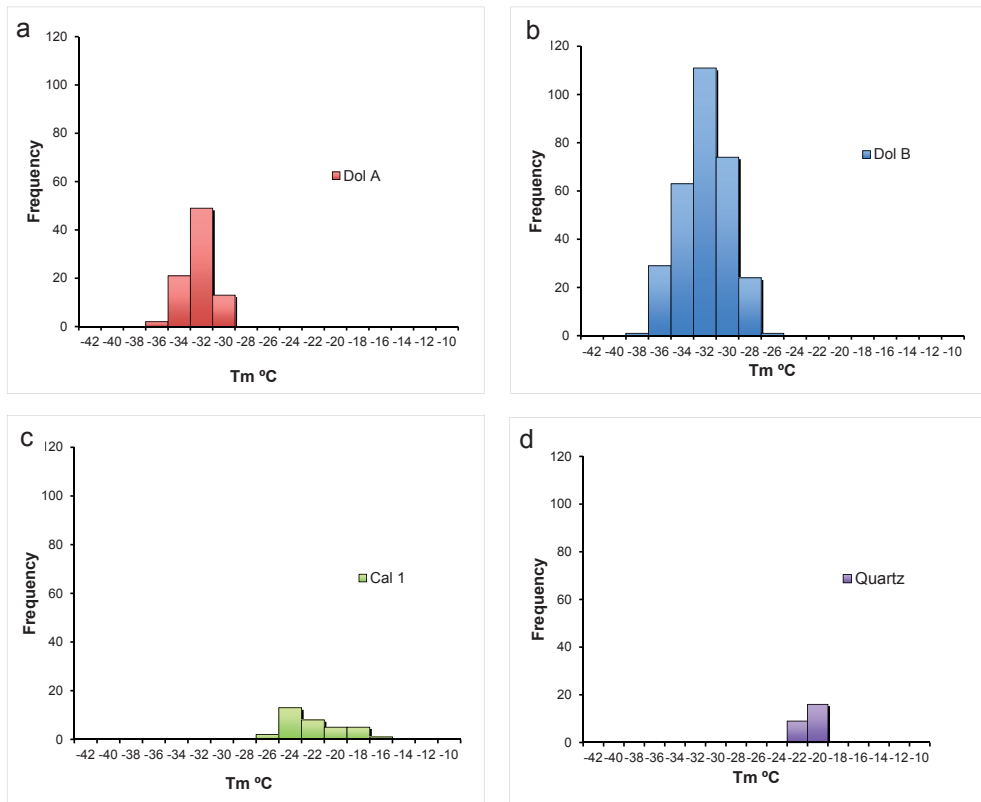


Fig. 9.3: Frequency histograms for melting temperatures (T_m) in different mineral phases. (a) Dol A; (b) Dol B; (c) Calcite 1; (d) Quartz.

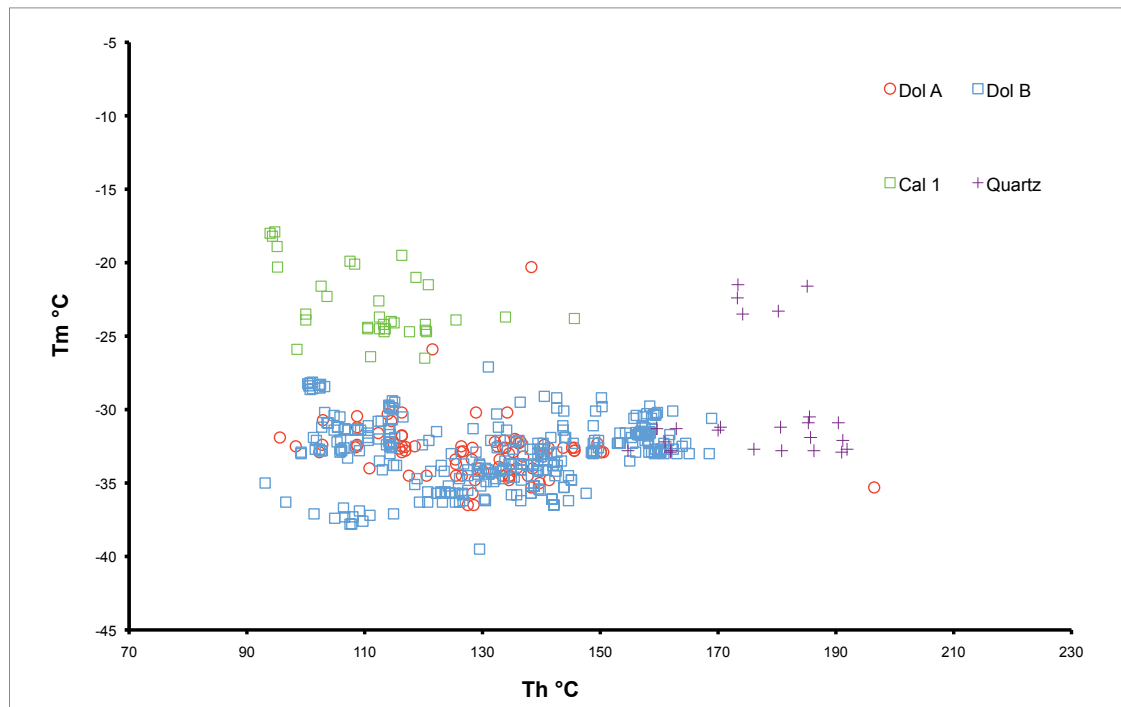


Fig. 9.4: Covariance plot T_m - Th , showing differences between the four mineral phases analyzed.

9.2.1 Microthermometry in Dol A

Specimens from 8 localities of the 18 analysed in total had measurable FIs in Dol A: 92 FIs were measured for T_h , resulting in a range of temperatures between 78.8 and 196.5 °C. 84 of the 92 measurements, corresponding to 91.3% of the data, fall in the 110-150 °C range. The frequency histogram for T_h shows an asymmetric distribution of data with a mode at 140 °C (Fig. 9.2a).

Temperatures higher than the mode were found in the localities Villanueva, Salien-
cia, Viadango II, Caldas, and Malva (Fig. 9.5a). T_m ice (which corresponds to T_m
final) ranges between -30.1 and -36.5 °C. The frequency histogram for T_m ice shows
a normal distribution. All of the values fall into a narrow range, with a distinct mode
at -32 °C (Fig. 9.5b).

The T_h - T_m ice plot for the FIs from these localities shows differences: the Salien-
cia samples have higher T_h than the others, whereas the Villanueva samples have a
lower T_m mean than the others (Fig. 9.5c).

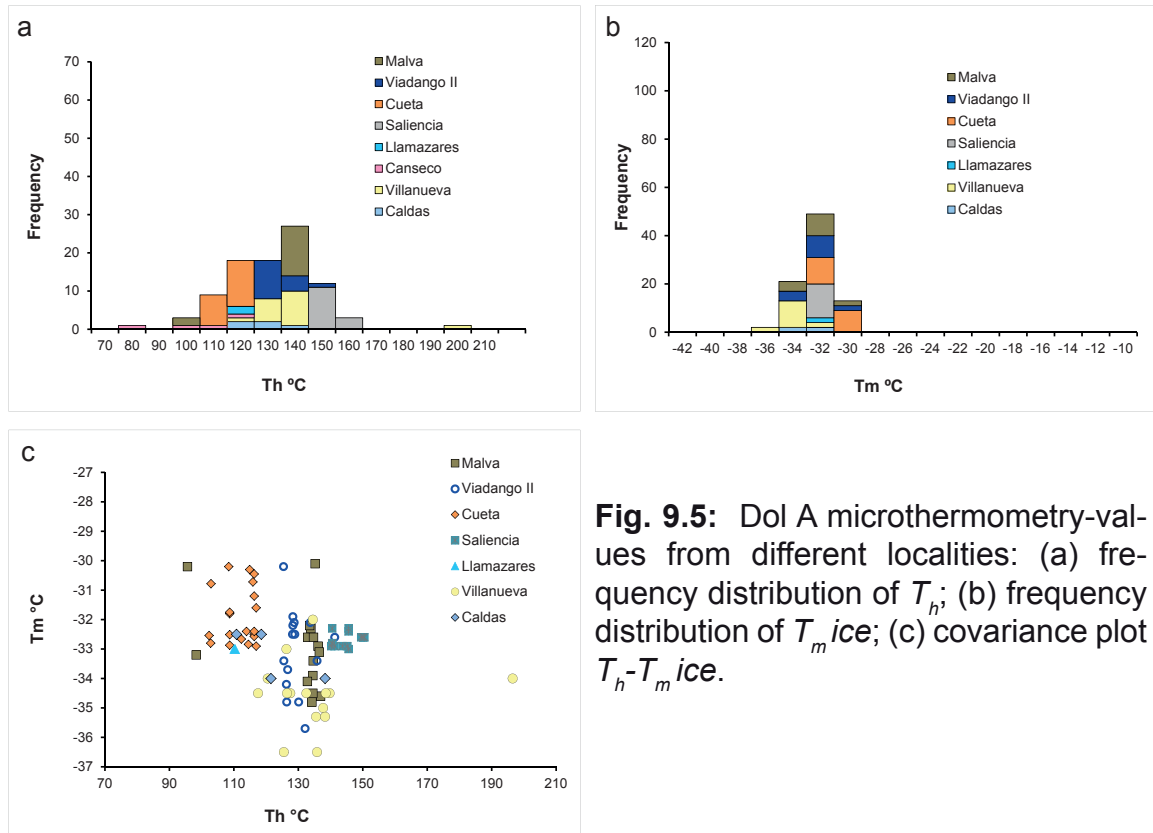


Fig. 9.5: Dol A microthermometry-values from different localities: (a) frequency distribution of T_h ; (b) frequency distribution of T_m ice; (c) covariance plot T_h - T_m ice.

9.2.2 Microthermometry of Dol B

15 localities of the 18 analyzed in total had measurable FI in Dol B: a total of 340 FIs were measured for T_h , ranging between 93.1 and 205.5 °C. 307 measurements, corresponding to 90.3% of the data, fall in the range 110-160 °C. The frequency his-

togram for T_h shows a normal distribution of data, with a broad mode at about 140 °C. A second mode may be suspected at 110 °C (Fig. 9.2b).

Temperatures higher than the mode were found at Cármenes, Isoba, Mina Talco, Crémenes, Villanueva, and Sierra del Turrón (Fig. 9.6a).

The T_m ice data range between -27.1 and -39.5 °C. 277 of 304 measurements (92 % of the data), fall in the range -30 to -36 °C. The frequency histogram for T_m ice shows a normal distribution with one well-defined mode at -32 °C (Fig. 9.6b).

The T_h - T_m ice plot for Dol B shows some differences between the various localities: Isoba and Mina Talco have higher T_h ; Villanueva samples have a higher T_m mean than the others, the ones from Piedrasecha have the minimum T_h and maximum (least negative) T_m values (Fig. 9.6c).

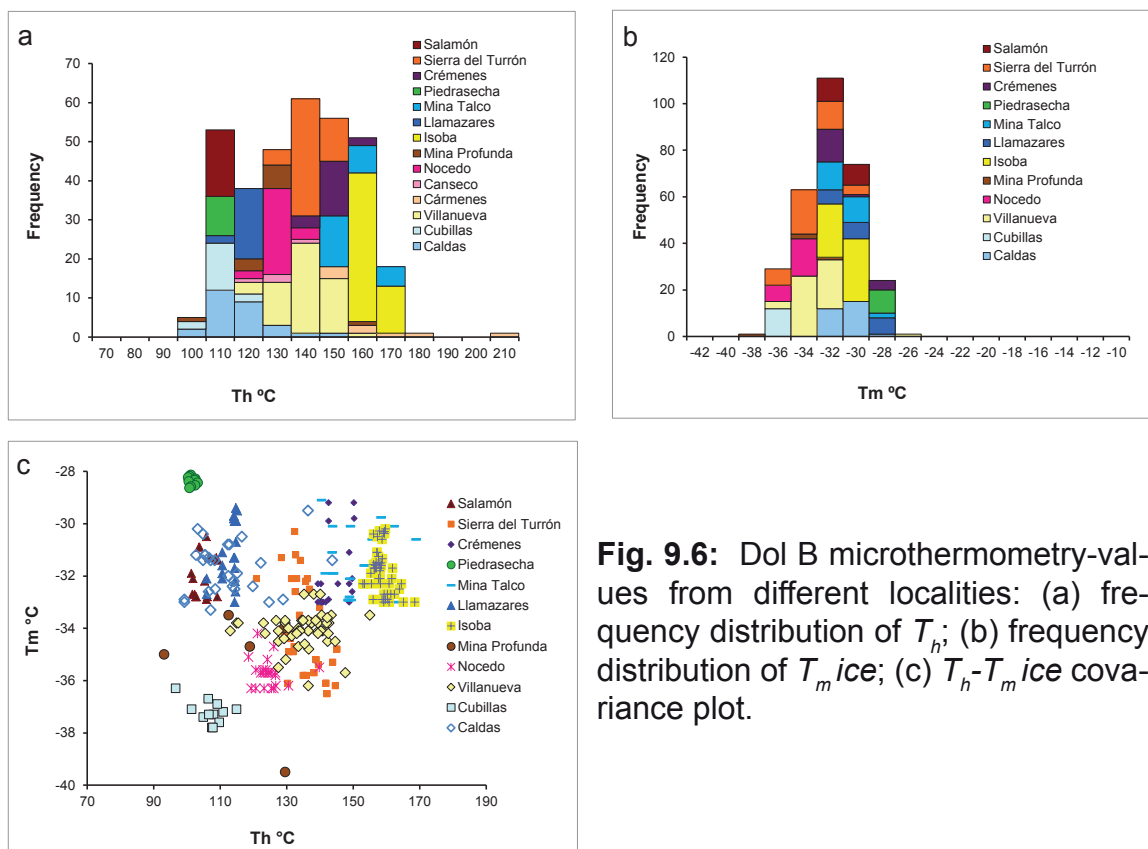


Fig. 9.6: Dol B microthermometry-values from different localities: (a) frequency distribution of T_h ; (b) frequency distribution of T_m ice; (c) T_h - T_m ice covariance plot.

9.3 Raman spectroscopy

The presence of aqueous solutions in the FIs of Dol B and Cal 1 was confirmed by Raman spectroscopy (Gasparini, 2003; Gasparini et al., 2006 a, b; Lapponi, 2007; Lapponi et al., 2007a, b): different heating-cooling experiments stabilized the measurements of the different assemblages. Due to the lack of own measurements, the following results are cited from the above-mentioned publications.

Although liquid water is usually difficult to recognize in carbonate crystals due to the high background signal of the host, FIs close to the sample surface revealed a broad peak typical for water (in the diagram between 3000 and 3700 cm⁻¹) (Fig 9.7A).

During the normal heating-cooling procedure, the inclusions show a metastable behaviour. During the cooling run down to -150 °C, the inclusions do not nucleate any recognizable crystalline phase, forming an amorphous solid (“glass”) with a Raman spectrum similar to the one of liquid H₂O (compare spectra at room temperature and at -150 °C in Fig. 9.7B). During the further heating-cooling procedure, the “glass” starts crystallizing, which is also indicated by the contraction of the bubble. Between -80 °C and -60 °C, this mass recrystallizes slowly to a microcrystalline, granular texture with a brownish colour; this phenomenon is confirmed by the appearance of the peak of ice and different salt hydrate phases in the Raman spectrum (Fig. 9.7C, D). If Raman spectroscopy had not been applied, the appearance of the granular texture could be easily mistaken for the eutectic stage. At this temperature, it is not possible to distinguish the peaks of different salt hydrate phases due to the small size of the crystals, which are randomly oriented inside the inclusions.

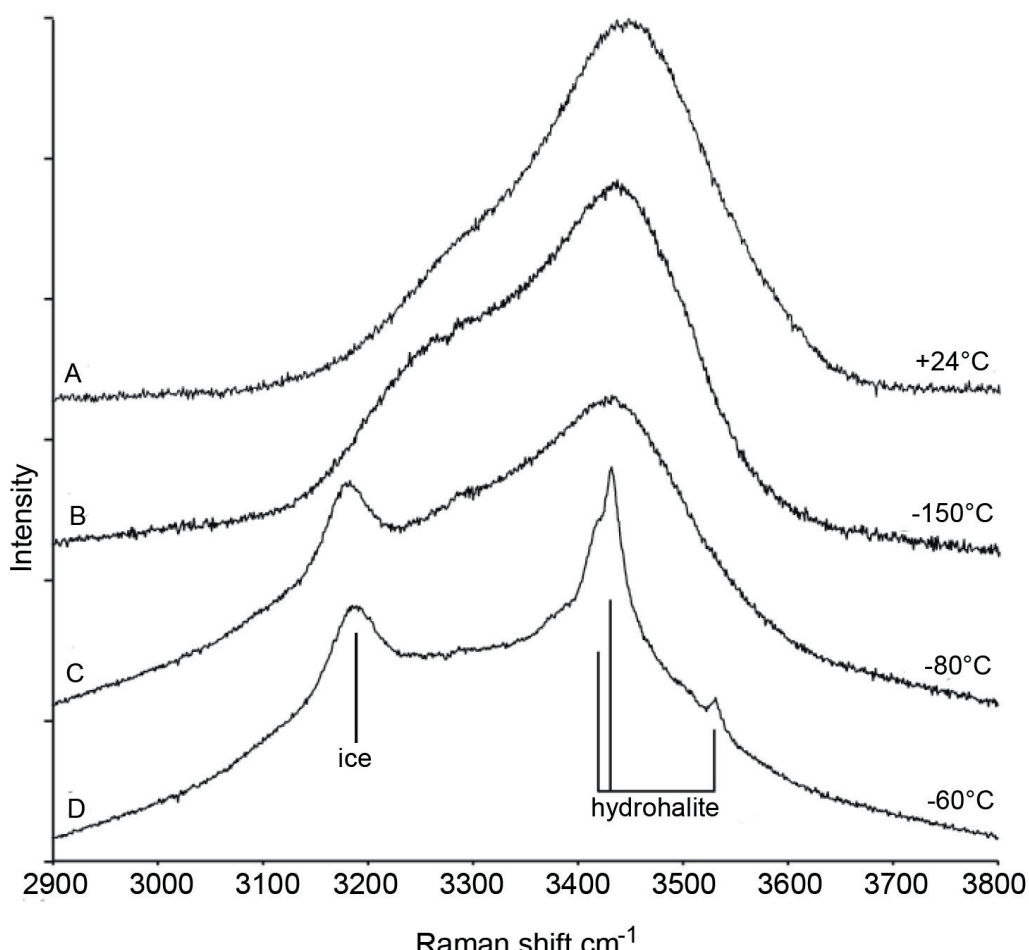


Fig. 9.7: Raman spectra (A) at room temperature; (B) after normal heating-cooling procedure at -150 °C; (C) after normal heating-cooling procedure at 80 °C; (D) after normal heating-cooling procedure at -60 °C (modified from Lapponi et al., 2007).

In a composite heating–cooling procedure of fluid inclusions, stable phase assemblages were observed at low temperatures. These differ substantially from the previously obtained assemblages. Probably, the most stable phase assemblage at -190 °C consists of ice, hydrohalite (Fig. 9.8A), and an unknown salt-hydrate (hydro-X) (Fig. 9.8B), which may include CaCl_2 , MgCl_2 , or a mixture of the two.

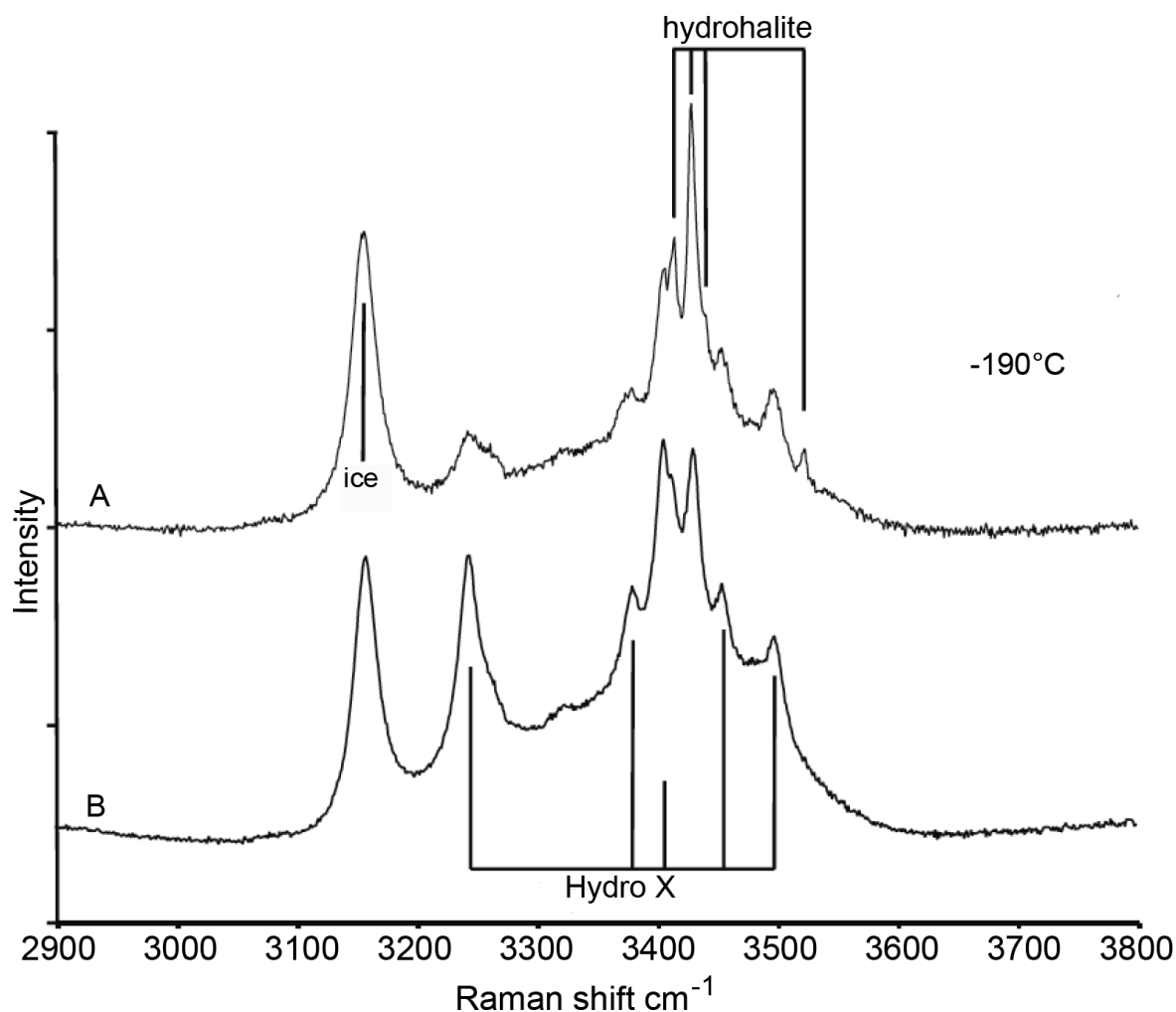


Fig. 9.8: Raman spectra in fluid inclusions at -190 °C after a composite heating–cooling procedure. Three different solid phases are recognizable: (A) ice and hydrohalite; (B) a third unknown salt-hydrate phase (hydro-X) (modified from Lapponi et al., 2007).

9.4 Preliminary discussion of microthermometric data

FIs in Dol A and in Dol B do not show any significant difference. Their degree of fill is in a similar, consistent range, the nucleation of vapor and ice-like phases is metastable. FIs in both dolomite phases have low T_{liq} and in the ice field display similar

final melting temperatures. They homogenize in the liquid phase and the measured T_h values show overlapping ranges. These FIs formed therefore from homogeneous fluids of similar composition and under similar thermal conditions.

The fluid trapped in Dol B belongs to a H_2O -salt system; the most likely stable configuration is the system $\text{H}_2\text{O}-\text{NaCl}-\text{XCl}$. X is an unknown cation of a different salt hydrate phase, which clearly nucleates together with hydrohalite in a salt mixture or alone. This complex system might be corresponding to $\text{MgCl}_2 + \text{CaCl}_2 + \text{NaCl}$.

The fluid inclusions trapped in the dolomite phases show a quite homogeneous composition and temperature for the different localities (Figs. 9.5c, 9.6c). The small range of variation observed in inclusions trapped in the same locality and also in the same crystal may be related to slight variations in salinity and temperatures of the fluid during precipitation of the crystal. The only exception is represented by the fluids trapped in the inclusions of Dol B from Mina Profunda, a former mining site: the strong scatter might be due to a later influence of thermal fluids.

FIs in Calcite 1 and Quartz are also characterized by a consistent degree of fill. The data indicate that these FIs formed from a homogeneous fluid, having a composition and possibly a temperature different from the solution causing the FIs in dolomite.

9.5 Salinity and temperature

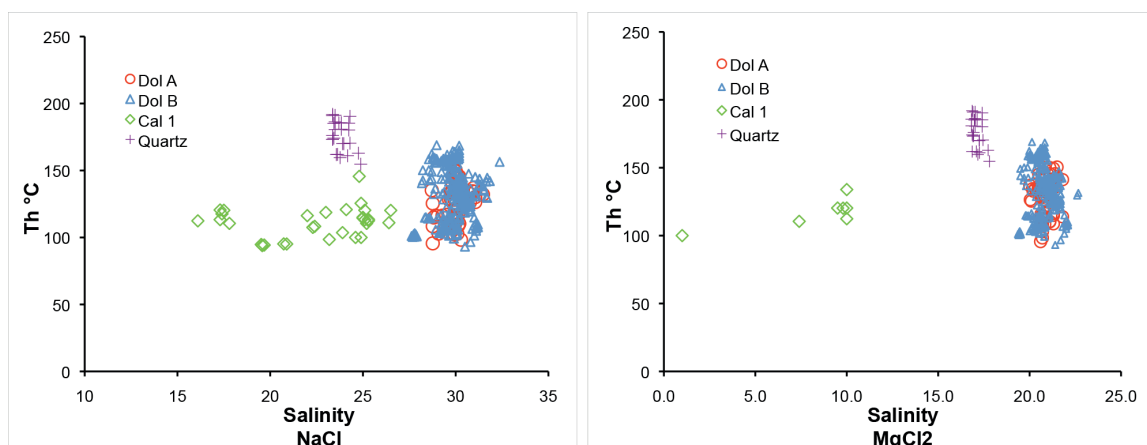
Raman spectroscopy at low temperatures combined with low temperature micro-thermometry revealed the presence of ice, hydrohalite (*hy*), and at least one additional phase, presumably a salt-hydrate. As mentioned earlier, the unknown phase could not be identified, due to the lack of experimental data for complex, highly saline fluid inclusions. Most likely the fluid belonged to the complex $\text{H}_2\text{O}-\text{MgCl}_2-(\text{NaCl}+\text{CaCl}_2)$ system. Salinity calculations in such a system are not possible because no equation of state is available. Magnesium surely represented one of the main components of the dolomitizing fluid at the time of dolomitization, but its concentration in the fluid trapped in the inclusion is strongly controlled by Mg consumption during dolomitization.

Due to the small size of the FIs, melting temperature hydrohalite (T_m *hy*) measurements were problematic; for this reason salinity is calculated in two ways: binary system $\text{H}_2\text{O}-\text{MgCl}_2$ and $\text{H}_2\text{O}-\text{NaCl}$, using the computer package FLUIDS (Bakker 2001b, Bakker 2003); the programs AQSO1 and AQSO3 were used to calculate salinities in the binary $\text{H}_2\text{O}-\text{NaCl}$ system (Bodnar 1993) and $\text{H}_2\text{O}-\text{MgCl}_2$ system (Dubois & Marignac 1997). The values for all the mineral phases studied are reported in Table 7.

Table 7: Main microthermometric values of different mineral phases.

Phase		Salinity MgCl_2 eq. wt %	Salinity NaCl eq. wt %
Dol A	Min	19.98	28.71
	Mean	20.83	30.06
	Max	21.80	31.47
Dol B	Min	19.36	27.62
	Mean	20.80	29.94
	Max	22.66	32.37
Calcite 1	Min	1.00	16.10
	Mean	8.24	22.35
	Max	10.00	26.50
Quartz	Min	16.82	23.36
	Mean	17.13	23.81
	Max	17.80	24.88

In both salinity calculations, the differences between the mineral phases are significant. Covariant plots between salinity and T_h show that dolomite phases A and B have similar mean properties: about 30 NaCl eq. wt %, or 21 MgCl₂ eq. wt %; T_h ranges between 93 to 205 °C. Quartz and Cal 1 have both lower mean salinity values than the dolomite phases (between 22.3 and 23.8 NaCl eq. wt %), but T_h is significantly different: higher in Quartz (mean 176 °C) and lower in Cal 1 (mean 112 °C) (Fig. 9.9).

**Fig. 9.9:** Covariance plots T_h -salinity, showing differences between four mineral phases: (a) salinity NaCl eq. wt %; (b) salinity MgCl₂ eq. wt %.

The T_h -salinities plot for the dolomite phases (Fig. 9.10) shows some differences between the various localities. The samples from Piedrasecha have the strongest variation, with lower salinities and T_h

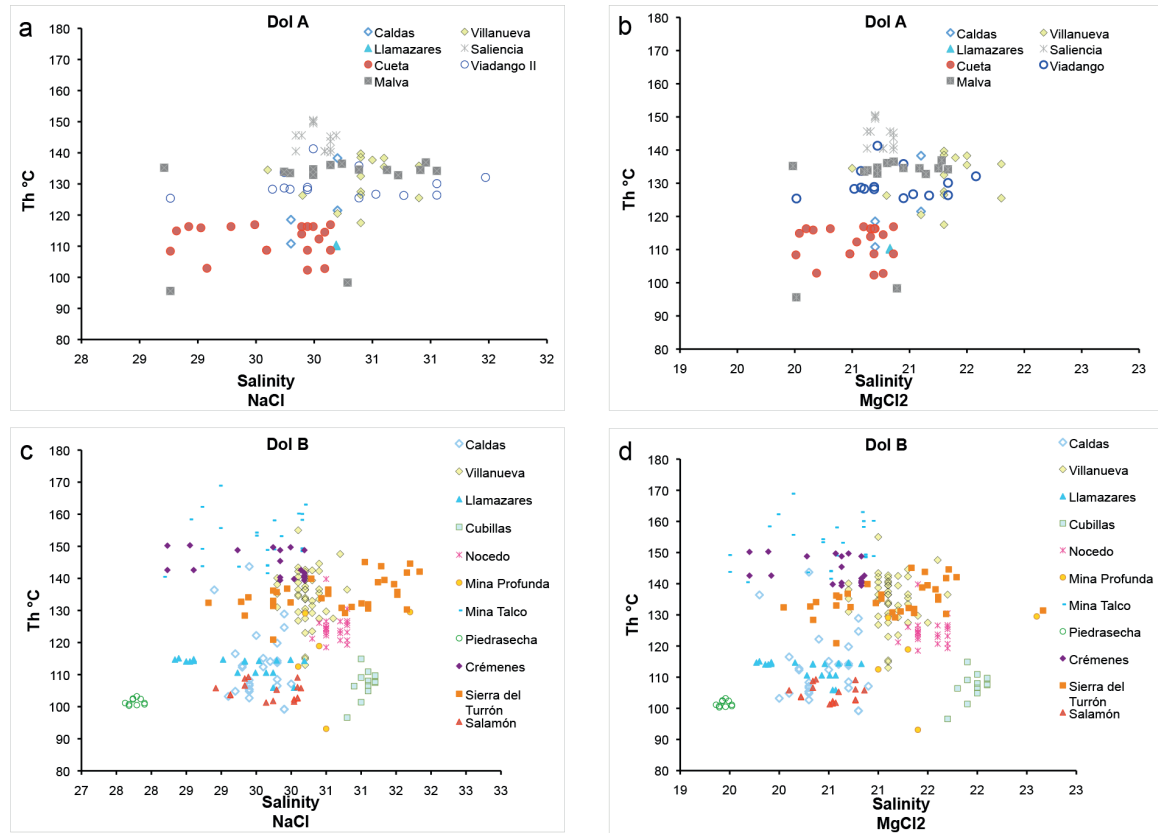


Fig. 9.10: Covariance plots T_h -salinity, showing differences between localities: (a) Dol A FIs, salinity in NaCl eq. wt %; (b) Dol A FIs, salinity in $MgCl_2$ eq. wt %; (c) Dol B FIs, salinity in NaCl eq. wt %; (d) Dol B FIs, salinity in $MgCl_2$ eq. wt %.

To derive trapping temperatures from the homogenization values, burial corrections are often applied (Gasparini et al., 2006b; Lapponi et al., 2007). This has not been done in this research for several reasons: (i) the dolomitizing fluids were most probably hydrothermal, their temperatures differ from the normal geothermic gradient; (ii) the pressure/depth conditions (lithostatic/hydrostatic) at the time of dolomitization, in a totally lithified but open system, are unclear.

9.6 Crush-leach analyses

Halogens are a very important constituent of sedimentary formation waters. Chlorine is usually the most important anion, accounting for more than 90%. Halogens are considered to behave conservatively, are mostly not involved in diagenetic water-rock interactions. This is because in clastic sedimentary rocks and carbonates only rarely halogen minerals form. Water-rock interactions are, however, important when water comes into contact with salt.

The amount of Na-Cl-Br-I can hardly be analysed precisely in minute fluid inclusions. Employing the crush-leach method, the relations of Na-Cl-Br-I in the FIs can

be analysed by the methodology described by Bottrell et al. (1988), improved by Banks & Yardley (1992) and Gleeson & Turner (2007). The data can best be evaluated by plots of Cl and Br vs. Na / Br vs. Cl / Br. The measured data should then be compared with the average composition of sea water, the evolution of sea water during evaporation, basinal brines, magmatic waters, as well as geothermal waters. The concentration of halogens present in sedimentary formation waters is an important point to consider before the attempt to delineate the origin of the dolomitizing fluids. For comparison purposes, the following discussion largely follows Lapponi et al. (2014).

Halogen ratios, specifically Cl/Br, are useful indicators of the source of salinity, especially if seawater is supposed to be one of the main components of the fluid. Cl and Br are conservative in solution and their concentrations are not affected by water/rock interaction, as long as halite dissolution and/or precipitation are not involved: during evaporation of seawater, the Cl and Br concentrations rise constantly, but the Cl/Br ratio is maintained constant until halite begins to precipitate. As halite precipitation proceeds, the Cl/Br ratio constantly decreases: Br is preferentially enriched in the residual brine because it is less compatible with the structure of halite (distribution coefficient of Br into halite is 0.032, Holser, 1979). In contrast to Cl and Br, elements such as Na, K and Li easily change their original concentration due to fluid-rock interactions (Fontes & Matray, 1994).

11 Carboniferous dolomite samples were investigated with the crush-leach method in the laboratories of Sarah Gleeson at the University of Alberta, Edmonton. Cl, Br, nitrate, phosphate, nitrite, and sulphate were analysed by ion chromatography, only Cl, Br and sulphate were detected; precision on replicate analyses was better than 1% for Cl, and within 5% for Br and sulphate. Na, K and Li were analysed by atomic absorption (AAS). Na and K were detected in all samples, but Li only in a few (see Annex 10).

According to the microthermometric data, the fluid trapped in the dolomites is very dense with a salinity well in excess of seawater. Potential processes for generating such a high salinity include subaerial evaporation of seawater and subsurface dissolution of evaporites. In the log (Cl) vs. log (Br) diagram (Fig. 9.11a), the data plot along the seawater evaporation line and are consistent with an origin of the dolomitizing fluid from seawater, which has been evaporated beyond halite precipitation. Dissolution of salt would shift the data away from the evaporation line.

In Fig. 9.11b the Na/Br vs. Cl/Br ratios during seawater evaporation are shown according to the diagram of Kesler et al. (1995). It is again indicated that the dolomitizing fluid was seawater, which has evaporated beyond the point of halite precipitation. Five of the samples plot on or close to the seawater evaporation line, and six plot slightly or strongly off the line (suggesting that they have lost some Na on the flow path). This might be due to the formation of clays, or Na-Ca exchange of the fluid with feldspars of terrigenous successions. Three of the mentioned 6 samples, plotting off the line, correspond to the western part of the study zone, and two samples to the easternmost region.

In Fig. 9.11c (K/Cl vs. Cl/Br plot) the data show more variability and do not align perfectly along the seawater evaporation line. Nevertheless, all of the samples have roughly the expected Na/K ratios for the degree of evaporation indicated by the Cl/Br ratios, showing that the original seawater values were modified only to a minor extent during water-rock interaction. Some samples are distinctly different from the other dolomites, because the relations of K/Cl suggest a brine interaction with potassium feldspar-rich siliciclastic rocks. The high amount of K in the fluid might be due to hydrolysis of K-feldspars. This assumed fluid-interaction with clastic rocks is also suggested by the K/Na vs. Li/Na plots (see Fig. 9.11 d): there is a distinct increase of Li. The contact with clastic rocks would explain also the radiogenic Sr isotope composition of the fluid observed.

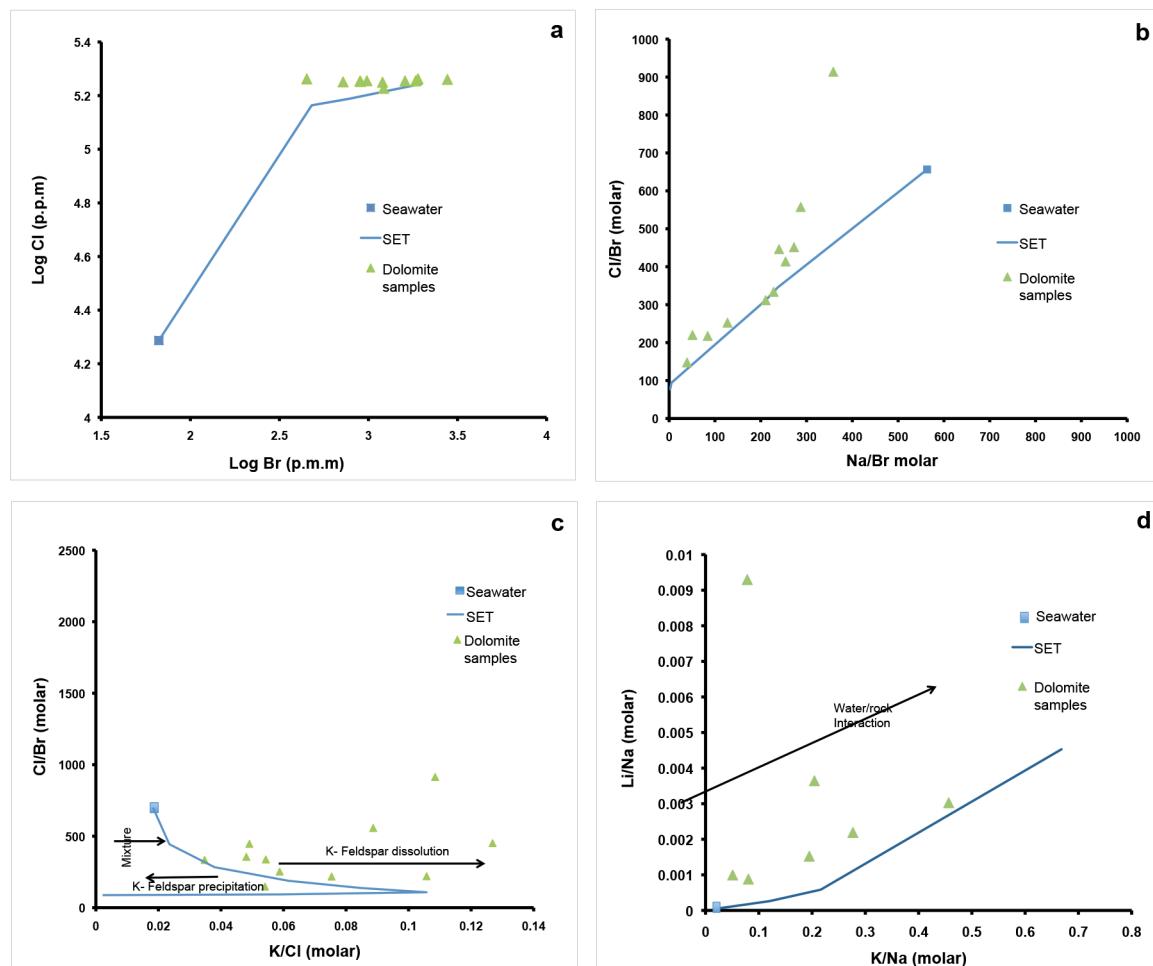


Fig. 9.11: Fluid inclusions crush-leach plots. (a) Log-log plot of Br versus Cl diagram; (b) plot of molar Na/Br versus Cl/Br ratios; (c) plot of molar K/Cl versus Cl/Br ratios; (d) water-rock interaction plot presenting molar K/Na versus Li/Na ratios.

Previous crush-leach analyzes (Lapponi, 2007; Lapponi et al., 2014) of dolomites of the Cantabrian zones were carried out on dolomite samples in Carboniferous and in Cambrian rocks. Br, Na, Cl, K, Li, Ca and Mg were measured and accurate microthermometric measurements were available in order to the best estimate of their

concentration in the fluid inclusions, from the salinity determined by microthermometry and Cl⁻ concentration in the crush leach solution. Results are consistent with the data from the additional samples taken in this research. The halogen content of the fluid inclusions indicate that the fluid, involved in the dolomitization of both Cambrian and Carboniferous rocks, was seawater, which has evaporated past the point where halite precipitation finishes. (Fig. 9.12)

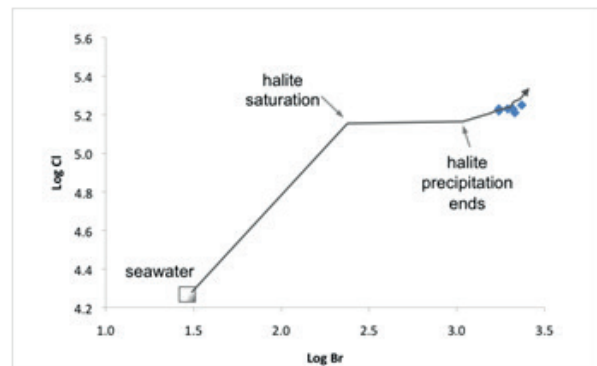


Fig. 9.12: Crush-leach fluid composition of Dol B from Carboniferous rocks in the Cantabrian zone: log (Cl) vs. log (Br) diagram (modified from Lapponi, 2007).

As mentioned by Lapponi (2007) and Lapponi et al. (2014), some of the analytical results might be due to the conversion of smectite to illite during deep burial diagenesis of the underlying clastic sedimentary successions, which has the effect of depleting the fluid in K and enriching in Na (Chaudhuri & Clauer, 1993). One can observe therefore (see Fig. 9.13) enrichment as well as depletion in the K content. The sample set is, however, too small to decide, if a regional gradient is present or not.

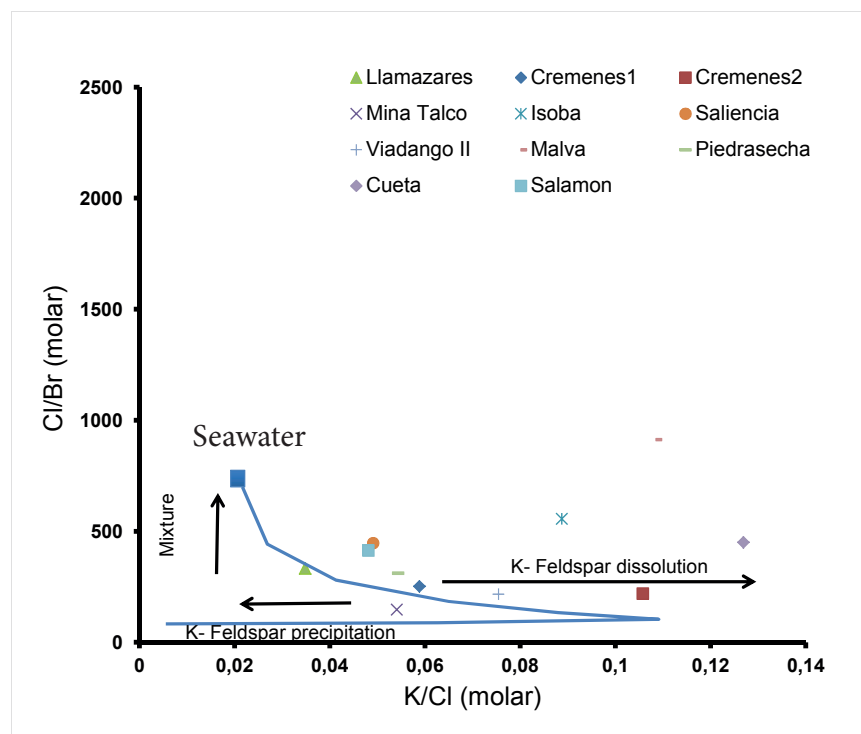


Fig. 9.13: Fluid Inclusions crush-leach plot of molar K/Cl versus Cl/Br ratios; K-feldspar dissolution indicated by localities.

10. DISCUSSION

10.1 Dolomite occurrence, petrography, and regional poroperm properties

The investigated dolomitization process was fabric destructive, with only rare remnants of former sedimentary features left. Characteristics typical for burial dolomitization (Gregg & Sibley, 1984; Gregg, 1985; Taylor & Sibley, 1986; Mountjoy & Amthor, 1994) are coarse crystallinity, non-planar textures, abundance of saddle dolomite cements, and zebra fabrics. Two main types of dolomitization are recognized: a widespread replacive (Dol A) and a volumetrically minor void-filling (Dol B). The process of replacive dolomitization was very effective: the analysed samples do not contain any remnants of the precursor limestone. Macroporosity is missing in the limestone sediments, it must have been created during (or after) replacive dolomitization. The void-filling Dol B cement then fills the cavities and fractures.

The transition from Dol A to Dol B is generally gradual and both phases exhibit the same cathodoluminescence colour, with the exception of the outer rim of Dol B. There is no sharp boundary between Dol A and Dol B, no reaction borders and/or corroded crystals were observed in between both dolomite types. A continuous dolomitization process affected the limestones, as already assumed by Gasparrini et al. (2006a, b) and Lapponi et al. (2014), which evolved in a nearly isochemical system from a replacive stage to a void-filling stage. Dol B precipitated in an environment of higher water/rock ratios.

The finely zoned and usually inclusion-free termination of the last generation of Dol B contains more Fe, as indicated by microprobe analyses and darker CL colour (Gasparrini et al., 2006a, b). A change in fluid chemistry, pressure, and/or fluid flow rate can be postulated, which brought the dolomitization process to an end. It is interesting to note, that the same zoned dolomite rim also occurs in Dol B crystals within Devonian (Schneider et al., 2008) and Cambrian (Lapponi, 2007; Lapponi et al., 2014) successions.

Field observations and petrographic analyses resulted in the definition of various dolomite groups. According to the outcrop aspect (massive, banded, and breccia) three different dolostone textures were defined. Distribution of porosity, crystal size and eventual rhythmicity patterns allowed to define the following fabrics: (i) zebra (micro- and meso-), (ii) vuggy, (iii) non macro porous coarse (sucrosic), and non macro porous fine.

Porosity and permeability measurements were carried out on almost all the samples; several representative samples were slabbed and photographed. Image analysis (IA) was performed on the slab pictures with main focus on the arrangement of the pores and the pore size. Comparing the different petrophysical parameters, the reservoir properties can be deduced. Generally, the best petrophysical characteristics in terms of poroperm values are found in the vuggy and micro zebra dolomites. Microporosity is an important factor improving reservoir quality, especially in

dolomites with micro zebra, meso zebra and non macro porous coarse (sucrosic) fabrics. The frequent over-dolomitization has a negative impact on porosity and permeability, cementing mostly the meso zebra dolomite.

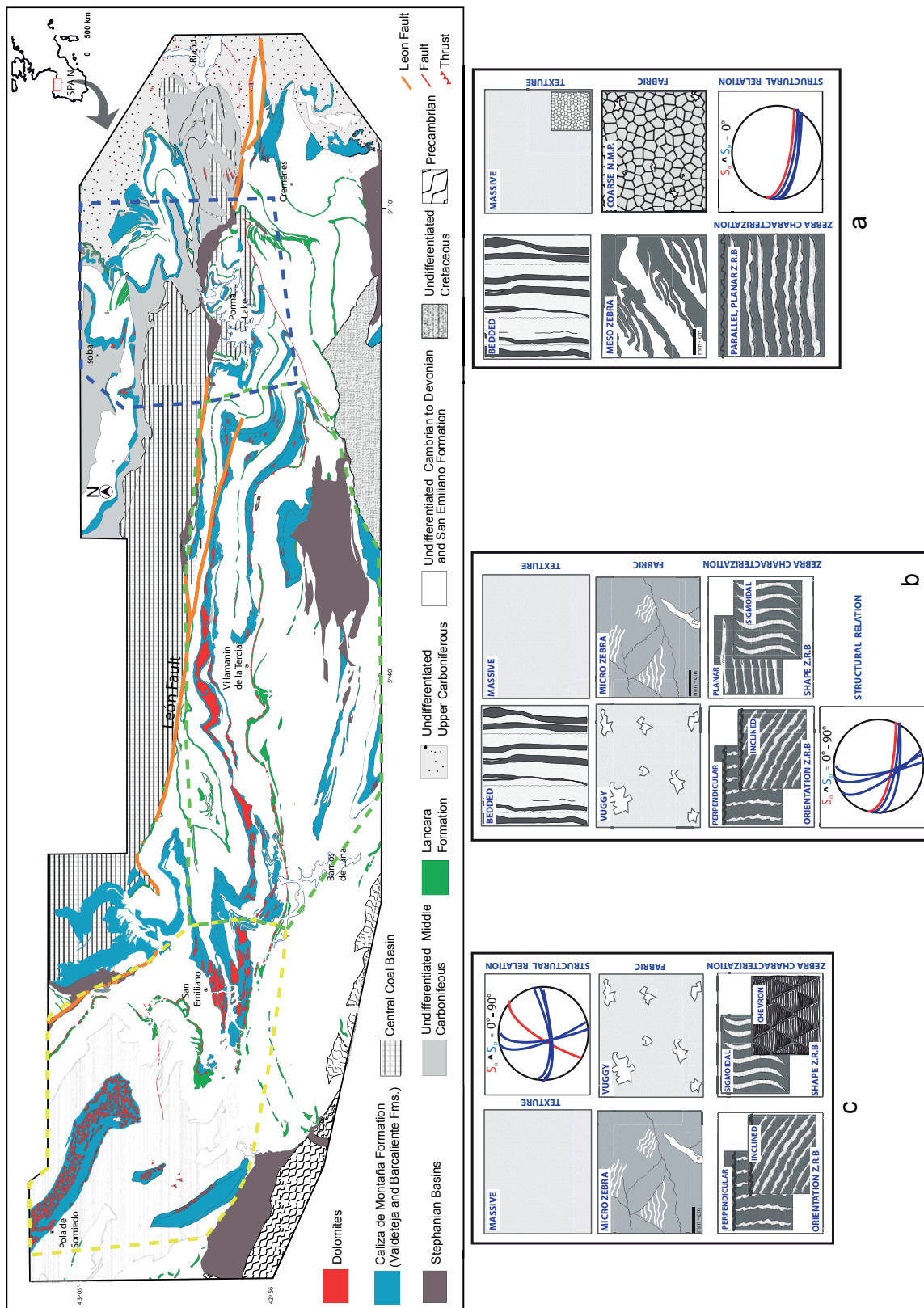
Three regional areas can be defined containing similar petrological and petrophysical properties, internal fabrics of dolomite bodies, structures of dolomite outcrops, structural setting, and regional distributions of dolomites. These regions comprise (i) outer parts of the core of the Cantabrian orocline in the east where the oroclinal curvature is open, (ii) a large intermediate area covering the central region of the working area, and (iii) the innermost core of the orocline in the west, containing the strongest folding of the arch. The most characteristic textures, fabrics, and structural relationships of the dolomite bodies, which define their poroperm properties, are sketched in Fig. 10.1.

The outer core of the Cantabrian orocline (eastern region of the transect) shows higher poroperm values in dolomites with low angle relationships (less than 30° to parallel) between bedding (S_o) and orientation of porosity (S_p). In the Barcaliente Fm., dolomite bodies are mainly banded, fabrics are frequently of the non macro-porous coarse and meso zebra types. The planar, rhythmic zebra bands are mainly parallel to bedding. Dolomite cements reduce dramatically the original porosity mainly in the meso zebra type. In IA this type shows apparent higher porosity values than other fabric types, because IA does not consider the microporosity of the latter (Fig. 10.1a).

The central region shows a wide variability between the main orientation of porosity (S_p) and bedding (S_o). The region is characterized by bedded to massive dolomite bodies. Vuggy fabrics represent the highest poroperm values due to their large pore diameters (Fig. 10.1b), followed by micro zebra and breccia fabrics. Higher poroperm values in micro zebras occur where the rhythmic zebra bands are oriented rectangularly to angularly to bedding. Zebra fabrics with sigmoidal to planar shape are common as well.

The innermost part of the core (western region) contains mainly more massive dolomite bodies, which show variable relationships between the average angle of bedding (S_o) and the porosity orientation (S_p). Higher poroperm values are found in the micro zebra fabrics, followed by vuggy types. Micro zebra fabrics are less cemented than elsewhere and therefore show large pore diameters; orientation of these rhythmic zebra bands is angular to rectangular to bedding. In this area, also chevron to sigmoidal zebra fabrics occur (Fig. 10.1c).

Fig. 10.1: Eastern zone (a), central zone (b), western zone (c), each showing similar poroperm values in the dolomites according to texture, fabric, and structural relationships.



10.2 Geochemistry

10.2.1 Stoichiometry and degree of order

Degree of order (OR) and stoichiometry have been used to outline three dolomite groups (Morrow, 1978; Lumsden & Chimahusky, 1980): (1) late diagenetic, coarse crystalline dolomites, generally nearly stoichiometric (about 50.0 to 51.0 mole % CaCO_3) and well ordered; (2) early diagenetic, fine crystalline dolomites, associated with evaporites and nearly stoichiometric as well; (3) early diagenetic, fine crystalline dolomites, not associated with evaporites and generally Ca-rich (54.0 to 56.0 mole % CaCO_3). OR values less than 0.4 have been interpreted as typical of early diagenetic, fine crystalline dolomite (Patterson, 1972). If dolomites formed at elevated temperatures (above 100 °C), OR should decrease with increasing temperatures (Goldschmidt & Graf, 1958).

The Cantabrian samples investigated have a nearly stoichiometric composition, ranging between 48.9 and 51.1 mole %; the degree of order varies between 0.54 and 1.0 and might be included in either dolomite group 1 or 2. Well-ordered dolomites of group 1 may reflect slow growth from dilute solutions, possibly aided by relatively high temperatures. These data are consistent with a burial origin, in agreement with the petrographic observation (e.g. abundant saddle dolomite of coarse crystallinity). The ample spread of the OR values can be the result of a complex interplay of precipitation rate and high salinity of the dolomitizing fluid. No regional trend can be observed in the data set.

10.2.2 Elemental geochemistry

The Sr-partitioning coefficient between stoichiometric dolomite and dolomitizing solution is not well constrained because of the lack of laboratory experiments under normal diagenetic conditions. Values available in literature encompass 0.0600 (Jacobson & Usdowsky, 1976), 0.025 (Katz & Matthews, 1977), and 0.0118 (Vahrenkamp & Swart, 1990): the former two values have been calculated from high temperature experimental studies, the latter value has been extrapolated from dolomite which formed from waters of normal or near-normal marine composition.

As Sr principally substitutes Ca in the dolomite lattice (Behrens & Land, 1972; Kretz, 1982), the distribution coefficient for Sr in dolomite should increase by about 0.0039 for every additional mole % CaCO_3 (Vahrenkamp & Swart, 1990). Assuming a value of about 0.020 for the Sr partitioning coefficient as well as the Sr and Ca concentration of seawater (8 ppm and 400 ppm respectively, Drever, 1982), the Sr concentration of dolomite in equilibrium with seawater (dolomite with about 51% Ca) should be about 150 ppm. Dolomite precipitated from evaporated seawater where gypsum precipitation has elevated the Sr/Ca molar ratio should have higher values (Behrens & Land, 1972; Land & Hoops, 1973). On the contrary, early diage-

netic dolomites, precipitated from hypersaline evaporitic brines that reached halite saturation, may have Sr concentrations as low as 50 ppm (Bein & Land, 1983). Due to the very high ionic strength of seawater compared with meteoric water, a mixture of both, with around 5% seawater has a Sr/Ca molar ratio similar to seawater, and even a dolomite precipitated from a mixture of about 20% seawater should have the typical marine Sr values (Tucker & Wright, 1990). Early diagenetic dolomite generally has a higher Sr content than late diagenetic dolomite, due to the very low partitioning coefficient that discriminate Sr in the fluid. Several authors (e.g. Mattes & Mountjoy, 1980; Morrow, 1990) reported Sr concentrations of a few tens of ppm in burial dolomites.

Sr contents in the range 10-152 ppm have been reported in saddle dolomites from several regions (see Spötl & Pitman, 1998, and reference therein). Nielsen et al. (1998) reported Sr concentrations of 33 ppm (mean value) in both replacive and void-filling burial dolomites forming zebra-fabrics. Other authors reported Sr concentrations of a few tens of ppm in burial diagenetic dolomites (e.g. Mattes & Mountjoy, 1980; Morrow et al., 1990; Barnaby & Read, 1992; Montañez, 1994).

All of the investigated dolomite samples have low Sr contents (see paragraph 8.1.2), which are incompatible with an origin as early dolomite directly precipitated from normal marine or evaporitic seawater (before reaching halite saturation). These low Sr contents suggest a late burial origin for both the replacive (Dol A1 and Dol A2) and the void-filling (Dol B) phases.

Also Na is strongly fractionated into the fluid during diagenesis and is considered a good indicator of the diagenetic evolution of the system. The Na concentrations of Dol A and B (between 100 and 600 ppm, see Table 3 and Fig. 8.6) are consistent with values of typical burial dolomites (Mattes & Mountjoy, 1980; Nielsen et al., 1998), and exclude the presence of evaporitic mineral inclusions. The concentration of Na in the precursor limestone (mean 221 ppm) is distinctly lower than the Na content of all dolomite phases. The measured high Na values of the dolomites might be strongly influenced by the high concentration of Na in the fluid inclusions, which are particularly abundant in the coarser crystals of Dol A and B. This trend can additionally be explained assuming a dolomitizing fluid with salinities higher than the diagenetic fluid in equilibrium with the precursor limestone.

Fe and Mn values tend to increase during diagenesis (Brand & Veizer, 1980) and correlate positively in burial dolomites. These two elements are particularly abundant in pore fluids at reducing conditions, which favour their concentration: early dolomites precipitated from near surface oxidizing fluids commonly have very low Fe and Mn contents, whereas burial dolomites have higher Fe and Mn values because most subsurface fluids are reducing (Land, 1980; Barnaby & Read, 1992).

The studied dolomites have higher Fe and Mn contents than the host limestones (see paragraph 8.1.2 and Fig. 8.8), also the partition ratio k for Fe and Mn is greater than 1, consistent with a burial diagenetic origin. The precursor limestone is characterised by high Sr/Ca and low Mn values compared to the dolomite phases but does not show any statistically significant correlation.

10.2.3 Isotope geochemistry

Oxygen and carbon isotopic composition

Sedimentary limestones of a certain age and depositional environment not much affected by diagenesis should show relatively uniform oxygen isotope values. The oxygen isotopic composition of carbonates reflects the isotopic signature of the fluid involved (e.g. dolomitizing fluid) and the temperature of precipitation. The Carboniferous limestones of similar facies show, however, a large spread in $\delta^{18}\text{O}$ values (between 0.5 to -4.5‰ V-PDB), which is probably due to regional differences in cementation and recrystallization during burial diagenesis. This hypothesis of recrystallization preceding dolomitization is consistent with the uniform CL displayed by the host limestones (Gasparrini, 2003). Recrystallization also affected Devonian limestones from the Correcilla Unit, characterized by a similar large spread in the $\delta^{18}\text{O}$ values (Schneider et al., 2004).

In dolomites, $\delta^{18}\text{O}$ values may be influenced by the isotopic signature of the calcium carbonate being replaced, occurring mostly in closed diagenetic systems of low water/rock interaction. Depletion in ^{18}O from matrix-replacing towards void-filling dolomites is a typical feature of many burial dolomites. It is commonly explained by an increase in temperature during the dolomitization process.

In terms of $\delta^{18}\text{O}$, Dol A and Dol B are, however, indistinguishable within one sample. Considering all samples, there is a distinct regional spread of the oxygen isotope data of Dol A and B (values between -1.6 to -13.7‰ V-PDB, see Fig. 8.10). Lower values, between -8 and -13‰ V-PDB, are typical of the Bodon Unit (Villanueva, Campolongo) and the eastern and central localities in the study area, especially Mina talco, Isoba, Pontedo, Viadango and Piedrasecha, which are also characterised by very high Dol B/Dol A ratios. The least negative $\delta^{18}\text{O}$ values (-1.76 to 4‰ V-PDB) were found in the western part between San Emiliano and Malva. The samples from the latter localities are usually inclusion-rich, display micro zebra fabrics and contain abundant open cavities. Only to a minor extent these cavities are filled by late calcite cements (see below). It is interesting to note, that the same regional trends in $\delta^{18}\text{O}$ can be observed in the dolomites within the Cambrian succession as well (Lapponi, 2007; Lapponi et al., 2014).

There is little isotopic fractionation of carbon with temperature. In contrast to oxygen isotopes, $\delta^{13}\text{C}$ values of dolomite are strongly influenced by the precursor limestone. The carbon isotopic signature of Dol A and Dol B is variable (between 1 and 5.4‰ V-PDB (mean value of 3.9 ‰ V-PDB); the measured values of the precursor limestone range from 3.1 to 5.3‰ V-PDB with a mean of 4.3‰ V-PDB.

The isotopic composition of the host limestones was compared with the one of Late Carboniferous seawater, deduced from the stable isotope composition of brachiopod shells from Spain (Grossman, 1994). The host limestones approximate the $\delta^{13}\text{C}$ signature of Late Carboniferous seawater with only slight depletion in ^{13}C . The later diagenetic phases, Cal 1 and Cal 2 exhibit wide-ranging and lower $\delta^{13}\text{C}$ values com-

pared to the previously mentioned carbonates. This might reflect varying contributions of light organic C and a meteoric origin (Figs. 8.12 and 10.2).

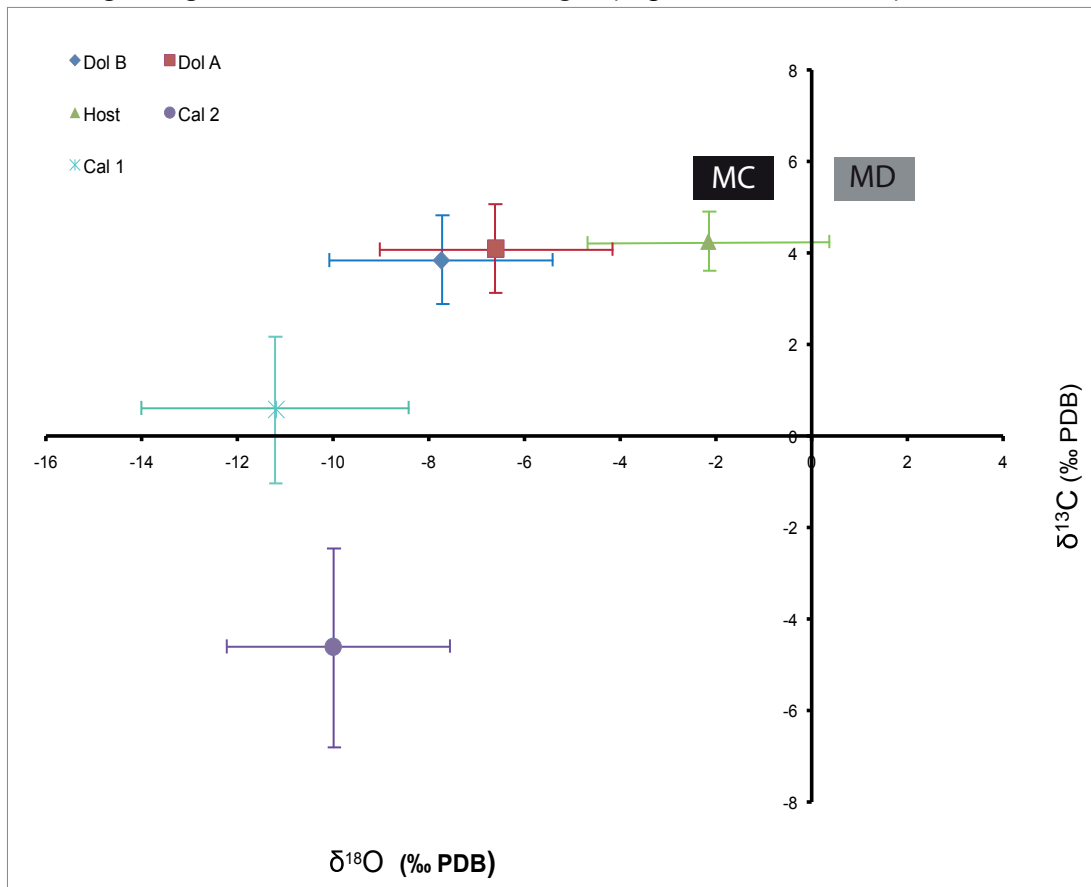


Fig. 10.2: O and C isotope composition of the different carbonate phases. The mean values of $\delta^{18}\text{O}$ and $\delta^{13}\text{C}$ are plotted together with the standard deviation range. The isotope composition of Late Carboniferous brachiopod shells from Spain (Grossman, 1994), employed as an indicator for sea water values (MC) is reported together with the hypothetical isotope composition of coeval marine dolomites (MD), assuming a 3‰ difference in $\delta^{18}\text{O}$ between calcite and dolomite (Land, 1980, 1985).

Strontium isotopic composition

The Sr isotopic composition of dolomite provides information on the dolomitizing fluid (seawater or diagenetic brine), because Sr isotopic fractionation during carbonate precipitation is negligible. The origin and migration pathway of the dolomitizing fluid can best be interpreted if the measured $^{87}\text{Sr}/^{86}\text{Sr}$ ratios are compared to the ones of potential Sr reservoirs (Fig. 10.3).

The $^{87}\text{Sr}/^{86}\text{Sr}$ ratios of Late Carboniferous - Early Permian seawater range between 0.7080 and 0.7085 (Burke et al., 1982; Smalley et al., 1994), the ratios of Late Permian seawater are somewhat less radiogenic, between 0.7070 and 0.7082 (Korte et al., 2003). The $^{87}\text{Sr}/^{86}\text{Sr}$ ratios of the Peña Prieta magmatic stock, corrected to 270-275 Ma, range between 0.7045 and 0.7069 (Gallastegui et al., 1990). These low

values are in agreement with the intermediate to basic nature of the intrusion. Pre-cambrian to Middle Devonian shales, which crop out all over the CZ, have distinctly more radiogenic $^{87}\text{Sr}/^{86}\text{Sr}$ ratios (corrected to 270-275 Ma) ranging between 0.7090 and 0.7731 (Nägler, 1990).

Both replacive and void-filling dolomites from the study area are slightly richer in radiogenic ^{87}Sr than the host limestones, which reflect the Sr isotope composition of Late Carboniferous seawater. Early Permian seawater has an even slightly lower Sr isotopic composition. All of the dolomites and calcites analysed have $^{87}\text{Sr}/^{86}\text{Sr}$ ratios higher than those of seawater of most geological times.

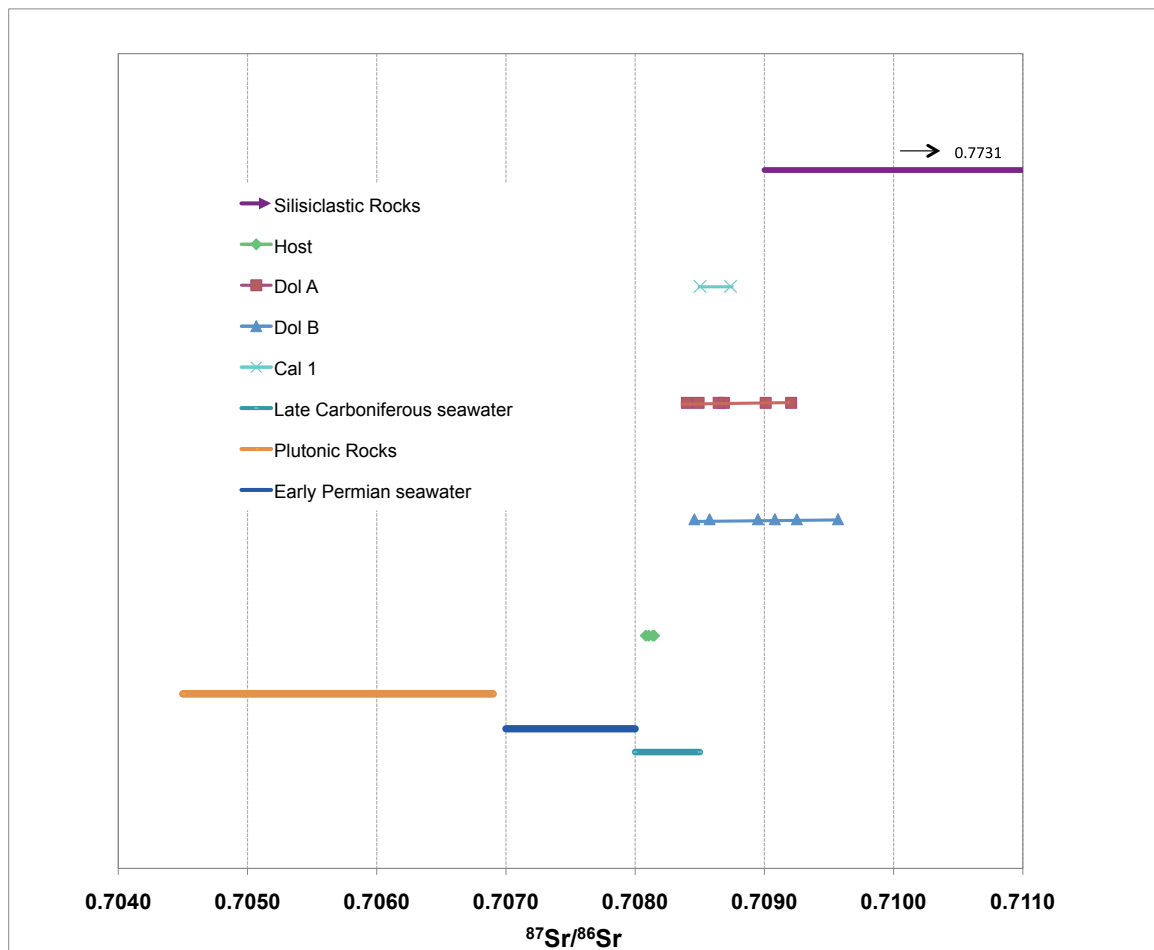


Fig. 10.3: $^{87}\text{Sr}/^{86}\text{Sr}$ ratios of the analysed dolomites and limestones compared to potential Sr reservoirs (corrected to 270–275 Ma).

The $^{87}\text{Sr}/^{86}\text{Sr}$ ratios of the igneous rocks are distinctly lower than those of the investigated dolomites. A contribution of Sr derived from igneous rocks can therefore not explain the more radiogenic character of the dolomites. Palaeozoic clastics have more radiogenic $^{87}\text{Sr}/^{86}\text{Sr}$ ratios than the dolomites (Fig. 10.3), which are as mentioned before more radiogenic than sea water of the Late Paleozoic. The dolomitizing fluid was therefore probably in contact with clastics. Potential sources of radiogenic ^{87}Sr are silicate minerals, of both detrital and igneous origin, with high Rb/Sr ratios (Clauer & Chaudhuri, 1992).

10.3 Fluid characterization

Primary, two-phase liquid-rich FIs, consisting of an aqueous liquid and a vapour bubble, were investigated in Dol A and Dol B, to a minor extent in Cal 1 and Cal 2, as well as in Quartz. For technical reasons the study focused on Dol B, showing homogenization temperatures in the range between 78.9 and 205.5 °C.

Major element composition and salinity are estimated from final melting temperatures of the fluid inclusions, but optical limits make the identification of these phase changes sometimes impossible. In general, the only recognizable phase observed is ice, which melts between -27.1 and -36.5 °C (see chapter 9, Figs. 9.3a, b). Raman spectroscopy combined with low temperature microthermometry revealed that a third salt-hydrate phase nucleated in the inclusions during cooling (Lapponi et al., 2007).

According to the data available, the system $\text{H}_2\text{O}-\text{NaCl}-\text{CaCl}_2$ plus unknown salt-hydrate(s) represents the most likely model composition of the fluid inclusions. According to the data available, salinity is calculated in two ways: binary system $\text{H}_2\text{O}-\text{MgCl}_2$ and $\text{H}_2\text{O}-\text{NaCl}$, according to the state equations from Dubois & Marignac (1997) and Bodnar (1993). Mg surely represented one of the main components of the original dolomitizing fluid, but its concentration in the trapped fluid inclusions is controlled by the fact that Mg is strongly fractionated during dolomitization (see crush-leach data). The values for Dol B range from 27.6 to 32.4 NaCl eq. wt. %. The dolomitizing fluids were brines several times more saline than modern seawater and with significant concentrations of Na, Mg and Ca. Raman spectroscopy combined with microthermometry revealed the presence of different cation species other than Na. The crush-leach data indicates that the fluid involved in the dolomitization was seawater, which has evaporated past halite precipitation. Local brine interaction with siliciclastic rocks rich in potassium feldspar can be assumed, leading to K enrichment in the fluid due to hydrolysis. The Br/Cl ratios indicate, that the dolomitizing fluids represent highly evaporated seawater, which was modified to a minor degree through fluid-rock interaction.

Combining microthermometry and isotope data of the dolomite phases, the O isotopic composition of the hydrothermal fluids can be characterized. Mode values of T_h were taken as approximate precipitation temperatures (no pressure correction applied). Using the fractionation equation of Land (1983), Gasparrini et al. (2006) plotted precipitation temperature of the carbonate phases versus O isotopic composition. All the samples analysed had $\delta^{18}\text{O}$ values between 0-13‰ SMOW (Fig. 10.4). At first sight, the $\delta^{18}\text{O}$ values of the dolomitizing fluids partly overlap with those of magmatic waters associated with Early Permian intrusions (Arcos, 1996), especially in the central area (localities Caldas, Nocedo, Mina Profunda, Villanueva, Siera del Turrón, and Pontedo). The above mentioned Sr-isotope data argue, however, against this relation. Combining the crush-leach and Sr-isotope data, the $\delta^{18}\text{O}$ values of fluids entrapped in dolomite more likely reflect an origin from Late Carboniferous-Early Permian seawater (Grossman, 1994) enriched in ^{18}O during evaporation. In addition to evaporation, fluid rock interaction with carbonates and/

or siliciclastic rocks (indicated by the slightly more radiogenic Sr isotopic ratios) can increase the $\delta^{18}\text{O}$ of the brine as well (Clayton et al., 1966; Hitchon et al., 1971; Land & Prezbindowski, 1981). Seawater (or modified seawater) is the only known source of fluids sufficiently abundant and rich in Mg to cause widespread dolomitization (Land, 1985; Machel & Mountjoy, 1986; Wilson et al., 1990; Spencer-Cervato & Mullis, 1992).

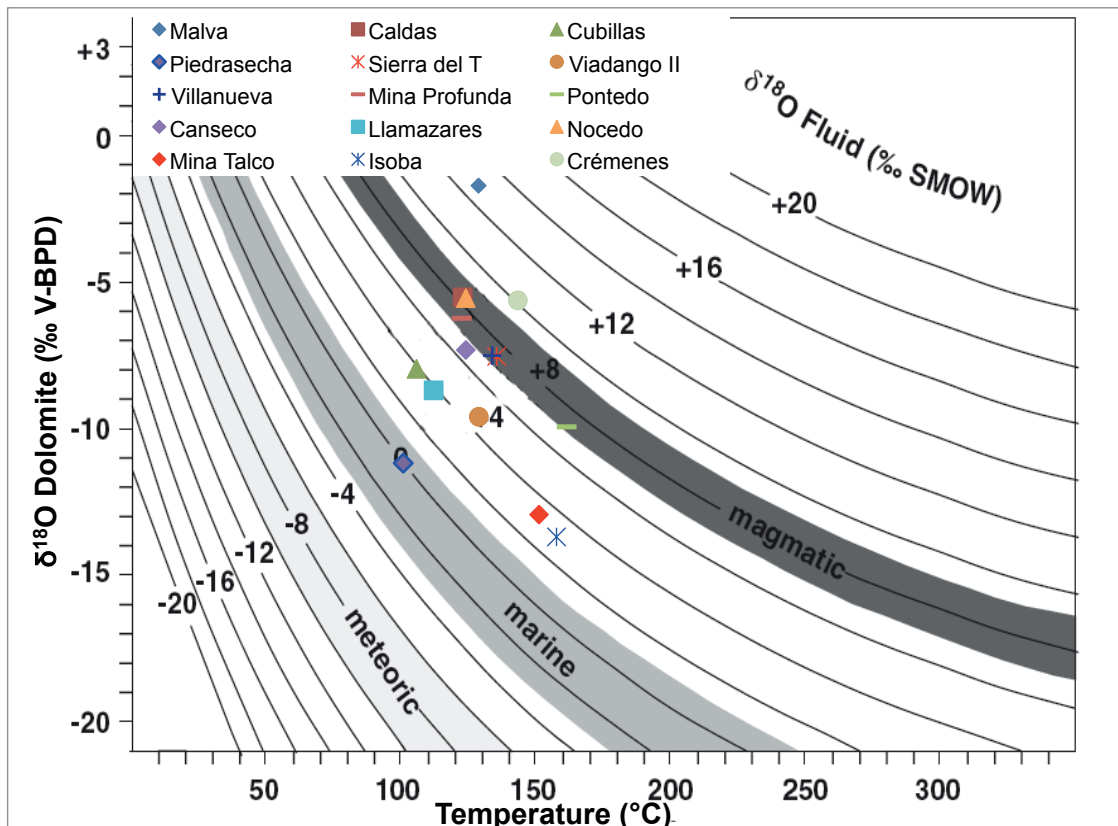


Fig. 10.4: Precipitation temperature versus O isotopic composition of the dolomite phases analysed. $\delta^{18}\text{O}$ of the fluid in equilibrium was calculated using the fractionation equation of Land (1983). Modified and enlarged from Gasparrini et al. (2006).

10.4 Age of dolomitization

The age of the dolomitization process can be constrained only indirectly. Geochemical and petrographic evidence (Lapponi, 2007; Lapponi et al., 2014) indicates, that the massive dolomitization of the Namurian and Westphalian carbonate succession was related to the same event that produced the dolomitization affecting the Cambrian carbonates: the two dolomites were precipitated from a fluid of similar composition. The fluid inclusions from the dolomites in the Cambrian show lower T_h than the ones in the Carboniferous. This indicates that the dolomitization took place after the emplacement of the main thrust sheets, when the Cambrian succession of the Correcilla Unit had already overthrust the Carboniferous succession of the Bodón Unit (Lapponi, 2007; Lapponi et al., 2007, 2014). If dolomitization would have taken place before thrusting, the opposite should be the case.

A post-Variscan origin of the Carboniferous-hosted dolomite is also clearly indicated by the spatial relationship between the Zebra fabrics in folded Namurian limestones: in one outcrop, described by Gasparrini et al. (2006b: Fig. 12), the zebra structures show a sub horizontal orientation on the different fold limbs and the axis of the fold. Similar examples clearly indicating post-folding dolomitization occur in the Cambrian-hosted dolomites as well (Lapponi, 2007; Lapponi et al., 2014).

Other indirect geological evidence can be used to constrain the timing of the dolomitization event further. The “Carboniferous-hosted” dolomite is the preferential site for small non-economic ore deposits. The two most important ones, Mina Profunda and Mina Providencia (close to the village of Carmenes) have been dated at 260–280 Ma, corresponding to the Middle-Late Early Permian (Paniagua et al., 1993). The dolomite hosting the deposits was therefore already present at the time of mineralization. The period between the end of the Variscan orogenesis and the Middle-Late Early Permian is therefore the most likely time for dolomitization. In this period a second thermal peak occurred, related to crustal thinning, intense volcanism, and sparse plutonism (Lepvrier & Martínez-García, 1990; Gutiérrez-Alonso et al., 2004, 2008, 2010; Weil et al., 2012). This period of rifting is associated with strike-slip and transtensional faults and represents a favourable time for dolomitization, not only in Northern Spain but in large parts of Pangaea as well (Boni et al., 2000).

Transtensional faults are associated with a change in the relative movement of the plate: changes in the strain pattern caused large-scale folding and bent the originally linear Variscan belt of Spain to form the spectacular orocline of the IAA (Ries & Shackleton, 1976; van der Voo et al., 1997; Weil et al., 2000, 2010, 2013; Weil & van der Voo, 2002; Aerden, 2004; Gutiérrez-Alonso et al., 2004a, 2012, b; Alonso et al., 2009; Pastor-Galán et al., 2011, 2012a, b, 2014; Shaw et al., 2012).

Temporal and spatial relationships of petrologic, geologic, geochemical and geochronologic data all point to magmatic and tectonothermal activity occurring pene-contemporaneously with oroclinal buckling over a short 10 m.y. time window at the end of the Carboniferous and link these processes with thinning in the outer arc, thickening in the inner arc, and ultimately foundering and delamination of the mantle lithosphere under western Europe. Such cause and effect linkages help explain many previously enigmatic geologic events related to post-orogenic Variscan Europe (Weil et al., 2013a; Pastor-Galán et al., 2014). One of the most spectacular events is the dolomitization studied.

Permian sediments crop out a few tens of kms north of the study area, recording the alternation of exposure and shallow water sedimentation under semiarid climatic conditions, indicating restricted circulation and high evaporation rates. This may represent the most likely environment characterizing the Cantabrian Zone during the Latest Carboniferous/Early Permian time. Evaporated seawater is extremely enriched in Mg and has the potential to deeply infiltrate the basin; at a time of tensional tectonics and strike slip movements associated with crustal thinning in the Latest Carboniferous/Early Permian the heated fluids may be pumped upwards to cause extensive dolomitization. The presence and extent of large (nowadays erod-

ed) “Permian basins” in the inner part of the Cantabrian Zone are hypothetical, however, and it is speculative therefore, if they could have provided a sufficiently large reservoir for fluids. The maximum temperature reached by the undolomitized Carboniferous carbonates from the study area can be derived using the conodont colour alteration index (CAI) method. The rock temperatures (reached for millions of years) are mostly lower than 70 to 95 °C (Raven & Van der Pluijm, 1996), distinctly less than the temperatures at the time of much more short-termed hydrothermal dolomite precipitation (Gasparrini, 2003; Gasparrini et al., 2006a).

There are indirect arguments for a former thicker cover of Latest Carboniferous/earliest Permian sediments. Several Stephanian Coal Basins are localized in the outer rim of the Cantabrian Zone and in the study area (Colmenero & Prado, 1993). The coal shows a mostly burial-related coalification gradient, controlled by an anomalously high geothermal gradient in the basin; calculations indicate an overburden in excess of 1000 m at the time of maximum coalification (Frings et al., 2004; Llorens et al., 2006). The amount of overburden depends, however, on the effects of hydrothermal activity assumed. Studies of illite crystallinity (IC) prove two thermal events, one in Variscan time and another one interpreted as late- or post-Variscan. This second event appears in unconformably overlying Stephanian rocks adjacent to the termination of the Leon fault. In these Stephanian outcrops, the coal rank is higher than temperatures indicated for the underlying pre-Stephanian Carboniferous rocks (Bastidas et al., 1999). This indicates the presence and movement of hydrothermal fluids, passing especially the porous Stephanian sediments and heating up the underlying successions much less than the overburden.

Independent data from fission track analysis (Carriere, 2006) indicate, that a larger area than just the coal basins underwent strong subsidence during the Early Permian. These data indicate that sufficient accommodation space was provided for the deposition of a thick Permian succession. A problem is, however, that the amount and effect of hydrothermal brines is difficult to model. Whatever the thickness and the extent of this Permian successions was, it was subsequently eroded, possibly due to Alpidic tectonics, which affected the area.

11. MODEL OF DOLOMITIZATION AND POROSITY FORMATION

The frequency of dolomite rocks in hydrocarbon carbonate reservoirs is one of the main reasons for this study. Understanding of the petrophysical properties, geochemistry and fluid inclusions, as well as fabrics and geometries of dolomite bodies, amount, types and regional distribution of porosity and permeability, and relation with the structural setting may lead to more accurate reservoir prediction and ultimately to more discoveries. The well-exposed massive dolomite bodies of the CZ represent an excellent outcrop analogue of dolomite reservoirs elsewhere. The present study also indicates that km-scale differences occur, where the relationship between structural development and fluid flow has a direct impact on the quality of reservoirs.

None of the models assuming early dolomitization at or close to the surface can be applied to the dolomites of the southwestern CZ. FI data indicate that dolomitization took place in the burial environment due to fluid flow of hydrothermal, hypersaline brines, showing isotopic signatures of chemically modified, highly evaporated Late Palaeozoic seawater (Gasparini et al., 2006a, b; Lapponi, 2007; Lapponi et al., 2014). The homogenization temperatures of FIs in the dolomites within the Carboniferous are higher than the long-term maximum temperatures reached. This indicates the hydrothermal setting. A source of highly evaporated seawater must have been in some distance to the sites of dolomitization. According to Machel (2004), an author sceptical to the regional importance of hydrothermal dolomites, the Cantabrian case is one of the few examples of large-scale hydrothermal dolomitization. Dolomitization occurred in the subsurface at the end of the Variscan orogeny (Fig. 11.1). Important tectonic changes occurred at this time, when the former Variscan E-W shortening changed to N-S compression. This led to a distinct steepening of bedding and overthrust planes and finally caused the formation of the Ibero-Armorican Arc (Ries & Shackleton, 1976; van der Voo et al., 1997; Weil et al., 2000, 2010, 2013; Weil & van der Voo, 2002; Aerden, 2004; Gutiérrez-Alonso et al., 2004a, 2012, b; Alonso et al., 2009; Pastor-Galán et al., 2011, 2012a,b, 2014; Shaw et al., 2012).

The arc underwent compression in its inner part and extension in the outer part (Fernández-Suárez et al., 2000; Gutiérrez Alonso et al., 2004, 2012). This oroclinical arc was closed to the west, open to the east, and most likely contained in its central part a residual, evaporitic marine water body. The main volumes of dolomite are concentrated in the Carboniferous succession in the northern part of the working area. The halogen ratios obtained by the crush-leach method are proof of the presence of highly evaporated seawater, slightly modified via water/rock interaction, which caused dolomitization. A northerly source of the evaporitic fluids is indicated by the distribution of the dolomites and of a few outcrops of Early Permian evaporites in northern areas, remnants of an assumed latest Carboniferous/earliest Permian succession, which once probably covered the Asturian coal basin. This restricted basin was affected by a semi-arid climate, causing high evaporation rates (Martínez-García, 1983). Fluids in this environment should have salinities and $\delta^{18}\text{O}$ values higher than normal latest Carboniferous/earliest Permian seawater: evaporitic brines may reach $\delta^{18}\text{O}$ values up to 7‰ SMOW (Knauth & Beeunas, 1986).

The subsequent closure of this marginal sea was associated with formation of a piggy-back thrusting succession (Merino-Tomé, 2009) at the northern side of the overthrust coal basin: in this Picos de Europa unit, large-scale dolomitization occurs as well (Gómez-Fernández et al., 1993), indicating again its former vicinity to the assumed evaporitic Mg-source in between the Picos de Europa area and our area of research in the southern CZ.

These dense brines entered the subsurface below the basin, and a radial outward-(southward- and northward) directed fluid flow (in the direction of extension) was initiated. To the south, fluids found several permeability barriers because of the subvertical orientation of the stratigraphic sequence, consisting of interbedded shaly successions. Better permeabilities were present along overthrust planes, especially because many of these were reactivated during orocline constriction. The major tectonic lineament in the area is the Leon fault (Alonso et al., 2009) that cuts the previous nappe structures and acted as curved dextral *strike-slip fault*, oriented ESE-WNW in the southern part of the orocline, and N-S further to the west, in the Somiedo area. This tectonic setting might have played an important control in the fluid circulation and the tectono-thermal evolution of the area. Dolomites occur also in vicinity to the Porma and Sabero-Bodón faults (Nijman & Savage, 1989; Aller et al., 2005), where pre- and syn-orocline bending joints are conjugated (Fig. 11.1).

Another important fact is the intrusion of granites at the same time (295 Ma), indicating that heat was available to set fluids into motion. According to Conodont Alteration Index (CAI) values, the peak temperatures obtained by the Carboniferous carbonates from the study area for a longer geologic time are mostly between 70-95 °C (Raven & Van der Pluijm, 1986). According to the latter authors these temperatures mirror a normal geothermal gradient at the time of maximum pre-Variscan burial. In post-Variscan time, ambient geothermal temperatures were probably less and therefore distinctly lower than those of dolomite precipitation inferred from FI (Gasparini et al. 2006a, b; Lapponi, 2007; Lapponi et al., 2014; own data). The FI data suggest that the emplacement of the studied dolomites was due to hydrothermal pulses, which probably correspond in time to the circulation of hydrothermal fluids in the Stephanian Coal Basins located south of the Bodón Unit (Ayllón et al., 2003; Frings et al., 2004). The spread of homogenization temperatures reported earlier does, however, not directly indicate fluid pathways, because our data are distributed over a large area, sampling different dolomite bodies, not directly connected to one fluid flow path.

Magmatic and tectonothermal activity occurred synchronously with orocinal buckling over a short 10 m.y. time window at the end of the Carboniferous, passing into the lowermost Permian (Gutiérrez-Alonso et al., 2004a, 2011a; Weil et al., 2013a; Pastor-Galán et al., 2014). Temporal and spatial relationships of petrologic, geological, geochemical and geochronologic data link these processes with thinning in the outer arc, thickening in the inner arc, and ultimately foundering and delamination of the mantle lithosphere. Such cause and effect linkages help to explain many previously enigmatic geologic events related to a post-orogenic Variscan Europe (Weil et al., 2013b). One of this is the large scale, pervasive dolomitization (see also Boni et al., 2000).

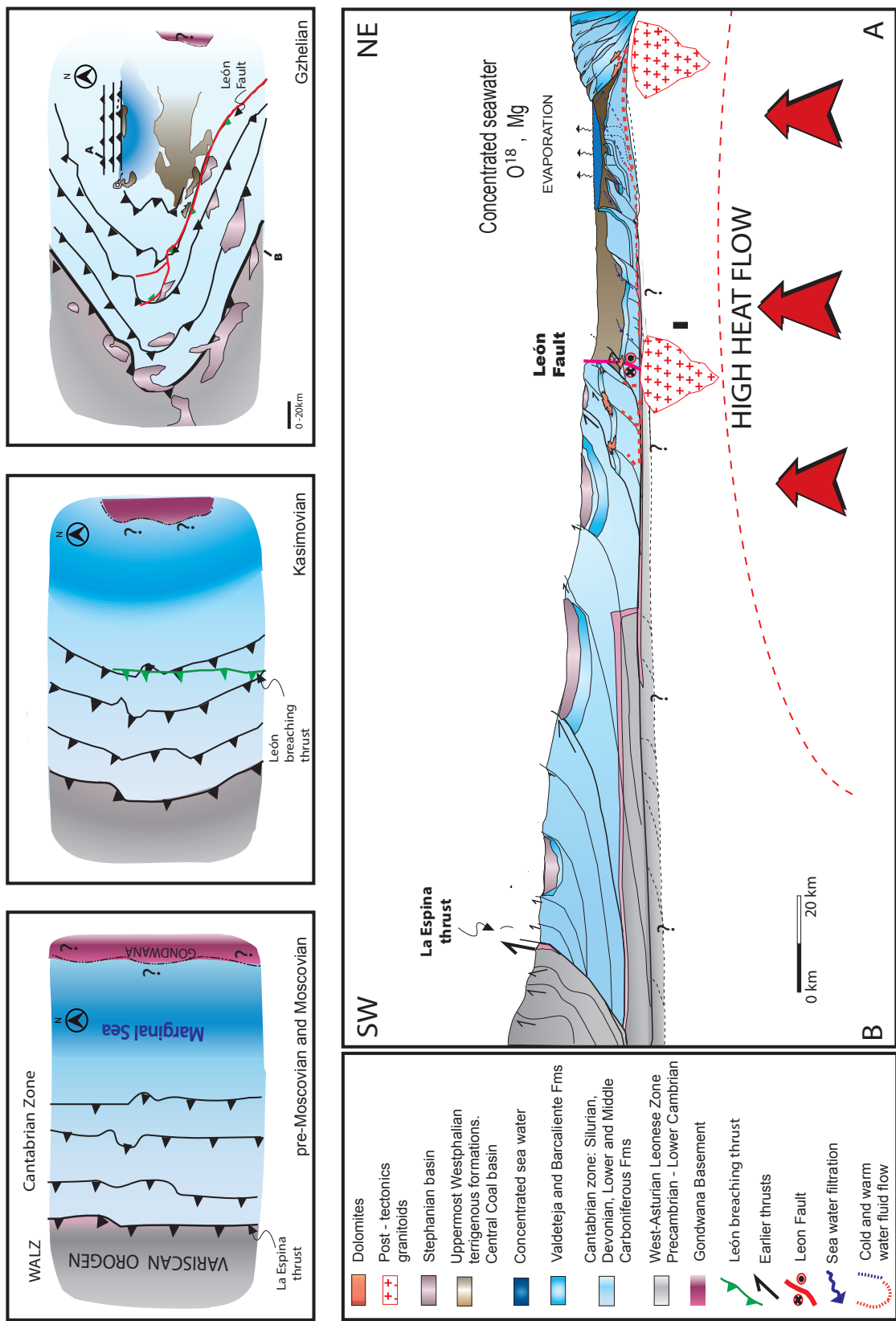


Fig. 11.1: Regional model of tectonic evolution and dolomitization scenario in the Cantabrian zone.

The southern Cantabrian zone has all of the requisites favouring a hydrothermal flow. The tectonic constraints during this time of post-orogenic orocinal folding are ideal: post-Variscan thinning and extension of crust, delamination, as well as increased heat flow (Sitter, 1962; Julivert, 1971; Pérez-Estaún et al., 1988; Fernández-Suárez et al., 2000; Gutiérrez Alonso et al., 2004, Weil et al, 2012). The orocline formation reactivated Variscan fault planes. Important for fluid pathways are pre- and syn-orocline bending joints (Pastor-Galán et al., 2009, 2011, 2012a, b).

Density-driven, seawater-derived brines percolated downwards through the structurally complex, deeply fractured subsurface rocks, favoured by the activation of strike-slip faults. This concentrated, evaporitic seawater furnished a continuous supply of Mg to the convection system (for an overview-model see Morrow, 1998) (Fig. 11.2), which was set in motion by the heat supply from the subsurface. The thermal convective flow of large amounts of an evolving fluid acted as a long lasting hydraulic pump, sufficiently effective to generate the large regional extent of massive dolomite bodies present in the Carboniferous of the CZ.

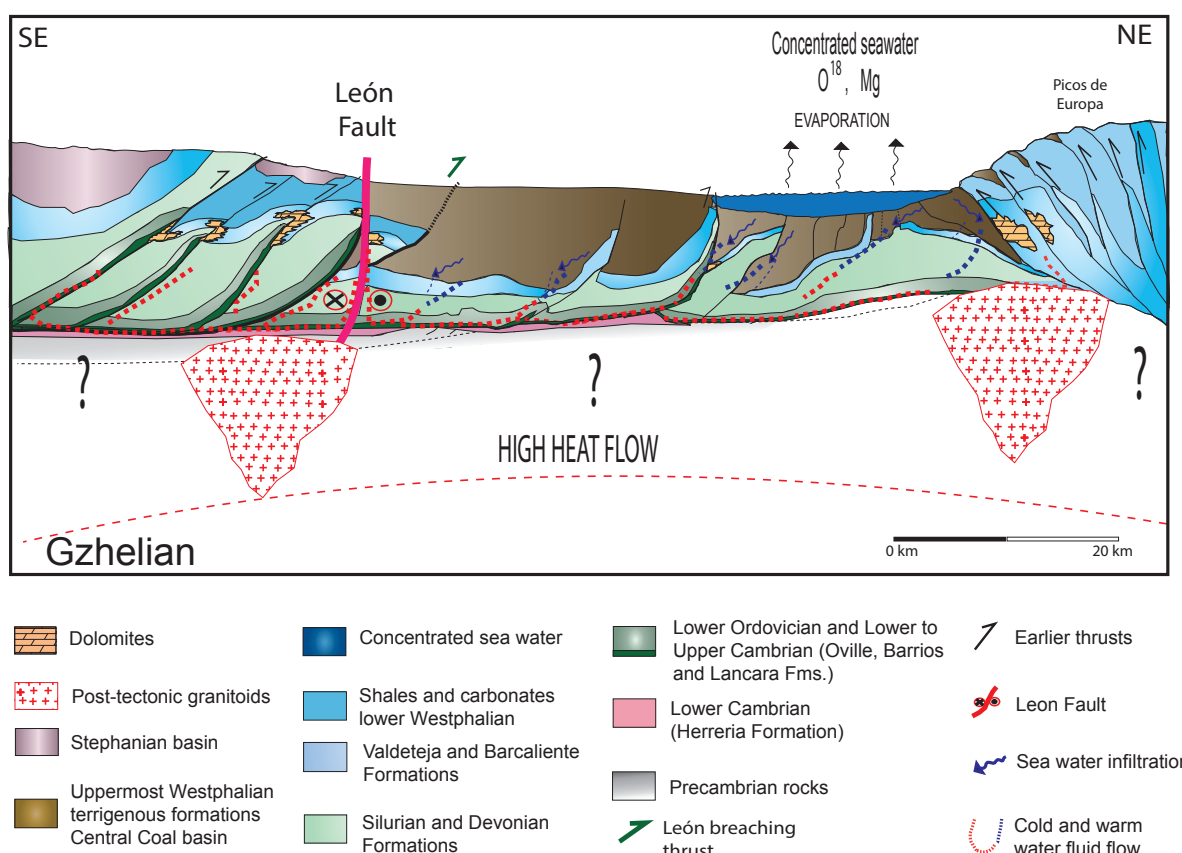


Fig. 11.2: Model of dolomitization: Shallow water basins in Early Permian time contain strongly evaporated seawater. This concentrated seawater percolated downward and was set into motion as convective fluid, dolomitizing areas further to the south (orange-brown areas of the figure) especially near larger faults, but also parts of the overthrusted Picos de Europa unit to the north. For further explanation see the text.

Assuming a normal geothermal gradient one might deduce the depth of dolomitization from the homogenization temperatures (see Gasparrini et al., 2006a, b), but such calculations give only maximum depths, because hydrotherms transport heat upwards into shallower levels. Such calculations are also strongly affected by the chosen PT conditions (hydrostatic or lithostatic pressure, geothermal gradient). The dolomitization depths were calculated with 3.9 ± 1 km for the Carboniferous (Gasparrini et al., 2006b) and 2-3 km for the (tectonically overlying) Cambrian, assuming (for the calculation only!) an open system and a hydrostatic regime (see Lapponi, 2007, and Lapponi et al., 2014). This gives the maximum possible depths of dolomitization, but in a hydrothermal regime dolomite emplacement probably occurred at distinctly shallower depths.

Dolomitization generated different internal fabrics in the carbonate rocks described earlier. The combination of abundant saddle dolomite, zebra fabrics, and breccias corresponds to dolomite bodies in other parts of the world interpreted as hydrothermal (e.g. Davies & Smith, 2006). According to the latter authors, most of the hydrothermal dolomites form at relatively shallow burial depths (<1 km) around basement-rooted strike-slip, extensional and most commonly transtensional faults. These are assumed to open conduits to great depth that are the pathways for upward flowing hydrothermal fluids that generally are of much higher pressure and temperature than those at shallower ambient conditions (see Sibson, 2000). When highly saline fluids flow up a fault from zones of high pressure to zones of lower pressure, the fluids become strongly supersaturated, due to the drop in pressure and temperature.

Large amounts of saddle dolomite formed from these highly supersaturated fluids. These dolomites first replaced calcite, and generated vugs as well as zebra fabrics. Although pressure diminished during the flow, the fluid was still overpressured for the relatively shallow depths affected by dolomitization. The zebra fabrics in the dolomites are probably related to these overpressure conditions, formed during periods of active faulting from fluids that are at a distinctly higher pressure (and temperature) than the ambient conditions (Davies & Smith, 2006). Fluid convection alone in the absence of faults is not likely to produce the pressures and the degree of super saturation required to make zebra fabrics cemented by abundant saddle dolomite. This dolomite cement filled the newly generated cavities to a large extent, all within one event of dolomitization (Gasparrini et al. 2006a, b; Lapponi et al., 2014).

In terms of porosity, the dolomitization process (see also Lapponi et al., 2014) represents a self-cannibalization: (i) replacive dolomitization created additional new porosity; (ii) hydrothermal fluids are focused into this new porosity, stabilizes it, and (iii) fills it subsequently. This dolomite cementation of the voids might be partly or totally, causing locally strong loss of porosity. This frequent over-dolomitization reduced dramatically or even sealed the porosity just created. This is especially negative for the meso zebra fabrics, where the former voids are often totally cemented.

Reservoirs in dolomite rocks commonly are multiple-porosity systems (Purser et al., 1994) that characteristically possess petrophysical heterogeneities. The specific types and relative percentages of pores present exert strong control on production

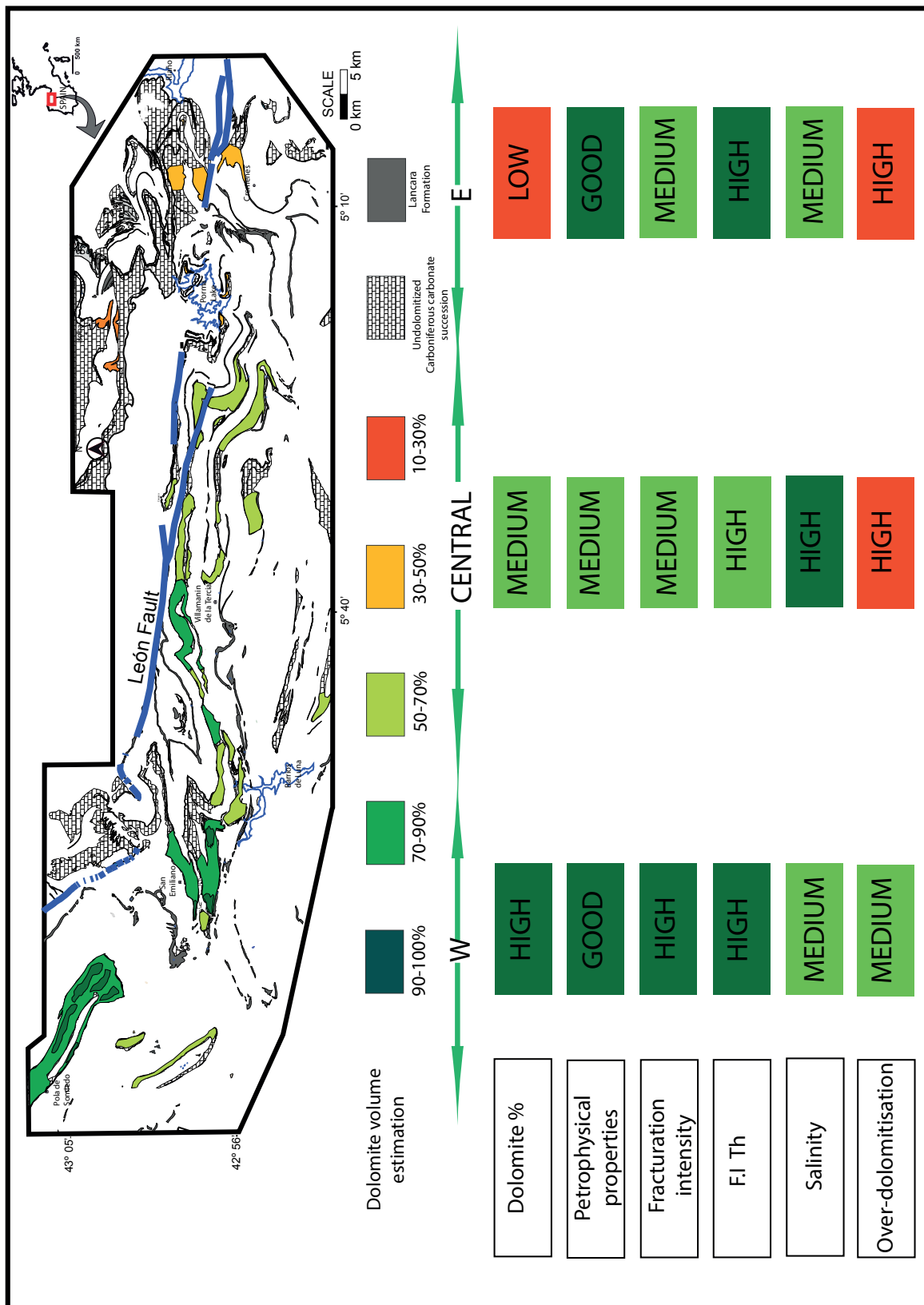
and stimulation characteristics of reservoirs (Amthor et al., 1994; Wardlaw, 1996). The origin of porosity during dolomitization is debatable (i.e. Qing & Mountjoy, 1994; Machel, 2005; Merino and Canals, 2011) and probably due to an interplay of host rock petrology, fluid supply/composition/pressure (see discussion before) and reaction kinetics. Whatever the process, which caused a distinct porosity gain, the Cantabrian dolomites are another example where dolomitization of the host limestone generated in many instants more than the theoretical maximum of 13% porosity, if a mole-per-mole replacement process would have been the case (Machel, 2005).

To achieve a better understanding of these lateral porosity differences, the volumes of dolomite bodies have been estimated due to mapping of the Namurian-Westphalian successions (Barcaliente and Valdeteja Fms.). This mapping was facilitated by the fact that the dolomitized rocks show a characteristic dark weathering colour, which is in contrast with undolomitized rocks, which have usually a light grey colour, due to different lichen populations covering the weathered surfaces. This can be seen clearly on orthophotos.

Using this map of dolomite volume and combining it with petrological and petrophysical properties, fabrics and internal structures of dolomite bodies, structural setting and fracturation intensity, microthermometry (FIs data, especially T_h) and amount of over-dolomitization, general patterns can be deduced to outline areas of better reservoir quality (Fig. 11.3).

The best reservoir characteristics of the investigated outcrop analogues are found in the western area where vuggy and micro zebra dolomites are frequent; the microporosity is an important factor improving reservoir quality. Also the abundance of dolomite bodies and the fracturing intensity is favourable in this area. Over-dolomitization has a negative impact cementing mostly the meso zebra dolostones: this phenomenon affects mainly the less favourable central and eastern areas.

Fig. 11.3: Patterns of outcrop analogues with reservoir characteristics in the Cantabrian zone ►



12. CONCLUSIONS

A strong dolomitization affected the Cantabrian Zone of Northern Spain, especially the southern part of it, somewhat less areas in the north. This dolomitization strongly improved the poroperm properties of the original host rock. In the investigated southern part of the CZ, the Late Carboniferous carbonate succession (mainly Valdeteja and Barcaliente Fms.) is most dolomitized, other carbonate successions like the Cambrian Láncara Fm. and, in the west of the working area, Devonian carbonates (Portilla and Santa Lucia Fms.) are less dolomitized. The dolomitization phenomenon is discontinuous and irregular but has a remarkable spatial distribution, occurring in different tectonic units of the Cantabrian Zone. The amount of dolomite clearly increases towards the west of the study area. This dolomite is burial in origin and hydrothermal (Gasparrini et al., 2006a; Lapponi et al., 2014).

Thick bodies of hydrothermal dolomites form reservoirs for hydrocarbons (and metallic deposits) in many parts of the world, but are often not easy to interpret. A better understanding of economically significant dolomite reservoirs and better constrained prediction might be aided by the study of reservoir analogues in outcrops. The dolomites in the southern Cantabrian zone provide one of the finest examples of large-scale hydrothermal dolomite bodies worldwide. Petrophysical analyses of dolomite samples from the investigated region show porosity values which cluster between 0.55% and 12% *phi*, and permeability values between 0.01 mD and 11.3 mD. These values strongly differ from the precursor limestones having much lower poroperm values. Study of these outcrop analogues, of fabrics and geometries of the dolomite bodies, amount, types and regional distribution of porosity and permeability, and relation with the structural setting may lead to more accurate reservoir prediction in the subsurface elsewhere.

The dolomitization in the southern Cantabrian zone strongly overprints the precursor rocks. Dolomite outcrops are differentiated in the field from the precursor limestones by the clear colour contrast: different darker brownish lichen populations are found on the dolomites, lighter grey ones on the limestones. The geometry of the dolomites differs from irregular small accumulations to large bodies with relatively sharp boundaries, possessing lateral extents from centimetres to several kilometres (see Fig. 11.3), and stratigraphic thicknesses of hundreds of metres.

Field observations and petrographic analyses resulted in the definition of various dolomite groups. The proposed classification incorporates on one hand the texture of dolomite outcrops, and on the other hand the internal fabrics. Textures were grouped into *massive*, *banded* and *breccia* types. Nearly 74% of the dolomite samples analysed correspond to the massive dolomite texture.

One can distinguish between macroporosity and microporosity. The latter term is applied to pores that cannot be investigated in image analysis; the term does not imply that these pores might be ineffective for petroleum migration and storage. The differing internal fabrics of the dolomites allow a more detailed classification, depending on the distribution of porosity, crystal size and eventual rhythmicity. Four

basic types are distinguished, *zebra* (meso or micro), *vuggy*, *non macroporous* (fine or coarse, the latter also called *sucrosic*), and *breccia*. The *zebra* fabric comprises a repetition of rhythmic, mosaic dolomite stripes with “sparry” dolomite (dolomite cement) stripes. 24% of the samples contain *micro zebra* fabrics, whereas 43% show *vuggy* structures.

Depending on the angular relationship of the rhythmic *zebra* bands with the bedding, the *parallel*, *perpendicular* and *inclined* types are distinguished. Further subtypes have been delineated: *chevron*, *planar* and *sigmoidal*, depending on the shape of the rhythmic *zebra* bands.

Petrographic analyses and cathodoluminescence clearly show different dolomite types. The first two (Dolomite A1, A2) represent replacement, and the other two (Dol B1, B2) are void filling. Intercrystalline porosity was recognized as well.

Petrophysical analyses of porosity and permeability were performed to investigate statistically the eventual relation of poroperm values of the dolomites with the above mentioned classification of textures and dolomite fabrics. In addition the eventual spatial distribution of the poroperm types was investigated, projecting the differing characteristics of the bodies of dolomite into an E-W transect through the study area.

Poropem values depend on the textures of the dolomites. Samples with *banded* textures have the best mean poroperm values (mean *phi*: 3.87%; mean *k*: 1.79 mD), followed by *massive* textures (mean *phi*: 3.42%; mean *k*: 0.58 mD), although this texture shows a wide range of values. *Breccia* textures, although they have good mean porosity values, have low permeabilities (mean *phi*: 3.14%, mean *k*: 0.37 mD).

According to the fabrics present in the dolomites, porosity and permeability values are distinctly different, also the size of the pores strongly differs. Samples showing the *coarse non macroporous (sucrosic)* fabric have the best poroperm values (mean *phi*: 5.31%; mean *k*: 2.69 mD), the pores clearly belong to microporosity.

In terms of favourable poroperm values, the *sucrosic* type is followed by dolomites with the *meso zebra* fabric (mean *phi*: 3.07%; mean *k*: 2.09 mD), and the *micro zebra* fabric (mean *phi*: 4.07%; mean *k*: 1.21 mD). Samples with different shapes of the *zebra* bands also show differences in their poroperm characteristics. Among these subtypes the best values are found in *parallel* and *planar* fabrics.

Macroporosity is highest in the *vuggy* and *zebra* types. Angles between the structural orientation of macroporous *zebra* bands (S_p) and bedding direction (S_o) vary from parallel ($S_o \wedge S_p \approx 0^\circ$) to perpendicular ($S_o \wedge S_p \approx 90^\circ$). Low angles (S_o and $S_p < 30^\circ$) favour porosity: these higher values might be due to the combination of bedding-parallel microporosities with the slightly inclined orientation of macroporosities. There is, however, a large spread of these structural data related to poroperm values.

Spatial distribution of attributes (structural data, types, internal fabrics and poropem values of dolomite bodies) were projected onto an E-W transect through the working

area, helping in the analysis and correlation of areas with similar characteristics. Three regional areas were defined. These regions comprise (i) outer parts of the core of the Cantabrian orocline in the east where the oroclinal curvature is open, (ii) a large central region of the working area, and (iii) the innermost core of the orocline in the west, containing the strongest folding of the arch.

The best potential reservoirs were found in the western area where favourable textural values occur: here *vuggy* and *micro zebra* dolostones are frequent, and microporosity is an important factor improving reservoir quality. Also abundance of dolomite bodies and fracturing intensity are favourable.

Over-dolomitization has a negative impact on reservoir quality, cementing mostly the *meso zebra* dolostones and reducing dramatically the porosity: this phenomenon affects mainly the central and eastern areas. This overdolomitization process could be called self-cannibalization of porosity: (i) replacive dolomitization created additional new porosity; (ii) hydrothermal fluids are focused into this new porosity, stabilizes it with some cement, and (iii) fills it subsequently, partly or totally.

The dolomites studied are characterized by partly highly negative $\delta^{18}\text{O}$ values, showing an ample regional range of values, but only minor differences on outcrop scale. In contrast, $\delta^{13}\text{C}$ values are regionally much more constant, buffered by the carbon signature of the precursor limestone. The $^{87}\text{Sr}/^{86}\text{Sr}$ data are slightly but constantly more radiogenic than Late Carboniferous – Early Permian seawater and the non-dolomitized precursor rocks, indicating contact of the dolomitizing fluids with terrigenous clastics. The minor element composition (Sr, Na, Fe, Mn) is consistent with the burial origin of the dolomite.

Fluid inclusion studies gave more insight into the composition of the dolomitizing fluids. High homogenization temperatures (T_h), low melting temperatures (T_m), and correspondingly high salinities characterize the FI data. The dolomites were formed by a highly saline, marine fluid in evolution, which first replaced the precursor carbonates generating new porosity, with values between 0.55% and 12% phi, and then precipitated dolomite cements in an almost isothermal and isochemical process. The fluids were originally highly evaporated, marine-derived modified brines, as suggested by the dominance of Na in the fluids and the Cl/Br ratios. The increased Li content of the fluids also indicates interaction with terrigenous clastics. The fluid was hydrothermal, because homogenization temperatures were higher than the temperatures of the precursor carbonates.

The formation of extended bodies of hydrothermal dolomite was favoured by a large reservoir of highly evaporated sea-water (confined by the orocline arch), extensive fracturing and reactivation of tectonic structures, fluid flow pathways, and high heat flow causing thermal convection. Oversaturation and dolomite replacement as well as dolomite cement precipitation occurred, when the overpressured fluids moved into higher horizons and lost temperature and pressure.

Late Variscan lithospheric delamination-induced extensional tectonics, and crustal thinning provided the heat required to trigger fluid convection and dolomite pre-

cipitation. Fluid circulation was facilitated by the reactivation or formation of highly permeable Variscan fault zones, as well as pre- and syn-oroclinal bending joints. Important regional tectonic lines exist, the complex thrust-breaching Leon Line in the north, at the contact between the Bodon Unit and the Central Coal Basin, the Porma fault in the east, and the Sabero-Gordon Line in the Correcillas Unit to the south. All these tectonic lines played important roles in controlling the fluid circulation and the tectono-thermal evolution in the area. The abundance of dolomitization in especially western areas is associated with the high amount of fractures there.

Timewise, these hydrothermal pulses seem to correspond to the circulation of hydrothermal fluids in the Stephanian Coal Basins located south of the Bodón Unit. A “simple” convective model is not able to predict the distribution of the dolomitized bodies throughout the stratigraphic succession of the study area. Effective fluid flow was only possible at the time of post-Variscan rifting and transtension, but the exact role of faults (present at the time of dolomitization) for fluid flow is difficult to assess. This is the case, because faults are partly Variscan, partly faults formed during the late Carboniferous-early Permian, and many of those were again reactivated or faults were newly formed during the Alpidic collision of Iberia with Europe.

REFERENCES

- Aerden, D.G.A.M., 2004. Correlating deformation in Variscan NW-Iberia using porphyroblasts; implications for the Ibero-Armorican Arc. *Journal of Structural Geology*, 26, 177-196.
- Águeda, J.A., Bahamonde, J.R., Barba, F.J., Barba, P., Colmenero, J.R., Fernández L.P., Salvador, C.I., Vera, C., 1991. Depositional environments in Westphalian coal-bearing successions of the Cantabrian Mountains, Northwest Spain. *Bulletin de la Société Géologique de France*, 162 (2), 325-333.
- Aller, J., Valin, M.L., Garcia-Lopez, S., Brime C., Bastida, F., 2005. Superposition of tectono-thermal episodes in the southern Cantabrian Zone (foreland thrust and fold belt of the Iberian Variscides, NW Spain). *Bulletin de la Société Géologique de France*, 176, 487-497.
- Alonso, J.L. 1987. Sequences of thrust and displacement in the superposed duplexes of the Esla Nappe Region (Cantabrian Zone, NW Spain). *Journal of Structural Geology*, 9-8, 969-983.
- Alonso, J.L., 1989. Fold reactivation involving angular unconformable sequences: theoretical analysis and natural examples from the Cantabrian Zone (Northwest Spain). *Tectonophysics*, 170, 57-77.
- Alonso, J.L., Crespo, J.L., 2002. The structural and stratigraphic control on sediment-hosted gold mineralization at the Salamón gold deposit (León, N of Spain). In: 2002 Denver Annual Meeting, Abstracts.
- Alonso, J.L., Marcos, A., Suárez, A., 2009. Paleogeographic inversion resulting from large out of sequence breaching thrusts: The León Fault, Cantabrian Zone, NW Iberia. A new picture of the external Variscan Thrust Belt in the Ibero-Armorican Arc. *Geologica Acta*, 7 (4), 451-473.
- Alonso, J.L., Pulgar, J.A., García-Ramos, J.C., Barba, P., 1996. W5. Tertiary basins and Alpine tectonics in the Cantabrian Mountains (NW Spain). In: J.C. Dabrio (Ed.), *Tertiary Basins of Spain: The Stratigraphic Record of Crustal Kinematics*. Cambridge University Press, Cambridge, 214-227.
- Alonso, J.L., Suárez-Rodríguez, A., Rodríguez-Fernández, L.R., Farias, P., Villegas, F.J., 1990. Hoja del Mapa Geológico Nacional de España 1:50.000, Memoria 104 La Pola de Gordón. IGME, Madrid, 138 pp., 1 map.
- Amthor, J.E., Mountjoy, E.W., Machel, H.G., 1993. Subsurface dolomites in Upper Devonian Luduc Formation buildups, central part of Rimbey-Meadowbrook reef trend, Alberta, Canada. *Bulletin of Canadian Petroleum Geologists*, 41-2, 164-185.

- Aramburu, C., Bastida, F., 1995. Geología de Asturias. TREA, Gijón, 314 pp.
- Arcos, D., 1996. Las mineralizaciones asociadas a la granodiorita en el depósito de Cu-Au de Carlés, Asturias. Unpubl. Ph.D. Thesis, University of Barcelona, Spain, 360 pp.
- Arenas, R., Farias, P., Gallastegui, G., Gil Ibarguchi, J.I., González Loderiro, F., Klein, E., Marquínez, J., Marín Parra, L.M., Martínez Catalán, J.R., Ortega, E., Pablo Maciá, J.G. de, Peinado, M., Rodríguez-Fernández, L.R., 1988. Características geológicas y significado de los dominios que componen la Zona de Galicia-Tras-os-Montes. II Congreso Geológico de España, Simposios, 75-84.
- Ayllon, F., Bakker, R.J., Warr, L.N., 2003. Re-equilibration of fluid inclusions in diagenetic-anchizonal rocks of the Ciñera-Matallana coal basin (NW Spain). *Geo-fluids*, 3(1), 49-68.
- Bakker, R.J., 2001 FLUIDS: new software package to handle microthermometric data and to calculate isochores. In: F. Noronha, A. Dória, and A. Guedes (Eds.), VI ECROFI, Porto, 23-25.
- Bakker, R.J., 2003. Package FLUIDS 1. Computer programs for analysis of fluid inclusion data and for modelling bulk fluid properties. *Chem. Geol.*, 194(1-3), 3-23.
- Banks, D.A., Yardley, B.W.D., 1992, Crush-leach analysis of fluid inclusions in small natural and synthetic samples: *Geochimica et Cosmochimica Acta*, 56, 245-248.
- Barnaby, R.J., Read, J.F., 1992. Dolomitization of a carbonate platform during late burial: Lower to Middle Cambrian Shady Dolomite, Virginia Appalachians. *Journal of Sedimentary Petrology*, 62, 1023-1043.
- Bastidas, F., Brime, C., García-López, S., Sarmiento, G.N. 1999. Tectono-thermal evolution in a region with thin-skinned tectonics: the western nappes in the Cantabrian Zone (Variscan belt of NW Spain). *International Journal of Earth Sciences*, 88, 34–48
- Behr, H.J., Horn, E.E., Frentzel-Beyme, K., Reutel, C., 1987. Fluid inclusion characteristics of the Variscan and post-Variscan mineralizing fluids in the Federal Republic of Germany. *Chemical Geology*, 61, 273-285.
- Behr, H.J., Gerler, J., Hein, U.F., Reutel, C., 1993. Tectonic brines und base-metal brines in den mitteleuropäischen Varisziden: Herkunft, metallogenetische Bedeutung und geologische Aktivität. *Göttinger Arb. Geol. Paläont.*, 58, 3-28.

Behrens, E.W., Land, L.S., 1972. Subtidal Holocene dolomite, Baffin Bay, Texas. *J. Sed. Petrol.*, 42, 155-166.

Bein, A., Land, L.S., 1983. Carbonate sedimentation and diagenesis associated with Mg-Ca-chloride brines: The Permian San Andreas Formation in the Texas Panhandle. *Journal of Sedimentary Petrology*, 53, 243-260.

Bodnar, R.J., 1993. Revised equation and table for determining the freezing point depression of H₂O-NaCl solutions. *Geochim. Cosmochim. Acta*, 57, 683-684.

Boni, M., Iannace, A., Villa, I.M., 2001. Multiple fluid flow events and mineralizations in SW Sardinia: from Variscan onward. *EUG XI*, Strasbourg, p. 272.

Boni, M., Parente, G., Bechstädt, T., De Vivo, B., Iannace, A., 2000. Hydrothermal dolomites in SW Sardinia: evidence for a widespread late Variscan fluid flow event. *Sedimentary Geology*, 131, 181-200.

Bottrell, S. H., Yardley, B., Buckley, F. 1988. A modified crush-leach method for the analysis of fluid inclusion electrolytes. *Bulletin de minéralogie*, 111(3-4), 279-290.

Brand, U., Veizer, J., 1980. Chemical diagenesis of a multicomponent carbonate system; 1, Trace elements. *Journal of Sedimentary Petrology*, 50-4, 1219-1236.

Burke, W.H., Denison, R.E., Hetherington, E.A., Koepnick, R.B., Nelson, H.F., Otto, J.B., 1982. Variation of seawater ⁸⁷Sr/⁸⁶Sr throughout Phanerozoic time. *Geology*, 10, 516-519.

Carrière, K., 2006. Neoproterozoic to Holocene tectonothermal evolution of the southern Cantabrian Mountains NW Iberia, revealed by apatite fission track thermochronology. Unpublished Ph.D. thesis, University of Heidelberg, Germany, 270 pp.

Chaudhuri, S., Clauer, N., 1993. Strontium isotopic composition and potassium and rubidium contents of formation waters in sedimentary basins: clues to the origin of the solutes. *Geochimica et Cosmochimica Acta*, 57, 429-437.

Clauer, N., Chaudhuri, S., 1992. Isotopic signatures of sedimentary rocks. *Lecture Notes in Earth Sciences*, 43, Springer, Berlin, 529 pp.

Clayton, R.N., Friedman, I., Graf, D.L., Mayeda, T.K., Meents, W.F., Shimp, N.F., 1966. The origin of saline formation waters: I. Isotopic composition. *J. Geophys. Res.*, 71, 3869-3882.

Colmenero, J.R., Bahamonde, J.R., Barba, P., 1993. Coal basins in the Cantabrian Mountains, northwestern Spain. *International Journal of Coal Geology*,

23 (1-4), 215-229.

Colmenero, J.R., Fernández, L.P., Moreno, C., Bahamonde, J.R., Barba, P. Heredia, N., González, F., 2002. Carboniferous. In: W. Gibbons and M.T. Moreno (Eds.), *The Geology of Spain*. Geol. Soc. of London, 93-116.

Colmenero, J. R., Suárez-Ruiz, I., Fernández-Suárez, J., Barba, P., Llorens, T., 2008. Genesis and rank distribution of Upper Carboniferous coal basins in the Cantabrian Mountains, Northern Spain. *International Journal of Coal Geology*, 76(3), 187-204.

Cone, M. P., Kersey, D. G., 1992. Porosity. In: D. Morton-Thompson, and A.M. Woods (Eds.), *Development Geology Reference Manual, Part 5 – Laboratory methods*. American Association of Petroleum Geologists, Methods in Exploration Series, No. 10, 204-209, Tulsa.

Conybeare, C. E. B., 1967. Influence of compaction on stratigraphic analysis: *Canadian Petroleum Geology Bull.*, v. 15, 331-345.

Crespo, J.L., Moro, M.C., Fadón, O., Cabrera, R., Fernández, A., 2000. The Salamón gold deposit, León, Spain. *Journal of Geochemical Exploration*, 71, 191-208.

Dallmeyer, R.D., Martínez Catalán, J.R., Arenas, R., Gil Ibarguchi, J.I., Gutiérrez Alonso, G., Farias, P., Bastida F., Aller, J., 1997. Diachronous Variscan tectonothermal activity in the NW Iberian Massif: evidence from $^{40}\text{Ar}/^{39}\text{Ar}$ dating of regional fabrics. *Tectonophysics*, 277, 307-337.

Davies, G.R., 2004. Hydrothermal (thermobaric) dolomitization: Rock fabrics and organic petrology. In: R. McAuley (Ed.), *Dolomites – The Spectrum: Mechanisms, Models, Reservoir Development*. Canadian Society of Petroleum Geologists, Seminar and Core Conference, January 13–15, 2004, Calgary, Extended Abstracts, on CD.

Davies, G.R., 2007. Hydrothermal dolomite reservoirs: characteristics, genesis and prediction. 17 October, 2007. Bilbao, Spain. Norsk Hydro. Abstract volume.

Davies, G.R., Smith, L.B., 2006. Structurally controlled hydrothermal dolomite reservoir facies: an overview. *American Association of Petroleum Geologist Bulletin*, 90-11, 1641-1690.

De Sitter, L. U., 1962. El Precambriano de la cadena cantábrica. *Notas Comun. Inst. Geol. Min. España*, 67, 145 pp.

Dewit, J., Foubert, A., El Desouky, H. A., Muchez, P., Hunt, D., Vanhaecke, F., Swennen, R., 2014. Characteristics, genesis and parameters controlling the development of a large stratabound HTD body at Matienzo (Ramales Platform,

Basque-Cantabrian Basin, northern Spain). *Marine and Petroleum Geology*, 55, 6-25.

Dewit, J., Huysmans, M., Muchez, P., Hunt, D. W., Thurmond, J. B., Vergés, J., Saura, E., Fernandez, N., Romaire, I., Esestime, P., Swennen, R., 2012. Reservoir characteristics of fault-controlled hydrothermal dolomite bodies: Ramales Platform case study. *Geological Society of London, Special Publications*, 370(1), 83-109.

Drever, J.I., 1982. *The geochemistry of natural waters*. Prentice-Hall, USA: 399 pp.

Dubois, M., Marignac, C., 1997. The $\text{H}_2\text{O}-\text{NaCl}-\text{MgCl}_2$ ternary phase diagram with special application to fluid inclusion studies. *Economic Geology*, 92, 114-119.

Ducea, M. N., 2011. Fingerprinting orogenic delamination. *Geology*, 39(2), 191-192.

Eichmüller, K., 1985. Die Valdeteja Formation: Aufbau und Geschichte einer oberkarbonischen Karbonatplattform, Kantabrisches Gebirge, Nordspanien. *Facies*, 13, 45-154.

Evers, H.J., 1967. Geology of the Leonides between the Bernesga and Porma rivers, Cantabrian Mountains, NW Spain. *Leidse Geologische Mededelingen*, 41, 83-151.

Farias, P., Gallastegui, G., González-Lodeiro, F., Marquínez, J., Martín-Parras, L.M., Martínez-Catalán, J.R., Pablo-Maciá, J.G., Rodríguez-Fernández, L.R., 1987. Aportaciones al conocimiento de la litoestratigrafía y estructura de Galicia Central. *Ann. Fac. Cienc. Univ. Porto*, 1, 411-431.

Faure, M., Leloix, C., Roig, J.Y., 1997. L'évolution polycyclique de la chaîne hercynienne. *Bulletin de la Société Géologique de France*, 168, 695-705.

Fernández, L.P., Bahamonde, J.R., Barba, P., Colmenero, J.R., Heredia, N., Rodríguez-Fernández, L.R., Salvador, C., Sánchez de Posada, E., Villa, E., Merino-Tomé, O., Motis, K., 2004. Secuencia sinorogénica. In: J.A. Vera (Ed.), *Geología de España*, SGE-IGME, chapter 2, p. 34-42.

Fernandez-Nieto, C., Torres-Ruiz, J., Subias Perez, I., Fanlo Gonzalez, I., Gonzalez Lopez, J., 2003. Genesis of Mg-Fe carbonates from the Sierra Menera magnesite-siderite deposits, Northeast Spain: evidence from fluid inclusions, trace elements, rare earth elements, and stable isotope data. *Economic Geology*, 98, 1413-1426.

Fernández-Suárez, J., Dunning, G.R. Jenner, J.A., Gutiérrez-Alonso, G., 2000. Variscan collisional magmatism and deformation in NW Iberia: constraints from U-Pb geochronology of granitoids. *Journal of the Geological Society*, 157, 565-576.

Folk, R.J., 1965. Some aspects of recrystallisation in ancient limestones. In: L.C. Pray and R.C. Murray (Eds.), *Dolomitization and Limestone Diagenesis – a Symposium*. SEPM Spec. Publ. 13, 14-48.

Fontes, J. C., Matray, J. M., 1994. Geochemistry and origin of formation brines from the Paris Basin, France. 1. Brines associated with Triassic salts. *Chemical Geology*, 109, 149-175.

Frings, K., Lutz, R., de Wall, H., Warr, L.N., 2004. Coalification history of the Stephanian Cinera-Matallana pull-apart basin, NW Spain; combining anisotropy of vitrinite reflectance and thermal modelling. *International Journal of Earth Sciences*. 93-1, 92-106.

Gallastegui, J., 2000. Estructura de la cordillera y margen continental cantábricos: perfiles ESCI-N. Universidad de Oviedo, Oviedo, Trabajos de Geología, 22, 221 pp.

Gallastegui, G., Heredia, N., Rodríguez-Fernández, L.R., Cuesta, A., 1990. El stock de Peña Prieta en el contexto del magmatismo de la Unidad del Pisueña-Carrión, Zona Cantábrica, N de España. *Cuadernos do Laboratorio Xeolóxico de Laxe*, 15, 203-217.

García-López, S., Bastida, Fernando, Aller, Jesús, Sanz-López, J., Marín, J.a, Blanco-Ferrera, Silvia, 2013. Ectothermal evolution of a major thrust system: the Esla–Valsurbio unit (Cantabrian Zone, NW Spain). *Geol. Mag.*, 1–15.

Gasparrini, M., 2003. Large-scale hydrothermal dolomitization in the southwestern Cantabrian Zone NW Spain: causes and controls of the process and origin of the dolomitizing fluids. Ph.D. thesis. University of Heidelberg, Germany, 193 pp.

Gasparrini, M., Bakker, R.J., Bechstädt, T., Boni, M., 2003. Hot dolomites in a Variscan foreland belt: hydrothermal flow in the Cantabrian Zone NW Spain. *Journal of Geochemical Exploration*, 78-79, 501-507.

Gasparrini, M., Bakker, R.J., Bechstädt, T., 2006a. Characterization of dolomitizing fluids in the Carboniferous of the Cantabrian zone NW Spain: A fluid inclusion study with cryo-Raman spectroscopy. *Journal of Sedimentary Research*, 76, 1304-1322.

Gasparrini, M., Bechstädt, T., Boni, M., 2006b. Massive hydrothermal dolomites in the southwestern Cantabrian Zone, Spain, and their relation to the Late Variscan evolution. *Marine and Petroleum Geology*, 23 (5), 543-568.

Gies, H., 1976. Zur Beziehung zwischen Photolumineszenz und Chemismus natürlicher Karbonate. Neues Jahrbuch für Mineralogie, Abhandlungen., 127, 1-46.

Gleeson, S.A., Turner, W.A., 2007. Fluid inclusion constraints on the origin of the brines responsible for Pb–Zn mineralization at Pine Point and coarse non-saddle and saddle dolomite formation in southern Northwest Territories. *Geo-fluids*, 7, 51-68.

Goldsmith, J.R., Graf, D.L., 1958a. Structural and compositional variations in some natural dolomites. *Journal of Geology*, 66(6), 678-693.

Goldsmith, J.R., Graf, D.L., 1958b. Relation between lattice constants and composition of the Ca-Mg carbonates. *American Mineralogist*, 43, 1-2, 84-101.

Goldstein, R.H., Reynolds, T.J., 1994. Systematics of fluid inclusions in diagenetic minerals. Society of Economic Paleontologists and Mineralogists (SEPM), Short Course, 31, 198 pp.

Gómez-Fernández, F., Both, R.A., Mangas, J., Arribas, A., 2000. Metallogenesis of Zn-Pb carbonate-hosted mineralisation in the southeastern region of the Picos de Europa, central northern Spain province: geologic, fluid inclusion, and stable isotope studies. *Economic Geology*, 95, 19-40.

Gómez-Fernández, F., Escayo-Morán, M.A., Alonso-López, J.A., Seibold Imbert, I., 1993. Caracterización y origen de las dolomías del sector sudeste de Picos de Europa, norte de España. *Estudios Geológicos*, 49, 343-350.

González-Lastra, J., 1978. Facies salinas en la Caliza de Montaña Cordillera Cantábrica. *Trabajos de Geología*, 10, 249-259.

Gregg, J. M., 1985. Regional epigenetic dolomitization in the Bonneterre Dolomite (Cambrian), southeastern Missouri. *Geology*, 13, .503-506.

Gregg, J.M., Sibley, D.F., 1984. Epigenetic dolomitization and the origin of xenotopic dolomite texture. *Journal of Sedimentary Petrology*, 54-3, 908-931.

Grimmer, J.O.W., Bakker, R.J., Zeeh S., Bechstädt, T., 2000. Dolomitization and brecciation along fault zones in the Cantabrian mountains. *Journal of Geochemical Exploration*, 69-70, 153-158.

Grossman, E.L., 1994. The carbon and oxygen isotope record during the evolution of Pangea: Carboniferous to Triassic. In: G.D. Klein (Ed.), *Pangea: Palaeoclimate, Tectonics, and Sedimentation during Accretion, Zenith and Breakup of a Supercontinent*. Geological Society of America Special Paper, 288, 207–228.

Gutiérrez-Alonso, G., Fernández-Suárez, J., Weil, A.B., 2004a. Orocline triggered lithospheric delamination. Geological Society of America Special Paper, 383, 121-130.

Gutiérrez-Alonso, G., Fernández-Suárez, J., Weil, A.B., 2004b. Oroclinales y delaminación: relaciones y efectos. In: C.L. Liesa et al. (Eds.), Geo - Temas, VI Congreso Geológico de España, 6, 69-72.

Gutierrez-Alonso, J. Fernandez-Suarez, A.B. Weil, J.B. Murphy, R.D. Nance, F. Corfu, Johnston, S.T., 2008. Self-subduction of the Pangaea global plate, *Nature Geosciences* 1, 549–553.

Gutiérrez-Alonso, G., Fernández-Suárez, J., Jeffries, T. E., Johnston, S. T., Pastor-Galán, D., Murphy, J. B., Gonzalo, J. C., 2011a. Diachronous post-orogenic magmatism within a developing orocline in Iberia, European Variscides. *Tectonics*, 30(5), TC5008, 17 pp.

Gutiérrez-Alonso, G., Murphy, J. B., Fernández-Suárez, J., Weil, A. B., Franco, M. P., Gonzalo, J. C., 2011b. Lithospheric delamination in the core of Pangea: Sm-Nd insights from the Iberian mantle. *Geology*, 39(2), 155-158.

Gutiérrez-Alonso, G., Johnston, S. T., Weil, A. B., Pastor-Galán, D., Fernández-Suárez, J., 2012. Buckling an orogen: The Cantabrian Orocline. *GSA Today*, 22(7), 4-9.

Gutierrez-Alonso, G., Pastor-Galán, D., Collins, A. S., 2013. Strike-slip accommodation during the development of the Cantabrian and Central-Iberian oroclines: $^{40}\text{Ar}/^{39}\text{Ar}$ geochronological ages of major shear zones. In *EGU General Assembly Conference Abstracts*, Vol. 15, p. 11480.

Heijlen, W., Muchez, P., Banks, D.A., 2001. Origin and evolution of high-salinity, Zn-Pb mineralising fluids in the Variscides of Belgium. *Mineral. Deposita*, 36, 165-176.

Hemleben, C., Reuther, C.D., 1980. Allodapic limestones of the Barcaliente Formation, Namurian A, between Luna and Cea Rivers, southern Cantabrian Mountains, Spain. *Neues Jahrbuch für Geologie und Paläontologie*, 1592, 225-255.

Heward, A.P., 1978a. Alluvial fan and lacustrine sediments from the Stephanian A and B (La Magdalena, Ciñera-Matallana y Sabero) coalfields, northern Spain. *Sedimentology*, 25, 451-488.

Heward, A.P., 1978b. Alluvial fan sequence and megasequence models. In: A.D. Miall (Ed), *Fluvial Sedimentology*. Canadian Society of Petroleum Geologists, Memoir 5, 669-702.

Heward, H.P., Reading, H.G., 1980. Deposits associated with a Hercyn-

ian to late Hercynian continental strike-slip system, Cantabrian Mountains, northern Spain. IAS Special Publication, 4, 105-125.

Hitchon, B., Billings, G.K., Klovan, J.E., 1971. Geochemistry and origin of formation waters in the Western Canada Sedimentary Basin. *Geochim. Cosmochim. Acta*, 35, 567-598.

Holmes, D. W., Williams, J. R., Tilke, P., Leonardi, C. R., 2011. Characterizing flow in oil reservoir rock using SPH: absolute permeability. *Int. J. Numer. Anal. Meth. Geomech*, 61(7), 1-6.

Holser, W.T., 1979. Trace elements and isotopes in evaporites. In: R.G. Burns (editor), *Marine Minerals*. Mineralogical Society of America, *Reviews in Mineralogy*, 6, 295–346.

Iriarte, E., López-Horgue, M. A., Schroeder, S., Caline, B., 2012. Interplay between fracturing and hydrothermal fluid flow in the Asón Valley hydrothermal dolomites (Basque–Cantabrian Basin, Spain). *Geological Society of London, Special Publications*, 370(1), 207-227.

Jacobson, R.L., Usdowski, H.E., 1976. Partitioning of strontium between calcite, dolomite and liquids. *Contribution to Mineralogy and Petrology*, 59, 171-185.

Julivert, M., 1971. Décollement tectonics in the Hercynian Cordillera of northwest Spain. *American Journal of Science*, 270, 1-29.

Julivert, M., 1978. Hercynian orogeny and Carboniferous paleogeography in Northwestern Spain: a model of deformation-sedimentation relationships. *Zeitschrift der Deutschen Geologischen Gesellschaft*, 129, 565-592.

Julivert, M., Fontbote, J. M., Ribeiro, A., Conde, L., 1972. Mapa Tectónico de la Península Ibérica y Baleares. Scale 1:1000000. Madrid: IGME.

Julivert, M., Marcos, A., 1973. Superimposed folding under flexural conditions in the Cantabrian Zone, Hercynian Cordillera, northwest Spain. *American Journal of Science*, 273, 353-375.

Katz, A., Matthews, A., 1977. The dolomitization of CaCO_3 : an experimental study at 252-295°C. *Geochimica et Cosmochimica Acta*, 41, 297-308.

Keelan, D. K., 1982. Core analysis for aid in reservoir description. *Journal of Petroleum Technology*, 34(11), 2-483.

Keller, M., Bahlburg, H., Reuther, C.D., Weh, A., 2007. Flexural to broken foreland basin evolution as a result of Variscan collisional events in northwestern Spain. *Geol. Soc. Am. Mem.*, 200, 489-510.

Kesler, S.E., Martini, A.M.; Appold, M.S., Walter, L.M., Huston, T.J., Furman,

F.C., 1996. Na-Cl-Br systematics of fluid inclusions from Mississippi Valley-type deposits, Appalachian Basin: constraints on solute origin and migration paths. *Geochimica et Cosmochimica Acta*, 60 (2), 225-233.

Kilias, S. P., Pozo, M., Bustillo, M., Stamatakis, M. G., Calvo, J. P., 2006. Origin of the Rubian carbonate-hosted magnesite deposit, Galicia, NW Spain: mineralogical, REE, fluid inclusion and isotope evidence. *Mineralium Deposita*, 41(7), 713-733.

Knauth, L.P., Beeunas, M.A., 1986. Isotope geochemistry of fluid inclusions in Permian halite with implications for the history of ocean water and the origin of saline formation waters. *Geochimica et Cosmochimica Acta*, 50, 419–433.

Korte, C., Kozur, H. W., Bruckschen, P., Veizer, J., 2003 Strontium-isotope evolution of Late Permian and Triassic seawater. *Geochimica et Cosmochimica Acta*, 67, 47–62.

Kretz, R., 1982. A model for the distribution of trace elements between calcite and dolomite. *Geochimica et Cosmochimica Acta*, 46-10, 1979-1981.

Kullmann, J., Reuther, C.D., Schönenberg, R., 1977. La transición del estadio geosinclinal a la orogénesis en la formación variscá de la Cordillera Cantábrica. *Breviora Geológica Astúrica*, 211, 4-11.

Land, L.S., 1980. The isotopic and trace elements geochemistry of dolomite: the state of the art. In: D.H. Zenger, J.B. Dunham, R.L. Ethington (Eds.), Concept and Models of Dolomitization. Society Economic Paleontologists Mineralogists (SEPM) Spec. Publ., 28, 87-110.

Land, L.S., 1983. The application of stable isotopes to studies of the origin of dolomites and to problems of diagenesis of clastic sediments. In: M.A. Arthur, T.F. Anderson, I.R. Kaplan, J. Veizer, L.S. Land (Eds.), Stable Isotopes in Sedimentary Geology. Society Economic Paleontologists Mineralogists (SEPM) Short Course, 10, 4.1-4.22.

Land, L.S., 1985. The origin of massive dolomite. *J. Geol. Educ.*, 33, 112-125.

Land, L.S., Hoops, G.K., 1973. Sodium in carbonate sediments: a possible index to the salinity of diagenetic fluids. *J. Sed. Petrol.*, 43, 614-617.

Land, L.S., Prezbindowski, D.R., 1981. The origin and evolution of saline formation water, Lower Cretaceous carbonates, south-central Texas, U.S.A. *J. Hydrology*, 54, 51-74.

Lapponi, F., 2007. Late burial, hydrothermal dolomitization of the Cambrian Láncara Fm., Cantabrian Zone (NW Spain): origin of the dolomitizing fluids and re-

lation to the geodynamic setting. Ph.D. thesis, University of Heidelberg, Germany, 173 pp.

Lapponi, F., Bakker, R.J., Bechstädt, T., 2007. Low temperature of natural saline fluid inclusions in saddle dolomite, Palaeozoic, NW Spain. *Terra Nova*, 19(6), 440-444.

Lapponi, F., Bechstädt, T., Boni, M., Banks, D., Schneider, J., 2014. Hydrothermal dolomitization in a complex geodynamic setting (Lower Paleozoic, northern Spain). *Sedimentology*, 61, 411–443.

Lepvrier, C., Martínez-García, E., 1990. Fault development and stress evolution of the post-Hercynian Asturian Basin (Asturias and Cantabria, northwestern Spain). *Tectonophysics*, 184, 345-356.

Llorens, T., Ruiz, I. S., Navarro, J. R. C., 2006. Petrografía de los carbones cantabrienses (Carbonífero sup) del Grupo Cea de la cuenca Guardo-Valderrueda (León-Palencia). *Geogaceta*, 40, 279-282.

Lobato, L., García-Alcalde, J.L., Sánchez de Posada, L.C., Truylos, J., Villegas, F.J., 1984. Hoja del Mapa Geológico Nacional de España (1:50000), Memoria 104 (Boñar). IGME, Madrid, 77 pp.

Lopez-Horgue, M.A., Iriarte, E., Schroder, S., Fernandez-Mendiola, P.A., Caline, B., Corneyllie, H., Fremont, J., Sudrie, M., Zerti, S., 2010, Structurally controlled hydrothermal dolomites in Albian carbonates of the Ason valley, Basque Cantabrian Basin, Northern Spain. *Marine and Petroleum Geology*, 27, 1069-1092.

Lopez-Cilla, I., Rosales, I., Gasparrini, M., Martin-Chivelet, J., 2013, Diagenesis of Lower Cretaceous platform carbonates from the northwestem margin of the Basque Cantabrian basin (norhem Spain). 30th IAS Meeting of sedimentology, Manchester, UK, .Abstracts.

Lotze, F., 1945. Zur Gliederung der Varisziden der Iberischen Meseta. *Geotekt. Forsch.*, 6, 78-92.

Lugli, S., Morteani, G., Blamart, D., 2002, Petrographic, REE, fluid inclusion and stable isotope study of magnesite from the Upper Triassic Burano Evaporites (Secchia Valley, northern Apennines): contributions from sedimentary, hydrothermal and metasomatic sources. *Mineralium Deposita*, 37, 480-494.

Lumsden, D.N., Chimahusky, J.S., 1980. Relationship between dolomite nonstoichiometry and carbonate facies parameters. In: D.H. Zenger, J.B. Dunham, R.L. Ethington (Eds.), Concepts and Models of Dolomitization. Society of Sedimentary Geology, Spec. Publ., 28, 87–110.

Luque, C., Martínez-García, E. and Ruiz, F., 1990. Metallogenesis. In: R.D.

Dallmeyer and E. Martínez- García (Eds.), Pre-Mesozoic Geology of Iberia. Springer, Berlin, 80-87.

Machel, H. G., 1985. Cathodoluminescence in calcite and dolomite and its chemical interpretation. *Geoscience Canada*, 12(4), 139–147.

Machel, H.G., 2004. Concept and models of dolomitization. In: C. J. R. Braithwaite, G. Rizzi, G. Darke (Eds.), *The Geometry and Petrogenesis of Dolomite Hydrocarbon Reservoirs*. Geological Society of London, Special Publication, 235, 7-63.

Machel, H.G., Mountjoy, E.W., 1986. Chemistry and environments of dolomitization: a reappraisal. *Earth Sci. Rev.*, 23, 9-25.

Marcos, A., 1968a. La tectónica de la Unidad de La Sobia-Bodón. Universidad de Oviedo, Trabajos de Geología, 2, 59-87.

Marcos, A., 1968b. Nota sobre el significado de la “Leon Line”. *Breviora Geológica Astúrica*, 12, 1-15.

Marcos, A., 1979. Facies differentiation caused by wrench deformation along a deep-seated fault system (León Line), Cantabrian Mountains, North Spain. Discussion. *Tectonophysics*, 60, 303-309.

Marcos, A., Pulgar, J.A., 1982. An approach to the tectonostratigraphic evolution of the Cantabrian foreland thrust and fold belt, Hercynian Cordillera of NW Spain. *Neues Jahrbuch für Geologie und Paläontologie, Abhandlungen*, 163(2), 256-260.

Marfunin, A S., 1979. Spectroscopy, luminescence and radiation centres in minerals. Springer-Verlag, Berlin, 352 pp.

Martínez Catalán, J.R., 1990. A non-cylindrical model for the northwest Iberian allochthonous terranes and their equivalents in the Hercynian belt of Western Europe. *Tectonophysics*, 179, 253-272.

Martínez Catalán, J.R., Arenas, R., Díaz García, F., Rubio Pascual, F.J., Abati, J., Marquínez, J., 1996. Variscan exhumation of a subducted Palaeozoic continental margin: the basal units of the Ordenes Complex, Galicia, NW Spain. *Tectonics*, 15, 106-121.

Martínez Catalán, J.R., Arenas, R., Díaz García, F., Abati, J., 1997. Variscan accretionary complex of Northwest Iberia, terrane correlation and succession of tectonothermal events. *Geology*, 25, 1103-1106.

Martínez Catalán, J.R., Arenas, R., Díaz García, F., González Cuadra, P., Gómez Barreiro, J., Abati, J., Castañedas, P., Fernández-Suárez, J., Sánchez Mar-

tínez, S., Andonaegui, P., González Clavijo, E., Díez Montes, A., Rubio Pascoal, F., Valle Aguado, B., 2007. Space and time in the tectonic evolution of the northwestern Iberian Massif: Implications for the Variscan Belt. In: R.D. Hatcher Jr., M.P. Carlson, J.H. McBride, J.R. Martínez Catalán, (Eds.), 4-D Framework of Continental Crust. Geologic Society of America, Boulder, 403-423.

Martínez Catalán, J.R.; Arenas, R.; Abati, J.; Sánchez Martínez, S.; Díaz García, F., Fernández Suárez, J.; González Cuadra, P., Castiñeiras P., Gómez Barreiro, J., Díez Montes A., González Clavijo, E., Rubio Pascual, F.J., Andonaegui, P., Jeffries, T.E., Alcock J.E., Díez Fernández, R., López Carmona, A., 2009. A rootless suture and the loss of the roots of a mountain chain: the Variscan belt of NW Iberia. *Comptes Rendus Geoscience*, 341, 114-126.

Martínez Catalán, J.R., Fernández-Suárez, J., Jenner, G.A., Belousova, E., Diez Montes, A., 2004. Provenance constraints from detrital zircon U-Pb ages in the NW Iberian Massif; implications for Palaeozoic plate configuration and Variscan evolution. *Journal of the Geological Society*, 161, 463-476.

Martinéz García, E., 1981. Tectónica y mineralizaciones Pérmicas en la Cordillera Cantábrica Oriental noroeste de España. *Cuadernos do Laboratorio Xeolóxico de Laxe*, 2, 263-270.

Martínez Garcia, E., 1983. El Pérmico en la Cordillera Cantábrica. In: D. C. Martínez (Ed.), Carbonífero y Pérmico de España. IGME, Madrid, pp. 389-402.

Matte, P., 1986. Tectonics and plate tectonic model for the Variscan belt of Europe. *Tectonophysics*, 126, 329-374.

Matte, P., 1991. Accretionary history and crustal evolution of the Variscan belt in western Europe. *Tectonophysics*, 196, 309-337.

Matte P., 2001. The Variscan collage and orogeny (480-290 Ma) and the tectonic definition of the Armorica microplate: a review. *Terra Nova*, 13, 122-128.

Mattes, B.W., Mountjoy, E.W., 1980. Burial dolomitization of the Upper Devonian Miette buildup, Jasper National Park, Alberta. In: D.H. Zenger, J.B. Dunham, R.L. Ethington (Eds.), Concepts and Models of Dolomitization. Society of Economic Paleontologists and Mineralogist (SEPM), Spec. Publ., 28, 259-297.

Merino, E., Canals, À., 2011. Self-accelerating dolomite-for-calcite replacement: Self-organized dynamics of burial dolomitization and associated mineralization. *American Journal of Science*, 311(7), 573-607.

Merino Tomé, O.A., Bahamonde, J.R., Colmenero, J.R.N., Villa, E., Farias P., 2009. Emplacement of the Cuera and Picos de Europa imbricate system at the core of the Iberian-Armorican Arc (Cantabrian Zone, north Spain); new precisions concerning the timing of arc closure. *Geological Society of America Bulletin*, 121(5-

6), 729-751.

Montañez, I. P., 1994. Late diagenetic dolomitization of Lower Ordovician, upper Knox carbonates: a record of the hydrodynamic evolution of the southern Appalachian Basin. *American Association of Petroleum Geologists Bull.*, 78-8, 1210-1238.

Mountjoy, E.W., Amthor, J.E., 1994. Has burial dolomitization come from age? Some answers from the Western Canada Sedimentary Basin. In: B.H. Purser, M.E. Tucker (Eds.), *Dolomites – a Volume in Honour of Dolomieu*. International Association of Sedimentologists, Special Publications, 21, 203-229.

Morrow, D.W., 1978. The influence of the Mg/Ca ratio and salinity on dolomitisation in evaporative basins. *Canadian Petroleum Geology Bulletin*, 26, 389-392.

Morrow, D. W., 1990a. Dolomite - Part 1: the chemistry of dolomitization and dolomite precipitation. In: I. A. McIlreath, D. W. Morrow (Eds.), *Diagenesis*. Geoscience Canada Reprint Series, 4, 113-124.

Morrow, D. W., 1990b. Dolomite - Part 2: dolomitization models and ancient dolostones. In: I. A. McIlreath and D. W. Morrow (Eds.), *Diagenesis*. Geoscience Canada Reprint Series, 4, 125-139.

Morrow, D.W., 1998. Regional subsurface dolomitization: models and constraints. *Geoscience Canada*, 25, 57–70.

Morrow, D. W., Cummings, G. L., Aulstead, K.L., 1990. The gas-bearing Devonian Manetoe facies, Yukon and Northwest Territories, *Geological Survey of Canada Bulletin*, 400, 267-280.

Muñoz-Quijano, I.N., Gutiérrez-Alonso, G., 2007. Modelo de evolución topográfica en el NO de la Península Ibérica durante la delaminación litosférica al final de la Orogenia Varisca. *Geogaceta*, 43, 43–46.

Nader, F. H., Lopez-Horgue, M. A., Shah, M. M., Dewit, J., Garcia, D., Swennen, R., Iriarte, E., Munchez, P., Caline, B., 2012. The Ranero hydrothermal dolomites (Albian, Karrantza Valley, Northwest Spain): Implications on conceptual dolomite models. *Oil & Gas Science and Technology–Revue d'IFP, Energies nouvelles*, 67(1), 9-29.

Nägler, T., 1990. Sm–Nd, Rb–Sr and common lead isotope geochemistry on fine-grained sediments of the Iberian Massif. Ph.D. thesis, ETH Zurich, Switzerland, 139 pp.

Nickel, E., 1978. The present status of cathode luminescence as a tool in sedimentology. *Minerals Science and Engineering*, 10(2), 73-100.

Nielsen, P., Swennen, R., Muchez, P., Keppens, E., 1998. Origin of Dinantian zebra dolomites south of the Brabant-Wales Massif, Belgium. *Sedimentology*, 45, 727–743.

Nijman W., Savage JF., 1989. Persistent basement wrenching as controlling mechanism of Variscan thin-skinned thrusting and sedimentation, Cantabrian Mountains, Spain. *Tectonophysics*, 169, 281–302.

Paniagua, A., Fontboté, L., Fenoll Hach-Alí, P., Fallick, A.E., Moreiras, D.B., Corretgé, L.G., 1993. Tectonic setting, mineralogical characteristics, geochemical signatures and age dating of a new type of epithermal carbonate-hosted, precious metal-five element deposits: the Villamanín area Cantabrian Zone, northern Spain. In: Current Research in Geology Applied to Ore Deposits, Second Biennal SGA Meeting, Granada, 531-534.

Paniagua, A., Rodríguez-Pevida, L.S., 1988. Genesis y evolución de las mineralizaciones de Cu-Co-Ni-U-Pb-Zn-Au-Ag ligadas a las estructuras tardihercinicas en el área Pajares-Villamanín-Boñar, Norte de León. *Boletín Sociedad Española de Mineralogía*, 112, 118-119.

Pastor-Galán, D., Gutiérrez-Alonso, G., Meere, P., Mulchrone, K., 2009. Factors affecting finite strain estimation in low-grade, low-strain clastic rocks. *Journal of Structural Geology*, 31, 1586-1596.

Pastor-Galán, D., Gutiérrez-Alonso, G., Weil, A. B., 2011. Orocline timing through joint analysis: insights from the Ibero-Armorican Arc. *Tectonophysics*, 5071), 31-46.

Pastor-Galán, D., Gutiérrez-Alonso, G., Weil, A. B., Fernández-Suárez, J., Johnston, S. T., Murphy, J. B., 2012a. A virtual tour of the Ibero-Armorican orocline. *Journal of the Virtual Explorer*, 43, paper 2.

Pastor-Galan, D., Gutierrez-Alonso, G., Zulauf, G., Zanella, F., 2012b. Analogue modeling of lithospheric-scale orocline buckling: constraints on the evolution of the Iberian–Armorican Arc. *Geol. Soc. Am. Bull.* 124, 1293–1309.

Pastor-Galán, D., Gutiérrez-Alonso, G., Murphy, J. B., Fernández-Suárez, J., Hofmann, M., Linnemann, U., 2013. Provenance analysis of the Paleozoic sequences of the northern Gondwana margin in NW Iberia: Passive margin to Variscan collision and orocline development. *Gondwana Research*, 23(3), 1089–1103.

Pastor-Galán, D., Martín-Merino, G., Corrochano, D., 2014. Timing and structural evolution in the limb of an orocline: The Pisuerga–Carrión Unit (southern limb of the Cantabrian Orocline, NW Spain). *Tectonophysics*, 622, 110-121.

Patterson, R.J., 1972. Hydrogeology and carbonate diagenesis on coastal sabkha in the Persian Gulf. Ph.D Thesis, Princeton University, U.S.A., 498 pp.

Pérez Estaún, A., Bastida, F., 1990. Cantabrian Zone: structure. In: R.D., Dallmeyer, E. Martínez García (Eds.), Pre-Mesozoic Geology of Iberia. Berlin, Springer-Verlag, 55-69.

Pérez-Estaún, A., Bastida, F., Alonso, J.L., Marquínez, J., Aller, J., Alvarez-Marrón, J., Marcos, A., Pulgar, J.A., 1988. A thin-skinned tectonic model for an arcuate fold and thrust belt: the Cantabrian Zone, Variscan Ibero-Armorican Arc. *Tectonics*, 7, 517-53.

Pérez Estaún, A., Martínez Catalán J.R., Bastida, F., 1991. Crustal thickening and deformation sequence in the footwall to the suture of the Variscan belt of northwest Spain. *Tectonophysics*, 191, 243-253.

Pulgar, J.A., Alonso, J.L., Espina, R.G., Marín, J.A., 1999. La deformación alpina en el basamento varisco de la Zona Cantábrica. *Trabajos de Geología*, 21, 283-294.

Purser, B. H., Tucker, M. E., Zenger, D. H., 1994. Problems, progress and future research concerning dolomites and dolomitisation. In: B. H. Purser, M. E. Tucker, D. H. Zenger (Eds.), *Dolomites - a Volume in Honour of Dolomieu*. International Association of Sedimentologists, Special Publication, 21, 3-20.

Quing, H., Mounjoy, E. W., 1994. Formation of coarsely crystalline, hydrothermal dolomite reservoir in the Presqu'ile Barrier, western Canada Sedimentary Basin. *American Association of Petroleum Geologists Bull.*, 78-1, 55-77.

Randazzo, A.F., Zachos, L.G., 1984. Classification and description of dolomitic fabrics of rocks from the Floridan aquifer, USA. *Sedimentary Geology*, 37, 151-162.

Raven, J.G.M., Van der Pluijm, B.A., 1986. Metamorphic fluids and transtension in the Cantabrian Mountains of northern Spain: an application of the conodont colour alteration index. *Geological Magazine*, 123(6), 673-681.

Reuther, C.D. 1977. Das Namur im südlichen Kantabrischen Gebirge (Nordspanien). Krustenbewegungen und Faziesdifferenzierung im Übergang Geo-synklinale-Orogen. *Clausthaler Geologische Abhandlungen*, 28, 122 pp.

Reuther, C.D., 1982. The Lower Carboniferous facies levelling and the first Upper Carboniferous tectonic events in the Cantabrian Mountains and the Pyrenees, Spain - a comparison. In: J. Kullmann, R. Schönenberg, J. Wiedmann (Eds.), *Subsidenz-Entwicklung im Kantabrischen Variszikum und an passiven Kontinentalrändern der Kreide*. *Neues Jahrbuch für Geologie und Paläontologie*, 163(2), 244-250.

Ries, A.C., Shackleton, R.M., 1976. Pattern of strain variation in arcuate fold belts. *Philosophical Transactions of the Royal Society of London, Series A, Mathematical and Physical Sciences*, 283, 121-138.

matical and Physical Sciences, 283, 281-288.

Rodríguez, J., Cosca, M.A., Gil Ibarguchi J.I., Dallmeyer, R.D., 2003. Strain partitionning and preservation of $^{40}\text{Ar}/^{39}\text{Ar}$ ages during Variscan exhumation of a subducted crust, Malpica-Tui Complex, NW Spain. *Lithos*, 70, 111-139.

Rodríguez Fernández, L.R., 1983. Evolución estructural de la Zona Cantábrica durante el Carbonífero. In: C. Martínez Díaz (Ed.), Carbonífero y Pérmico de España, X Inter. Congr. Carbonif. Perm. Stratigr. Geol., Madrid, IGME, 1, 151-162.

Roedder, E., 1984. Fluid inclusions. *Reviews in Mineralogy*, 12. Min. Soc. America, Chelsea, 644 pp.

Rossi P., Cocherie A., Fanning M., Deloule E., 2006. Variscan to eo-Alpine events recorded in European lower-crust zircons sampled from the French Massif Central and Corsica, France. *Lithos*, 87, 235–260.

Sánchez de la Torre, L., Águeda, J.A., Colmenero, J.R., García-Ramos, J.C., González Lastra, J., 1983. Evolución sedimentaria y paleogeográfica del Carbonífero en la Cordillera Cantábrica. In: C. Martínez Díaz (Ed.), Carbonífero y Pérmico de España, X Inter. Congr. Carbonif. Perm. Stratigr. Geol., Madrid, IGME, 1, 133-150.

Shepherd, T.J., Rankin, A.H., Alderton, D.H.M., 1985. A practical guide to fluid inclusion studies. Blackie & Son, Glasgow, 239 pp.

Schneider, J., 2000. Indirekte Rb-Sr-Chronometrie postorogener Hydrothermalsysteme und assoziierter Gangmineralisationen im Rhenohercynikum. Ph.D. thesis, Justus-Liebig-Universität Giessen, Germany, 162 pp.

Schneider, J., Bakker, R.J., Bechstädt, T., Littke, R., 2008. Fluid evolution during burial diagenesis and subsequent uplift: the La Vid Group (Cantabrian Zone, NW-Spain). *J. Sed. Res.*, 78(4), 282-300.

Shah, M. M., Nader, F. H., Garcia, D., Swennen, R., Ellam, R., 2012. Hydrothermal dolomites in the Early Albian (Cretaceous) platform carbonates (NW Spain): nature and origin of dolomites and dolomitising fluids. *Oil & Gas Science and Technology–Revue d’IFP Energies nouvelles*, 67(1), 97-122.

Shaw, J., Johnston, S. T., Gutiérrez-Alonso, G., Weil, A. B., 2012. Oroclines of the Variscan orogen of Iberia: Paleocurrent analysis and paleogeographic implications. *Earth and Planetary Science Letters*, 329, 60-70.

Sibley, D.F., Gregg, J.M., 1987. Classification of dolomite rock textures. *J. Sed. Petrol.*, 57(6), 967-975.

Sibson, R. H., 2000. Fluid involvement in normal faulting. *J. of Geodyn.*, 29, 469–499.

Smalley, P.C., Higgins, A.C., Howarth, R.J., Nicholson, H., Jones, C.E., Swinburne, N.H.M., Bessa, J., 1994. Seawater Sr isotope variations through time: a procedure for constructing a reference curve to date and correlate marine sedimentary rocks. *Geology*, 22, 431–434.

Spencer-Cervato, C., Mullis, J., 1992. Chemical study of tectonically controlled hydrothermal dolomitization: an example from the Lessini Mountains, Italy. *Geol. Rundsch.*, 81(2), 347-370.

Spötl, C., Pitman, J.K., 1998. Saddle (baroque) dolomite in carbonates and sandstones: a reappraisal of a burial-diagenetic concept. In: S. Morad (Ed.), *Carbonate Cementation in Sandstones: Distribution Patterns and Geochemical Evolution*. International Association of Sedimentologists, Special Publication 26, 437–460.

Swennen, R., Dewit, J., Fierens, E., Muchez, P., Shah, M., Nader, F., Hunt, D., 2012. Multiple dolomitization events along the Pozalagua Fault (Pozalagua Quarry, Basque–Cantabrian Basin, Northern Spain). *Sedimentology*, 59(4), 1345–1374.

Symons, D. T., Lewchuk, M. T., Kawasaki, K., Velasco, F., Leach, D. L., 2009. The Reocín zinc–lead deposit, Spain: paleomagnetic dating of a late Tertiary ore body. *Mineralium Deposita*, 44(8), 867-880.

Taylor, T. R., Sibley, D. F., 1986. Petrographic and geochemical characteristics of dolomite types and the origin of ferroan dolomite in the Trenton Formation, Ordovician, Michigan Basin, USA. *Sedimentology*, 33(1), 61-86.

Tiab, D., Donaldson, E. C., 2011. *Petrophysics: theory and practice of measuring reservoir rock and fluid transport properties*. Gulf Professional Publishing. 910 pp.

Tornos, F., Spiro, B.F., 2000. The geology and isotope geochemistry of the talc deposits of Puebla de Lillo (Cantabrian Zone, Northern Spain). *Economic Geology*, 95, 1277-1296.

Torsæter, O., Abtahi, M., 2003. Experimental reservoir engineering laboratory work book. Department of Petroleum Engineering and Applied Geophysics, Norwegian University of Science and Technology (NTNU), Trondheim, 107 pp.

Tucker, M.E., Wright, V.P., 1990 *Carbonate Sedimentology*, Blackwell, Oxford. 482 pp.

Vahrenkamp, V.C., Swart, P.K., 1990. New distribution coefficient for the incorporation of strontium into dolomite and its implications for the formation of ancient dolomites. *Geology*, 18(5), 387-391.

Van der Voo, R., Stamatakos J.A., Parés, J.M., 1997. Kinematic constraints

on thrust-belt curvature from syndeformational magnetizations in the Lagos del Valle syncline in the Cantabrian Arc, Spain. *Journal of Geophysical Research*, 102, 10105-10119.

Veselovsky, Z., Bechstädt, T., Zühlke, R., 2008. Structural, reverse basin and forward stratigraphic modelling of the Southern Cantabrian Basin, NW-Spain.- In: P. L. de Boer, G. Postma, C.J. van der Zwan P., P.M. Burgess, P. Kukla (Eds.), Analogue and Numerical Forward Modelling of Sedimentary Systems; from Understanding to Prediction. *Intern. Ass. Sedimentol., Spec. Publ.* 40, 65-96.

Velasco, F., Herrero, J. M., Gil, P. P., Alvarez, L., Yusta, I., 1994. Mississippi Valley-type, sedex, and iron deposits in Lower Cretaceous rocks of the Basque-Cantabrian basin, northern Spain. In: L. Fontboté, M. Boni (Eds.), *Sediment-Hosted Zn-Pb Ores*, Special Publication of the Society for Geology Applied to Mineral Deposits, 10, Springer Berlin Heidelberg, 246-270.

Velasco, F., Herrero, J. M., Yusta, I., Alonso, J. A., Seibold, I., Leach, D., 2003. Geology and geochemistry of the Reocín zinc-lead deposit, Basque-Cantabrian basin, Northern Spain. *Economic Geology*, 98(7), 1371-1396.

Velasco, F., Pesquera, A., Arce, R., Olmedo, F., 1987, A contribution to the ore genesis of the magnesite deposit of Eugui, Navarra (Spain). *Mineralium Deposita*, 22, 33-41.

Wagner, R.H., Winkler Prins, C.F., Riding, R.E., 1971. Lithostratigraphic units of the lower part of the Carboniferous in northern León, Spain. *Trabajos de Geología*, 4, 603-663.

Wardlaw, N.C., 1996. Factors affecting oil recovery from carbonate reservoirs and prediction of recovery. In: G.V. Chilingarian, S.J. Mazzullo, H.H. Rieke (Eds.), *Carbonate Reservoir Characterization: A Geologic-Engineering Analysis, Part II. Developments in Petroleum Science*, 44. Elsevier, Amsterdam, 867–903.

Weil A., Gutiérrez-Alonso G., Conan J., 2010. New time constraints on lithospheric-scale oroclinal bending of the Ibero-Armorian Arc: a palaeomagnetic study of earliest Permian rocks from Iberia. *Journal of the Geological Society*, 167, 127-143.

Weil, A.B., Gutiérrez-Alonso, G., Johnston, S.T., Pastor-Galán, D., 2013a. Kinematic constraints on buckling a lithospheric-scale orocline along the northern margin of Gondwana: A geologic synthesis. *Tectonophysics*, 582, 25-49.

Weil, A.B., Gutiérrez-Alonso, G., Wicks, D., 2013b. Investigating the kinematics of local thrust sheet rotation in the limb of an orocline: a paleomagnetic and structural analysis of the Esla tectonic unit, Cantabrian–Asturian Arc, NW Iberia. *Int. J. Earth Sci.*, 102, 43–60.

Weil, A.B., Van der Voo, R., Van der Pluijm B.A., Parés, J.M., 2000. The formation of an orocline by multiphase deformation: a paleomagnetic investigation of the Cantabria-Asturias Arc, northern Spain. *Journal of Structural Geology*, 22, 735-756.

Weil, A.B., Van der Voo, R., 2002. Insights into the mechanism for orogen-related carbonate remagnetization from growth of authigenic Fe-oxide: A scanning electron microscopy and rock magnetic study of Devonian carbonates from northern Spain. *Journal of Geophysical Research*, 107(B4), p. 2063.

Wendt, J., Aigner, T., 1985. Facies patterns and depositional environments of Palaeozoic cephalopod limestones. *Sedimentary Geology*, 44, 263-300.

Wilkinson, J.J., Jenkin, G.R.T., Fallick, R.P., Foster, R.P., 1995. Oxygen and hydrogen isotopic evolution of Variscan crustal fluids, south Cornwall, U.K. *Chemical Geology*, 123, 239-254.

Wilson, E.N., Lawrence, A.H., Philips, O.M., 1990. Dolomitization front geometry, fluid flow patterns, and the origin of massive dolomite: the Triassic Latemar buildup, northern Italy. *Am. J. Sci.*, 290, 741-796.

Woody, R. E., Gregg, J. M., Koederitz, L. F., 1996. Effect of texture on petrophysical properties of dolomite: evidence from the Cambrian-Ordovician of southeastern Missouri. *American Association of Petroleum Geology Bulletin*, 80(1), 119-131.

Yui, T. F., Gong, S. Y., 2003. Stoichiometry effect on stable isotope analysis of dolomite. *Chemical Geology*, 201(3), 359-368.

**ANNEX 1
DIGITAL FILE ATTACHMENT
GEOLOGICAL AND DOLOMITE DISTRIBUTION MAP**

ANNEX 2
MACROSCOPIC DESCRIPTION

Locality	Section Number	Sample Number	Colour	Formation	Lithology	Macro Aspect			Structures and Porosity						Pore Shape	Pore Filling	General Remarks									
						Crystal Size			Zebra			Non macroporous														
						Banded	Massive	Breccia	Fine	Medium	Coarse	Micro	Meso	Vuggy	fine	coarse	Breccia	Small <5mm	Medium 5-10mm	Large >10mm	Scattered	Aligned	Rounded	Elongated	Angular	
Caldas de L.	XXI	91	Pink+White	Vallencia Fm.	Dolomite	X				X							X	X			X					
Caldas de L.	XXI	92	Grey	Vallencia Fm.	Dolomite		X			X							X		X							Microfractures
Caldas de L.	XXI	93	Grey+White	Vallencia Fm.	Dolomite		X			X							X				X					Chevron Zebra
Caldas de L.	XXI	94	Grey	Vallencia Fm.	Dolomite		X			X						X										Microfractures, Stylobates
Rabledo de C.	XXXII	95	White	Vallencia Fm.	Dolomite		X			X																
Rabledo de C.	XXXII	96	White+Grey	Vallencia Fm.	Dolomite		X			X							X		X		X					Calcite
Sera de Luna	XXXIII	97	Grey+White	Vallencia Fm.	Dolomite		X			X							X		X							Microfractures
Sera de Luna	XXXIII	98	Grey	Vallencia Fm.	Dolomite		X			X						X		X			X					
Sera de Luna	XXXIII	99	Reddish	Vallencia Fm.	Dolomite		X			X						X		X			X					
Sera de Luna	XXXIII	100	Yellow	Vallencia Fm.	Dolomite		X			X						X		X			X					
Villalba	XIX	101	Pink	Vallencia Fm.	Dolomite		X			X						X		X			X					
Villalba	XIX	102	Yellow	Vallencia Fm.	Dolomite		X			X						X		X			X					
San Emiliano	XXXIV	103	Pink+Grey	Barcaliente Fm.	Dolomite		X			X						X		X			X					Perpendicular Microzona
San Emiliano	XXXIV	104	Pink	Barcaliente Fm.	Dolomite		X			X						X		X			X					Microzona, Fractures
San Emiliano	XXXIV	106	Yellow	Barcaliente Fm.	Dolomite		X			X						X		X			X					Chevron Microzona
San Emiliano	XXXIV	107	Pink+Grey	Barcaliente Fm.	Dolomite		X			X						X		X			X					
San Emiliano	XXXIV	108	Pink	Barcaliente Fm.	Dolomite		X			X						X		X			X					Microzona repeat
San Emiliano	XXXIV	109	Pink	Barcaliente Fm.	Dolomite		X			X						X		X			X					Microzona
San Emiliano	XXXIV	110	Pink	Barcaliente Fm.	Dolomite		X			X						X		X			X					Micro pores
San Emiliano	XXXIV	111	Pink	Barcaliente Fm.	Dolomite		X			X						X		X			X					Pores filled
San Emiliano	XXXIV	112	Pink	Vallencia Fm.	Dolomite		X			X						X		X			X					Stylobates
San Emiliano	XXXIV	113	Pink	Vallencia Fm.	Dolomite		X			X						X		X			X					Fractures, Veins
San Emiliano	XXXIV	114	Pink	Vallencia Fm.	Dolomite		X			X						X		X			X					
San Emiliano	XXXIV	115	Pink	Vallencia Fm.	Dolomite		X			X						X		X			X					
Villarino	XXV	116	Beige	Vallencia Fm.	Dolomite		X			X						X		X			X					
S. Emiliano 2	XXXVI	118	Pink+Grey	Barcaliente Fm.	Dolomite		X			X						X		X			X					
S. Emiliano 2	XXXVI	119	Grey	Barcaliente Fm.	Dolomite		X			X						X		X			X					
S. Emiliano 2	XXXVI	120	Grey	Barcaliente Fm.	Dolomite		X			X						X		X			X					
Salencia	XXXVII	121	Grey	Caliza Morata Fm.	Dolomite		X			X						X		X			X					
Salencia	XXXVII	122	Grey	Caliza Morata Fm.	Dolomite		X			X						X		X			X					Lamination
Salencia	XXXVII	123	Grey	Caliza Morata Fm.	Dolomite		X			X						X		X			X					
Salencia	XXXVII	124	Mottled	Caliza Morata Fm.	Dolomite		X			X						X		X			X					
Salencia	XXXVII	125	Pink	Caliza Morata Fm.	Dolomite		X			X						X		X			X					
Salencia	XXXVII	126	Pink	Caliza Morata Fm.	Dolomite		X			X						X		X			X					
Salencia	XXXVII	127	Pink	Caliza Morata Fm.	Dolomite		X			X						X		X			X					
Salencia	XXXVII	129	Grey+White	Caliza Morata Fm.	Dolomite		X			X						X		X			X					
Salencia	XXXVII	130	Grey	Reddish	Caliza Morata Fm.		X			X						X		X			X					
Salencia	XXXVII	131	Grey	Caliza Morata Fm.	Dolomite		X			X						X		X			X					
Salencia	XXXVII	132	Grey	Caliza Morata Fm.	Dolomite		X			X						X		X			X					
Salencia	XXXVII	133	Grey	Caliza Morata Fm.	Dolomite		X			X						X		X			X					
Salencia	XXXVII	134	Reddish	Caliza Morata Fm.	Dolomite		X			X						X		X			X					
Salencia	XXXVII	135	Reddish	Caliza Morata Fm.	Dolomite		X			X						X		X			X					
Salencia	XXXVII	136	Grey	Red/Pink	Caliza Morata Fm.		X			X						X		X			X					
Salencia	XXXVII	137	Red/Pink	Caliza Morata Fm.	Dolomite		X			X						X		X			X					
Salencia	XXXVII	138	Pink	Caliza Morata Fm.	Dolomite		X			X						X		X			X					
Salencia	XXXVII	139	White	Caliza Morata Fm.	Dolomite		X			X						X		X			X					

Locality	Section Number	Sample Number	Colour	Formation	Lithology	Macro Aspect			Crystal Size			Structures and Porosity			Pores distribution			Pore Shape			General Remarks								
						Banded			Massive			Brecchia			Zebra			Vuggy			Non macroporous								
						Fine	Medium	Coarse	Micro	Meso	Macro	fine	coarse	Brassica	fine	coarse	Brassica	fine	coarse	Brassica	fine	coarse	Small	Medium	Large	>10 mm	Scattered	Aligned	Rounded
Salencia	XXVII	140	Pink	Caliza Morana	Dolomite	x						x			x			x			x			x					
Pedraira	XXVIII	141	Grey	Valedesja Fm.	Dolomite	x			x			x			x			x			x			x					
Pedraira	XXIX	142	Grey	Valedesja Fm.	Dolomite		x		x			x			x			x			x			x					
Pedraira	XXX	143	Grey	Valedesja Fm.	Dolomite		x		x			x			x			x			x			x					
Pedraira	XXXI	144	Grey	Valedesja Fm.	Dolomite		x		x			x			x			x			x			x					
Viadango	XXXII	145	Grey	Valedesja Fm.	Dolomite	x			x			x			x			x			x			x					
Viadango	XXXIII	146	Grey	Valedesja Fm.	Dolomite	x			x			x			x			x			x			x					
Viadango	XXXIV	147	Grey	Valedesja Fm.	Dolomite	x			x			x			x			x			x			x					
Viadango	XXXV	148	Grey	Valedesja Fm.	Dolomite	x			x			x			x			x			x			x					
Viadango	XXXVI	149	Grey	Valedesja Fm.	Dolomite	x			x			x			x			x			x			x					
Viadango	XXXVII	150	Grey	Valedesja Fm.	Dolomite	x			x			x			x			x			x			x					
Viadango	XXXVIII	151	Grey	Valedesja Fm.	Dolomite	x			x			x			x			x			x			x					
Viadango	XXXIX	152	Matte	Valedesja Fm.	Dolomite	x			x			x			x			x			x			x					
Viadango	XXXX	153	Grey	Valedesja Fm.	Dolomite	x			x			x			x			x			x			x					
Viadango	XXXI	154	Pink	Valedesja Fm.	Dolomite	x			x			x			x			x			x			x					
Viadango	XXXII	155	Pink	Valedesja Fm.	Dolomite	x			x			x			x			x			x			x					
Viadango	XXXIII	156	Pink	Valedesja Fm.	Dolomite	x			x			x			x			x			x			x					
Viadango	XXXIV	157	Pink	Valedesja Fm.	Dolomite	x			x			x			x			x			x			x					
Viadango	XXXV	158	Matte	Valedesja Fm.	Dolomite	x			x			x			x			x			x			x					
Viadango	XXXVI	159	Matte	Valedesja Fm.	Dolomite	x			x			x			x			x			x			x					
Viadango	XXXVII	160	Pink+Red	Valedesja Fm.	Dolomite	x			x			x			x			x			x			x					
Viadango	XXXVIII	161	Matte	Valedesja Fm.	Dolomite	x			x			x			x			x			x			x					
Viadango	XXXIX	162	Matte	Valedesja Fm.	Dolomite	x			x			x			x			x			x			x					
Saint del T.	XXXI	163	Pink	Barcaliente Fm.	Dolomite	x			x			x			x			x			x			x					
Saint del T.	XXXII	164	Grey+White	Barcaliente Fm.	Dolomite	x			x			x			x			x			x			x					
Saint del T.	XXXIII	165	Grey+White	Barcaliente Fm.	Dolomite	x			x			x			x			x			x			x					
Saint del T.	XXXIV	166	Grey+White	Barcaliente Fm.	Dolomite	x			x			x			x			x			x			x					
Saint del T.	XXXV	167	Grey+Pink	Barcaliente Fm.	Dolomite	x			x			x			x			x			x			x					
Saint del T.	XXXVI	168	Grey+White	Barcaliente Fm.	Dolomite	x			x			x			x			x			x			x					
Saint del T.	XXXVII	169	Grey	Barcaliente Fm.	Dolomite	x			x			x			x			x			x			x					
Saint del T.	XXXVIII	170	Grey	Barcaliente Fm.	Dolomite	x			x			x			x			x			x			x					
Saint del T.	XXXIX	171	Grey+Beige	Barcaliente Fm.	Dolomite	x			x			x			x			x			x			x					
Saint del T.	XXXI	172	Grey+Red	Barcaliente Fm.	Dolomite	x			x			x			x			x			x			x					
Saint del T.	XXXII	173	Grey+White	Barcaliente Fm.	Dolomite	x			x			x			x			x			x			x					
Saint del T.	XXXIII	174	White+Grey	Barcaliente Fm.	Dolomite	x			x			x			x			x			x			x					
Saint del T.	XXXIV	175	Pink	Barcaliente Fm.	Dolomite	x			x			x			x			x			x			x					
Saint del T.	XXXV	176	White+Grey	Barcaliente Fm.	Dolomite	x			x			x			x			x			x			x					
Saint del T.	XXXVI	177	White+Grey	Barcaliente Fm.	Dolomite	x			x			x			x			x			x			x					
Saint del T.	XXXVII	178	Beige	Barcaliente Fm.	Dolomite	x			x			x			x			x			x			x					
Saint del T.	XXXVIII	179	Grey	Barcaliente Fm.	Dolomite	x			x			x			x			x			x			x					
Saint del T.	XXXIX	180	Grey	Barcaliente Fm.	Dolomite	x			x			x			x			x			x			x					
Briña	v	181	Pink	Valedesja Fm.	Dolomite	x			x			x			x			x			x			x					
Briña	v	182	Pink	Valedesja Fm.	Dolomite	x			x			x			x			x			x			x					
Briña	v	183	Pink	Valedesja Fm.	Dolomite	x			x			x			x			x			x			x					

Locality	Section Number	Sample Number	Colour	Formation	Lithology	Macro Aspect			Structures and Porosity						Pore Shape				General Remarks				
						Crystal Size			Zebra			Vuggy			Non macro por.			Pore distribution					
						Banded	Massive	Brecia	Fine	Medium	Coarse	Micro	Meso	Coarse	fine	coarse	Breccia	Small <5mm	Medium 5-10 mm	Large >10 mm	Elongated	Rounded	
Salamón	X.L	236	Gris	Los-Ogíenes Fm.	Dolomite	X	X							X			X	X				Calcite	Completely filled
Salamón	X.L	237	Redish	Los-Ogíenes Fm.	Dolomite	X	X							X			X	X				Sulfate	Data C?
Salamón	X.L	239	Dark Grey	Los-Ogíenes Fm.	Dolomite	X	X							X									
Salamón	X.L	241	Grey	Los-Ogíenes Fm.	Dolomite	X								X									
Salamón	X.L	242	Rosa	Los-Ogíenes Fm.	Dolomite	X	X							X			X					Calcite	
Salamón	X.L	243	Beige	Los-Ogíenes Fm.	Dolomite	X	X							X			X					Sulfate	
Salamón	X.L	244	Dark reddish	Los-Ogíenes Fm.	Dolomite	X	X							X			X					Sulfate	
Piedrascha	XXXVII	245	G-B	Bucalcáñer Fm.	Dolomite	X								X			X					Lander	
Piedrascha	XXXVIII	246	G-B	Bucalcáñer Fm.	Dolomite	X								X			X					Z.P.B	
Cueta	XXXIX	247	G-B	Portillo Fm.	Dolomite	X								X			X					Portilla Formation	
Cueta	XXXIV	248	yellow	Portillo Fm.	Dolomite	X								X			X					Tardopozo PF	
Cacabello	XXXVI	250	Rosa	Santa Lucía Fm.	Dolomite	X								X			X					Santa Lucia	
Cacabello	XXXVII	251	GR	Santa Lucía Fm.	Dolomite	X								X			X					Extinct reef	
Cacabello	XXXVII	252	R-B	Santa Lucía Fm.	Dolomite	X								X			X					Santa Lucia	
Cacabello	XXXVII	253	R-B	Santa Lucía Fm.	Dolomite	X								X			X					Santa Lucia	
Cueta II	XXXV	255	Grey	Caliza Monzónia Fm.	Dolomite	X								X			X					Muy fina	
Cueta II	XXXV	257	G-W	Caliza Monzónia Fm.	Dolomite	X								X			X					All filled	
Cueta II	XXXV	258	G-W-R	Caliza Monzónia Fm.	Dolomite	X								X			X					Z.P.B	
Cueta II	XXXV	259	Grey	Caliza Monzónia Fm.	Dolomite	X								X			X					All filled	
Cueta II	XXXV	260	G-P	Caliza Monzónia Fm.	Dolomite	X								X			X					Z.B	
Cueta II	XXXV	261	Pink	Caliza Monzónia Fm.	Dolomite	X								X			X					Calcareous cemented	
Cueta II	XXXV	262	Grey	Caliza Monzónia Fm.	Dolomite	X								X			X					Calcareous cemented	
Cueta II	XXXV	263	G-W	Caliza Monzónia Fm.	Dolomite	X								X			X					Sandie Braun	
Cueta II	XXXV	264	G-P+B	Caliza Monzónia Fm.	Dolomite	X								X			X					microporous	
San Emilio	XXXV	265	Y-G	Valldejúcar Fm.	Dolomite	X								X			X					3 Types	
Vélez	XXXVI	266	Y-G	Valldejúcar Fm.	Dolomite	X								X			X					Lander	
Vélez	XXXVII	267	P-Y	Valldejúcar Fm.	Dolomite	X								X			X					Lander	
Vélez	XXXVII	268	P-Y	Valldejúcar Fm.	Dolomite	X								X			X					Lander, cemented	
Vélez	XXXVII	269	P-Y	Valldejúcar Fm.	Dolomite	X								X			X					Cemented	
Vélez	XXXVII	270	Grey	Valldejúcar Fm.	Dolomite	X								X			X					Cemented	
Vélez	XXXVII	272	Grey	Valldejúcar Fm.	Dolomite	X								X			X					Cemented	
V. Lago	XXXII	273	Grey	Caliza Monzónia Fm.	Dolomite	X								X			X						
V. Lago	XXXII	274	G-P+Y	Caliza Monzónia Fm.	Dolomite	X								X			X					Z.I.B	
V. Lago	XXXII	275	Pink	Caliza Monzónia Fm.	Dolomite	X								X			X					Calcite	
V. Lago	XXXII	276	P+G	Caliza Monzónia Fm.	Dolomite	X								X			X					Breccia	
Májiva	XXXII	277	Pink	Caliza Monzónia Fm.	Dolomite	X								X			X					Calcareous cemented	
Májiva	XXXII	278	G-P	Caliza Monzónia Fm.	Dolomite	X								X			X					Cemented	
Májiva	XXXII	279	P+Y+R	Caliza Monzónia Fm.	Dolomite	X								X			X					Z.P.B	
Májiva	XXXII	280	Grey	Caliza Monzónia Fm.	Dolomite	X								X			X					Cemented	
Májiva	XXXII	281	G-P	Caliza Monzónia Fm.	Dolomite	X								X			X						
Májiva	XXXII	282	Grey	Caliza Monzónia Fm.	Dolomite	X								X			X					Microbreccia esparsa	
Májiva	XXXII	283	Pink	Caliza Monzónia Fm.	Dolomite	X								X			X						
Salamón II	X.L	284	Pink	Caliza Monzónia Fm.	Dolomite	X								X			X					Z.I.B	
Salamón II	X.L	285	G-P	Caliza Monzónia Fm.	Dolomite	X								X			X					Cemented	
Salamón II	X.L	286	G-P	Caliza Monzónia Fm.	Dolomite	X								X			X					Cemented	
Salamón II	X.L	287	Grey	Caliza Monzónia Fm.	Dolomite	X								X			X						
Salamón II	X.L	288	Grey	Caliza Monzónia Fm.	Dolomite	X								X			X						

ANNEX 3
PETROGRAPHIC DESCRIPTION

ANNEX 4
CATHODOLUMINESCENCE DESCRIPTION

Section Number	Locality	Sample Number	MINERAL COMPOSITION						LUMINESCENCE						General remarks
			Dol A1	Dol A2	Dol B1	Dol B2	Dol Cal 1	Dol Cal 2	Calcite phases	Others	Dull red unzoned (%)	Zonated dark red (%)	Bright orange unzoned or slightly (%)	Intense concentric zonation bio (%)	Others (%)
I	Colinal	2	x	x	x	x	x	x		70	25	4	1		Dark Red
I	Colinal	3	x	x	x	x	x	x		70	20	5	5		Dark Red
I	Colinal	4			x	x	x	x	x	50		48			Oxides, Dark red Dol A
I	Colinal	6	x	x	x	x	x	x		70	20	5	5		Oxides, Dark red Dol A
II	Sona	10	x	x	x	x	x	x		60	25	10	5		Ct in fractures, dark red DolA
II	Sona	12	x	x	x	x	x	x		75	20	5	5		Dark Red
II	Sona	13	x	x	x	x	x	x		55	45				Dark Red
II	Sona	15	x	x	x	x	x	x		75	20	5	5		Dark Red
II	Sona	17	x	x	x	x	x	x		50	25				Micrite, lithics
II	Sona	18	x	x	x	x	x	x		80	15	4	1		Dark Red
IX	Nina Talco	23	x	x	x	x	x	x		70	10	5	5		Talc
IX	Nina Talco	24	x	x	x	x	x	x		75	15				Talc
IX	Nina Talco	25	x	x	x	x	x	x		70	25	3	2		Talc
X	Nina Talco	26	x	x	x	x	x	x		65	30	3	2		Talc
III	Llamazales	27	x	x	x	x	x	x		70	20	10	2		Calcite filled pores and fractures
IV	Uqueros	28	x	x	x	x	x	x		80	15	3	2		Some pores filled with C2
V	Parrilla	29	x	x	x	x	x	x		40	30	25	5		2 fluids? 1 so dark red, Breccia veins
XVIII	Fabanal	82	x	x	x	x	x	x		90		5	5		Crinoids, Dark red mottled
XVIII	Fabanal	84	x	x	x	x	x	x		98		2	2		Small sizes crystals
XIX	Villafeliz	85	x	x	x	x	x	x		98		2	2		Small sizes crystals, elongated porosity
XIX	Villafeliz	86	x	x	x	x	x	x		98		2	2		Luminiscence uniform
XXII	Frobledo de C	95	x	x	x	x	x	x			2				black
XXII	Frobledo de C	96	x	x	x	x	x	x			2				black
XXII	Frobledo de C	97	x	x	x	x	x	x			2				black
XXIII	Sena de L.	98	x	x	x	x	x	x		60	15	2	8		Diferents fluids? Dedolomitized?
XXIII	Sena de L.	99	x	x	x	x	x	x		90		10			Crinoids, Dark red DolA
XXIII	Sena de L.	100	x	x	x	x	x	x		95		5			Fossils, Hydronactites filled with black material nonluminous
XXIV	San Emiliano	104	x	x	x	x	x	x		80	5	15	2		2 fluids? 1 so dark red, other dark yellow
XXIV	San Emiliano	105	x	x	x	x	x	x		95		5			Contact limit
XXVI	San Emiliano	107	x	x	x	x	x	x		100					Uniform Luminiscence

Section Number	Locality	Sample Number	MINERAL COMPOSITION							LUMINESCENCE										General remarks								
			Dolomite A			Dolomite B		Calcite phases		Others			Dull red unzoned (%)			Zonated dark red (%)			Bright orange unzoned or yellow (%)			Intense concentric zonation bio (%)			Others (%)			
			Dol A1	Dol A2	Dol B1	Cal 1	Cal 2	Others	0-25	26-50	51-75	76-100	0-25	26-50	51-75	76-100	0-25	26-50	51-75	76-100	0-25	26-50	51-75	76-100	0-25	26-50	51-75	
XXIV	San Emiliano	108	x	x	x	x	x						70															
XXIV	San Emiliano	111	x	x	x	x	x						75	15														2 Fluids?
XXIV	San Emiliano	113	x	x	x	x	x						70	20														Pores completely filled
XXIV	San Emiliano	115	x	x	x	x	x						95															Fossils
XXVI	S. Emiliano 2	118	x	x	x	x	x						60	25														All pores are filled
XXVI	S. Emiliano 2	119	x	x	x	x	x						80															Breccia, filled with dull orange material
XXVI	S. Emiliano 2	120	x	x	x	x	x						80	5														2 Fluids?
XXVII	Salencia	121	x	x	x	x	x						90	10														Dolomite Dull orange-red
XXVII	Salencia	124	x	x	x	x	x						75	10														Hydrofractures C2 cement,
XXVII	Salencia	125	x	x	x	x	x						60	10														Pores completely filled C1 y C2
XXVII	Salencia	137	x	x	x	x	x						90															Styloites, oxides, slight variations in red color luminescence
XXVII	Salencia	138	x	x	x	x	x						90															Styloites, oxides, slight variations in red color luminescence
XXVII	Salencia	139	x	x	x	x	x						95	8													Slight variations in red color luminescence	
XXVIII	Foladura	141	x	x	x	x	x						85	10													Oxides, slight variations in red color luminescence	
XXVIII	Foladura	143	x	x	x	x	x						90	5													Styloites, oxides	
XXIX	Viadango	146	x	x	x	x	x						85	8													C1 filled fractures, oxides, fossils	
XXX	Viadango	148	x	x	x	x	x						60														Oxides, slight variations in red color luminescence	
XXX	Viadango II	154	x	x	x	x	x						60	20													C1 filled fractures, oxides	
XXX	Viadango II	155	x	x	x	x	x						70														Crystallomorphic (dedolomitized?)	
XXX	Viadango II	156	x	x	x	x	x						90														Breccia? Matrix dull orange luminescence	
XXX	Viadango II	157	x	x	x	x	x						90														Fractures filled C2	
XXX	Viadango II	158	x	x	x	x	x						90	5													Slight variations in red color luminescence	
XXX	Viadango II	161	x	x	x	x	x						90	5													Slight variations in red color luminescence	
XXX	Viadango II	162	x	x	x	x	x						80														C1 filled fractures, oxides	
XXXI	Sierra del T.	163	x	x	x	x	x						80														Breccia, fragments calcite	
XXXI	Sierra del T.	167	x	x	x	x	x						80	10													maybe Dol C, more dark luminescence, stylolites	
XXXI	Sierra del T.	168	x	x	x	x	x						70	25													Big Porosity, Saddle dolomite slight variations luminescence	
XXXI	Sierra del T.	173	x	x	x	x	x						75	15													Slight variations in red color luminescence	

Section Number	Locality	Sample Number	MINERAL COMPOSITION						LUMINESCENCE						General remarks			
			Dolomite A	Dolomite B	Calcite phases	Others	Dull red unzoned (%)	Zonated dark red (%)	Bright orange unzoned or light (%)	Intense concentric zonation ble (%)	26-50	51-75	76-100	0-25	26-50	51-75		
XXXI	Sierra del T.	175	x	x	x		0-25	26-50	51-75	76-100	0-25	26-50	51-75	76-100	0-25	26-50	51-75	76-100
V	Eraña	186	x	x	x			80	15									
III	Jamazales	202	x	x	x			80	5									
IV	Luguieros	203	x	x	x			60		30	10							
XVIII	Rabanal	216	x	x	x			80	15		5							
XXV	Villancino	219	x	x	x			90	8									
XXV	Villancino	220	x	x	x			80	5		15							
XXXIX	Cremenes	229	x	x	x			90	10									
XXXIX	Cremenes	230	x	x	x			95			5							
XXXIX	Cremenes	235	x	x	x			70	25		5							
XL	Salamón	237	x	x	x			60	40									
XL	Salamón	243	x	x	x			90	8									
XL	Salamón	244	x	x	x			70	25		5							
XXXVIII	Piedrasech	245	x	x	x	x		60	25		15							
XXXIV	Cueta	248	x	x	x			50		35	10							
XXXIV	Cueta	249	x	x	x	x		80	15		5							
XXXVI	Cacabillo	252	x	x	x			75	15		5							
XXXV	Cueta II	256	x	x	x			80	15		5							
XXXV	Cueta II	258	x	x	x			95			5							
XXXVII	Cueta II	260	x	x	x			90	5		3							
XXXV	S Emiliano	265	x	x	x			75	15		10							
XXXVII	Vejós	269	x	x	x			70	20		10							
XXXII	V. Lago	274	x	x	x			80	10		5							
XXXIII	Malva	278	x	x	x			90	10									
XXXIII	Malva	281	x	x	x			75	10		15							
XL	Salamón II	289	x	x	x			90			10							

ANNEX 5
STRUCTURAL DATA

Locality	Porosity Orientation		Details
	Dip	Dip Direction	
Cofiñal	55	350	350/60 Bedding
	60	355	
	55	350	
	50	360	
	50	355	
	55	360	
	60	355	
	60	350	
	55	355	
Isoba	40	310	330/40 Bedding
	40	340	
	40	310	
	40	340	
	40	340	
	50	315	
	35	320	
	40	330	
	35	330	
	40	330	
	40	320	
	80	230	210/70 Bedding
	80	230	
	80	230	
	55	240	
	70	210	
	70	210	
	40	340	
	50	235	
	60	240	
	80	230	
	80	230	
	80	230	
Talc Mine (old)	60	320	300/70 Bedding
	60	330	
	70	320	
	65	330	
	62	324	
	62	320	
	68	325	
	64	328	
Talc Mine (new)	80	220	215/80 Bedding
	80	215	
	80	215	
	75	220	
	80	220	
	80	230	
	75	230	
	74	225	
	78	215	
	80	215	
	75	230	
Valdecastillo	70	330	310/80 Bedding
	75	330	
	80	320	
	80	330	
	75	320	
	78	324	
	78	330	
	75	326	
	80	328	
Nocedo de C.	80	10	330/80 Bedding
	80	10	
	75	15	
	80	15	
	70	10	
	70	15	
	80	10	
	74	14	
	74	16	
	80	12	
	80	10	
	78	12	
Braña	60	250	150/70 Bedding
	60	250	
	65	250	
	65	245	
	65	255	
	60	245	
	60	250	
	65	240	
	65	250	

Locality	Porosity Orientation		Details
	Dip	Dip Direction	
Lugueros	65	10	10/60 Bedding
	65	15	
	60	10	
	65	20	
	60	20	
	65	15	
	65	18	
	60	15	
Llamazares	60	305	35/50 Bedding
	60	304	
	55	305	
	60	300	
	55	300	
	60	305	
	50	40	
	55	35	
	50	35	
	45	40	
Getino	10	260	80/350 Bedding
	15	250	
	10	255	
	20	255	
	15	260	
	30	230	
	25	220	
	30	240	
	35	230	
	15	220	
	15	235	
	20	230	
	25	240	
	15	220	
	15	235	
	15	230	
	15	230	
Valporquero	10	260	350/70 Bedding
	15	265	
	10	265	
	15	260	
	25	230	
	20	230	
	25	220	
	20	225	
	20	228	
	25	230	
	12	265	
	10	268	
	15	260	

Locality	Porosity Orientation		Details
	Dip	Dip Direction	
Millaró	60	25	25/80 Bedding
	60	25	
	55	25	
	58	24	
	58	20	
	56	26	
	20	115	
	25	114	
	24	116	
	25	114	
	20	115	
	24	114	
	25	116	
	24	116	
	20	75	142/88 Fault Plane
	22	74	
	24	76	
	20	72	
	25	75	
	22	76	
	24	75	
	20	114	
	24	112	
	22	118	
	25	114	
	20	115	
	24	116	
	22	114	
	24	116	
	70	15	
	75	16	
	70	18	
	72	15	
	70	16	
	74	18	
	72	16	
	70	16	
Villanueva	40	100	20/50 Bedding
	45	110	
	42	112	
	44	110	
	40	112	
	38	110	
	40	130	
	45	132	
	44	130	
	40	135	
	44	134	
	44	130	
	40	110	
	42	112	
Villanueva	42	110	
	44	130	
	45	135	
	45	134	
Pobladura deT.	20	300	25/70 Bedding
	22	300	
	20	310	
	20	295	
	22	294	
	20	292	
	22	292	
	20	294	
	22	294	
Viadangos	60	340	320/50 Bedding
	60	342	
	62	340	
	60	338	
	64	340	
	62	342	
	62	338	
	65	340	
	65	338	
	63	340	
	64	342	
Viadango II	20	340	15/80 Bedding
	25	330	140/80 Bedding
	22	325	
	20	320	
	25	320	
	22	320	
	24	325	
	20	322	
	22	320	
Sierra del Turrón	25	60	330/70 Bedding
	20	60	85/20 Breccia
	22	60	
	22	62	
	24	65	
	22	64	
	20	65	
	70	332	
	65	330	
	68	334	
	70	330	
	22	65	
	22	60	
	22	62	
	24	64	

Locality	Porosity Orientation		Details
	Dip	Dip Direction	
Sierra del T	24	62	
	20	60	
	24	60	
	22	60	
	20	64	
	22	64	
Cubillas de A.	30	240	150/70 Bedding
	25	230	220/70 Joint
	22	232	
	25	235	
	28	230	
	28	234	
	26	234	
	26	240	
Caldas de L.	50	180	185/70 Bedding
	60	182	
	52	184	
	54	184	
	50	184	
	58	182	
	54	182	
	50	180	
	50	10	
	45	5	
	42	8	
	44	8	
	44	6	
	42	6	
	44	10	
Robledo de C.	60	220	235/60 Bedding
	62	220	
	62	224	
	64	224	
	62	225	
	62	220	
	64	222	
	65	224	
	65	220	
	62	224	
Sena de Luna	72	220	225/70 Bedding
	70	220	
	70	222	
	70	219	
	72	218	
	70	210	
	70	200	
	70	202	
	72	202	

Locality	Porosity Orientation		Details
	Dip	Dip Direction	
San Emiliano	20	44	Middle
	22	44	Middle
	20	43	Middle
	22	44	Middle
	25	40	Middle
	24	42	Middle
	25	40	Middle
	70	330	Middle
	70	333	Middle
	68	335	Middle
	68	332	Middle
	70	328	Middle
	68	328	Middle
	30	215	North
	32	212	North
	30	212	North
	30	215	North
	30	216	North
	32	215	North
	30	214	North
	32	215	North
	30	212	North
Villasecino	80	60	330/80 Bedding
	82	62	
	80	64	
	80	58	
	78	60	
	78	58	
	78	64	
	80	58	
	20	330	
	22	328	
	22	330	
	20	325	
	20	326	
	22	325	
	20	330	
	82	64	
	78	66	
S. Emiliano II	20	280	5/40 Bedding
	22	278	170/80 Fault Plane
	20	276	
	22	275	
	20	270	
	20	272	
	20	274	
	20	278	
	22	273	
	50	5	
	50	6	
	52	10	
S. Emiliano II	50	8	
	52	5	
	50	6	
	50	10	
Somiedo	60	300	35/80 Bedding L1
	60	304	40/80 Bedding L1
	60	302	30/80 Bedding L2
	62	300	160/60 Bedding L3
	60	308	Lake 1
	62	305	Lake 1
	60	304	Lake 1
	64	300	Lake 1
	62	302	Lake 1
	60	304	Lake 1
	62	305	Lake 1
	10	300	Lake 1
	12	300	Lake 1
	10	302	Lake 1
	10	300	Lake 1
	12	305	Lake 1
	12	302	Lake 1
	10	304	Lake 1
	10	300	Lake 1
	12	302	Lake 1
	12	310	Lake3
	12	312	Lake3
	10	314	Lake3
	12	314	Lake3
	10	310	Lake3
	14	315	Lake3
	15	315	Lake3
	15	315	Lake3
	16	310	Lake3
	16	312	Lake3
	18	318	Lake3
	70	270	Lake2
	60	270	Lake2
	65	272	Lake2
	65	270	Lake2
	62	274	Lake2
	65	275	Lake2
	62	272	Lake2
	30	270	Lake2
	35	272	Lake2
	34	270	Lake2
	30	274	Lake2
	30	272	Lake2
	32	275	Lake2
	34	270	Lake2

Locality	Porosity Orientation		Details
	Dip	Dip Direction	
Valle d. Lago	70	40	Bedding 1
	70	60	Bedding 2
	40	30	Bedding 3
	65	20	Bedding 4
	60	70	Bedding 5
	25	340	b5
	20	342	b5
	28	345	b5
	25	338	b5
	20	340	b5
	25	342	b5
	20	290	b4
	25	292	b4
	25	295	b4
	24	290	b4
	20	280	b4
	20	285	b4
	22	280	b4
	22	285	b4
	20	300	b3
	25	305	b3
	22	310	b3
	20	305	b3
	25	302	b3
	24	300	b3
	20	310	b3
	25	305	b3
	15	330	b2
	12	325	b2
	15	328	b2
	15	325	b2
	18	330	b2
	20	325	b2
	20	330	b2
	25	310	b1
	20	310	b1
	22	312	b1
	20	315	b1
	25	315	b1
	24	310	b1
	22	305	b1
	25	310	b1
	20	315	b1
Malva	85	230	Bedding 1
	5	330	B1
	10	330	B1
	12	325	B1
	15	320	B1
	12	330	B1
	10	320	B1
	35	20	Bedding 2
	20	280	

Locality	Porosity Orientation		Details
	Dip	Dip Direction	
Malva	22	285	B2
	25	285	B2
	20	282	B2
	25	280	B2
	25	285	B2
	70	30	Bedding 3
	20	290	B3
	25	295	B3
	22	298	B3
	20	295	B3
	20	298	B3
	25	290	B3
La Cueta I	70	250	Bedding
	25	350	
	25	355	
	30	360	
	25	358	
	30	355	
	30	358	
La Cueta II	70	265	Bedding 1
	25	360	B1
	22	362	B1
	20	365	B1
	25	365	B1
	24	360	B1
	25	360	B1
	22	366	B1
	65	265	Bedding 2
	25	365	B2
	20	355	B2
	25	360	B2
	30	355	B2
	25	365	B2
	20	360	B2
	55	160	Bedding 3
	20	70	B3
	22	72	B3
	18	70	B3
	20	72	B3
	18	72	B3
	60	100	Bedding 4
	30	10	B4
	25	12	B4
	28	5	B4
	30	5	B4
	28	10	B4
Cacabalillo	75	70	
	15	340	
	10	330	
	18	340	
	10	342	
	15	335	

Locality	Porosity Orientation		Details
	Dip	Dip Direction	
Cacabalillo	20	310	
	20	300	
	18	300	
	20	305	
	22	305	
Vega Viejos	85	230	Bedding
	15	340	
	15	330	
	18	330	
	15	335	
	10	335	
	10	340	
	20	338	
	15	320	
	15	310	
	20	320	
	20	315	
	10	310	
	15	360	
	10	360	
	15	355	
	20	355	
Cremenés	65	10	Bedding
	25	280	
	20	290	
	30	290	
	25	285	
	30	288	
	30	300	
	30	310	
	25	300	
	25	310	
	28	305	
	25	305	
	30	312	
	40	15	
	45	20	
	50	18	
Salamon I	75	210	Bedding
	15	300	
	18	310	
	10	305	
	15	310	
	10	300	
	15	330	
	10	330	
	18	335	
	15	335	
	15	350	
	10	350	
	10	345	
	10	342	
Salamon II	70	335	Bedding 1
	10	230	
	15	240	
	15	235	
	10	240	
	12	235	
	20	230	
	25	230	
	20	240	
	50	310	Bedding 2
	30	210	
	35	220	
	35	210	
	32	215	
	34	215	
	30	215	
	36	210	
	10	280	
	15	280	
	10	285	
	10	282	
	12	284	
	15	282	
	25	230	
	25	235	
	20	235	
	25	234	
	22	235	
	24	232	
	24	235	
Piedrasecha	80	30	Bedding 1
	20	300	
	20	295	
	18	298	
	20	295	
	18	300	
	20	298	
	20	30	Bedding 2
	20	300	
	22	298	
	25	300	
	80	20	Bedding 3
	20	295	
	15	298	
	25	300	
	20	290	
	18	285	
	20	285	
	20	280	

ANNEX 6
POROPERM RCA & IMAGE ANALYSES

Locality	Section Number	Sample Number	Colour	Formation	Lithology (dolomite-limestone)	Fabric	Porosity (%)	Permeability (md)	Image analysis						Maximum diameter classes vs. Porous area										
									Avg. Maximum diameter (mm)	Maximum diameter (mm)	% cements	% porosity loss	<1	1-3	3-5	5-7	7-9	9-11	11-15	15-20	20-25	25-30			
Mina Tacio	IX	24	Grey+White	Bucaillete Fm.	Dolomite	2	2.83	0.34	0.22	3.22		10	0.236	0.0898	0.021718	0	0	0	0	0	0	0			
Mina Tacio	IX	23/ALC	Grey+White	Bucaillete Fm.	Dolomite	2	2.69	3.27	0.66	0.2	1.26	10	0.5593	0.0949	0	0	0	0	0	0	0	0			
Mina Tacio	IX	23-001	Grey+White	Bucaillete Fm.	Dolomite	2	1.31	0.02	0.46	0.26	1.35	99.05	0.4032	0.000963	0	0	0	0	0	0	0	0			
Caballito Cabeza	XV	20648	Brown+Beige	Valedesa Fm.	Dolomite	2	0.74	0.24	0.24	1.02		10	0.2169	0.001015	0	0	0	0	0	0	0	0			
Caballito Cabeza	XV	59-009	Yellow	Valedesa Fm.	Dolomite	2	0.39	0.39	0.76	1.23	33.1	98.94	0.3693	0.00205	0	0	0	0	0	0	0	0			
Franco Cabeza	XV	59-002	Yellow	Valedesa Fm.	Dolomite	2	0.24	0.29	0.29	2.03		10	0.2364	0.011998	0	0	0	0	0	0	0	0			
Milloró	XVI	68	Beige	Bucaillete Fm.	Dolomite	2	1.71	0.18	0.27	1.53	17.74	99	0.2157	0.0229	0	0	0	0	0	0	0	0			
El Fraile-aucha	XXI	296	Grey+White	Bucaillete Fm.	Dolomite	2	3.50	2.83	0.44	9.81	11.56	80.33	0.4425	0.2184	0.194958	0.256277	0.289	1.3254	0	0	0	0			
Cabezas de Luna	XXI	91	Grey+White	Valedesa Fm.	Dolomite	2	1.35	0.04	0.11	0.26	1.27	10	0.0718	0.039	0	0	0	0	0	0	0	0			
Salinilla	XXVII	33	Light Redish	Valedesa Fm.	Dolomite	3	2.20	0.04	1.03	0.8	4.82	11.98	92.08	0.0003	0.0024	0.007326	0	0	0	0	0	0	0		
Nació del Cuneo	VI	25-001	White+Pink	Bucaillete Fm.	Dolomite	3				3.68	0.53	2.9	37.17	90.99	0.5883	1.3493	0.1433	0	1.07	0	0.5344	0	0	0	
Mina Tacio	IX	25-001	Grey	Bucaillete Fm.	Dolomite	3	2.56	0.02	4.33	0.24	14.09	90.33	0.2361	0.291744	0.42272	0.295247	0	0	0	0	0	0	0		
Vadecastillo	VIII	79	Grey+White	Valedesa Fm.	Dolomite	3	2.90	0.01	5.05	0.77	15.28	80.41	0.2361	0.2662	0.411692	0.440874	0.2625	0.41193	0	0	0.520553	0	0	0	
Villanueva de la Ter	XVII	79	Grey+White	Bucaillete Fm.	Dolomite	3	3.88	0.26	2.15	0.97	5.81	11.64	84.41	0.1119	0.2095	0.741364	0.587341	0	0	0	0	0	0	0	
Milloró	XVI	69	Beige	Bucaillete Fm.	Dolomite	3				3.56	2.22	8.49	17.46	83.26	0.0388	0.7395	0.384104	0	2.401	0	0	0	0	0	0
Fonledo	XII	48-001	Grey	Bucaillete Fm.	Dolomite	3	2.39	0.05	7.29	0.65	26	34.89	82.72	0.2164	0.2102	0.33978	0.845676	0	0	0	0	0	0	5.68	
Canteco	X	39	Grey	Bucaillete Fm.	Dolomite	3	3.96		3.78	0.48	15.27	81.52	0.4365	0.2969	0.554129	0	0.574	0	0	1.816239	0	0	0		
Milloró	XVI	2114	Grey	Bucaillete Fm.	Dolomite	3	2.92	0.05	6.09	0.52	9.18	22.53	78.72	1.1727	1.1472	0.776668	0.589817	0.8464	0.8066	0	0.735354	0	0	0	
Siete de Luna	XXXII	98	Grey	Valedesa Fm.	Dolomite	3	3.59	0.02	3.88	0.26	10.99	12.56	76.4	0.2875	0.1419	0.563428	0.79266	1.2024	1.5034	0	0	0	0	0	0
Villanueva de la Ter	XVII	80	Grey	Bucaillete Fm.	Dolomite	3	4.65	0.06	4.68	0.25	20.14	73.03	0.5989	0.2886	0.292904	0.50161	0	0.1072	0	0	0	2.9946	0	0	
Mina Prodeccia	XI	41	Grey	Valedesa Fm.	Dolomite	3	2.99		7.32	1.89	24.2	12.67	63.55	0.0942	0.192944	0.464748	1.113	0	0	0	0.5054	0	0	0	
Cubillas de Abas	XX	59	Medium	Valedesa Fm.	Dolomite	3	4.02	0.35	0.95	0.39	7.52	1.11	53.88	0.2014	0.1651	0.320548	0	0.362	0	0	0	0	0	0	
Lloba	II	B	White	Bucaillete Fm.	Dolomite	3	4.71		1.33	1	6.97	10	0.0365	0.2638	0.461947	0.417072	0	0	0	0	0	0	0		
Urbasa	II	11	White+Grey	Bucaillete Fm.	Dolomite	3	4.78	0.36	6.09	0.52	9.18	22.53	78.72	1.1727	1.1472	0.776668	0.589817	0.8464	0.8066	0	0.735354	0	0	0	
Montueto	VII	30	Pink	Valedesa Fm.	Dolomite	3	3.80		2.27	0.53	10.13	10	0.2466	0.0116	0.056693	0.341402	0.8581	0	0	0	1.8513	0	0	0	
Montueto	VII	34	Grey	Fri Llancara	Dolomite	3	4.04		2.6	0.47	11.82	10	0.2185	0.202562	0	0	0	0	0	0	0	0	0	0	
Montueto	VII	35	Grey	Fri Llancara	Dolomite	3	3.50																		
Mina Prodeccia	XI	42	Grey	Bucaillete Fm.	Dolomite	3	3.13	0.03																	
Fonledo	XII	48	Medium	Bucaillete Fm.	Dolomite	3	4.49		1.56	1.26	10.12	10	0.0444	0.1217	0.103121	0	0.559	0.6982	0	0	0	0	0	0	
Cesme	XIII	49	Pink	Bucaillete Fm.	Dolomite	3	2.35	0.01	2.7	0.53	10.7	10	0.2678	0.6167	0.001099	0.022958	0.001	0.0044	0	0	0	0	0	0	
Cesme	XIII	52	Redish	Bucaillete Fm.	Dolomite	3	1.23	0.01	3.79	0.59	11.11	10	0.3277	0.1663	0.637946	0.3	0.523301	0.698	0	1.0997	0	0	0		
La Riojana	XIV	57	Grey	Bucaillete Fm.	Dolomite	3	3.06	0.01	2.1	0.72	10.63	10	0.1619	0.2106	0.330614	1.113069	0	0.2789	0	0	0	0	0	0	
Milloró	XVI	64	Grey+White	Bucaillete Fm.	Dolomite	3	3.45																		
Fabanal	XVIII	82	Pink	Valedesa Fm.	Dolomite	3	4.48	2.84	0.7	0.9	1.18	4.61	10	0.0602	0.1886	0.35057	0	0	0	0	0	0	0		
Milloró	XVI	67	Grey+White	Valedesa Fm.	Dolomite	3	3.32	0.03	5.74	1.13	6.3	10	0.1713	1.2774	0.265682	1.135352	0	0	0	0	0	0	0		
Milloró	XVI	75	White+Pink	Valedesa Fm.	Dolomite	3	5.30	0.07	3.83	0.85	11.88	10	0.3673	1.2629	0.525778	0.1649618	0.464	0	0	0	0	0	0		
Milloró	XVI	76	White+Pink	Valedesa Fm.	Dolomite	3	3.22		3.53	0.47	9.29	10	0.2953	1.2324	0.291159	0	0.5878	0	0	0	0	0	0		
Villanueva de la Ter	XVII	78	White+Grey	Valedesa Fm.	Dolomite	3	2.06	0.04	4.07	0.38	11.63	10	0.5299	0.5119	0.611463	0	0	0	2.4141	0	0	0			
Siete de Luna	XIII	99	Reddish	Valedesa Fm.	Dolomite	3	2.07	0.07	0.48	0.96	2.73	10	0.0301	0.1462	0	0	0	0	0	0	0	0	0		
Siete de Luna	XIII	100	Yellow	Valedesa Fm.	Dolomite	3	4.18	0.07	1.15	1.25	3.96	10	0.1929	0.0304	0.149817	0	0	0	0	0	0	0			
Villafeliz	XIX	101	Pink	Valedesa Fm.	Dolomite	3	3.79	0.04	0.47	0.4	4.1	10	0.296	0.1787	0.35226	0.151502	0	0	0	0	0	0	0		
Villafeliz	XIX	102	Yellow	Valedesa Fm.	Dolomite	3	4.01	1.18	2.89	0.38	6.28	10	0.1791	0.1663	0.35226	0.151502	0	0	0	0	0	0	0		
Villafeliz	XIX	102	Yellow	Valedesa Fm.	Dolomite	3	4.70	0.04	1.18	0.49	5.09	10	0.2673	0.1367	0.353548	0	0.5878	0	0	0	0	0	0		
Villafeliz	XIX	102	Yellow	Valedesa Fm.	Dolomite	3	3.36	0.02	2.35	0.37	2.41	10	0.0718	0.1921	0	0	0	0	0	0	0	0	0		
Villafeliz	XIX	102	Yellow	Valedesa Fm.	Dolomite	3	7.46	0.40	1.67	0.6	4.73	10	0.2352	0.4574	1.080387	0	0	0	0	0	0	0			

Locality		Sample Number	Colour	Formation	RCA			Maximum diameter classes vs. Porous area															
Section Number	Number				Lithology (dolomite-limestone)	Fabric porosity (%)	Permeability (mD)	porosity (%)	Avg. maximum diameter (mm)	% cements	% porosity loss	< 1	1-3	3-5	5-7	7-9	9-11	11-15	15-20	20-25	25-30		
San Emiliano	XXIV	107	Pink-Grey	Bucalcén Fm.	Dolomite	3	4.15	0.41	0.155	4.89	10	0.1038	0.1632	0.159052	0	0	0	0	0	0			
San Emiliano	XXV	109	Pink	Bucalcén Fm.	Dolomite	3	4.67	0.59	1.47	0.118	10	1.077	0.2952	0.094903	0	0	0	0	0	0			
San Emiliano	XXVI	110	Pink	Bucalcén Fm.	Dolomite	3	11.4	1.26	2.53	0.6	7.83	10	0.7147	0.7737	0.183565	0	0.861	0	0	0	0		
San Emiliano	XXVII	111	Pink	Bucalcén Fm.	Dolomite	3	1.18	0.02	2.88	0.64	19.01	10	0.5381	0.6977	0.150916	0	0	0	1.495546	0	0		
San Emiliano	XXVIII	113	Pink	Vadileta Fm.	Dolomite	3	0.93	0.83	4.09	0.155	10	0.2285	0.4152	0.283924	0	0	0	0	0	0			
San Emiliano	XXIX	116	Pink	Vadileta Fm.	Dolomite	3	3.40	0.13	1.11	0.52	2.03	10	0.5673	0.5414	0	0	0	0	0	0	0		
San Emiliano	XXXI	120	Grey	Bucalcén Fm.	Dolomite	3	3.40	0.13	1.11	0.52	2.03	10	0.2107	0.3301	0.288065	0.26336	0.761	0	0	0	0	0	
San Emiliano	XXXII	121	Grey	Catala de Morata Fm.	Dolomite	3	1.25	0.45	4.26	0.155	10	0.3278	0.3359	0.419956	0	0	0	0	0	0			
San Emiliano	XXXIII	122	Grey	Catala de Morata Fm.	Dolomite	3	2.93	1.73	2.26	5.65	10	0.0472	0.0467	1.014042	0.324924	0	0	0	0	0	0		
San Emiliano	XXXIV	129	Grey/White	Catala de Morata Fm.	Dolomite	3	2.51	1.29	0.35	5.53	10	0.2716	0.0868	0.610907	0.31962	0	0	0	0	0	0		
San Emiliano	XXXVII	130	Grey	Catala de Morata Fm.	Dolomite	3	2.65	1.08	3.14	0.54	15.14	10	0.4959	0.4499	0.360349	0.340244	0.194	0	0.4737	0.611969	0	0	
San Emiliano	XXXVII	131	Grey	Catala de Morata Fm.	Dolomite	3	3.40	1.25	1.65	0.39	7.4	10	0.2107	0.3301	0.288065	0.26336	0.761	0	0	0	0	0	0
San Emiliano	XXXVII	132	Grey	Catala de Morata Fm.	Dolomite	3	2.87	1.26	0.65	25.22	10	0.2591	0.2424	0.273837	0.621117	0	1.5698	0	0	0	0	4.37	
San Emiliano	XXXVII	133	Grey	Catala de Morata Fm.	Dolomite	3	3.57	0.47	4.4	0.77	12.61	10	0.2453	0.8244	0.19013	0	0.494	0	2.632	0	0	0	
San Emiliano	XXXVII	134	Reddish	Catala de Morata Fm.	Dolomite	3	2.17	0.01	2.15	1.97	9.93	10	0.0489	0.0645	0.300062	0	0.873	0.867	0	0	0	0	
San Emiliano	XXXVII	135	Reddish	Catala de Morata Fm.	Dolomite	3	1.74	0.01	2.91	0.88	7.18	10	0.123	0.1028	0.561913	0	1.211	0	0	0	0	0	
San Emiliano	XXXVII	136	Grey	Catala de Morata Fm.	Dolomite	3	3.87	0.02	1.57	0.41	5.45	10	0.4591	0.5333	0.252563	0.310342	0	0	0	0	0	0	
San Emiliano	XXXVII	137	Red+Pink	Catala de Morata Fm.	Dolomite	3	3.51	0.02	1.34	0.48	3.5	10	0.4705	0.5005	0.36964	0	0	0	0	0	0		
San Emiliano	XXXVII	139	White	Catala de Morata Fm.	Dolomite	3	3.12	0.01	4.79	1.72	13.67	10	0.0215	0.5489	0.216707	0	1.153	0.4477	2.3563	0	0	0	
San Emiliano	XXXVII	140	Pink	Catala de Morata Fm.	Dolomite	3	1.36	0.29	0.51	0.43	3.12	10	0.2293	0.1445	0.083811	0	0	0	0	0	0	0	
San Emiliano	XXXVII	143	Grey	Vadileta Fm.	Dolomite	3	6.46	0.42	0.44	7.56	10	0.5343	0.1653	0.967766	0	0.97	0	0	0	0	0		
San Emiliano	XXXVII	144	Grey	Vadileta Fm.	Dolomite	3	5.49	0.1	0.34	4	2.71	10	0.2389	0.1274	0.1539	0.134	0.27	0	0	0	0	0	
San Emiliano	XXXVII	145	Grey	Vadileta Fm.	Dolomite	3	4.69	0.50	0.51	0.37	6.11	10	0.1539	0.134	0.536954	0.624802	0	0	0	0	0	0	
San Emiliano	XXXVII	146	Grey	Vadileta Fm.	Dolomite	3	3.74	0.44	1.46	0.56	6.11	10	0.304	0.331	0.288628	0.387746	0	0	0	0	0	0	
San Emiliano	XXXIX	147	Grey	Vadileta Fm.	Dolomite	3	1.59	0.08	1.31	0.44	6.68	10	0.1791	0.2242	0	0	0	0	0	0	0		
San Emiliano	XXXIX	148	Grey	Vadileta Fm.	Dolomite	3	2.53	0.32	0.92	0.44	14.71	10	0.1412	0.3808	0.085565	0	0	0	0	0	0	0	
San Emiliano	XXXIX	149	Grey	Vadileta Fm.	Dolomite	3	1.45	0.01	0.61	0.78	4.47	10	0.0263	0.3709	0	0	0	0	0	0	0		
San Emiliano	XXXIX	150	Grey	Vadileta Fm.	Dolomite	3	1.68	0.11	0.4	0.72	2.44	10	0.201	0.4516	0.331971	0.185718	0	0	0	0	0	0	
San Emiliano	XXXIX	151	Grey	Vadileta Fm.	Dolomite	3	1.67	0.02	15.24	1.18	18.86	10	0.3368	0.3625	0.626297	0.022551	0	0	1.445	2.063394	0	0	
San Emiliano	XXXIX	164	Grey/White	Vadileta Fm.	Dolomite	3	1.97	1.01	0.22	12.37	10	0.3451	0	0.272473	0	1.83	0	3.7508	0	0	0		
Sierra de la Tuería	XXXI	165	Grey/White	Bucalcén Fm.	Dolomite	3	5.72	0.16	8.33	0.63	27.91	10	0.2331	0.1676	0.692293	0.6716678	0	0.9475	1.1549	0	4.058	0	
Sierra de la Tuería	XXXI	166	Grey/White	Bucalcén Fm.	Dolomite	3	3.49	4.56	0.51	18.98	10	0.1256	0.125	0.011538	0	0.352	0	0	0	0	0	0	
Sierra de la Tuería	XXXI	167	White+Grey	Bucalcén Fm.	Dolomite	3	4.03	0.75	0.62	6.47	10	0.1443	0.2131	0	0.292635	0	0	0	0	0	0		
Sierra de la Tuería	XXXI	170	Grey	Bucalcén Fm.	Dolomite	3	4.63	5.18	0.52	18.03	10	0.0524	0.1146	0.09817	0	0	0	0	0	0	0		
Sierra de la Tuería	XXXI	171	Grey+Beige	Bucalcén Fm.	Dolomite	3	4.59	4.06	6.2	0.22	12.37	10	0.3451	0	0.272473	0	1.83	0	3.7508	0	0		
Sierra de la Tuería	XXXI	173	Grey/White	Bucalcén Fm.	Dolomite	3	0.84	4.40	0.84	4.33	0.43	10	0.203	0.2054	0.127498	0.292023	0	0	0	3.3424765	0	0	
Sierra de la Tuería	XXXI	174	White+Grey	Bucalcén Fm.	Dolomite	3	3.40	0.75	0.77	0.34	3.49	10	0.319	0.483	0.075281	0	0	0	0	0	0		
Sierra de la Tuería	XXXI	176	White+Grey	Bucalcén Fm.	Dolomite	3	3.00	1.31	0.27	0.6	4	10	0.0524	0.1146	0.09817	0	0	0	0	0	0		
Sierra de la Tuería	XXXI	181	V	Vadileta Fm.	Dolomite	3	4.14	2.34	0.14	3	6.45	10	0.3105	0.553	0.773979	1.323855	0	0	0	0	0	0	
Sierra de la Tuería	XXXI	188	Mottled	Vadileta Fm.	Dolomite	3	3.85	0.10	3.19	0.41	17.24	10	0.3262	0.1416	0.126466	0	0	0	3.3424765	0	0		
Sierra de la Tuería	XXXI	190	Pink	Vadileta Fm.	Dolomite	3	3.94	0.70	1.81	0.4	8.65	10	0.4692	0.2115	0.162073	0	0.959	0	0	2.654505	0	0	
Sierra de la Tuería	VII	193	Grey	Lancara formation	Dolomite	3	3.69	0.21	1.69	0.33	6.34	10	0.407	0.2992	0.873905	0.361383	0	0	0	0	0	0	
Sierra de la Tuería	VII	194	Grey	Lancara formation	Dolomite	3	7.15	0.04	1.65	0.58	9.83	10	0.1679	0.593	1.44613	0.312521	0	0.4358	0	0	0	0	0
Sierra de la Tuería	VII	195	Grey	Lancara formation	Dolomite	3	5.98	1.48	3.05	0.7	7.16	10	0.1832	0.3944	0.592455	1.612888	0.353	0	0	0	0	0	

Maximum diameter classes vs. Porous area											
Locality	Section Number	Sample Number	Colour	Formation	Lithology (dolomite-limestone)	RCA		Image analysis			
						Fabric porosity (%)	Permeability (mD)	porosity (%)	Avg. maximum diameter (mm)	% cements	% porosity loss
Isba Nacebo de Culequi	II	19	Grey	Barcaliente Fm.	Dolomite	4	1.14	0.03			
	VI	32	White+Pink	Valedesa Fm.	Dolomite	4	2.11				
	VIII	36	Grey	Barcaliente Fm.	Dolomite	4	2.46	0.01			
	XI	40	Grey	Barcaliente Fm.	Dolomite	4	2.80				
Pontes ^{ob}	XII	47	Matited	Barcaliente Fm.	Dolomite	4	3.07	0.03			
	XIV	54	Grey	Barcaliente Fm.	Dolomite	4	1.71	0.01			
	XV	55	Grey	Barcaliente Fm.	Dolomite	4	0.68	0.01			
	XVI	61	Grey	Barcaliente Fm.	Dolomite	4	1.71	0.01			
	XVII	62	Beige	Barcaliente Fm.	Dolomite	4	1.86	0.05			
	XVII	63	Beige	Barcaliente Fm.	Dolomite	4	2.33				
	XVII	65	Grey+White	Barcaliente Fm.	Dolomite	4	1.75	0.08			
Villanueva de la Torre	XVIII	77	Grey	Valedesa Fm.	Dolomite	4	1.16				
Catedral de Atascos	XX	90	Matited	Valedesa Fm.	Dolomite	4	2.81	0.03			
Catedral del Lura	XXI	94	Grey	Valedesa Fm.	Dolomite	4	3.02	0.13			
San Ezequielo	XIX	112	Pink	Valedesa Fm.	Dolomite	4	0.64	0.29			
San Ezequielo	XIX	114	Pink	Valedesa Fm.	Dolomite	4	2.51	0.14			
San Silvestre 2	XVII	119	Grey	Valedesa Fm.	Dolomite	4	1.37	0.03			
Posada	XXIX	142	Grey	Valedesa Fm.	Dolomite	4	4.50	0.09			
Vidabasq	XXX	145	Grey	Valedesa Fm.	Dolomite	4	2.18	0.04			
Vidabasq	XXX	153	Grey	Valedesa Fm.	Dolomite	4	3.73	0.38			
Vidabasq II	XXX	156	Pink	Valedesa Fm.	Dolomite	4	2.91	0.16			
Vidabasq II	XXX	157	Pink	Valedesa Fm.	Dolomite	4	2.42	0.01			
Vidabasq II	XXX	161	Matited	Valedesa Fm.	Dolomite	4	1.93	0.02			
Santa María del Turón	XXXI	177	White+Grey	Barcaliente Fm.	Dolomite	4	1.93	0.06			
Branda	V	183	Pink	Valedesa Fm.	Dolomite	4	2.50	0.09			
Branda	V	184	Pink	Valedesa Fm.	Dolomite	4	2.70	0.17			
Branda	V	185	Reddish	Valedesa Fm.	Dolomite	4	0.78	1.75			
Branda	V	186	Grey+Red	Valedesa Fm.	Dolomite	4	1.62	0.03			
Nacebo de Culequi	VII	187	Matited	Valedesa Fm.	Dolomite	4	3.34	0.06			
Nacebo de Culequi	VII	189	Pink	Valedesa Fm.	Dolomite	4	3.06	0.02			
Pontes ^{ob}	All	196	Grey	Barcaliente Fm.	Dolomite	4	1.47	0.27			
	XII	198	Grey	Barcaliente Fm.	Dolomite	4	2.38	0.01			
Pontes ^{ob}	XII	199	Grey	Barcaliente Fm.	Dolomite	4	2.83	0.01			
Pontes ^{ob}	XII	200	Grey	Barcaliente Fm.	Dolomite	4	1.95	0.03			
Pontes ^{ob}	XII	201	Grey	Barcaliente Fm.	Dolomite	4	1.28	0.01			
Vidabasq	XIV	210	Grey+Red	Barcaliente Fm.	Dolomite	4	0.55	0.02			
Vidabasq	XIV	211	Reddish	Barcaliente Fm.	Dolomite	4	1.32	0.02			
Vidabasq	XIV	213	Pink	Barcaliente Fm.	Dolomite	4	2.29	0.11			
Vidabasq	XVII	216	Pink	Valedesa Fm.	Dolomite	4	3.19	0.04			
Vidabasq	V	224	Reddish	Valedesa Fm.	Dolomite	4	0.80	0.08			
Salamón	XL	239	Dark Grey	Bachended Member	Dolomite	4	0.13	0.2	0.51		
Salamón	XI	241	Grey	Bachended Member	Dolomite	4	0.3	0.22	1.56		
Salamón	XI	248	Grey	Bachended Member	Dolomite	4					
Capacatillo	XXXVI	251	G-R	Santa Lucia Fm.	Dolomite	4	0.16	0.38	1.87		
Cuetaro II	XXXX	256	Grey	Cártaza de Monzalva	Dolomite	4	0.14	0.23	1.68		
Cuetaro II	XXXX	260	G-P	Cártaza de Monzalva	Dolomite	4					
Cuetaro II	XXXX	262	Grey	Cártaza de Monzalva	Dolomite	4					
Vides	XXXXII	270	Grey	Cártaza de Monzalva	Dolomite	4					
Vides	XXXXII	272	Grey	Cártaza de Monzalva	Dolomite	4	0.92	0.24	6.99	Is vugonal	
Salamón II	XII	285	G-P	Cártaza de Monzalva	Dolomite	4	0.03	0.24	0.59		
Salamón II	XII	286	G-P	Cártaza de Monzalva	Dolomite	4	0.2	0.23	0.69		

Locality	Section Number	Sample Number	Colour	Formation	Lithology (dolomite-limestone)	Fabric porosity (%)	Permeability (mD)	RCA						Image analysis						Maximum diameter classes vs. Porous area					
								Av. porosity (%)	Maximum diameter (mm)	% cements (mm)	% porosity loss	< 1	1-3	3-5	5-7	7-9	9-11	11-15	15-20	20-25	25-30				
Salomon II	XI	290	Grey	Catíz de Monatía Fm.	Dolomite	4		0.42	0.46	1.73		0.1919	0.2273	0	0	0	0	0	0	0	0	0			
Salomon II	XI	291	Grey	Catíz de Monatía Fm.	Dolomite	4																			
Salomon II	XI	292	Grey	Catíz de Monatía Fm.	Dolomite	4		0.67	0.3	2.59		0.5317	0.1342	0	0	0	0	0	0	0	0	0			
Salomon II	XI	293	Grey	Burcalliente Fm.	Dolomite	4																			
Codifial	I	1	Mottled	Burcalliente Fm.	Dolomite	5	4.12	0.72	0.7	0.35	1.56		0.5232	0.1803	0	0	0	0	0	0	0	0			
Iloba	II	22b	Grey	Burcalliente Fm.	Dolomite	5	4.26	5.94																	
Iloba	II	10	White-Grey	Burcalliente Fm.	Dolomite	5	4.34	1.24																	
Codifial	I	4	Pink+Grey	Burcalliente Fm.	Dolomite	5	6.15	2.89																	
Iloba	II	7	Pink+Grey	Burcalliente Fm.	Dolomite	5	7.70	2.68																	
Iloba	II	17	Grey	Burcalliente Fm.	Dolomite	6	4.16	0.07	2.74	0.36	7.3	17.54	B6,49	0.3692	0.2764	0	0.057911	0.302	0	0	1.233112	0			
Eratia	V	29	Red+Grey	Valdepeña Fm.	Dolomite	6	2.68	0.43																	
Ains Procedencia	XI	45	Reddish	Burcalliente Fm.	Dolomite	6	2.35	0.64																	
Gelino	XIII	53	Reddish	Burcalliente Fm.	Dolomite	6																			
Vájocueso	XIV	56	Grey+Red	Burcalliente Fm.	Dolomite	6	2.64	0.01																	
Vájocueso	XV	58	Reddish	Burcalliente Fm.	Dolomite	6	2.77	0.76																	
Alminto	XVI	74	Mottled	Valdepeña Fm.	Dolomite	6	4.20																		
Salinera	XXXVII	123	Grey	Catíz de Monatía Fm.	Dolomite	6	1.65	0.18																	
Salinera	XXXVII	124	Mottled	El Rincón Fm.	Dolomite	6	1.71																		
Salinero II	XXXIX	154	Pink	Valdepeña Fm.	Dolomite	6	2.83	0.07																	
Salinero II	XXXIX	155	Pink	Valdepeña Fm.	Dolomite	6	2.51	0.19																	
Salinero II	XXXIX	160	Pink+Red	Valdepeña Fm.	Dolomite	6	1.51	0.97																	
Sierra del Turón	XXXI	163	Pink	Burcalliente Fm.	Dolomite	6	4.29	0.17																	
Moncuetos	VII	192	Grey	Llano de la Cabeza Fm.	Dolomite	6	12.00	1.41																	
Milloró	XVI	215	Grey+White	Burcalliente Fm.	Dolomite	6	2.05	0.02	2.42	0.12	11.33	23.15	90.54	0.0624	0.2059	0.143146	0	0	0	0	0	0			
Cedras de Lina	XXI	217	Mottled	Catíz de Monatía Fm.	Dolomite	6	1.43																		
V. Laizo	XXXII	276	P+G	Burcalliente Fm.	Dolomite	6																			
Iloba	II	20	Grey	Burcalliente Fm.	Limestone		0.37																		
Iloba	II	21	Grey	Burcalliente Fm.	Limestone		0.26																		
Vélez	XIV	213B					1.83	0.08																	
Salomon	XI	238	Dark Grey	Bachicinde Member	Limestone																				
Salomon	XI	240	Dark Grey	Bachicinde Member	Limestone																				
Vélez	XXXVII	271	Grey	Catíz de Monatía Fm.	Limestone																				
Salomon II	XI	287	Red	Catíz de Monatía Fm.	Limestone																				
Salomon II	XI	288	Grey	Catíz de Monatía Fm.	Limestone																				

DOLOMITE FABRIC		ZEBRA		MICRO		1	
POROUS		MACRO		VUGGY		2	
NON MACRO		FINE		3		3	
COARSE		COARSE		4		4	
BREJA		BREJA		5		5	

ANNEX 7
ELEMENTAL GEOCHEMISTRY

Locality	Sample	Formation	Phase	Ca (%)	Mg (%)	Sr (ppm)	Na (ppm)	Fe (ppm)	Mn (ppm)
Caldas	134	Alba (top)	H	36,49	0,33	256	200	2000	463
Caldas	CBL1M	Barcalliente (middle)	H	32,57	0,17	450	200	3100	117
Caldas	CVL1B	Valdeteja (base)	H						
Caldas	136	Alba (top)	Dol B	19,24	10,29	25	400	3200	553
Caldas	138	Barcalliente (middle)	Dol B	17,48	10,71	15	300	1000	364
Caldas	136	Alba (top)	Dol A2	18,35	10,62	23	500	3400	558
Caldas	138	Barcalliente (middle)	Dol A2	17,43	10,69	19	500	1000	230
Caldas	144I	Valdeteja (base)	Dol A2						
Canseco	CBL3T	Barcalliente (top)	H	33,08	0,07	459	100	800	131
Canseco	CBD1T	Barcalliente (top)	Dol B						
Canseco	45	Barcalliente (top)	Dol B	22,73	10,86	10,2	100	5500	901
Canseco	CBD1T	Barcalliente (top)	Dol A2						
Canseco	45	Barcalliente (top)	Dol A2	18,4	10,7	41	200	6100	814
Canseco	CBD1T	Barcalliente (top)	Dol A1	17,21	10,56	28	300	5200	716
Cármenes	CaBL2B	Barcalliente (base)	H	39,26	0,28	752	300	300	15
Cármenes	CaBL1T	Barcalliente (top)	H						
Cármenes	CaV1,4T	Valdeteja (top)	H						
Cármenes	CaV1I	Valdeteja (interf.)	H						
Cármenes	CaBD2B	Barcalliente (base)	Dol B	18,77	11,1	20	200	1700	346
Cármenes	CaVD4T	Valdeteja (top)	Dol B						
Cármenes	CaVD1	Valdeteja (interf.)	Dol B						
Cármenes	CaBD2B	Barcalliente (base)	Dol A2	18,69	11,02	24	500	2000	359
Cármenes	42	Barcalliente (top)	Dol A2						
Cármenes	CaVD4T	Valdeteja (top)	Dol A2						
Cármenes	CaV1D1	Valdeteja (interf.)	Dol A2						
Cubillas	VaVL4	Valdeteja (interf.)	H	38,52	0,31	335	100	500	39
Cubillas	CuBL3M	Barcalliente (middle)	H	39,43	0,25	725	200	200	12
Cubillas	CuBL4T	Barcalliente (top)	H						
Cubillas	CuVL2T	Valdeteja (top)	H						
Cubillas	VaVD2	Valdeteja (interf.)	Dol B	20,21	10,16	22	200	4600	655
Cubillas	CuBD1M	Barcalliente (middle)	Dol B	18,11	10,6	15	300	1800	391
Cubillas	VaVD2	Valdeteja (interf.)	Dol A2	19,05	9,89	20	200	3300	514
Cubillas	CuBD1M	Barcalliente (middle)	Dol A2	17,93	10,65	17	200	1300	179
Cubillas	CuBD2T	Barcalliente (top)	Dol A2						
Cubillas	CuVD2T	Valdeteja (top)	Dol A2						

Locality	Sample	Formation	Phase	Ca (%)	Mg (%)	Sr (ppm)	Na (ppm)	Fe (ppm)	Mn (ppm)
Cubillas	CuBD1M	Barcaliente (middle)	Dol A1	18	10,55	30	300	1400	222
Cubillas	CuBD2T	Barcaliente (top)	Dol A1						
Milaró	MBL2M	Barcaliente (middle)	H	39,95	0,24	950	400		8
Milaró	MAL1T	Alba (top)	H						
Milaró	MBL1B	Barcaliente (base)	H	37,68	0,04	802	100		9
Milaró	MAD1T	Alba (top)	Dol B						
Milaró	MBD1B	Barcaliente (base)	Dol B						
Milaró	40	Barcaliente (base)	Dol B						
Milaró	173	Barcaliente (middle)	Dol B	19,48	11,69	20	500	600	213
Milaró	38	Valdeteja (base)	Dol B						
Milaró	38	Valdeteja (base)	Dol A2						
Milaró	MAD1T	Alba (top)	Dol A2						
Milaró	MBD1B	Barcaliente (base)	Dol A2						
Milaró	40	Barcaliente (base)	Dol A2						
Milaró	173	Barcaliente (middle)	Dol A2	18,91	11,29	23	500	800	167
Milaró	40	Barcaliente (base)	Dol A1						
Mina Profunda	MPAL1M	Alba (top)	H						
Mina Profunda	MPBL1M	Barcaliente (middle)	H	38,39	0,25	806	300	900	56
Mina Profunda	MPVL1B	Valdeteja (base)	H						
Mina Profunda	MPVL2	Valdeteja (interf.)	H	39,1	0,34	254	100	300	57
Mina Profunda	CBM15	Valdeteja (interf.)	Dol B						
Mina Profunda	MPBD2M	Barcaliente (middle)	Dol B	19,41	10,34	16	200	4600	412
Mina Profunda	MPVD2M	Valdeteja (base)	Dol B						
Mina Profunda	MPVD3	Valdeteja (interf.)	Dol B	19,73	10,65	12	200	2700	301
Mina Profunda	CBM15	Valdeteja (interf.)	Dol A2						
Mina Profunda	MPAD1M	Alba (top)	Dol A2						
Mina Profunda	MPBD2M	Barcaliente (middle)	Dol A2	17,72	10,47	16	200	2900	411
Mina Profunda	MPVD1B	Valdeteja (base)	Dol A2						
Mina Profunda	MPVD3	Valdeteja (interf.)	Dol A2	19,16	11,48	12	300	1200	274
Montuerto	1	Barcaliente	H						
Montuerto	5	Barcaliente	Dol B						
Montuerto	3	Barcaliente	Dol A2						
Montuerto	3	Barcaliente	Dol A1						
Noledo	NBL1B	Barcaliente (base)	H						
Noledo	NBL2M	Barcaliente (middle)	H						
Noledo	NBL3T	Barcaliente (top)	H						

Locality	Sample	Formation	Phase	Ca (%)	Mg (%)	Sr (ppm)	Na (ppm)	Fe (ppm)	Mn (ppm)
Nocedo	NVL1B	Valdeteja (base)	H	35,87	0,31	179	200	200	49
Nocedo	NVL2M	Valdeteja (middle)	H						
Nocedo	NVL3T	Valdeteja (top)	H						
Nocedo	101	Barcaliente (base)	Dol B						
Nocedo	NBD2T	Barcaliente (top)	Dol B						
Nocedo	NVD1B	Valdeteja (base)	Dol B						
Nocedo	NBD2T	Barcaliente (top)	Dol A2						
Nocedo	NVD1B	Valdeteja (base)	Dol A2	19,21	11,33	16	300	1400	310
Nocedo	NVD2M	Valdeteja (middle)	Dol A2						
Nocedo	NVD3T	Valdeteja (top)	Dol A2						
Nocedo	101	Barcaliente (base)	Dol A1		11,59	71		4851	318
Nocedo	NBD1M	Barcaliente (middle)	Dol A1		12,31	12		1558	714
Nocedo	NBD2T	Barcaliente (top)	Dol A1						
Valdecastillo	109 I	Barcaliente (middle)	H						
Valdecastillo	109 II	Barcaliente (middle)	Dol B		11,67	108		4236	469
Valdecastillo	109 II	Barcaliente (middle)	Dol A2						
Valporquero	WVD4M	Valdeteja (middle)	Dol A1						
Valporquero	WVD4M	Valdeteja (middle)	Dol A2						
Villamarín	VBBL1	Barcaliente	H	37,18	0,13	699	200	200	15
Villamarín	VBBD2	Barcaliente	Dol B	19,29	11,62	14	300	600	221
Villamarín	VBBD1	Barcaliente	Dol A2	20,61	12,25	16	400	800	226
Villanueva	153	Valdeteja (top)	H		0,2	600	300	900	80
Villanueva	VCVL3	Valdeteja (middle interf.)	H						
Villanueva	VCVL2	Valdeteja (top interf.)	H	33,58	0,45	749	400	1300	130
Villanueva	VC172	Alba (top)	Dol B						
Villanueva	VCAD1T	Alba (top)	Dol B	18,95	10,41	24	300	1900	338
Villanueva	46	Barcaliente (base)	Dol B						
Villanueva	VCBD1B	Barcaliente (base)	Dol B	18,75	11,1	16	300	2100	263
Villanueva	31	Valdeteja (top)	Dol B	18,29	10,69	24	600	1400	320
Villanueva	29	Valdeteja (middle interf.)	Dol B						
Villanueva	26	Valdeteja (top interf.)	Dol B	19,01	11,15	17	300	1900	317
Villanueva	VC172	Alba (top)	Dol A2						
Villanueva	VCAD1T	Alba (top)	Dol A2	18,57	10,94	17	500	11700	326
Villanueva	46	Barcaliente (base)	Dol A2						
Villanueva	VCBD1B	Barcaliente (base)	Dol A2	19,37	10,99	16	300	2300	361
Villanueva	31	Valdeteja (top)	Dol A2	18,83	11,23	25	400	1000	268
Villanueva	29	Valdeteja (middle interf.)	Dol A2						
Villanueva	26	Valdeteja (top interf.)	Dol A2	18,61	10,6	20	400	1800	316

ANNEX 8
ISOTOPE GEOCHEMISTRY

Locality	Sample	Formation	Phase	$\delta^{18}\text{O}$	$\delta^{13}\text{C}$	$87\text{Sr}/86\text{Sr}$
Cacaballito	dl252	Santa Lucia Fm	Dol A	-8,32	1,36	
Caldas	134	Alba (top)	H	-2,02	3,14	
Caldas	CIBL1M	Barcaliente (middle)	H	1,12	4,54	
Caldas	CIVL1B	Valdeteja (base)	H	-1,55	3,32	
Caldas	136	Alba (top)	Dol B	-9,85	3,57	
Caldas	138	Barcaliente (middle)	Dol B	-4,48	3,65	
Caldas	136	Alba (top)	Dol A2	-9,83	3,61	
Caldas	138	Barcaliente (middle)	Dol A2	-3,61	4,66	
Caldas	144I	Valdeteja (base)	Dol A2	-2,96	3,16	
Caldas	147	Barcaliente (middle)	Cal 2	-11,72	-3,18	
Caldas	143	Valdeteja (base)	Cal 2	-6,77	-7,93	
Caldas	136	Alba (top)	Cal 1	-8,12	-2,64	
Canseco	CBL3T	Barcaliente (top)	H	-4,52	4,19	
Canseco	CBD1T	Barcaliente (top)	Dol B	-5,84	5,3	
Canseco	45	Barcaliente (top)	Dol B	-8,69	3,91	
Canseco	CBD1T	Barcaliente (top)	Dol A2	-5,73	5,42	
Canseco	45	Barcaliente (top)	Dol A2	-6,49	4,42	
Canseco	CBD1T	Barcaliente (top)	Dol A1	-5,36	5,28	
Canseco	45	Barcaliente (top)	Cal 1	-13,44	-0,79	
Cármenes	CaBL2B	Barcaliente (top)	H	-0,24	4,5	0,708147
Cármenes	CaBL1T	Barcaliente (top)	H	-3,8	3,75	
Cármenes	CaVL4T	Valdeteja (top)	H	-2,88	4,26	
Cármenes	CaVL1	Valdeteja (interf.)	H	-3,91	4,33	
Cármenes	CaBD2B	Barcaliente (base)	Dol B	-9,06	4,16	0,709251
Cármenes	CaVD4T	Valdeteja (top)	Dol B	-11,97	1,74	
Cármenes	CaVD1	Valdeteja (interf.)	Dol B	-8,66	2,97	
Cármenes	CaBD2B	Barcaliente (base)	Dol A2	-7,24	4,17	0,709207
Cármenes	42	Barcaliente (top)	Dol A2	-9,52	3,69	
Cármenes	CaVD4T	Valdeteja (top)	Dol A2	-11,86	1,86	
Cármenes	CaVD1	Valdeteja (interf.)	Dol A2	-8,8	3,22	
Cármenes	CaBD2B	Barcaliente base)	Cal 2	-12,77	-4,11	0,708416

Locality	Sample	Formation	Phase	$\delta^{18}\text{O}$	$\delta^{13}\text{C}$	$^{87}\text{Sr}/^{86}\text{Sr}$
Crémenes	dl235	Caliza de Montaña	Dol B	-5,57	3,10	0,70957
Crémenes	dl235	Caliza de Montaña	Dol A	-6,05	2,85	
Cubillas	VaVL4	Valdeteja (interf.)	H	-4,09	5,29	
Cubillas	CuBL3M	Barcaliente (middle)	H	2,05	4,55	0,708105
Cubillas	CuBL4T	Barcaliente (top)	H	0,36	5,13	
Cubillas	CuVL2T	Valdeteja (top)	H	-2,74	4,48	
Cubillas	VaVD2	Valdeteja (interf.)	Dol B	-9,07	5,23	
Cubillas	CuBD1M	Barcaliente (middle)	Dol B	-6,75	4,02	0,708576
Cubillas	VaVD2	Valdeteja (interf.)	Dol A2	-8,71	4,39	
Cubillas	CuBD1M	Barcaliente (middle)	Dol A2	-5,34	3,96	0,708687
Cubillas	CuBD2T	Barcaliente (top)	Dol A2	-7,28	5,23	
Cubillas	CuVD2T	Valdeteja (top)	Dol A2	-5,44	4,46	
Cubillas	CuBD1M	Barcaliente (middle)	Dol A1	-5,3	4	0,708491
Cubillas	CuBD2T	Barcaliente (top)	Dol A1	-7,2	5,25	
Cubillas	VaVD2	Valdeteja (interf.)	Cal 1	-14,23	2,52	
Cuetilla	dl256	Caliza de Montaña	Dol A	-1,99	5,36	
Isoba	dl14	Barcaliente Fm	Dol B2	-13,66	3,55	
Llamazares	dl202	Valdeteja Fm	Dol B	-8,65	3,58	
Malva	dl278	Caliza de Montaña	Dol A	-1,64	4,80	0,70901
Milaró	MBL2M	Barcaliente (middle)	H	0,77	4,44	
Milaró	MA11T	Alba (top)	H	0,28	3,73	
Milaró	MBL1B	Barcaliente (base)	H	1,56	4,53	0,708137
Milaró	MAD1T	Alba (top)	Dol B	-9,43	2,41	
Milaró	MBD1B	Barcaliente (base)	Dol B	-8,59	3,87	
Milaró	40	Barcaliente (base)	Dol B	-6,91	4,77	
Milaró	173	Barcaliente (middle)	Dol B	-7,93	3,54	
Milaró	38	Valdeteja (base)	Dol B	-5,41	4,4	
Milaró	38	Valdeteja (base)	Dol A2	-4,97	4,37	
Milaró	MAD1T	Alba (top)	Dol A2	-7,76	3,16	
Milaró	MBD1B	Barcaliente (base)	Dol A2	-7,53	4,69	

Locality	Sample	Formation	Phase	$\delta^{18}\text{O}$	$\delta^{13}\text{C}$	$^{87}\text{Sr}/^{86}\text{Sr}$
Milaró	40	Barcaliente (base)	Dol A2	-6,52	4,82	
Milaró	173	Barcaliente (middle)	Dol A2	-7,72	4,4	
Milaró	40	Barcaliente (base)	Dol A1	-6,53	4,91	
Milaró	172	Barcaliente (middle)	Cal 2	-9,53	-1,82	
Milaró	MBD1B	Barcaliente (base)	Cal 1	-10,5	1,97	
Mina Profunda	MPAL1M	Alba (top)	H	-0,72	3,08	
Mina Profunda	MPBL1M	Barcaliente (middle)	H	-0,46	4,75	0,708082
Mina Profunda	MPVL1B	Valdeteja (base)	H	-2,96	4,45	
Mina Profunda	MPVL2	Valdeteja (interf.)	H	-2,99	4,16	
Mina Profunda	CBM15	Valdeteja (interf.)	Dol B	-8,82	4,77	
Mina Profunda	MPBD2M	Barcaliente (middle)	Dol B	-5,63	4,07	0,709081
Mina Profunda	MPVD2M	Valdeteja (base)	Dol B	-9,26	1,71	
Mina Profunda	MPVD3	Valdeteja (interf.)	Dol B	-7,25	3,44	
Mina Profunda	CBM15	Valdeteja (interf.)	Dol A2	-6,6	4,67	
Mina Profunda	MPAD1M	Alba (top)	Dol A2	-6,66	3,26	
Mina Profunda	MPBD2M	Barcaliente (middle)	Dol A2	-5,72	4,19	0,7084
Mina Profunda	MPVD1B	Valdeteja (base)	Dol A2	-8,74	3,99	
Mina Profunda	MPVD3	Valdeteja (interf.)	Dol A2	-7,47	3,39	
Mina Profunda	CBM15	Valdeteja (interf.)	Cal 2	-9,23	-2,44	
Mina Profunda	MPVD1B	Valdeteja (base)	Cal 2	-6,98	-4,47	
Mina Profunda	MPVD3	Valdeteja (interf.)	Cal 2	-7,35	-5,75	
Mina Profunda	MPBD2M	Barcaliente (middle)	Cal 1	-12,72	1,95	0,708502
Mina Talco	d125	Barcaliente Fm	Dol B1	-12,90	3,53	
Montuerto	1	Barcaliente	H	0,65	4,67	
Montuerto	5	Barcaliente	Dol B	-5,88	2,19	
Montuerto	3	Barcaliente	Dol A2	-5,41	4,74	
Montuerto	3	Barcaliente	Dol A1	-5,38	4,87	
Nocedo	NBL1B	Barcaliente (base)	H	-5,09	3,24	
Nocedo	NBL2M	Barcaliente (middle)	H	-0,41	4,61	

Locality	Sample	Formation	Phase	$\delta^{18}\text{O}$	$\delta^{13}\text{C}$	$87\text{Sr}/86\text{Sr}$
Nocedo	NBL3T	Barcaliente (top)	H	-1,63	4,63	
Nocedo	NVL1B	Valdeteja (base)	H	-2,68	4,14	
Nocedo	NVL2M	Valdeteja (middle)	H	-7,73	3,55	
Nocedo	NVL3T	Valdeteja (top)	H	-4,66	4,49	
Nocedo	101	Barcaliente (base)	Dol B	-5,56	3,07	
Nocedo	NBD2T	Barcaliente (top)	Dol B	-4,19	4,52	
Nocedo	NVD1B	Valdeteja (base)	Dol B	-6,71	4,4	
Nocedo	NBD2T	Barcaliente (top)	Dol A2	-3,22	4,48	
Nocedo	NVD1B	Valdeteja (base)	Dol A2	-8,15	4,7	
Nocedo	NVD2M	Valdeteja (middle)	Dol A2	-6,86	4,68	
Nocedo	NVD3T	Valdeteja (top)	Dol A2	-5,09	4,33	
Nocedo	101	Barcaliente (base)	Dol A1	-2,99	4,2	
Nocedo	NBD1M	Barcaliente (middle)	Dol A1	-4,07	4,2	
Nocedo	NBD2T	Barcaliente (top)	Dol A1	-3,67	4,6	
Nocedo	NBD1M	Barcaliente (middle)	Cal 2	-11,1	-6,65	
Nocedo	NVD1B	Valdeteja (base)	Cal 2	-11,08	-2,12	
Prié d'asecha	dl245	Barcaliente Fm	Dol A	-11,14	3,51	
Salientia	dl125	Caliza de Montaña	Dol A2	-7,95	5,28	
San Emiliano	dl115	Barcaliente Fm	Dol B	-3,08	4,55	
Sierra del Turrión	dl168	Barcaliente Fm	Dol B	-7,48	4,95	0,70895
Sierra del Turrión	dl168	Barcaliente Fm	Dol A	-6,33	4,53	
Valdecastillo	109 I	Barcaliente (middle)	H	-6,3	3,3	
Valdecastillo	109 II	Barcaliente (middle)	Dol B	-10,37	4	
Valdecastillo	109 II	Barcaliente (middle)	Dol A2	-10,58	3,85	
Valle Lago	dl275	Caliza de Montaña	Dol A	-6,63	0,87	
Vaporquero	VVD4M	Valdeteja (middle)	Dol A1			
Vaporquero	VVD4M	Valdeteja (middle)	Dol A2			
Vega Viejos	dl268	Caliza de Montaña	Dol A	-4,04	2,43	
Viadango II	dl155	Valdeteja Fm	Dol A2	-9,55	2,66	

Locality	Sample	Formation	Phase	$\delta^{18}\text{O}$	$\delta^{13}\text{C}$	$^{87}\text{Sr}/^{86}\text{Sr}$
Villamarín	ViBL1	Barcaliente	H	-0,05	5,21	
Villamarín	ViBD2	Barcaliente	Dol B	-6,18	4,38	
Villamarín	ViBD1	Barcaliente	Dol A2	-6,18	4,44	
Villanueva	153	Valdetea (top)	H	-4,2	3,82	
Villanueva	VCVL3	Valdetea (middle interf.)	H	-3,25	5,13	
Villanueva	VCVL2	Valdetea (top interf.)	H	-4,86	4,57	
Villanueva	VC172	Alba (top)	Dol B	-8,48	3,71	
Villanueva	VCAD1T	Alba (top)	Dol B			
Villanueva	46	Barcaliente (base)	Dol B	-7,79	4,54	
Villanueva	VCBD1B	Barcaliente (base)	Dol B	-8,23	3,06	0,708458
Villanueva	31	Valdetea (top)	Dol B	-6,4	4,45	
Villanueva	29	Valdetea (middle interf.)	Dol B	-5,55	4,1	
Villanueva	26	Valdetea (top interf.)	Dol B	-8,28	4,97	
Villanueva	VC172	Alba (top)	Dol A2	-8,53	3,87	
Villanueva	VCAD1T	Alba (top)	Dol A2			
Villanueva	46	Barcaliente (base)	Dol A2	-9,63	4,02	
Villanueva	VCBD1B	Barcaliente (base)	Dol A2	-7,96	4,26	0,708646
Villanueva	31	Valdetea (top)	Dol A2	-4,38	4,53	
Villanueva	29	Valdetea (middle interf.)	Dol A2	-5,27	4,19	
Villanueva	26	Valdetea (top interf.)	Dol A2	-8,43	5,03	
Villanueva	31	Valdetea (top)	Cal 2	-13,45	-7,6	
Villanueva	VC172	Alba (top)	Cal 1	-15,39	0,76	
Villanueva	VCAD1T	Alba (top)	Cal 1			
Villanueva	VCBD1B	Barcaliente (base)	Cal 1	-8,42	0,18	0,708738
Villanueva	29	Valdetea (middle interf.)	Cal 1	-8,54	0,21	
Villanueva	26	Valdetea (top interf.)	Cal 1	-9,3	1,05	

ANNEX 9
MICROTHERMOMETRY (FI)

Locality: Isoba

Sample DL15

Phase	FL	Th °C	Tn _{gas} °C	Tn _{ice} °C	Tm _{ice} °C	MgCl ₂	NaCl	CaCl ₂	Salinity (eq. Wt %)	Molar Vol	Bulk composition			
											xH ₂ O	xMg ²⁺	xNa ⁺	xCa ²⁺
Dol B	fi1	168,5	-56,5	-67,8	-33,0	20,8	30,2		19,53	0,790		0,105		0,105
Dol B	fi2	160,8	-57,4	-62,6	-32,3	20,6	29,8		19,33	0,792		0,104		0,104
Dol B	fi3	159,2	-57,2	-60,1	-33,0	20,8	30,2		19,22	0,790		0,105		0,105
Dol B	fi4	158,2	-54,8	-65,2	-32,3	20,6	29,8		19,25	0,792		0,104		0,104
Dol B	fi5	160,3	-64,2	-32,7	20,5	30,0			19,28	0,791		0,105		0,105
Dol B	fi6	162,4	-64,8	-32,7	20,5	30,0			19,35	0,791		0,105		0,105
Dol B	fi7	164,5	-55,3	-65,2	-32,3	20,6	29,8		19,45	0,792		0,104		0,104
Dol B	fi8	161,6	-54,8	-65,7	-32,1	20,6	29,7		19,38	0,793		0,103		0,103
Dol B	fi9	158,7	-52,5	-66,2	-32,9	20,9	30,1		19,21	0,790		0,105		0,105
Dol B	fi10	160,8		-66,7	-33,0	20,8	30,2		19,27	0,790		0,105		0,105
Dol B	fi11	152,9	-50,9	-67,2	-32,3	20,6	29,8		19,08	0,792		0,104		0,104
Dol B	fi12	165,1		-33,0	20,8	30,2			19,41	0,790		0,105		0,105
Dol B	fi13	157,1		-66,2	-31,1	20,3	29,2		19,32	0,797		0,101		0,101
Dol B	fi14	159,2		-65,7	-32,9	20,9	30,1		19,23	0,790		0,105		0,105
Dol B	fi15	161,3	-53,7	-60,2	-32,7	20,7	30,0		19,32	0,791		0,105		0,105
Dol B	fi16	153,4	-51,8	-60,7	-32,3	20,6	29,8		19,10	0,792		0,104		0,104
Dol B	fi17	155,5		-61,2	-32,3	20,6	29,8		19,17	0,792		0,104		0,104
Dol B	fi18	157,6		-60,7	-32,1	20,6	29,7		19,25	0,793		0,103		0,103
Dol B	fi19	159,7		-61,2	-32,9	20,9	30,1		19,25	0,790		0,105		0,105
Dol B	fi20	161,8	-59,2	-61,7	-31,7	20,5	29,5		19,42	0,795		0,085		0,085
Dol B	fi21	163,9	-59,9		-32,5	20,7	29,9		19,42	0,792		0,103		0,103
Dol B	fi22	156,0	-51,3	-62,7	-32,9	20,9								
Dol B	fi23	158,1	-53,4	-63,2	-32,1	20,6	29,7		19,27	0,793		0,103		0,085
Dol B	fi24	160,3		-53,7	-32,9	20,9	30,1		19,27	0,790		0,105		0,105
Dol B	fi25	159,3	-59,5	-61,2	-32,7	20,7	30,0		19,25	0,791		0,105		0,105

Locality: Isoba

Sample DL226

Phase FL	FL	Th °C	T _{Ngas} °C	T _{Hice} °C	T _{Mice} °C	Salinity (eq. Wt %)			Molar Vol	Bulk composition				
						MgCl ₂	NaCl	CaCl ₂		xH ₂ O	xMg ²⁺	xNa ⁺	xCa ²⁺	xCl ⁻
Quartz	fi1	162,9		-50,6	-23,3	17,7	24,8		19,94	0,831		0,084	0,084	
Quartz	fi2	162,0		-51,1	-21,6	17,1	23,6		19,97	0,840		0,080	0,080	
Quartz	fi3	161,9		-50,3	-21,5	16,9	23,6		19,97	0,840		0,080	0,080	
Quartz	fi4	161,0		-49,5	-22,4	17,3	24,2		19,92	0,836		0,082	0,082	
Quartz	fi5	154,7		-41,5	-23,5	17,8	24,9		19,74	0,830		0,085	0,085	
Quartz	fi6	170,4		-41,4	-22,6	17,5	24,3		20,12	0,835		0,083	0,083	
Quartz	fi7	159,6		-47,3	-21,8	17,2	23,8		19,91	0,839		0,081	0,081	
Quartz	fi8	170,0		-47,4	-22,0	17,3	23,9		20,13	0,838		0,081	0,081	
Quartz	fi9	170,0		-41,2	-22,1	17,3	24,0		20,12	0,837		0,081	0,081	
Quartz	fi10	186,3			-21,4	17,0	23,5		20,47	0,841		0,080	0,080	
Quartz	fi11	191,2			-21,4	17,0	23,5		20,57	0,841		0,080	0,080	
Quartz	fi12	176,1			-21,2	16,9	23,4		20,27	0,842		0,079	0,079	
Quartz	fi13	191,0			-45,4	-21,2	16,9	23,4		20,57	0,842		0,079	0,079
Quartz	fi14	191,9			-45,9	-21,2	16,9	23,4		20,59	0,842		0,079	0,079
Quartz	fi15	180,8			-46,5	-21,9	16,8	23,8		20,35	0,838		0,081	0,081
Quartz	fi16	185,7			-47,0	-21,9	16,8	23,8		20,46	0,838		0,081	0,081
Quartz	fi17	180,6			-47,5	-21,4	17,0	23,5		20,36	0,841		0,080	0,080
Quartz	fi18	185,5				-21,7	17,1	23,7		20,45	0,839		0,080	0,080
Quartz	fi19	190,4				-22,6	17,4	24,3		20,55	0,835		0,083	0,083
Quartz	fi20	185,3				-22,5	17,4	24,2		20,44	0,835		0,082	0,082
Quartz	fi21	180,2			-48,1	-22,5	17,4	24,2		20,33	0,835		0,082	0,082
Quartz	fi22	185,1			-48,6	-21,3	17,0	23,4		20,45	0,841		0,079	0,079
Quartz	fi23	173,4				-21,2	16,9	23,4		20,21	0,842		0,079	0,079
Quartz	fi24	173,3				-21,2	16,9	23,4		20,21	0,842		0,079	0,079
Quartz	fi25	174,2				-21,3	16,9	23,4		20,23	0,841		0,079	0,079

Locality: Isoba

Sample DL14

Phase FL	FL	Th °C	Tn _{gas} °C	Tn _{ice} °C	Tm _{ice} °C	Salinity (eq. Wt %)			Molar Vol	Bulk composition			
						MgCl ₂	NaCl	CaCl ₂		xH ₂ O	xMg ²⁺	xNa ⁺	xCa ²⁺
DolB	fi1	155,3		-61,9	-31,9	20,5	29,6		19,19	0,794		0,103	
DolB	fi2	158,4		-61,5	-31,5	20,4	29,4		19,33	0,795		0,102	
DolB	fi3	156,1		-62,5	-30,4	20,1	28,9		19,34	0,800		0,100	
DolB	fi4	156,4		-62,4	-31,7	20,5	32,4		18,65	0,772		0,114	
DolB	fi5	156,7		-63,5	-31,7	20,5	29,5		19,26	0,795		0,103	
DolB	fi6	157,0		-61,8	-31,7	20,5	29,5		19,27	0,795		0,103	
DolB	fi7	157,3		-62,5	-30,5	20,1	28,9		19,37	0,800		0,100	
DolB	fi8	157,6		-71,1	-31,3	20,3	29,3		19,32	0,796		0,102	
DolB	fi9	157,9		-61,3	-30,3	20,0	29,0		19,38	0,799		0,100	
DolB	fi10	158,2		-62,5	-31,7	20,5	29,5		19,30	0,795		0,103	
DolB	fi11	158,5		-62,7	-31,6	20,4	29,5		19,32	0,795		0,102	
DolB	fi12	158,8		-62,9	-31,3	20,3	29,3		19,35	0,796		0,102	
DolB	fi13	159,1		-60,4	-30,4	20,1	28,9		19,43	0,800		0,100	
DolB	fi14	159,4		-62,3	-30,4	20,1	28,9		19,44	0,800		0,100	
DolB	fi15	159,7		-62,5	-30,2	20,0	28,8		19,47	0,801		0,100	
DolB	fi16	158,0		-62,7	-31,8	20,5	29,6		19,29	0,794		0,103	
DolB	fi17	156,3		-61,9	-31,7	20,5	29,5		19,68	0,795		0,103	
DolB	fi18	156,6		-61,1	-31,6	20,4	29,5		19,26	0,795		0,102	
DolB	fi19	156,9		-61,3	-31,5	20,4	29,4		19,28	0,795		0,102	
DolB	fi20	157,2		-61,5	-31,1	20,3	29,2		19,32	0,797		0,101	
DolB	fi21	157,5		-63,7	-31,5	20,4	29,4		19,30	0,795		0,102	
DolB	fi22	157,8			-31,5	20,4	29,4		19,31	0,795		0,102	
DolB	fi23	156,1		-62,1	-31,6	20,4	29,5		19,25	0,795		0,102	
DolB	fi24	159,4		-60,3	-30,3	20,0	28,8		19,45	0,800		0,100	
DolB	fi25	158,7		-60,5	-30,6	20,1	29,0		19,41	0,799		0,100	

Locality: Piedrascha Sample DL245

Phase FL	FL	T _h °C	T _{h_{gas}} °C	T _{h_{ice}} °C	T _{m_{ice}} °C	Salinity (eq. Wt %)	Molar Vol	Bulk composition				
								MgCl ₂	NaCl	CaCl ₂	xH ₂ O	xMg ²⁺
C1	fi1	95,1		-59,5	-18,9	20,89	19,01				0,894	
C1	fi2	94,7	-40,3	-57,7	-17,9	19,52	19,00				0,894	
C1	fi3	94,3		-56,0	-18,2	19,68	19,00				0,893	
C1	fi4	93,9	-39,1	-54,2	-18,0	19,57	18,99				0,894	
DolB	fi5	101,1		-71,7	-28,1	19,4	27,62				17,96	0,810
DolB	fi6	100,7		-70,0	-28,2	19,4	27,68				17,94	0,809
DolB	fi7	100,3		-68,2	-28,2	19,4	27,68				17,92	0,809
DolB	fi8	102,5		-66,5	-28,3	19,4	27,74				17,98	0,809
DolB	fi9	102,3		-64,7	-28,3	19,4	27,74				17,97	0,809
DolB	fi10	100,5		-63,0	-28,4	19,5	27,79				17,91	0,808
DolB	fi11	103,2		-61,2	-28,4	19,5	27,79				17,98	0,808
DolB	fi12				-28,5							
DolB	fi13	102,4		-62,45	-28,5	19,5	27,85				17,95	0,808
DolB	fi14	101,1		-60,7	-28,6	19,5	27,90				17,90	0,807
DolB	fi15	100,7		-69,0	-28,6	19,5	27,90				17,89	0,807

Locality: Talc Mine **Sample DL25**

Phase FL	FL	Th °C	Tn _{gas} °C	Tn _{ice} °C	Tm _{ice} °C	Salinity (eq. Wt %)			Molar Vol	Bulk composition			
						MgCl ₂	NaCl	CaCl ₂		xH ₂ O	xMg ²⁺	xNa ⁺	xCa ²⁺
Dol B	fi1	168,9		-66,7	-30,6	20,1	29,0		19,71	0,799		0,100	
Dol B	fi2	141,6		-70,0	-31,9	20,5	29,6		18,76	0,794		0,103	
Dol B	fi3	155,7		-74,1	-30,6	20,1	29,0		19,32	0,799		0,100	
Dol B	fi4	140,5		-72,4	-29,1	19,7	28,2		18,99	0,805		0,097	
Dol B	fi5	160,1		-71,7	-32,9	20,8	30,1		19,26	0,790		0,105	
Dol B	fi6	162,3		-68,9	-30,1	20,0	28,7		19,55	0,801		0,099	
Dol B	fi7	160,2		-69,8	-32,8	20,9	30,1		19,27	0,790		0,105	
Dol B	fi8	163,0		-67,8	-33,0	20,8	30,2		19,35	0,790		0,105	
Dol B	fi9	158,1		-66,5	-32,1	20,6	29,7		19,27	0,793		0,103	
Dol B	fi10	153,2		-65,3	-32,3	20,6	29,8		19,09	0,792		0,104	
Dol B	fi11	158,2				-32,9	20,8	30,1	19,20	0,790		0,105	
Dol B	fi12	153,3		-62,9	-31,6	20,4	29,5		19,16	0,795		0,102	
Dol B	fi13	158,4		-61,7	-29,8	19,9	28,6		19,46	0,802		0,099	
Dol B	fi14	148,5		-60,5	-32,9	20,9	30,1		18,88	0,790		0,105	
Dol B	fi15	148,6		-59,3	-32,9	20,9	30,1		18,88	0,790		0,105	
Dol B	fi16	143,6		-58,1	-31,1	20,3	29,2		18,90	0,797		0,101	
Dol B	fi17	148,7		-56,9	-32,9	20,9	30,1		18,89	0,790		0,105	
Dol B	fi18	143,8		-55,7	-30,1	19,5	28,7		19,00	0,801		0,099	
Dol B	fi19	148,9		-54,4	-32,8	20,9	29,6		18,90	0,790		0,105	
Dol B	fi20	144,0		-53,2	-31,9	20,5	29,6		18,84	0,794		0,103	
Dol B	fi21	149,0		-52,0	-32,1	20,6	29,7		18,98	0,793		0,103	
Dol B	fi22	144,1		-50,8	-31,9	20,5	29,6		18,84	0,794		0,103	
Dol B	fi23	149,2		-52,6	-30,1	19,5	28,7		19,16	0,801		0,099	
Dol B	fi24	154,3		-54,4	-31,6	20,4	29,5		19,19	0,795		0,102	
Dol B	fi25	149,4		-52,2	-32,9	20,9	30,1		18,91	0,790		0,105	

Locality: Llamazares **Sample** DL202

Phase FL	FL	Th °C	T _{h_{gas}} °C	T _{h_{ice}} °C	T _{m_{ice}} °C	Salinity (eq. Wt %)			Molar Vol	Bulk composition			
						MgCl ₂	NaCl	CaCl ₂		xH ₂ O	xMg ²⁺	xNa ⁺	xCa ²⁺
Dol A2	fi1	110,1		-61,2	-33,0	20,8	30,189		17,60	0,790		0,105	
Dol A2	fi2	110,4		-61,5	-33,0	20,8	30,189		17,61	0,790		0,105	
Dol B	fi3	114,7		-60,8	-29,9	19,9	28,6053		18,14	0,802		0,099	
Dol B	fi4	114,1		-60,1	-29,7	19,9	28,4987		18,15	0,803		0,099	
Dol B	fi5	114,3		-60,4	-31,3	20,3	29,3361		17,96	0,796		0,102	
Dol B	fi6	110,6		-60,7	-31,9	20,5	29,6413		17,77	0,794		0,103	
Dol B	fi7	105,9		-60,1	-32,1	20,6	29,742		17,59	0,793		0,103	
Dol B	fi8	114,7		-59,8	-30,7	20,2	29,0262		18,05	0,799		0,101	
Dol B	fi9	114,6		59,8	-32,6	20,7	29,9916		17,81	0,791		0,104	
Dol B	fi10	114,3		-60,9	-29,9	19,9	28,6053		18,13	0,802		0,099	
Dol B	fi11	110,6		-60,2	-31,1	20,3	29,2334		17,87	0,797		0,101	
Dol B	fi12			-60,5	-31,3								
Dol B	fi13	114,4		-60,8	-32,2	20,6	29,7922		17,85	0,793		0,104	
Dol B	fi14			-60,8									
Dol B	fi15	114,3		-60,1	-31,7	20,5	29,5401		17,91	0,795		0,103	
Dol B	fi16	110,6		-60,4	-31,6	20,4	29,4893		17,81	0,795		0,102	
Dol B	fi17	115,1		-60,9	-29,5	19,8	28,3916		18,20	0,804		0,098	
Dol B	fi18	114,7		-60,1	-29,4	19,8	28,3378		18,20	0,804		0,098	
Dol B	fi19	114,1		-60,8	-31,3	20,3	29,3361		17,96	0,796		0,102	
Dol B	fi20	114,3		-60,1	-33,0	20,8	30,189		17,74	0,790		0,105	
Dol B	fi21	110,6		-60,4	-32,1	20,6	29,742		17,74	0,793		0,103	
Dol B	fi22	105,9		-60,7	-32,7	20,5	30,0411		17,51	0,791		0,105	
Dol B	fi23				-32,6								
Dol B	fi24	114,1		-60,1	-29,8	19,9	28,5521		18,14	0,802		0,099	
Dol B	fi25	114,8		-60,4	-29,9	19,9	28,6053		18,15	0,802		0,099	

Locality: Crémenes **Sample DL233**

Phase FL	FL	Th °C	T _{h_{gas}} °C	T _{h_{ice}} °C	T _{m_{ice}} °C	Salinity (eq. Wt %)			Molar Vol	Bulk composition			
						MgCl ₂	NaCl	CaCl ₂		xH ₂ O	xMg ²⁺	xNa ⁺	xCa ²⁺
DolC	fi1	140,5	-68,2	-70,8	-32,1	20,6	29,742		18,70	0,793		0,103	
DolC	fi2	150,5	-67,4	-70,2	-29,8	19,9	28,5521		19,23	0,802		0,099	
DolC	fi3	145,4	-69,1	-75,9	-33,0	20,8	30,189		18,77	0,790		0,105	
DolB	fi4				-33,0								
DolB	fi5	150,2	-67,4	-71,2	-29,2	19,7	28,2297		19,27	0,805		0,098	
DolB	fi6	139,4	-75,9	-33,0	20,8	30,189			18,57	0,790		0,105	
DolB	fi7	140,5	-68,2	-69,8	-33,0	20,8	30,189		18,61	0,790		0,105	
DolB	fi8	142,6	-67,4	-70,2	-29,2	19,7	28,2297		19,05	0,805		0,098	
DolB	fi9	148,8	-70,1	-75,9	-33,0	20,8	30,189		18,88	0,790		0,105	
DolB	fi10	140,2		-70,8	-33,0	20,8	30,189		18,60	0,790		0,105	
DolB	fi11				-29,8								
DolB	fi12	141,7	-69,4	-75,9	-33,0	30,2	30,2		18,65	0,790		0,105	
DolB	fi13	140,9	-68,2	-75,8	-33,0	30,2	30,2		18,62	0,790		0,105	
DolB	fi14	150,3	-67,4	-70,2	-29,8	19,9	28,5521		19,22	0,802		0,099	
DolB	fi15	139,4		-75,9	-32,3	20,6	29,8422		18,65	0,792		0,104	
DolB	fi16	140,3	-68,2	-70,8	-32,3	20,6	29,8422		18,68	0,792		0,104	
DolB	fi17	149,7	-67,3	-70,2	-32,1	20,6	29,742		19,00	0,793		0,103	
DolB	fi18	142,6		-70,2	-32,9	20,9	30,1398		18,69	0,790		0,105	
DolB	fi19	148,8		-75,9	-32,3	20,6	29,8422		18,95	0,792		0,104	
DolB	fi20				-32,3								
DolB	fi21	145,4		-70,2	-32,3	20,6	29,8422		18,84	0,792		0,104	
DolB	fi22	139,8		-75,9	-32,7	20,5	30,0411		18,62	0,791		0,105	
DolB	fi23	149,7		-70,8	-32,6	20,7	29,9916		18,95	0,791		0,104	
DolB	fi24	142,6		-70,2	-29,9	19,9	28,6053		18,98	0,802		0,099	
DolB	fi25	148,8		-69,8	-31,1	20,3	29,2334		19,06	0,797		0,101	

Locality: Saliencia Sample: DI125

Phase FL	FL	Th °C	T _{h_{gas}} °C	T _{h_{ice}} °C	T _{m_{ice}} °C	Salinity (eq. Wt %)			Molar Vol	Bulk composition			
						MgCl ₂	NaCl	CaCl ₂		xH ₂ O	xMg ²⁺	xNa ⁺	xCa ²⁺
C1	fi1	98,5	-42,5	-76,6	-25,9		23,2		19,18	0,872		0,043	0,085
C1	fi2	95,2	-49,5	-77,8	-20,3		20,7		19,05	0,887		0,038	0,075
DolA2	fi3	140,5	-58,2	-69,1	-32,8	20,8	30,0905		18,63	0,790	0,105		0,105
DolA2	fi4	140,2	-57,6	-68,7	-32,9	20,9	30,1398		18,61	0,790	0,105		0,105
DolA2	fi5	145,6	-59,4	-69,1	-32,3	20,6	29,8422		18,85	0,792	0,104		0,104
DolA2	fi6	150,1	-55,6	-64,7	-32,6	20,7	29,9916		18,96	0,791	0,104		0,104
DolA2	fi7	149,5		-69,1	-32,6	20,7	29,9916		18,94	0,791	0,104		0,104
DolA2	fi8	145,2		-68,3	-32,9	20,9	30,1398		18,77	0,790	0,105		0,105
DolA2	fi9	145,6		-69,2	-32,4	20,7	29,8922		18,84	0,792	0,104		0,104
DolA2	fi10	150,5		-64,7	-32,6	20,7	29,9916		18,98	0,791	0,104		0,104
DolA2	fi11	140,5		-69,1	-32,8	20,8	30,0905		18,63	0,790	0,105		0,105
DolA2	fi12	143,7		-68,7	-32,9	20,9	30,1398		18,72	0,790	0,105		0,105
DolA2	fi13	145,6		-67,1	-33,0	20,8	30,189		18,78	0,790	0,105		0,105
DolA2	fi14	150,1		-65,6	-32,6	20,7	29,9916		18,96	0,791	0,104		0,104
DolA2	fi15	140,5		-65,4	-32,3	20,6	29,8422		18,68	0,792	0,104		0,104
DolA2	fi16	141,2		-68,7	-32,9	20,9	30,1398		18,64	0,790	0,105		0,105

Locality: Sierra del Turrón

Sample: DL169

Phase FL	FL	Th °C	T _{h_{gas}} °C	T _{h_{ice}} °C	T _{m_{ice}} °C	Salinity (eq. Wt %)			Molar Vol	Bulk composition			
						MgCl ₂	NaCl	CaCl ₂		xH ₂ O	xMg ²⁺	xNa ⁺	xCa ²⁺
DolB	fi1	131,4	-74,2	-78,8	-32,1	22,7	29,74		18,41	0,793		0,103	
DolB	fi2	144,6	-80,1	-84,2	-36,2	21,7	31,70		18,39	0,778		0,111	
DolB	fi3	142,1		-82,9	-36,5	21,8	31,84		18,26	0,776		0,112	
DolB	fi4	138,2	-77,5	-79,6	-35,7	21,6	31,47		18,22	0,779		0,110	
DolB	fi5	141,8	-79,7	-81,6	-36,1	21,7	31,66		18,30	0,778		0,111	
DolB	fi6	139,5		-81,1	-35,4	21,5	31,33		18,30	0,781		0,110	
DolB	fi7	135,8											
DolB	fi8	145,1	-80,2	-86,5	-34,8	21,3	31,05		18,57	0,783		0,109	
DolB	fi9	138,8	-80,3	-83,8	-35,2	21,4	31,24		18,30	0,781		0,109	
DolB	fi10	143,8		-81,5	-84,7	-35,3	21,5	31,29		18,47	0,781		0,110
DolB	fi11					-33,2							
DolB	fi12					-36,2							
DolB	fi13	142,1		-82,9	-36,5	21,8	31,84		18,26	0,776		0,112	
DolB	fi14	138,2	-77,5	-79,6	-35,7	21,6	31,47		18,22	0,779		0,110	
DolB	fi15	141,8	-79,7	-81,6	-36,1	21,7	31,66		18,30	0,778		0,111	
DolB	fi16				-35,4								
DolB	fi17	135,8		-79,3	-35,8	21,6	31,52		18,12	0,779		0,110	
DolB	fi18	145,1	-80,2	-86,5	-34,8	21,3	31,05		18,57	0,783		0,109	
DolB	fi19	138,8	-80,3	-83,8	-35,2	21,4	31,24		18,30	0,781		0,109	
DolB	fi20	143,8											
DolB	fi21	139,9	-73,4	-79,2	-33,2	20,9	30,29		18,57	0,789		0,106	
DolB	fi22	142,1	-80,8	-82,9	-36,5	21,8	31,84		18,26	0,776		0,112	
DolB	fi23	138,8	-80,5	-86,5	-35,2	21,4	31,24		18,30	0,781		0,109	
DolB	fi24	143,8	-80,3	-83,8	-35,3	21,5	31,29		18,47	0,781		0,110	
DolB	fi25	139,9	-80,7	-84,7	-33,2	20,9	30,29		18,57	0,789		0,106	

Locality: Cueta **Sample DL249**

Phase FL	FL	Th °C	Tn _{gas} °C	Tn _{ice} °C	Tm _{ice} °C	Salinity (eq. Wt %)			Molar Vol	Bulk composition			
						MgCl ₂	NaCl	CaCl ₂		xH ₂ O	xMg ²⁺	xNa ⁺	xCa ²⁺
DolA2	fi1	114,9	-62,8	70,1	-30,3	20,0	28,8		19,02	0,800	0,100	0,100	
DolA2	fi2	116,3	-63,4	-65,3	-32,5	20,7	29,9		17,87	0,792	0,104	0,104	
DolA2	fi3	113,9	-62,5	-69,6	-32,4	20,7	29,9		17,81	0,792	0,104	0,104	
DolA2	fi4	108,7	-67,4		-31,8	20,5	29,6		17,72	0,794	0,103	0,103	
DolA2	fi5	102,8	-68,1		-32,8	20,8	30,1		17,39	0,790	0,105	0,105	
DolA2	fi6	116,3	-70,1	-73,9	-30,5	20,1	28,9		18,12	0,800	0,100	0,100	
DolA2	fi7	116,9	-72,0	-78,2	-32,9	20,9	30,1		17,84	0,790	0,105	0,105	
DolA2	fi8	108,7	-73,9		-32,5	20,7	29,9		17,63	0,792	0,104	0,104	
DolA2	fi9	102,3	-75,8		-32,5	20,7	29,9		17,42	0,792	0,104	0,104	
DolA2	fi10	116,3	-77,7	-62,5	-32,6	20,7	30,0		17,86	0,791	0,104	0,104	
DolA2	fi11	116,9	-79,6	-66,8	-31,6	20,6	29,5		18,01	0,795	0,102	0,102	
DolA2	fi12	108,4	-81,5	-70,5	-30,2	20,0	28,8		17,92	0,801	0,100	0,100	
DolA2	fi13	112,3		-72,1	-32,7	20,5	30,0		17,72	0,791	0,105	0,105	
DolA2	fi14	116,3	-85,3	-61,1	-31,2	20,3	29,3		18,04	0,797	0,102	0,102	
DolA2	fi15	115,9	-87,2	-65,4	-30,7	20,2	29,0		18,09	0,799	0,101	0,101	
DolA2	fi16	108,7	-89,1		-31,8	20,5	29,6		17,72	0,794	0,103	0,103	
DolA2	fi17	102,9	-91,0		-30,8	20,2	29,1		17,67	0,798	0,101	0,101	
DolA2	fi18	116,3	-92,9	-69,7	-32,4	20,7	29,9		17,89	0,792	0,104	0,104	
DolA2	fi19	114,5		-64,0	-32,8	20,8	30,1		17,78	0,790	0,105	0,105	
DolA2	fi20	108,7			-32,9	20,9	30,1		17,57	0,790	0,105	0,105	

Locality: Sierra del Turrón

Sample: DL223

Phase FL	FL	Th °C	T _{H_{gas}} °C	T _{H_{ice}} °C	T _{m_{ice}} °C	Salinity (eq. Wt %)			Molar Vol	Bulk composition				
						MgCl ₂	NaCl	CaCl ₂		xH ₂ O	xMg ²⁺	xNa ⁺	xCa ²⁺	xCl ⁻
DolB	fi1	130,8	-70,1	-76,1	-34,1	21,1	30,72		18,16	0,785		0,107		0,107
DolB	fi2	120,9	-69,5	-75,8	-32,1	20,6	29,74		18,07	0,793		0,103		0,103
DolB	fi3	132,5	-68,5	-77,4	-32,6	20,7	29,99		18,39	0,791		0,104		0,104
DolB	fi4	135,2		-75,1	-33,7	21,0	30,53		18,35	0,787		0,107		0,107
DolB	fi5	137,9												
DolB	fi6	130,6	-70,5	-34,9	21,4	31,10		18,05	0,782		0,109		0,109	
DolB	fi7			-33,0										
DolB	fi8	136,2		-32,1	20,6	29,74		18,57	0,793		0,103		0,103	
DolB	fi9	132,7	-68,5	-63,6	-31,2	20,3	29,28		18,55	0,797		0,102		0,102
DolB	fi10	132,4		-61,3	-30,3	20,0	28,82		18,64	0,800		0,100		0,100
DolB	fi11	134,1	-68,5	-68,1	-31,4	20,4	29,39		18,57	0,796		0,102		0,102
DolB	fi12	136,8		-66,5	-32,5	20,7	29,94		18,54	0,792		0,104		0,104
DolB	fi13	129,5												
DolB	fi14	132,2		-62,1	-34,7	21,3	31,01		18,13	0,783		0,108		0,108
DolB	fi15	134,9	-68,5	-69,8	-35,8	21,6	31,52		18,09	0,779		0,110		0,110
DolB	fi16				-36,9									
DolB	fi17	130,3	-68,5	-61,9	-36,1	21,7	31,66		17,89	0,778		0,111		0,111
DolB	fi18	133,0		-69,6	-32,1	20,6	29,74		18,46	0,793		0,103		0,103
DolB	fi19	135,7	-68,5	-67,3	-32,2	20,6	29,79		18,54	0,793		0,104		0,104
DolB	fi20	128,4		-65,0	-31,3	20,3	29,34		18,41	0,796		0,102		0,102
DolB	fi21	131,1	-68,5	-68,4	-34,4	21,2	30,86		18,13	0,784		0,108		0,108
DolB	fi22	133,8		-65,0	-33,5	21,0	30,43		18,33	0,788		0,106		0,106
DolB	fi23	136,5		-64,3	-33,7	21,0	30,53		18,40	0,787		0,107		0,107
DolB	fi24	129,2		-68,6	-34,2	21,2	30,77		18,09	0,785		0,108		0,108
DolB	fi25	131,9		-34,9	21,4	31,10		18,10	0,866	0,782		0,782		0,782

Locality: Viadango II **Sample** DL155

Phase FL	FL	Th °C	T _{Ngas} °C	T _{hice} °C	T _{mice} °C	Salinity (eq. Wt %)			Molar Vol	Bulk composition			
						MgCl ₂	NaCl	CaCl ₂		xH ₂ O	xMg ²⁺	xNa ⁺	xCa ²⁺
DolA2	fi1	126,7		-63,5	-33,7	21,0	30,53		18,07	0,787		0,107	0,107
DolA2	fi2	126,3		-62,8	-34,2	21,2	30,77		17,99	0,785		0,108	0,108
DolA2	fi3	125,5		-64,3	-33,4	20,9	30,38		18,06	0,788		0,106	0,106
DolA2	fi4	130,1	-60,1	-61,8	-34,8	21,3	31,05		18,05	0,783		0,109	0,109
DolA2	fi5	128,2		-62,4	-32,5	20,7	29,94		18,26	0,792		0,104	0,104
DolA2	fi6	128,7	-61,8	-63,1	-32,1	20,6	29,74		18,32	0,793		0,103	0,103
DolA2	fi7	126,4		-62,8	-34,8	21,3	31,05		17,92	0,783		0,109	0,109
DolA2	fi8	133,7		-64,3	-32,1	20,6	29,74		18,49	0,793		0,103	0,103
DolA2	fi9	141,3		-65,6	-32,6	20,7	29,99		18,68	0,791		0,104	0,104
DolA2	fi10	135,8	-60,4	-67,2	-33,4	20,9	30,38		18,41	0,788		0,106	0,106
DolA2	fi11	128,3	-60,736	-62,3	-32,2	20,6	29,79		18,30	0,793		0,104	0,104
DolA2	fi12	125,4		-64,1	-30,2	20,0	28,76		18,44	0,801		0,100	0,100
DolA2	fi13	132,1	-60,721	-63,8	-35,7	21,6	31,47		18,00	0,779		0,110	0,110
DolA2	fi14	128,9	-60,714	-62,1	-32,5	20,7	29,94		18,28	0,792		0,104	0,104
DolA2	fi15	128,3	-60,707	-62,1	-31,9	20,5	29,64		18,33	0,872		0,794	0,794

Locality: Salamón

Sample DL244

Phase FL	FL	Th °C	Tn _{gas} °C	Tn _{ice} °C	Tm _{ice} °C	Salinity (eq. Wt %)			Molar Vol	Bulk composition		
						MgCl ₂	NaCl	CaCl ₂		xH ₂ O	xMg ²⁺	xNa ⁺
DolC	fi1	101,5		-60,2	-25,2	18,3	25,939		18,31	0,822	0,089	0,089
DolC	fi2	101,2		-62,4	-25,2	18,3	25,939		18,30	0,822	0,089	0,089
DolC	fi3	100,8	-60,1	-65,1	-24,4	18,5	25,4485		18,38	0,8226	0,087	0,087
DolC	fi4	98,2		-42,8	-25,1	18,4	25,8783		18,23	0,823	0,089	0,089
DolC	fi5	99,8		50,8	-26,6	18,9	26,7702		18,10	0,816	0,092	0,092
DolB	fi6	108,8		-70,4	-31,3	20,3	29,3361		17,79	0,796	0,102	0,102
DolB	fi7	102,6		-75,1	-32,8	20,8	30,0905		17,38	0,790	0,105	0,105
DolB	fi8	105,8		-75,4	-32,9	20,9	30,1398		17,48	0,790	0,105	0,105
DolB	fi9	105,3		-72,5	-32,2	20,6	29,7922		17,56	0,793	0,104	0,104
DolB	fi10	106,1		-74,1	-32,8	20,8	30,0905		17,50	0,790	0,105	0,105
DolB	fi11				-31,2							
DolB	fi12	106,6		-74,1	-31,3	20,3	29,3361		17,72	0,796	0,102	0,102
DolB	fi13	109,8										
DolB	fi14	109,3		-72,3	-31,4	20,4	29,3873		17,79	0,796	0,102	0,102
DolB	fi15	109,1		-74,9	-32,8	20,8	30,0905		17,60	0,790	0,105	0,105
DolB	fi16	101,8		-74,4	-32,1	20,6	29,742		17,46	0,793	0,103	0,103
DolB	fi17	101,6		-74,1	-32,7	20,5	30,0411		17,37	0,791	0,105	0,105
DolB	fi18				-32,9							
DolB	fi19	102,3		-73,5	-32,7	20,5	30,0411		17,39	0,791	0,105	0,105
DolB	fi20	102,8		-74,1	-32,8	20,8	30,0905		17,39	0,790	0,105	0,105
DolB	fi21	101,3		-72,3	-31,9	20,5	29,6413		17,47	0,794	0,103	0,103
DolB	fi22				-31,2							
DolB	fi23	105,8		-70,4	-30,5	20,1	28,9218		17,80	0,800	0,100	0,100
DolB	fi24	103,6		-75,1	-30,9	20,2	29,1301		17,68	0,798	0,101	0,101
DolB	fi25	103,8		-75,7	-30,9	20,2	29,1301		17,68	0,798	0,101	0,101

Locality: Malva

Sample DL281

Phase FL	FL	Th °C	T _{Ngas} °C	T _{hice} °C	T _{mice} °C	Salinity (eq. Wt %)			Molar Vol	Bulk composition			
						MgCl ₂	NaCl	CaCl ₂		xH ₂ O	xMg ²⁺	xNa ⁺	xCa ²⁺
DolA2	fi1	98,3		-64,4	-33,2	20,9	30,29		17,19	0,789		0,106	
DolA2	fi2	95,6		-62,5	-30,2	20,0	28,76		17,52	0,801		0,100	
DolA2	fi3	136,9		-60,1	-34,6	21,3	30,96		18,31	0,783		0,108	
DolA2	fi4	134,2		-60,1	-34,8	21,3	31,05		18,24	0,783		0,109	
DolA2	fi5	134,5		-60,2	-34,5	21,3	30,91		19,30	0,784		0,108	
DolA2	fi6	134,5		-59,8	-33,9	21,1	30,63		18,31	0,786		0,107	
DolA2	fi7	134,6		-60,1	-33,4	20,9	30,38		18,37	0,788		0,106	
DolA2	fi8	132,8		-61,4	-34,1	21,1	30,72		18,23	0,785		0,107	
DolA2	fi9	132,9		-61,6	-32,6	20,7	29,99		18,40	0,791		0,104	
DolA2	fi10	134,7		-60,8	-32,6	20,7	29,99		18,46	0,791		0,104	
DolA2	fi11	133,9		-60,1	-32,3	20,6	29,74		18,49	0,793		0,103	
DolA2	fi12	133,5		-60,1	-32,2	20,6	29,79		18,47	0,793		0,104	
DolA2	fi13	136,1		-60,2	-32,9	20,8	30,14		18,47	0,790		0,105	
DolA2	fi14	136,5		-59,8	-33,1	20,9	30,24		18,47	0,870		0,105	
DolA2	fi15	135,2		-61,3	-30,1	20,0	28,71		18,74	0,801		0,099	

ANNEX 10
CRUSH LEACH DATA

Locality	Sample Number	Dolomite Phase	Cl ppm IC	Br ppm IC	SO4 ppm IC	Na ppm AAS	K ppm AAS	Li ppm AAS	C. Balance AAS	Cl ppm	Br ppm	Cl/Br molar	SO4/Br molar	Na/Br	K/Na	Li/Na	K/Cl
Llamazares	DL202	Dol B	16.92227	0.1140454	0.5027077	7.4896	0.648	0.00225	0.7017341	17712.62	1199.0183	333.96378	3.6687105	228.13919	11.61094	0.0508941	0.0009956
Cremenes	DL233	Dol B	68.98358	0.6149897	0.98031	22.5483	4.467		0.5551486	179915.05	1603.602	252.51625	1.3266951	127.36934	14.842878	0.1165342	0.0587799
Cremenes	DL233	Dol C	240.6987	2.4615002	2.5603934	36.135	28.04	0.033	0.334732	179915.05	1839.8974	220.08594	0.8657298	50.997293	23.278133	0.4564682	0.0030266
Mina Talco	DL25	Dol B2	63.638813	0.9692403	0.7508307	10.9115	3.79	0.012	0.3157533	182220.87	2775.2845	147.77775	0.6447422	39.108571	7.9805704	0.2043176	0.0036447
Isoba	DL14	Dol B	24.17922	0.0976235	0.5639168	8.0736	2.362		0.5929603	178398.06	720.28177	557.45026	4.7224299	287.29733	49.44192	0.172932	0.088693
Sallentia	DL125	Dol A2	53.360464	0.2690263	1.3958492	18.5815	2.885		0.574173	179004.85	902.48489	446.41964	4.3183647	239.94129	21.913972	0.0913306	0.0490883
Viadangoo II	DL155	Dol A2	52.0277951	0.5381597	2.8938732	13.047	4.32	0.006	0.4433483	183313.11	1896.1295	217.59251	4.4755234	84.220614	16.403728	0.1947799	0.0015241
Malva	DL281	Dol A2	89.293811	0.2198897	3.1902408	22.685	10.67	0.015	0.4888762	182949.03	450.51959	913.97613	12.075193	358.38745	99.1584	0.2766793	0.0021914
Piedras Viejas	DL245	Dol B	77.350334	0.55883947	1.0358857	33.862	4.63	0.009	0.7217682	186889.32	1217.7739	311.7736	1.5439958	210.66397	16.943758	0.0804303	0.0008808
Cueta	DL249	Dol A2	113.21045	0.5643522	6.4492433	44.281	15.82		0.6995646	179611.65	895.36109	451.49684	9.5111729	272.57507	57.283068	0.2101552	0.1268737
Salamanca	DL244	Dol B	17.019546	0.0925563	0.5175547	6.7724	0.902	0.019	0.6573463	180157.77	979.74081	413.86645	4.6539915	254.18818	19.914544	0.0783457	0.0092978

